Effect of Flow Blockages on Interfacial Area in Two-Phase Flows

EFFECT OF FLOW BLOCKAGES ON INTERFACIAL AREA IN TWO-PHASE FLOWS

BY

KENNETH LEUNG, B.Eng.Mgt., M.A.Sc. (Engineering Physics)

McMaster University, Hamilton, Canada

A THESIS

SUBMITTED TO THE DEPARTMENT OF ENGINEERING PHYSICS

AND THE SCHOOL OF GRADUATE STUDIES

OF MCMASTER UNIVERSITY

IN PARTIAL FULFILMENT OF THE REQUIREMENTS

FOR THE DEGREE OF

DOCTOR OF PHILOSOPHY

Doctor of Philosophy (2014) McMaster University

(Engineering Physics) Hamilton, Ontario, Canada

TITLE: Effect of Flow Blockages on Interfacial Area in Two-Phase Flows

AUTHOR: Kenneth Leung

B.Eng.Mgt., M.A.Sc. (Engineering Physics)

McMaster University, Hamilton, Canada

SUPERVISOR: Dr. D. R. Novog

NUMBER OF PAGES: xxiii, 218

Abstract

The interfacial area between two fluid phases governs the rate which mass, momentum and energy can be exchanged. Modern approaches to calculating the evolution of the interfacial area in a fluid system involves modelling each of the coalescence and fragmentation mechanisms. A review of current literature suggests that all of the phenomena have not entirely been characterised.

The current study experimentally examines how bubble fragmentation in a co-current upwards air-water flow is enhanced by a flow obstruction. When the two-phase flow was pumped through a circular orifice, the air bubbles were observed to break apart into 2 daughter particles due to shear at low superficial fluid velocities over time scales of $\Delta t \approx 10\ ms$. Increasing the tube liquid superficial velocity to $j_f = 0.702\ m/s$ caused turbulence to be the dominant process as characterized by the generation of several daughter particles over time scales of $\Delta t < 1\ ms$. Both mechanisms are considered consistent with observations in literature. A unique fragmentation phenomena was observed where the bubbles became entrained in the *vena contracta* downstream of the leading edge of the orifice, leading to a very large number of small $d < 1000\ \mu m$ fragments being pulled off.

The measurement of bubble chord sizes was conducted using ultra fast shutter speed photography at different j_f and j_g. In the free-stream, a sharp peak in the bubble chord size distribution was observed to form at $d < 1000\ \mu m$ when j_f was increased from $j_f = 0.442\ m/s$ to $j_f = 0.702\ m/s$, and is postulated to be the threshold of the start of the turbulent fragmentation mechanism. A joint probability distribution function was applied to the acquired chord data to estimate the bubble mean diameters, and it was found that the mean chord size was about 15% lower than the estimated mean diameter. However, once the bubble began to fragment a bimodal chord size distribution curve formed which incorrectly skewed the transform

results.

In the free stream, the mean bubble aspect ratios ($\overline{AR}$) were measured to be $\overline{AR} = 1.204$ ($\sigma_{AR} = 0.301$) when the flow was at $j_f = 0.191\ m/s$, and decreasing to $\overline{AR} = 0.994$ ($\sigma_{AR} = 0.254$) as the liquid superficial velocity was increased to $j_f = 0.702\ m/s$. Under flow conditions of $j_f = 0.191\ m/s$, the orifice with a blockage ratio of 0.36 was observed to elongate the mean aspect ratio to $\overline{AR} = 1.245$ ($\sigma_{AR} = 0.290$). Increasing the blockage ratio to 0.84 made it more likely for the bubbles to fragment, and this is demonstrated by the bubble population's mean aspect ratio decreasing to $\overline{AR} = 0.932$ ($\sigma_{AR} = 0.223$).

Four effects were found to simultaneously affect the interfacial area when air bubbles were passed through the orifice. Flow concentration and enhanced fragmentation were found to increase the local a_i, while the change in aspect ratio and the increased likelihood of coalescence served to decrease a_i. Examination of the area distribution functions found that in order for bubbles with smaller chord lengths ($d < 1000\ \mu m$) to contribute significantly with the overall interfacial area, the larger parent bubbles needed to be completely broken apart. Flow obstructions with high blockage ratios were found to be much more efficient in completely fragmenting the larger bubble population.

Acknowledgements

This project has evolved and overcome many challenges since its inception, and there have been many people who have influenced it in one way or another. I am most grateful to Brad Statham for his fruitful discussions and being one of the sources of good advice throughout the course of this work. I am also tremendously appreciative of James Strack both for sharing his expertise with the high speed camera and his support in all matters around the lab. I am also indebted to Sarah Chiste for her help during the construction phase of the test facility and Fabricia Piñeiro for her efforts during the initial commissioning of the LDA.

I also sincerely appreciate the love and support from my parents and my brothers over the years. Without their encouragement and understanding throughout my endeavours, it would certainly not have been possible to finish a project of this magnitude. I would also like to thank Stephanie for always being there with her love, as well as her family who have been so kind to me over the last few years.

Finally, I would like to acknowledge my committee members, Drs. D. R. Novog, J. Luxat, L. Leung and M. Lightstone for their patience and guidance over the past few years.

Contents

List of Tables

List of Figures

List of Abbreviations

Abbreviation	Meaning
ADF	Area Distribution Function
AR	Aspect Ratio
BASH	Bourne-again Shell
CAD	Computer Aided Design
CCD	Charge Coupled Device
CADF	Cumulative Area Distribution Function
CDF	Cumulative Distribution Function
CFD	Computational Fluid Dynamics
CT	Computed Tomography
EC	Electrical Conductivity (Probe)
ERT	Electro Resistive Tomography
FFT	Fast Fourier Transform
GIMP	GNU Image Manipulation Program
HSV	High Speed Video
IAC	Interfacial Area Concentration
IATE	Interfacial Area Transport Equation
ID	Inner Diameter
LDA	Laser Doppler Anemometry
LDV	Laser Doppler Velocimetry
LFD	Laser Focus Displacement
MUSIG	Multiple Bubble Size Group

Abbreviation	Meaning
NPT	National Pipe Thread
OD	Outer Diameter
PDF	Probability Distribution Function
PDPA	Phase Doppler Particle Analyzer
PNVG	Point of Net Vapour Generation
RMS	Root Mean Squared
STP	Standard Temperature and Pressure
RTD	Resistance Temperature Detector
VFD	Variable Frequency Drive

List of Symbols

Symbol	Meaning	Units
A_i	Interfacial Area	m^2
A_{tube}, $A_{orifice}$	Tube and Orifice Flow Area	m^2
a_i	Volume Averaged Interfacial Area	m^{-1}
$B(x,y)$	Composite Image	-
$\overline{B}(x,y)$	Average Image	-
C_{TL}	Transverse Lift Coefficient	-
C_{LF}	Shear Lift Coefficient	-
$C_n(x,y)$	Test Image	-
C_0	Drift flux correlation coefficient	-
c	Chord Size	m
$D_{d,\infty}$	Maximum bubble diameter	m
d_{32}	Sauter mean diameter	m
d_{hyd}	Hydraulic diameter	m
e	Ellipticity	-
f	Frequency	Hz
$\vec{F}_{TL}$	Transverse Lift Force	N
$\vec{F}_{LF}$	Shear Lift Force	N
F	Focal Length	m
$\vec{g}$	Gravitational Acceleration	$m/s^{2]}$
H_l, H_g	Enthalpy	kJ/kg
H_{lg}, H_{gl}	Latent Heat of Vapourization	kJ/kg
h_{conv}	Convective Heat Transfer Coeff.	$W/m^2 \cdot K$

Symbol	Meaning	Units
$I_n(x, y)$	Subtracted Image	-
$I(x, y)$	Pixel Intensity at x,y	-
j_l, j_g	Liquid and gas superficial velocities	m/s
k	Wave number	-
k_l, k_g	Thermal Conductivity	$W/m \cdot K$
L	Sample Length	-
M_{ki}	Interfacial drag	Pa/m
$\dot{m}$	Mass Flow Rate	kg/s
n	Bubble Density	m^{-3}
n_{acr}, n_{water}, n_{air}	Acrylic, water and air optical index of refraction	-
P	Pressure	Pa
$P(y\|D)$	Probability of sampling a chord of size y, given a bubble of diameter D.	-
$\mathbf{q}$	Heat Flux	W
$q_{l,i}, q_{g,i}$	Interfacial Heat Transfer	W
q''	Heat Flux	W/m^2
q'''	Volumetric Heat Flux	W/m^3
R_B	Bubble Radius	m
R	Tube Radius	m
s	Fringe Spacing	m
S	Particle Source or Sink Term	-
T	Temperature	$^\circ C$ or K
t	Time	s
u, $\vec{u}$	Velocity	m/s
$\overline{u}$	Mean or Bulk Velocity	m/s
u'	Turbulent/Fluctuating Velocity	m/s
V	Volume	m^3
x, $\vec{x}$	Spatial Coordinate	m
y	Spatial Coordinate	m
z	Spatial Coordinate	m

Greek Symbols	Meaning	Units
α_k	k^{th} Phase Fraction	-
α_g	Void Fraction	-
β	Minor Axis Size Ratio	
χ	Particle Size Distribution Parameter	-
δ	Delta Dirac Function	-
ϵ	Turbulent Dissipation Rate	m^2/s^3
Γ_l, Γ_g	Mass Jump Term	kg/s
γ_0	Interface Velocity	m/s
γ	Ridge Regression Coefficient	-
$\mathcal{F}$	Fourier Transform	-
μ	Viscosity	$Pa \cdot s$
λ	Wavelength	nm
ϕ_{YY}^{X}	Group X a_i source or sink term caused by YY	-
ψ	Shape Factor	-
ρ_l	Liquid density	kg/m^3
ρ_v, ρ_g	Vapour/Gas density	kg/m^3
σ	Surface Tension	$N \cdot m$
σ_x	Scaling Factor	-
τ_k^{μ}	Momentum Source from Viscous Effects	Pa
τ_k	Momentum Source from Turbulence	Pa
θ_0	Laser beam half angle	rad

Subscript	Meaning
c	Continuous Phase
l	Liquid Phase
v	Vapour Phase

Dimensionless Numbers	
Ca	Capillary Number
Fr	Froude Number
Nu	Nusselt Number
Pr	Prandtl Number
Re	Reynolds Number
We	Weber Number

Declaration of Achievement

The project was conceived based on advice and suggestions received from the author's supervisory committee. The design, specification, acquisition and construction of all element of the experimental facility were performed by the author. S. Chiste assisted with the construction of the facility and the design of several key components. F. Piñeiro assisted with the commissioning of the velocity measurement equipment. Manufacturing of the test section was done entirely by the author.

All data acquisition was performed by the author. The post processing software used was entirely conceived of and developed by the author except for some elements of the Python package sci-py which were used where indicated. Some results were validated against external work as indicated and credit is given to the authors as appropriate.

Drs. M. Lightstone and D. R. Novog provided valuable suggestions and feedback on the preliminary draft of the thesis.

Introduction

Understanding and controlling fluids has spurred human development for thousands of years; yet despite its importance, there remain numerous areas which are not yet fully understood. One such area is the behaviour of fluid systems containing more than one phase. In systems where the phases are inhomogeneous, such as in air-water or steam-water flows, the behaviour of the system is difficult to model due to the interaction between the two phases. The ability to accurately predict the behaviour of such systems is of particular interest in the design and analysis of nuclear reactors.

Most modern nuclear power plants utilize a liquid coolant to remove heat generated by fission events occurring within the uranium fuel. In some designs, under normal operating conditions the coolant is allowed to approach or reach its boiling point resulting in a two-phase mixture of liquid and vapour being circulated through parts of the heat transport circuit. In other designs, two-phase flows will occur during abnormal or accident conditions. Safety analysis pertaining to the heat transport circuits of nuclear reactors requires the understanding of the physics governing the fluid systems. An inherent band of uncertainty will surround the results of any analysis due to inaccuracies and imperfections which exist in the underlying models. Logically one of the ongoing research objectives of the field is to better understand the phenomena which occur under two-phase conditions.

Interfacial area transport has been identified by researchers as possibly one of the most important terms in the study of two-phase flows [1]. The rationale behind this statement is that the interfacial area between two phases governs the rate by which inter-phasic interactions can occur. The rates of mass, momentum and energy exchange between the phases are all directly proportional to the available interfacial area.

Despite its importance, the difficulty in measuring the surface area of bubbles or droplets in internal flows means that experimental data is scarce. Several frameworks have been developed to model the behaviour of interfacial area [2, 3], and work is ongoing in integrating these with modern, state-of-the-art computational tools [4]. One of the major challenges which remain in the topic is the representation of the source terms governing the creation and destruction of interfacial area. These source terms are driven in part by the continual coalescence and fragmentation of bubbles in the flow as they interact with one another, the surrounding fluid and the system components.

The current work aims to provide experimental data on the behaviour of isolated bubbles in an air-water mixture as it passes by an obstruction in the flow. It is postulated that the turbulence generated by the obstruction as well as the increase in the magnitude of the local velocity gradients will cause the bubble to fragment, increasing the interfacial area. The goal is to provide new experimental data and enable a better understanding of the mechanisms behind the bubble fragmentation process, which will ultimately allow for the further development and refinement of existing models.

1.1 Background

1.1.1 Single Phase Flow

To describe the behaviour of a fluid, several pieces of information are required. Basic physical properties of the fluid such as its temperature, T, viscosity, μ, and density, ρ, may be derived as a function of its state variables - namely pressure, P and enthalpy, H. If a fluid is in motion, quantities such as its velocity, $\vec{u}$ may also be of interest. Each of these quantities may vary in both time and space. Since describing the behaviour of the fluid at every point in the temporal and spatial domain is impractical for engineering applications, a substantial degree of averaging is typically employed - however a formalized discussion on averaging is beyond the scope of the current work.

Equations (1), (2) and (3) represent the basic local instantaneous conservation equations for mass, momentum and energy (enthalpy) in a single phase fluid according to Ishii [5]. Each equation is expressed per unit volume and time (e.g. $kg \cdot \frac{1}{m^3 s}$, $\frac{kg \cdot m}{s} \cdot \frac{1}{m^3 s}$ $J \cdot \frac{1}{m^3 s}$).

The left hand side of the three equations contain the time rate of change and advection terms. The right hand side of equation (2) contains momentum source terms related to the pressure gradient, viscous stress τ, and gravitational acceleration, $\vec{g}$ [5]. The source terms on the right side of equation (3) represent contributions from an applied heat flux $\mathbf{q}$, pressure changes DP/Dt, shear stresses $\tau \nabla \vec{u}$ and body heating, $\dot{q}$ [5].

$$\frac{\partial \rho}{\partial t} + \nabla \cdot (\rho \vec{u}) = 0 \tag{1}$$

$$\frac{\partial \rho \vec{u}}{\partial t} + \nabla \cdot (\rho \vec{u} \vec{u}) = -\nabla P + \nabla \cdot \tau + \rho \vec{g} \tag{2}$$

$$\frac{\partial \rho H}{\partial t} + \nabla \cdot (\rho H \vec{u}) = -\nabla \cdot \mathbf{q} + \frac{DP}{Dt} + \tau \nabla \vec{u} + \dot{q} \tag{3}$$

1.1.2 Two Fluid Model

In two-phase flows, the complexity of the governing equations increases signficantly in order to account for the interactions between the two phases. In the 'two-fluid' model, two sets of continuity, momentum and energy equations are required. An extensive derivation of these equations was published by Ishii, however many of the terms are well beyond the scope of this study [5]. In light of this, a simplified version of these equations for "practical applications" serves as the basis of the current discussion [6]. Equations (4), (5) and (6) represent the local instant formulation for the mass, momentum and enthalpy equations for phase, k, with α_k representing the volume fraction of that phase [6].

$$\frac{\partial (\alpha_k \rho_k)}{\partial t} + \nabla \cdot (\alpha_k \rho_k \vec{u}_k) = \Gamma_k \tag{4}$$

$$\frac{\partial\left(\alpha_k\rho_k\vec{u}_k\right)}{\partial t}+\nabla\cdot\left(\alpha_k\rho_k\vec{u}_k\vec{u}_k\right)=-\nabla\left(\alpha_k P_k\right)+\nabla\cdot\left[\alpha_k\left(\tau_k^{\mu}+\tau_k^{T}\right)\right]+\alpha_k\rho_k\vec{g}+M_{ki}+u_{ki}\Gamma_k-\nabla\alpha_k\cdot\tau_i \tag{5}$$

$$\frac{\partial\left(\alpha_k\rho_k H_k\right)}{\partial t}+\nabla\cdot\left(\alpha_k\rho_k H_k\vec{u}_k\right)=-\nabla\cdot\alpha_k\left(q_k+q_k^T\right)+\alpha_k\frac{D_k}{Dt}P_k+h_{ki}\Gamma_k+\frac{q''_{ki}}{L_s}+\phi_k \tag{6}$$

Once again, the left hand sides of all three equations represent the storage and advective terms of the mass, momentum and energy. For the discussion of the source terms - particularly those where exchanges occur between phases, it is noted that the interfacial area refers to the boundary between the two fluids as illustrated in figure 1. In the subsequent equations, a_i refers to the interfacial area concentration, which holds units of $m^2/m^3 = 1/m$.

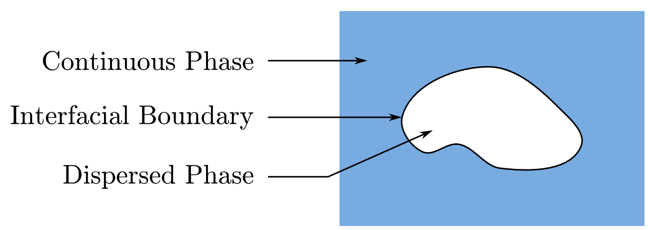

Figure 1: Definition of the interfacial area

The Γ_k on the right hand side of equation (4) represents the rate of mass transfer (in units of kg/m^3s) between the two phases. This term is the mass jump condition, and is restricted by equation (7) which is a statement of mass conservation indicating that any gain in the mass of one phase must be offset by a loss in the other [5]. The Γ_k term is defined in the form of equation (8) according to [5]. The equation indicates that the interfacial mass transfer rate for phase k (in units of kg/m^3s) is equal to the product of the interfacial area concentration (in units of $1/m$) and the mass flux (in units of kg/m^2s) from phase k [5].

$$\sum_{k=1}^{2}\Gamma_k = 0 \tag{7}$$

$$\Gamma_k = a_i G_k \tag{8}$$

In equation (5) the right hand source terms represent [6]:

- $-\nabla(\alpha_k P_k)$ represents momentum sources due to the pressure gradient.
- The terms containing the τ_k^μ and τ_k^T represent the momentum source contributions due to viscous effects and turbulence.
- $\alpha_k \rho_k \vec{g}$ accounts for the gravitational forces acting on phase k.
- M_{ki} is the interfacial drag.
- $u_{ki}\Gamma_k$ is the momentum transfer from phase change
- $-\nabla\alpha_k \cdot \tau_i$ is the interfacial shear stresses.

In the enthalpy equation, the source terms on the right represent [6]:

- q_k is the heat flux from conduction.
- q_k^T represents the contributions of turbulent energy convection and turbulent work.
- $\Gamma_k H_{k,i}$ is the energy contributions due to interfacial mass exchange
- $\frac{q''_{k,i}}{L_s}$ is the inter-phasic heat exchange.
- ϕ_k represents the heat dissipation rate.

The two inter-phasic terms are typically expressed as equation (9) where $H_{k,i}$ is the enthalpy of the interface, h_{ki} is the interfacial heat transfer coefficient and T_k and T_i are the temperatures of phase k and the interface respectively [6]. These inter-phase transfer terms are particularly important in nuclear reactor thermal-hydraulics where for example, the high heat fluxes can cause vapour bubbles to form in a subcooled fluid. Given identical void fractions, a flow with a high concentrations of interfacial area will force the two phases back into equilibrium much faster than a flow with a lower a_i.

$$\Gamma_k H_{k,i} + \frac{q''}{L_s} = a_i \left[\dot{m}_k H_{k,i} + h_{ki} \left(T_i - T_k \right) \right] \tag{9}$$

From these equations, it is evident that any interaction between the two phases will be dependent on the interfacial area. Authors such as Emonot generalize this by saying that the magnitude of the interfacial transfer term is proportional to the product of some constant, the interfacial area and a physical variable [7]. Others such as Ishii propose that the interfacial transfer term is proportional simply to the product of the interfacial area and a 'driving force' [6]. Regardless of the terminology, it is clear that in order to accurately represent the transfer of mass, momentum or energy between two or more phases, the interfacial area must be known.

1.1.3 Need for a New Approach

1.1.3.1 Current Approaches

Codes currently used in the thermalhydraulic analysis of nuclear reactors typically do not explicitly track the interfacial area as a function of space and time. Instead, in modern tools such as RELAP, TRACE or ASSERT, parameters such as the local void fraction, mass fluxes or superficial velocities are computed or tracked. Based on these values the flow regime is determined using a map similar to table 1 and an appropriate relationship for the interfacial area is selected. However there is little agreement among the models as to which input parameters the interfacial area concentration is a function of.

Table 1: Simplified flow regime maps for selected codes at $G = 1500\ kg/m^2 \cdot s$ for vertical, upwards flow.

Code	Bubbly	Slug	Churn/Transistion	Annular
RELAP5-3D [8]	$\alpha_g \leq 0.25$	$0.25 < \alpha_g \leq 0.80$	N/A	$\alpha_g \geq 0.80$
TRACE [9]	$\alpha_g \leq 0.30$	$0.30 < \alpha_g \leq 0.50$	$0.50 < \alpha_g \leq 0.75$	$\alpha_g \geq 0.75$
ASSERT [10]	$\alpha_g \leq 0.20$	$0.20 < \alpha_g \leq 0.50$	$0.50 < \alpha_g \leq 0.80$	$\alpha_g > 0.80$

Each code calculates the interfacial area in a slightly different manner. To demonstrate this point, the interfacial area relationships of the three codes listed in table 1 are examined for an vertical, upwards flow in the bubbly regime.

RELAP5-3D defines the interfacial area concentration according to equation (10) to be a function of the critical Weber number [8]. The critical Weber is representative of the theoretical maximum stable bubble diameter, and is discussed in more detail in section 2.2.1.1.

$$a_i = (0.72\alpha_g)\frac{\rho_l\left(u_g - u_l\right)^2}{\sigma} \tag{10}$$

TRACE uses an approximation for distorted bubbles based on so-called Laplace coefficients, La, as indicated in equation (11) [9]. These Laplace coefficients appear to be derived from the maximum supportable bubble radius based on the Young-Laplace equation [1].

$$a_i = \frac{6\alpha_g}{2 \cdot La} = \frac{6\alpha_g}{2 \cdot \sqrt{\sigma / g\left(\rho_l - \rho_g\right)}} \tag{11}$$

ASSERT approximates the bubble mean diameter by setting it as a linear function of the void fraction [10].

$$a_i = \frac{6\alpha_g}{d_{bubble,ASSERT}} \tag{12}$$

$$d_{bubble,ASSERT} = \begin{cases} d_{min} + \dfrac{d_{max} - d_{min}}{0.2}\alpha_g & d < d_{max} \\ d_{max} & \text{otherwise} \end{cases} \tag{13}$$

In equation (13) the minimum diameter is fixed as per equation (14) while the maximum diameter is the channel hydraulic diameter according to equation (15) [10].

$$d_{min} = 0.000508\ m \tag{14}$$

$$d_{max} = d_{hyd} \tag{15}$$

1.1.3.2 Deficiencies in the Current Approach

[1] The recent work of Talley *et al.* deals with the implementation of the one-group interfacial area transport equation in TRACE [11].

Despite requiring a_i to be known in order to compute the inter-phasic jump conditions, the interfacial area concentration is currently approximated in many different ways. Interpretations range from efforts which attempt to hold true to first principles (TRACE) to empirical (ASSERT).

The difficulty and subsequent lack of data on the interfacial area of two-phase systems means that the models used are heavily approximated. These models are weakly linked to the underlying physics behind interfacial transport, and do not necessarily represent what is actually occuring in the systems being analyzed.

> In non-equilibrium flows, lack of knowledge on interfacial area transport remains a significant contributor to the uncertainty of the codes used.

Each of the methods documented above imply that for a given void fraction and mass flux, there is only <u>one</u> corresponding interfacial area concentration. In some cases, this may be an overly simplified representation of what is actually occuring. In fuel channels, variations in the hydraulic flow area due to obstructions such as end plates, mixing vanes or spacer grids will cause an acceleration of the surrounding fluid. When a vapour bubble is forced through this region, it is subjected to significant inertial and turbulent forces which may cause it disintegrate into numerous smaller daughter bubbles. This bubble fragmentation event will cause the local interfacial area to increase, while conserving the volume of vapour. This in turn will lead to an increase in both the local pressure drop, as well as the rate of vapour condensation if the surrounding fluid is subcooled.

> The current framework in analysis codes does not track or allow for any variation in the bubble configuration. Fragmentation and coalescence are not modelled in modern codes.

1.1.3.3 Premise of a New Approach

Recognizing that the current approach to modelling the interfacial area may be improved, several research groups have begun work on a 'interfacial area transport equation' (IATE), which is discussed in depth in the section 2.1 of the literature review. Briefly, the premise of the IATE is to treat the interfacial area concentration in a two-phase fluid system as a transported scalar. Source and sink terms would account for the creation and destruction of a_i due to bubbles fragmenting or coalescing. One of the challenges is therefore to document and understand each of the complex mechanisms by which bubbles may interact with the flow and with one another.

Next generation codes for nuclear reactor thermalhydraulic safety analysis such as CATHARE 3 aim to fully incorporate some form of interfacial area transport [7]. Other codes such as TRACE have recent "experimental" versions developed to evaluate the IATE [11, 12].

1.2 Study Objectives and Scope

The literature review in Chapter 2 will demonstrate that the sources and sinks of interfacial area are still not well understood - specifically when the two-phase mixture passes through a region where the flow area changes. Recent studies have shown that complex geometries such as mixing vanes or grid spacers cause a substantial increase in the a_i, over and above what is expected with the current source and sink terms [13].

When a two-phase mixture passes through a flow obstruction, changes to the local velocity and turbulence intensity along the bubble surface may increase the likelihood of fragmentation. A single bubble which breaks up into many smaller bubbles will be 'reconfigured' into a arrangement with more interfacial area, representing a source term.

> The goal of this study is to experimentally examine how the bubble fragments when forced through a flow obstruction.

One of the end goals of the IATE is to augment existing thermalhydraulics models, particularly those in use in nuclear safety analysis codes. While it would admittedly be useful for flow geometries resembling reactor fuel channels to be studied, the literature review will demonstrate that there is very little existing data on interfacial area changes through flow obstructions. Since complex geometries such as those found in a reactor fuel channel will make it difficult to isolate the fragmentation mechanisms, a simplified geometry will be studied.

> The blockage will consist of a simple sharp edged, circular orifice, through which an air water mixture will be pumped.

Chapter 2 also indicates that a large number of fragmentation and coalescence mechanisms have already been documented in literature, and emphasizes the need to exercise caution in selecting the flow conditions. While it may be impossible to isolate each one of the mechanisms for individual study, it is possible to reduce the likelihood of bubble coalescence by keeping population density of the bubbles low. Furthermore, a carefully designed flow injection nozzle can reduce the formation of large cap (Taylor) bubbles which have an entirely seperate set of associated fragmentation and coalesence mechanisms.

> This work will focus strictly on the fragmentation of small (non-Taylor) bubbles due to flow obstructions. Low void fraction conditions ($\alpha < 0.05$) will be maintained in order to reduce the influence of concurrently occuring coalescence mechanisms.

A substantial body of the fragmentation theory literature reviewed suggests that the breakup of the bubble is a balance between the turbulent and surface tension forces. While the surface tension forces acting on the bubble may be inferred by observation or some type of assumption (e.g. that all bubbles hold a spherical shape), the turbulence in the continuous phase must be measured directly. This may be difficult to do when two phases are present, so single phase measurements will be conducted.

> Laser Doppler Anemometry will be used to non-invasively measure the velocity and turbulence fields in the region surrounding the orifice.

The literature review also demonstrates that the most common method of measuring interfacial area are conductivity probes which consist of an array of sub-millimeter wires which must be placed in the path of the flow. The highest fluid velocity used in the conductivity probe experiments reported in literature is about 5 m/s, and almost all take place in flows which are axially dominant - that is, there is relatively little lateral component to the flow. The fluid velocities in the current work are expected to be higher in the orifice region, and contain a significant lateral component which may distort or damage a wire probe, thus a non-invasive interfacial area measurement technique needs to be used. When operating in the very low void fraction regime, the ability to use optical based techniques is possible.

> High Speed Video will be used to measure both the velocity and the chord diameter of the bubbles as they pass through the orifice.

1.3 Organization

The current work is organized into six chapters. Chapter 2 is a thorough examination of the current work on the subject of interfacial area transport, and summarizes the experiments conducted on the topic as well as the methods developed to measure a_i. It highlights the areas in the field where data is inadequate - specifically the source and sink terms of the IATE relating to bubble fragmentation.

Chapter 3 provides an overview of measurement techniques used in the current work. The theory behind the laser doppler anemometer (LDA) used to measure the single phase velocity and turbulence intensities is described. High speed video was taken as part of a qualitative description of the bubble fragmentation process, and the camera setup is described. Images taken from high shutter speed tests were post-processed extensively, and both the theory and implementation of the image post-processing programs written are also summarized in this section.

Chapter 4 summarizes the experimental facility which was designed constructed in order to study the bubble fragmentation phenomena. Computer rendered images and a brief description of the instrumentation used is supplied in this portion of the work. Detailed and fully dimensioned drawings are supplied in full in Appendix A.

Chapter 5 is a discussion on the results obtained through each of these measurement techniques. Owing to the significant volume of data acquired, the chapter is meant to be a summary of the highlights and interpretation of the results. A comprehensive compilation of the data obtained is supplied in Appendix B, while discussions on the uncertainties are found in Appendix C.

Chapter 6 is documents the conclusions and suggests extensions of the current work.

Literature Review

The literature review is split into four major areas. The development of the interfacial area transport equations (IATE) is covered in the first section, and an overview of the work conducted over the past 30 years by the various researchers involved are covered. The second section deals with both the theoretical and experimental work conducted in the field of bubble dynamics, with an emphasis on fragmentation mechanisms. The third section presents a discussion on the various techniques which researchers have used to measure the interfacial area concentration in a two-phase flow. In section four, an overview of the experiments performed in the area of interfacial area transport is presented, along with the major conclusions and findings of these works. Since such a large body of information is presented in this chapter, section five distills the key facts from each of the previous sections and explicitly discusses how they shape the objectives of the current study.

2.1 Interfacial Area Transport Equation

2.1.1 One Group IATE

Kocamustafaogullari and Ishii formulated the initial interfacial area concentration transport equations based on the Boltzmann transport theorem [2]. The Boltzmann transport equation was adopted by the authors to describe the behaviour of a set of 'fluid particles' as indicated in equation (16) [2]. The $f(\vec{x}, V, t)$ in the equation is stated by [2] to be a particle volume density distribution which describes the number

Table 2: Source and Sink Terms of the Fluid Particle Transport Equation [2]

Term	Meaning
S_1	Particle volume density sources due to break-up.
S_2	Particle volume density sink due to break-up.
S_3	Particle volume density sources due to coalesence.
S_4	Particle volume density sink due to coalesence.
S_{ph}	Net particle source or sink due to phase change.

of ‘particles’ at some position $\vec{x}$, having a volume V, and at time t. The S terms on the right hand side of equation (16) represent sources and sinks in the particle number density as indicated in table 2 [2].

$$\frac{\partial f\left(\vec{x},V,t\right)}{\partial t}+\nabla\cdot\left(f\left(\vec{x},V,t\right)u_p\right)=\sum_{j=1}^{4}S_j+S_{ph} \tag{16}$$

By multiplying the particle number density equation by the interfacial area, $A_i(V)$ of a particle and then integrating over all particle volumes, the authors arrive at an expression describing the interfacial area concentration transport as indicated in equation (17) [2].

$$\frac{\partial a_i}{\partial t}+\nabla\cdot a_i\vec{u_i}=\phi_{dis}-\phi_{co}+\phi_{ph} \tag{17}$$

In the equation a_i represents the average interfacial area per unit volume (in units of $m^2/m^3 = 1/m$), while $\vec{u_i}$ is the interfacial velocity [2]. The left hand terms represent the interfacial area concentration storage and advection in a control volume. The authors propose that the mechanisms which create or destroy interfacial area are: bubble fragmentation, coalescence and phase change, and these are represented by the three terms on the right hand side of the equation [2]. The physical mechanisms represented by these terms are listed in table 3. In order to fully define the closure relations for any break-up mechanism, the authors state that the maximum bubble volume, daughter bubble size distribution, number of daughter bubbles and the break-up frequency must be known [2]. Similarly for coalescence, the minimum bubble

Table 3: IAC Source and Sink Terms

Term	Meaning
ϕ_{dis}	Net interfacial area concentration change due to bubble fragmentation.
ϕ_{co}	Net interfacial area concentration change due to bubble coalescence.
ϕ_{ph}	Loss or gain of interfacial area due to condensation or evaporation.

volume, collision frequency and coalescence efficiency must be known [2].

The authors in [14] derive the general form of the interaction probability and frequency for coalesence, by assuming that each bubble was a sphere and making several assertions as how they are 'packed'. However, citing a lack of experimental data, the proposed equations were not complete, and the authors retained 'adjustable' coefficients of proportionality in each equation [14].

The work of Wu *et al.* also linked equation (17) to the void fraction by starting with the particle number density transport equation which assumes that the advected scalar is the bubble density, n rather than the interfacial area [14].

$$\frac{\partial n}{\partial t} + \nabla \cdot \vec{u}_{particle} n = \sum_j S_{n,j} + S_{n,ph} \tag{18}$$

In the equation, S represent particle source and sink terms. Then, by assuming that the number density is related to the void fraction by a shape factor of ψ, the authors derived the one-group interfacial area transport equation as:

$$n = \frac{\alpha}{V_{bub}} = \psi \left(\frac{a_i^3}{\alpha^2} \right) \tag{19}$$

$$\frac{\partial a_i}{\partial t} + \nabla \cdot (a_i \vec{u}_{bub}) = \frac{1}{3\psi} \left(\frac{\alpha}{a_i} \right)^2 \left[\sum_j S_{n,j} + S_{n,ph} \right] + \left(\frac{2a_i}{3\alpha} \right) \left[\frac{\partial \alpha}{\partial t} + \nabla \cdot (u_g \alpha) \right] \tag{20}$$

The $S_{n,j}$ terms on the right hand side represent the sources and sinks of particles resulting from the various coalescence and fragmentation mechanisms, while the $S_{n,ph}$

term represents the contributions of phase change [15]. According to the authors, the second term on the right side of the equation relates the change in void fraction to a change in interfacial area, although in their comparison with experimental data, they have neglected it on the basis that the bubbles are incompressible [14]. The validity of this assumption was subsequently rejected in [15], and experiments demonstrate that this term in fact plays a major role. The shape factor for spheres was provided by the authors as [14]:

$$\psi = \frac{1}{36\pi} \tag{21}$$

Equation (20) is referred to as the one group IATE since a single transport equation is used to determine the behaviour of the interfacial area concentration. This infers that the bubbles which make up the interfacial area are all subject to the same fragmentation and coalesence mechanisms. The next section demonstrates that this may be improved by taking into account the differences between Taylor and non-Taylor bubbles.

2.1.2 Two Group IATE

While the authors in [14] were able to fit their equation to experimental data, no data points were taken with $\alpha > 0.10$. One of the major short-comings of the one-group IATE is the assumption that the bubbles are spherical, and so it is only applicable in low void fraction scenarios where this assumption is appropriate [14, 15]. When the void fraction is increased, the rate of coalescence also increases until cap-bubbly or slug flows occur. These flows may occupy the entire diameter of the channel and renders the packing assumptions in the one-group IATE inadequate [15]. In order to overcome this, Hibiki and Ishii proposed a two-group IATE which is somewhat analogous to the two-group neutron transport equations [15].

In the two-group treatment, parts of the dispersed phase consisting of spherical bubbles are referred to as the Group I bubbles [15]. Logically, cap/slug bubbles are referred to as the Group II bubbles, and both are illustrated in Figure 2 [15]. In this framework, both the Group I bubbles and the Group II bubbles are governed by their own transport equations and have their own interfacial area source and sink relationships which are mechanistically derived [15]. The two-group IATE has undergone significant development starting with an initial formulation in [15], to

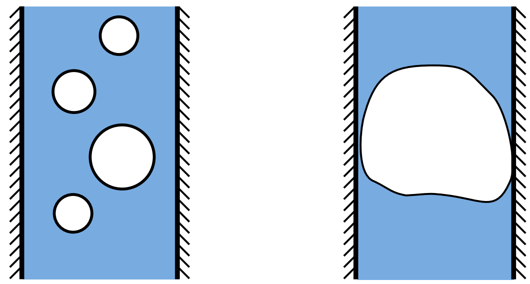

Figure 2: Definition of the shape of Group I (left) and Group II (right) bubbles tracked by the IATE according to Hibiki [15].

versions with more emphasis on the inter-group transfer mechanisms in [16] and [17], and finally the most recent version from Ishii [1]. For the sake of simplicity, the isothermal version of this equation is represented as:

$$\frac{\partial a_{i,1}}{\partial t} + \nabla \cdot (a_{i,1}\vec{u}_{i,1}) = \left[\frac{2}{3} - \chi \left(D_{c1}^{*}\right)^{2}\right] \frac{a_{i,1}}{\alpha_{g,1}} \left[\frac{\partial \alpha_{g,1}}{\partial t} + \nabla \cdot (\alpha_{g,1}\vec{u}_{g,1})\right] + \sum_{j} \phi_{j} \tag{22}$$

$$\begin{aligned} \frac{\partial a_{i,2}}{\partial t} + \nabla \cdot (a_{i,2}\vec{u}_{i,2}) = {} & \frac{2}{3}\frac{a_{i,2}}{\alpha_{g,2}} \left[\frac{\partial \alpha_{g,2}}{\partial t} + \nabla \cdot (\alpha_{g,2}\vec{u}_{g,2})\right] \\ & + \chi \left(D_{c1}^{*}\right)^{2} \frac{a_{i,1}}{\alpha_{g,1}} \left[\frac{\partial \alpha_{g,1}}{\partial t} + \nabla \cdot (\alpha_{g,1}\vec{u}_{g,1})\right] + \sum_{j} \phi_{j} \end{aligned} \tag{23}$$

The left hand side of equations (22) and (23) are simply the time rate of change and advection terms for the interfacial area concentrations of the Group I, $a_{i,1}$, and Group II $a_{i,2}$ bubbles respectively.

The term preceded by $\frac{2}{3}$ in both equations accounts for the compressibility of the dispersed phase, and is ultimately derived from a conservation of volume [16]. It accounts for the change in the interfacial area concentration due to a change in the volume of each bubble [16].

The term preceded by $\chi \left(D_{c1}^{*}\right)^{2}$ represents the contributions to the IAC of each group when a Group I bubble grows and is reclassified as Group II bubble or vice versa [16]. In this inter-group transfer term, $D_{c,1}$ is a dimensionless diameter term which is defined as:

$$D_{c,1}^* = \frac{D_c}{D_{sm,1}} \tag{24}$$

χ represents a particle size distribution parameter derived by Ishii and Kim and is based on work by [16] who recognized that the volume of each bubble was not fixed, but rather followed some type of distribution. The authors noted that one of the major barriers to fully describing the inter-group transfer terms was the lack of an accurate model for describing such a function [16].

The ϕ_j terms represent the numerous interfacial area sources and sinks, and are described in the next section. An example of the physical process which may require such a relationship to be examined or quantified would be a Group II slug bubble violently flowing through a pipe while shedding smaller Group I spherical bubbles. In most of the literature reviewed, the IATE is compared against experimental data from air-water experiments, and so typically ϕ terms dealing with phase change are not considered [5].

2.1.3 Source and Sink Terms

A complete and concise formulation of the interfacial area source and sink terms for the two-group IATE has not yet been established. One of the major barriers to this is the covariance between the terms in the one-dimensional formulation [15]. For the sake of simplicity the discussion in this section will not include sources and sinks due to phase change.

When Hibiki and Ishii developed the two-group IATE, it was understood that the mechanisms could cause the bubbles to become reclassified into a different group after the interaction had taken place, and so the authors identified 8 distinct classifications or interactions which may occur [15]. These intergroup terms are listed in table 4.

The mechanisms identified by Wu *et al.* formed the basis of the development of the source and sink terms [14]. Additional work by Hibiki and Ishii suggest that each of the interaction classifications above would be the result of [14, 15]:

- Coalescence resulting from random, turbulent collisions.
- Coalescence resulting from wake entrainment.

Table 4: Two-Group Interaction Types

Start Bubbles	Interaction	End Bubbles
2 Group I Bubbles	Coalesce	1 Group I Bubble
2 Group I Bubbles	Coalesce	1 Group II Bubble
1 Group I Bubble and 1 Group II Bubble	Coalesce	1 Group II Bubble
2 Group II Bubbles	Coalesce	1 Group II Bubble
1 Group II Bubble	Fragment	2 Group II Bubbles
1 Group II Bubble	Fragment	1 Group II Bubble and 1 Group I Bubble
1 Group II Bubble	Fragment	2 Group I Bubbles
1 Group I Bubble	Fragment	2 Group I Bubbles

- Fragmentation due to an impact with turbulent eddies.
- Fragmentation due to shearing - specifically that which occurs when small bubbles break off of cap bubbles.
- Fragmentation due to flow instabilities

Further work by Ishii identified the following additional physical mechanisms [1, 16]:

- Fragmentation caused by shearing off the base of cap bubbles
- Fragmentation due to surface instabilities of large bubbles
- Fragmentation due to laminar shear
- Coalescence resulting from the rise velocity difference of two nearby bubbles
- Coalescence resulting from velocity gradients.

In the most recent literature [13], a total of 13 distinct source and sink terms have been identified and modelled, and a summary of these are listed in tables 5 and 6. Despite this, the authors suggest the list may still be incomplete. A recent review by Hibiki *et al.* took interfacial area concentration measurements from numerous adiabatic and boiling experiments and compared them data to predictions made using the

Table 5: Coalescence Source and Sink Terms in the 2-Group IATE [13]

Symbol	Meaning	Symbol	Meaning
$\phi_{RC}^{(1)}$	Random collision between a Group I bubble and another Group I bubble resulting in the creation of a Group I bubble	$\phi_{WE}^{(1)}$	Wake entrainment of a Group I bubble by another Group I bubble causing the creation of a Group I bubble
$\phi_{RC}^{(11,2)}$	Random collision between a Group I bubble and another Group I bubble resulting in the creation of a Group II bubble	$\phi_{WE}^{(11,2)}$	Wake entrainment of a Group I bubble by a Group I bubble causing the creation of a Group II bubble
$\phi_{RC}^{(12,2)}$	Random collision between a Group I bubble and a Group II bubble resulting in the creation of a Group II bubble	$\phi_{WE}^{(12,2)}$	Wake entrainment of a Group I bubble by a Group II bubble causing the creation of a Group II bubble
$\phi_{RC}^{(2)}$	Random collision between a Group II bubble and another Group II bubble resulting in the creation of a Group II bubble	$\phi_{WE}^{(2)}$	Wake entrainment of a Group II bubble by a Group II bubble causing the creation of a Group II bubble

IATE [18]. The authors found deviations ±30% were not uncommon, suggesting that the field of interfacial area concentration transport is far from mature [18]. The focus of the current work is on fragmentation of Group I bubbles as they are accelerated due to an obstruction, which is a possible interaction according to table 4, but is not explicitly listed in Table 6.

All of the source and sink terms are mechanistically derived, and can be quite complex. For example, Wu *et al.* originally derived the $\phi_{RC}^{(1)}$ as a function of the packing limit of spheres, the mean distance between two bubbles, and the probability that they will move toward one another [14]. After some further refinement since the original derivation, the term used in the most recent literature is [13]:

$$\phi_{RC}^{(1)} = -0.17C_{RC}^{(1)} \frac{\epsilon^{1/3}\alpha_{i,1}^{1/3}\alpha_{i,1}^{5/3}}{\alpha_{1,max}^{1/3}\left(\alpha_{1,max}^{1/3} - \alpha_1^{1/3}\right)} \left[1 - exp\left(-C_{RC1}\frac{\alpha_{1,max}^{1/3}\alpha_1^{1/3}}{\alpha_{1,max}^{1/3} - \alpha_1^{1/3}}\right)\right] \quad (25)$$

Table 6: Fragmentation Source and Sink Terms in the 2-Group IATE [13]

Symbol	Meaning	Symbol	Meaning
$\phi_{TI}^{(1)}$	Turbulent impact of a Group I bubble causing the creation of two Group I bubbles	$\phi_{SI}^{(2)}$	A Group II becomes unstable and breaks into 2 Group II bubbles
$\phi_{TI}^{(2,11)}$	Turbulent impact of a Group II bubble causing the creation of two Group I bubbles	$\phi_{SO}^{(2,12)}$	A Group II bubble has Group I bubbles sheared off of it, resulting in the creation of one Group II bubble and N Group I bubbles
$\phi_{TI}^{(2)}$	Turbulent impact of a Group II bubble causing the creation of a two Group II bubbles		

2.2 Bubble Fragmentation Theory

One of the earliest studies on the topic was conducted by Taylor who examined Couette flows of syrup containing drops of oil in an attempt to determine the maximum amount which the droplet could be stretched before bursting [19]. The understanding at the time was that bubble fragmentation occurred as a result of shear stresses induced on the interface [19], and this was the focus of many works for the next 20 years. As the field developed, Hinze recognized that the bubble destruction was also being caused by fluctuations of the dynamic pressure across surface - or quite simply, turbulence [20].

Hinze described the bubble fragmentation process as starting from a spherical “globule” and then evolving in one of three ways depending on the hydrodynamic forces present [20]. Type 1 or “Lenticular deformation” occurs when the bubble or droplet is suddenly decelerated, and is esentially flattened into an oblate ellipsoid [20]. Type 2 or “Cigar-shaped deformation” occurs when the globule is accelerated and stretched into an elongated prolate ellipsoid [20]. Type 3 or “bulgy” deformation occurs when local variations in the velocity field cause “protuberances” to occur on the surface of the bubble [20]. Unorthodox descriptions aside, almost all subsequent works in the field have attributed bubble fragmentation to some combination of acceleration, turbulence or interfacial instability [21]. The two former mechanisms are considered relevant to this work, and are examined in this section.

The turbulence induced fragmentation mechanism typically occurs when both the continuous and dispersed phase have similar velocities. Velocity fluctuations along the interfacial boundary create pressure differences which when strong enough can cause the bubble to break apart. If the fluctuations are below the threshold to fragment the bubble, they will deform it chaotically, leading to the "bulgy" type shapes documented by Hinze [20]. Acceleration induced fragmentation occurs when the dispersed and continuous phases have very different velocities, and the bubble or droplet is stretched out. Kolev suggests that the separation occurs because of changes in the coefficient of drag along the bubble surface [21]. Interfacial instabilities are a special class of fragmentation mechanism typically associated with free surfaces, although in specific cases may be applicable to bubble dynamics. For the purposes of this work, only the turbulent and acceleration based fragmentation mechanisms are examined.

Sections 2.2.1 and 2.2.2 discuss how previous authors have explained the bubble fragmentation process. These are general descriptions which are not explicitly linked to the IATE, however many of the underlying concepts are used to develop the interfacial area concentration source and sink terms.

2.2.1 Turbulence Induced Fragmentation

Luo and Svendsen examined a number of turbulent fragmentation models and found that describing the process itself is very complex, and that a number of assumptions or simplifications were required [22]. Table 7 lists the 4 most important simplifications according to Luo, and the justification [22].

Studies conducted by Martínez-Bazán *et al.* [23, 24], utilized a combined High Speed Video and PDPA system to determine the breakup frequency and the probability distribution functions of the size of the resultant daughter bubbles. The authors concluded that the two main factors in determining whether or not a bubble will fragment were the turbulent dissipation rate of the fluid, ϵ, and the diameter of the initial bubble. The fundamental basis for this theory is a balance between the restraining surface tension forces given in equation 26 and destructive turbulent forces in equations 27 and 28 [23]. It is noted that the two left most terms in equation 28 represent the difference in the fluctuating component of the velocity at two different points

Table 7: Common Assumptions in Turbulent Fragmentation Models [22]

Assumption	Rationale
All turbulent interactions are assumed to occur in an isotropic field	This is an assumption which is made to simplify the problem.
All turbulent fragmentation is assumed to result in binary breakage.	The authors found several experiments indicating that turbulent fragmentation almost always results in two daughter particles being formed. They note that while a parent bubble may jettison more than two daughter bubbles in quick succession due to turbulence, these may be considered seperate events.
The size of the resulting daughter bubbles is a stochastic variable.	It is very difficult to create an accurate model to describe the size of the daughter bubbles. Instead, probability distribution functions are used.
Eddies with a larger diameter than that of the bubble are assumed to have no effect on the breakage of the bubble. Instead, they are assumed to convect the bubble.	Larger eddies are assumed to sweep the bubble up by affecting all points on its surface uniformly. This serves the constrain the length scales of the turbulence which are applicable to the fragmentation problem.

along the interface separated by some distance, D, and that the term on the far right is the result obtained by integrating over all turbulent scales [20, 23, 25].

$$\tau_s(D) = 6\frac{\sigma}{D} \tag{26}$$

$$\tau_t(D) = \frac{\rho\overline{\Delta u^2}(D)}{2} \tag{27}$$

$$\overline{\Delta u^2}(D) = \overline{|u(x+D,t) - u(x,t)|^2} = \beta(\epsilon D)^{2/3} \tag{28}$$

The authors experimentally demonstrated that the probability of turbulent fragmentation is proportional to the difference between the two forces, with the minimum required turbulence required to initiate the fragmentation process being $\tau_t = \tau_s$.

2.2.1.1 Weber Number

The fragmentation process begins with a spherical droplet or bubble immersed in some fluid. Some external force acts on the bubble causing it to deform while surface tension at the interface attempts to restore the spherical shape. The bubble stays as a 'single unit' until the external forces exceed some threshold, after which it splits into one or more daughter particles. Based on this understanding, the analysis of the bubble dynamics requires evaluating the balance between the inertial and surface tension forces acting upon the interface.

The dimensionless parameter used to describe the state of the bubble and its surroundings is the Weber number which represents the ratio of the inertial forces acting on the bubble to the surface tension [21]. The exact formulation of the Weber number depends on both the scenario being analyzed and in many cases the justification of the author of the work. The general form of the Weber number is supplied in equation (29) where the density, velocity and length scale are all divided by the surface tension.

$$We = \frac{\rho u^2 d}{\sigma} \tag{29}$$

Hinze recognized that if turbulence were the main cause of fragmentation, then the kinetic energy being supplied by the fluid must be accounted for in the Weber number, and attempted to incorporate it via equation (30) [20]. The $\overline{\Delta u'}^2$ term represents the expected variation in the turbulence between two points separated by a distance, d_{max}. By assuming that the turbulence is homogeneous and isotropic, Hinze was able to tie it into the work of Kolmogorov and Bachelor - specficially the turbulent dissipation rate of the fluid, ϵ [23, 25].

$$We = \frac{\rho_l \overline{(\Delta u'^2)} d_{max}}{\sigma} = \frac{2\rho\epsilon^{2/3} d^{5/3}}{\sigma} \tag{30}$$

Kolev proposes that in air-water flows, the Weber number for acceleration based processes may be represented as equation (31) [21].

$$We_{d,\infty,accel} = \frac{\rho_c \left(u_c - u_{d,\infty}\right)^2 D_{d,\infty}}{\sigma} \tag{31}$$

The ρ_c term represents the density of the continuous phase, u_c is the velocity of the continuous phase, $u_{d,\infty}$ is the velocity of the disperse phase, $D_{d,\infty}$ is the maximum bubble diameter, and σ is the surface tension.

2.2.1.2 Critical Weber Number

The critical Weber number (We_{cr}) is used to delineate the threshold at which bubble fragmentation occurs, however the exact value is dependent on a number of factors and is a topic of extended debate in literature [2, 21]. Several criteria encountered in literature for both the turbulent and acceleration induced fragmentation mechanisms are listed in table 8. This value is often cited and discussed in literature since it represents the maximum stable size a bubble may hold without disintegrating as demonstrated in equation (32).

$$d_{max} = \frac{\sigma We_{crit}}{\rho u^2} \tag{32}$$

2.2.1.3 Fragmentation Models

Two schools of thought exist in the modelling of the turbulent fragmentation rate. Authors such as Luo and Delichatsios use multiple probability distribution functions to describe the likelihood of turbulent eddies hitting a bubble, the fragmentation

[1] This result is unique as the experiment was performed under micro-gravity conditions.

Table 8: Fragmentation Criteria

Reference	Type	Frag. Criteria	Rationale
Kocamustafaogullari [2]	Both	$We_{cr} \geq 1.0$	Hydrodyn. Stability
Wu [14]	Turbulence Induced	$We_{cr} = 2.0$	Experiment (air/water)
Prince [26]	Turbulence Induced	$We_{cr} = 2.3$	Experiment (air/water)
Risso [27]	Turbulence Induced	$We_{cr} = 4.5$	Experiment (air/water)[1]
Ishii [6]	Turbulence Induced	$We_{cr} = 6.0$	Experiment (air/water)
Kolev [21]	Acceleration Induced	$We_{cr} \approx 12$	Lit. Review (steam/water)

efficiency, and the volume distribution of the daughter particles [22, 28]. Since PDFs are used, the equations end up having to be integrated within certain size and velocity bounds, and so the end result is quite complex. These models are more theoretical in nature and further simplifications are generally required before they are in a usable form.

The IATE uses the model for the turbulent fragmentation rate developed by Wu [14]. It relates the source term to the turbulent Weber number (see equation 30) and the critical Weber number (defined as some value from table 8) as indicated by equation (33).

$$R_{TI} = C_{TI}\frac{nu_t}{d_{bub}}exp\left(-\frac{We_{cr}}{We}\right)\sqrt{1-\frac{We_{cr}}{We}} \tag{33}$$

In the equation, R_{TI} is the bubble number source/sink per unit volume, C_{TI} represents an arbitrary scaling constant while n is the incident bubble number density. The source term is plotted in figure 3 for $We_{crit} = 6$, and an interesting feature of this model is that no turbulent fragmentation for a given bubble diameter is expected to occur for any value of $We < We_{crit}$. This underscores the importance of determining the correct value of We_{crit}, which is something that according to table 8 is still not agreed upon.

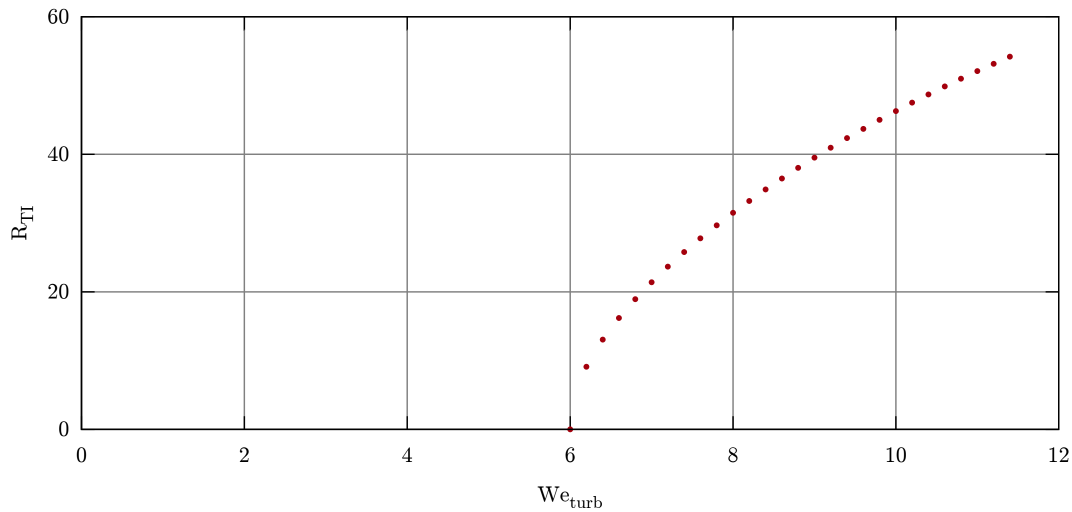

Figure 3: Source term for the bubble number generation due to impact with a turbulent eddy for $We_{crit} = 6$.

2.2.2 Shear Induced Fragmentation

Shear induced fragmentation occurs when the bubble is stretched or pulled apart due to different portions of its surface being exposed to unequal fluid velocities.

Studies in this field trace their lineage back to the work conducted by Taylor who placed a small, neutrally buoyant droplet into a square box with rollers at each corner [19]. When the rollers were rotated, a velocity field emerged in the fluid which eventually stretches the droplet into a ellipse until some finite limit or threshold is reached. Beyond this limit, the bubble or droplet is observed to split into two or more fragments [19].

Over 50 years later, Stone and Leal used a similar apparatus to examine the fragmentation under transient conditions [29]. The key to the success of these experiments was keeping the Reynolds number in the surrounding fluid to a minimum, thus reducing the effects of turbulence [29]. The authors claim conditions of $Re \approx (10^{-4})$ were achieved.

One of the major reviews of the topic was conducted by Stone who indicated that the maximum deformation of the drops was dependent on the Capillary number, Ca, and the relative viscosity ratio, λ_μ, of the two fluids [30].

The Capillary number is used in studies on shear fragmentation to describe the state of the surrounding fluid. As indicated in equation (34) it is the ratio of the fluid viscosity μ and fluid velocity u_f to the surface tension, σ. According to Stone, the bubble will fragment via shear when at $0.1 < Ca < 0.3$ [30].

$$Ca = \frac{\mu u_f}{\sigma} \tag{34}$$

2.3 Interfacial Area Measurement Techniques

The measurement of interfacial area concentration in an internal flow is a non-trivial task since a volume average of a moving two-phase flow must be taken. In order to do so, several methods of estimating the interfacial area concentration exist, with a fairly recent review conducted as part of work done by Zhao *et al.* [31]. Experiments conducted using probes inserted into the flow typically will relate a_i to the interfacial velocity, since these types of devices can look for phase changes in the time domain at a fixed point. When measurements of the radius or bounding box of the bubbles are available, relationships between a_i and the bubble volume may be employed.

2.3.1 Electrical Conductivity Probes

The earliest use of the electrical conductivity probes was attributed to Neal and Bankoff in the 1960's, although it was Kataoka *et al.* [32] and Revankar and Ishii [33] who began using them to measure the local interfacial area concentration. Each probe consists of a pair of thin wires which when immersed in a fluid will close a circuit between them. The greatly reduced resistivity of air means that when a bubble is pierced by the probe, the circuit will be broken. By placing one probe several millimetres downstream of another, the interface velocity (in the direction of the flow) can be calculated by autocorrelating the signals obtained by the two devices [32]. If both the velocity and probe separation distance were known, the bubble size may be computed [32]. Kataoka *et al.* [32] demonstrated that the interfacial area concentration is proportional to the harmonic mean of the interfacial velocity by assuming:

- All bubbles passing the probes were spherical
- The probe passes every part of the bubble with equal probability
- There is no relationship between the surface normal of the interface and the interfacial velocity
- The angle between the bulk flow direction and the interfacial velocity was random

The authors demonstrate that this may be extended to 3-dimensions by representing the surface of each moving bubble in 3-dimensions as a smooth function f_j as in equation (35), where the subscript j represents the index of each passing bubble [32] [2].

$$f_j\left(x,y,z,t\right)=0 \tag{35}$$

In the 3-dimensional case, the local instantaneous interfacial area concentration is the sum of the interfacial contributions from each bubble as indicated in equation (36) [32]:

$$a_i\left(x,y,z,t\right)=\sum_{j=0}^{N}\left|\nabla f_j\right|\delta\left(f_j\left(x,y,z,t\right)\right) \tag{36}$$

Since most experimental techniques such as the two-probe method measure the bubble characteristics at a fixed point (eg x_0, y_0, z_0), Kataoka time averaged the above equation, and made assumptions on the angle between the surface normal of the bubble and its velocity vector, γ_0 [32]. Ultimately, equations (37) and (38) were developed relating the interfacial area concentration to the reciprocal of the harmonic mean of the interface velocity, $\overline{1/u_{j,z}}$, and the standard deviation of the interfacial velocity distribution, $\sigma_{u_{j,z}}$ [32].

$$\overline{a_i}\left(x_0,y_0,z_0\right)=\frac{4N_t\left[\frac{1}{u_{j,z}}\right]}{1-cot\frac{1}{2}\gamma_0 ln\left(cos\frac{1}{2}\gamma_0\right)-tan\frac{1}{2}\gamma_0 ln\left(sin\frac{1}{2}\gamma_0\right)} \tag{37}$$

$$\frac{sin2\gamma_0}{2\gamma_0}=\frac{1-\left(\frac{\sigma_z^2}{\overline{u_{j,z}}^2}\right)}{1+3\left(\frac{\sigma_z^2}{\overline{u_{j,z}}^2}\right)} \tag{38}$$

Additional work conducted Kalkach-Navarro [34] related the chordal measurements made by the probes to the bubble diameters by deriving a joint probability distribution function which related the likelihood of measuring a chord of one length to the probability of it belonging to a bubble of a different diameter.

Further work by Wu [35] attempted to quantify the contributions to the interfacial area of bubbles which did not pass through both probes due to a high lateral velocity,

[2] The function is set equation to 0 to satisfy the definition of the Dirac function: $\int_{-\infty}^{\infty}\delta\left(x-x_0\right)dx=1$ and $\delta\left(x-x_0\right)=0$ for $x\neq x_0$.

and would have otherwise been rejected from the measurements.

Dongjian *et al.* [31] compared both the accuracy and the reliability of the statistical assumptions that Kataoka [32], Hibiki [36], Kalkach-Navarro [34] and Wu [35] made, and found that the original assumptions made by Kataoka best matched the experimental data which they obtained. They also noted that depending on the assumptions or distributions used, the interfacial area concentration reported would differ by about a factor of 4 [31].

Revankar and Ishii [33] and Kalkach-Navarro [34] reported asymmetries in the 'shape' of the signal as the bubble entered and exited the measurement plane, and this was attributed to the bubble deformation which took place as the interface approached and was pierced by the tip of the probe. This was overcome in part with signal conditioning and calibration against optical methods [33].

Kalkach-Navarro [34] noted that when the probe was positioned near a wall, the assumptions originally made by Kataoka would fail as the probe can no longer be assumed to pass through each point of bubble with equal probability. Additionally, the angle between the bulk flow direction and the interfacial velocity vector could no longer be assumed to be random [34]. Hibiki and Ishii [37] estimated that the region which valid measurements could be taken in a circular tube could be defined as $0 \leq r/R \leq 1 - R_B/R$, where R_B is the bubble radius and R is the tube radius [37]. Thus, in a tube with a diameter of 25.4 mm and bubbles of 2 mm in diameter, the authors estimated that the effective measurement region would be defined by $0 \leq r/R \leq 0.84$ [37].

Spurred by some of the limitations of the two-sensor probe method of measuring the interfacial area concentration, Kataoka *et al.* tested and developed a four-probe method [38, 39]. The 4-probe method consists of a single common 'up-stream' probe and 3 'down-stream' probes positioned orthogonally allowing for the interfacial velocity in all three directions to be measured [39]. However since the interface now has to cross 3 pairs of sensors in order to obtain a valid sample, 'escaping' bubbles become an issue, especially in flows with smaller bubbles [39, 40]. Revankar and Ishii developed one of the preliminary 4-probe designs, although size limitations constrained them to measuring the interfacial area concentration in a region defined by $r/R < 0.75$ in a 5.08 cm diameter tube [41]. Kim *et al.* [42, 40] developed a much smaller version of the 4-probe design which served to address some of the concerns noted by [39]. Additionally, the authors describe further signal processing techniques which allows the bubbles to be classified according to the shape data ascertained from the chordal measurements [42].

In the works reviewed, the number of bubbles 'sampled' at each location would vary depending on the author. Using a Monte Carlo approach, Wu and Ishii [35] calculated that by using the electrical conductivity probes with a sample size of 1000 bubbles, there would be a statistical error of $\sigma = \pm 7\%$.

2.3.2 Optical Fiber

The bi-optical or double fiber technique is nearly identical to the electrical conductivity 2-probe methods except that instead of a change in resistance being measured, a change in the index of refraction is detected [43]. Kiambi *et al.* attached phototransistors to one end of a pair of optical fibers, and placed the other end in a bubbly flow [43]. The authors demonstrated that when the fibers are immersed in the liquid, the light is refracted into the surrounding medium [43]. On the other hand, when an air bubble was pierced, the light is reflected back into the fiber, thus allowing the two-phases to be distinguished [43]. However since the authors made use of the same assumptions that Kataoka derived in order to calculate the interfacial area concentration, it can be inferred that the technique will have the same limitations [43].

Further work by Le Corre *et al.* extended the concept to use a set of 4 optical probes in the same manner as the electrical conductivity technique [44]. The authors compared the results obtained from the 4-optical probe technique to those from the 4-conductivity probe technique and found good agreement [44].

2.3.3 Camera Based Methods

Quite often optical methods are used to confirm the void fraction and interfacial area measurements conducted at low void fractions. These methods typically involve one or more cameras focused at a measurement plane. The advantages of such techniques are that they are non-invasive, and can often be used in situations where the geometry of the channel may prevent the electrical conductivity probes from being employed. However a considerable amount of post-processing is typically required in order to get the desired data.

The simplest optical based method involves using a single camera to obtain an estimate of the void fraction. Studies conducted by Revankar and Ishii [33], Dongjian *et al.* [31] and Kim *et al.* [45] for example all utilized some form of video capture in order to validate the measurements obtained. Revankar *et al.* processed images in a stagnant bubble column by manually tracing hundreds of bubbles on projection paper and measuring the diameter [33]. Dongjian *et al.* imported the images into a commercial software package (MSPaint) and manually measured the bubble size and aspect ratios [31]. Kim *et al.* based their measurements on an algorithm developed by Zhang and Ishii for measuring droplet sizes collected by a probe [45, 46]. No specific details were supplied about the algorithm in the paper of Zhang, although the authors do cite Fantini several times who proposed an algorithm for droplet sizing using basic intensity based thresholding [47].

Stereo-imaging was used by Takamasa *et al.* [48], Hibiki *et al.* [49] and Kato *et al.* [50] to ascertain the interfacial area, void fraction and Sauter mean diameter of bubbly flow in a small channel. Takamasa *et al.* positioned their cameras at an angle of 90° from one another, and noted that the stereo imaging technique is useful for flows where $\alpha < 10\%$ due to the bubble crowding and shape changes which occurred beyond this [48]. The authors in [50] show that the accuracy of such a method is about $\sigma = \pm 3\%$ when 3000-4000 bubbles are sampled. Although the stereo-imaging technique is non-invasive, it is useful only under low void fraction conditions, or in small channels where the bubble diameter is on the same order of magnitude as the channel diameter. In an attempt to validate the results of the stereo-imaging technique, Takamasa compared the twin-camera results to those obtained by the 2-probe technique and found excellent agreement in the interfacial area concentration measurements [48]. However, the authors also found that the gas phase velocities measured by the two techniques deviated by ±13.3% [48].

2.3.4 Laser Focus Displacement

The Laser Focus Displacement (LFD) technique is a relatively new way of measuring the interfacial area between two phases [51]. The method focuses a laser beam through an objective lens which oscillates at a known frequency [51]. The motion of the objective lens causes the focal point of the beam to move back and forth near the measurement point of interest [51]. When the focal point intersects with the interface being examined, a high intensity reflection will be observed by an optical receiving element [51]. This when coupled with the position of the lens yields the location of the interface [51].

This technique has been used by Takamasa and Kobayashi to determine thickness of a liquid film, specifically to study the amplitude of the waves on the surface of the interface [52]. Subsequent work by Hazuku et. al. applied this technique to a much smaller channel, and the authors reported being able to detect sub micrometer perturbations in the film thickness [53]. LFD is best suited for high void flows, and in both the studies of [52] and [53], the technique was used to measure flows in the slug or annular regimes.

2.3.5 Wire Mesh

Wire mesh sensors make use of the same principle as the electrical conductivity probes in order to measure the phase of a flow passing through a location [54]. Two planes of wires perpendicular to one another are placed into a flow forming a grid [54]. The two planes are separated by a small distance axially (on the order of $\approx 1.5\ mm$) [54]. Each point where the wires cross constitutes a measurement location [54]. A voltage difference is applied sequentially to each intersection and a current measurement is taken which allows the phase at that point to be determined [54].

Prasser *et al.* initially demonstrated this technique by measuring the void fraction in an air-water flow using a grid size of 16×16 in a $\phi = 0.0512\ m$ diameter pipe [54]. Subsequent work by the authors using video analysis in conjuction with the mesh sensors found that the grid tended to cause passing bubbles to fragment [55]. The authors found that this fragmentation is only an issue at low gas superficial velocities ($j_g \approx 0.05\ m/s$) since at higher air flow rates, the bubble fragments would quickly re-coalesce [55]. The work also demostrated how the technique could be used to measure the bubble size distributions [55]. Work was also conducted by Prasser *et al.* comparing the technique to X-Ray Tomography which found the wire sensors to be better suited to detecting smaller ($d \approx 5\ mm$) bubbles owing to the faster sampling time [56].

Manera *et al.* demonstrated that the wire sensors were also suitable for steam-water flows, and that it was possible to determine the bubble velocities by cross correlating the signals of two sets of meshes a short distance from one another [57]. The author also calculated the interfacial area of a two phase flow by interpolating the point measurements of the wire grid [58] - a technique first demonstrated by Prasser [59]. The study found good agreement between the interpolated grid measurements and those by made using a four-tip needle probe [58].

Additional studies using the wire mesh sensors have been conducted by Prasser *et al.* and Lucas *et al.* to understand how two-phase flows develop axially along a vertical pipe [59, 60]. Using results from these studies, Krepper *et al.* developed the Multiple Bubble Size Group (MUSIG) model and implemented it in the CFD code ANSYS-CFX [3, 4, 61].

More recent studies have involved the TOPFLOW facility in the study air-water and steam-water flows through large diameter ($\phi = 195\ mm$) pipes [59, 62]. Work by Krepper *et al.* and Frank *et al.* have investigated the behaviour of these flows as they are forced around a semi-circular blockage [4, 63]. It is interesting to note that as the bubbles in these flows move past the obstruction, no bubbles were observed with a $d < 2.0\ mm$, which is roughly the axial spacing between the two sets of wires in each mesh [4].

2.3.6 Other Methods

The previous sections reviewed the major methods used to measure the interfacial area in a two-fluid system. However, there exist other, perhaps less reliable methods which should be mentioned in the interest of completeness. These include: ultrasonic beam attenuation [64], chemical absorption (CO_2 gas into a NaOH solution) [65], and X-Ray CT [56].

2.4 Interfacial Area Measurement Experiments

One of the overarching objectives in the development of the interfacial area transport equations is to model the interactions between the two phases [17]. Although authors such as Kocamustafaogullari [2], Wu [14] and Hibiki [66] have gone to great lengths to derive such relationships, ultimately these models need to be validated or verified against experimental data. To facilitate this, a growing number of experiments have been conducted in tube, bundle and duct geometries. Most of the experiments are done with co-current upwards air-water flows, and in a recent review Kataoka noted the popularity of using Electrical Conductivity (EC) probe method to measure a_i in tubes of varying diameters [67].

Table 9: Experiments with the 2 EC Probe Method (1986-2001)

Reference	Method	Meas.	Geom.	Fluids	j_f (m/s)	j_g (m/s)	α_g
Kataoka (1986) [32]	2-Probe EC	u_{int}	6 cm ID tube	air-water	$0.442 - 1.03$	$0.135 - 0.402$	-
Kataoka (1990) [38]	2-Probe EC	u_{int}	3 cm ID tube	air-water	0.5	0.1	-
Revankar (1992) [33]	2-Probe EC	u_{int}	5.08 cm ID tube	air-water	$0.1 - 1.0$	$0.0034 - 0.1212$	-
Kalkach (1993) [34]	2-Probe EC	u_{int}	6 cm ID tube	air-water	$0.3 - 1.25$	$0.081 - 0.4$	$<$ 40%
Hogsett (1997) [68]	2-Probe EC	u_{int}	5.08 cm ID tube	air-water	$0.60 - 1.30$	$0.039 - 0.147$	$1.8 - 7.2$%
Wu (1998) [14]	2-Probe EC	u_{int}	5.08 cm ID tube	air-water	$0.77 - 1.58$	$0.023 - 0.117$	$<$ 10%
Hibiki (1999) [37]	2-Probe EC, Hot-film, γ-Dens.	u_{int},α_g, d_{sm}	2.54 cm ID tube	air-water	$0.292 - 3.49$	-	$3 - 27$%
Bartel (2001) [69]	2-Probe EC	u_{int}	3.81 cm OD, 1.91 cm ID, annulus	steam-water	$0.401 - 1.667$ kg/s	-	-
Hibiki (2001) [70]	2-Probe EC, Hot-film	u_{int}	5.08 cm ID tube	air-water	$0.491 - 5.00$	$0.01 - 5.0$	$4.9 - 44.2$%

Table 10: Experiments with the 2 EC Probe Method (2002-2011)

Reference	Method	Meas.	Geom.	Fluids	j_f (m/s)	j_g (m/s)	α_g
Kim (2002) [45]	2-Probe EC	u_{int}	20 cm^2 duct	air-water	$0.3 - 2.0$	$0.05 - 0.2$	-
Ishii (2002) [6]	2-Probe EC	u_{int}	2.54 cm ID tube	air-water	$0.25 - 3.5$	$0.06 - 0.7$	-
Ishii (2002) [6]	2-Probe EC	u_{int}	5.08 cm ID tube	air-water	$0.6 - 5.0$	$0.04 - 2.0$	-
Ishii (2002) [6]	2-Probe EC	u_{int}	10.16 cm ID tube	air-water	1.0	$0.05 - 0.1$	-
Situ (2004) [71, 72]	2-Probe EC	u_{int}	3.81 cm OD, 1.91 cm ID, annulus	steam-water	$0.5 - 1.22$	-	-
Dongjian (2005) [31]	2-Probe EC, Video	u_{int}, d_{sm}	4.0 cm ID tube	air-water	0.492	$0.011 - 0.033$	$< 35\%$
Yun (2008) [73]	2-Probe EC	u_{int}	3×3 rod bundle	steam-water	$266 - 513$ kg/m^2s	-	$< 15\%$
Kondo (2011) [74]	2-Probe EC	u_{int}	5.0 cm ID tube	air-water	$0.5 - 1.22$	-	-

Table 11: Experiments with the 4 EC Probe Method

Reference	Method	Meas.	Geom.	Fluids	j_f (m/s)	j_g (m/s)	α_g
Revankar (1993) [41]	4-Probe EC	u_{int}	5.08 cm ID tube	air-water	-	$0.006 - 0.041$	7%
Ishii (2001) [40]	4-Probe EC	u_{int}	5.08 cm ID tube	air-water	0.321	$0.052 - 0.432$	$<$ 75%
Ishii (2001) [40]	4-Probe EC	u_{int}	2.54 cm ID tube	air-water	$0.262 - 3.49$	$0.055 - 0.702$	$<$ 75%
Ishii (2001) [40]	4-Probe EC	u_{int}	5.08 cm ID tube	air-water	$0.986 - 5.00$	$0.242 - 1.79$	$<$ 75%
Paranjape (2010) [75]	4-Probe EC	u_{int}	8×8 rod bundle	air-water	$-3.1 - 5.0$	< 10	$<$ 60%
Ozar (2011) [76]	4-Probe EC	u_{int}	3.81 cm OD, 1.91 cm ID, annulus	steam-water	$0.06 - 1.11$	-	$<$ 10%
Yang (2011) [13]	4-Probe EC	u_{int}	8×8 rod bundle	air-water	$0.06 - 1.11$	$0.02 - 4.08$	$2 -$ 77%
Schlegel (2011) [77]	4-Probe EC	u_{int}	15.2 cm ID tube	air-water	$0.4 - 1$	$0.2 - 3.5$	$<$ 70%

Table 12: Experiments Using the Other Methods

Reference	Method	Meas.	Geom.	Fluids	j_f (m/s)	j_g (m/s)	α_g
Takamasa (2000) [52]	LFD	δ	2.6 cm ID tube	air-water	$80 < Re < 2700$	-	-
Kiambi (2001) [43]	2-Optical	u_i	9.4 cm ID tube	air-water	0	$0.003 - 0.09$	-
Takamasa (2003) [48]	Stereo Imaging	α_g, d_{sm}, a_i, N_b, u_g	9.0 mm ID tube	air-water	$0.58 - 1.0$	$0.013 - 0.052$	$< 7\%$
Le Corre (2003) [44]	4-Optical	u_i	5.08 cm ID tube	air-water	$0.163 - 1.231$	$0.090 - 0.368$	$5.6 - 27.8\%$
Hazuku (2005) [53]	LFD	δ	0.2 cm ID tube	air-water	$0.07 - 1.1$	$0.44 - 22$	-
Hazuku (2007) [78]	LFD	δ	1.1 cm ID tube	air-water	$0.088 - 0.790$	$42.4 - 75.0$	-
Hibiki (2007) [49]	Stereo Imaging	α_g, d_{sm}, a_i, N_b, u_g	0.102 cm ID tube	air-water	$1.02 - 4.89$	-	$.98 - 24.6\%$
Prasser (2007) [59]	Wire-Mesh	a_i	19.53 cm ID tube	air-water	1.02	$0.0094 - 0.53$	$< 40\%$
Kato (2009) [50]	Stereo Imaging	α_g, d_{sm}, a_i, N_b	1.03 mm ID tube	air-water	$1.06 - 5.31$	$0.104 - 0.529$	-

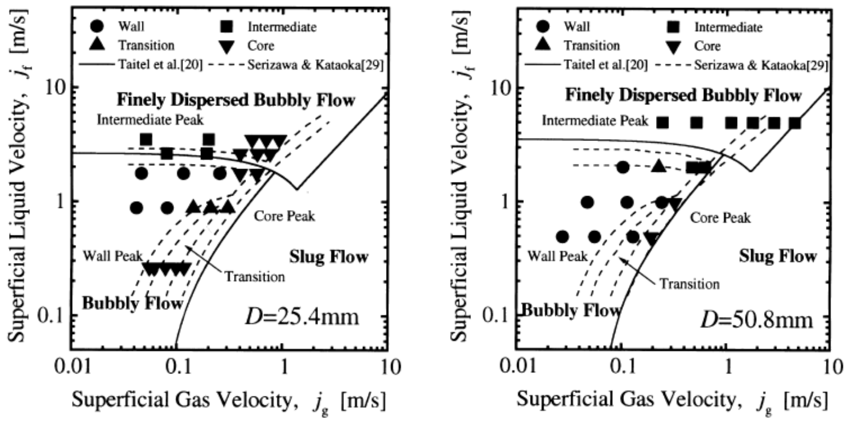

Figure 4: Classification of IAC in bubbly flow [66]

2.4.1 Radial IAC Distribution

In describing the radial distribution of the interfacial area concentration under the bubbly flow regime, the general consensus among the literature involving tube geometries is that there are four IAC classifications: core-peaked, wall-peaked, intermediate, or transition. Figure 4 illustrates the approximate regions where the classifications occur for tube diameters of 25.4 and 50.8 mm [3].

2.4.1.1 Experimental Observations

Hibiki and Ishii observed that in tubes, at low liquid and gas superficial velocities ($j_f \approx 0.26$ m/s, $j_g < 0.1$ m/s), the center-line of the tube contains the highest concentrations of interfacial area and void [37]. Takamasa *et. al.* obtained similar results in their work ($j_l < 1.0$ m/s) using stereo imaging, and also noted that this center-line interfacial area concentration peak is more predominant near the inlet [48]. They suggested that this was characteristic of a flow with many small bubbles all clustered near the center of the channel [48]. As the flow was allowed to develop axially, the smaller bubbles had more opportunities to coalesce forming larger pockets of void, and the authors found that as the measurement point moved away from the

[3] Reprinted from Int. J. Heat Mass Transfer, vol 43, T. Hibiki and M. Ishii, One-group interfacial area transport of bubbly flows in vertical round tubes, 2711-2726, 2000, with permission from Elsevier.

inlet, the smaller bubbles seemed to be pushed out towards the wall, causing the IAC peak to be moved outwards [48].

When the superficial liquid velocity is increased, the peak concentration of the interfacial area moves outwards towards the wall of the tube [31, 34, 37, 70]. Kim *et al.* [45] also demonstrated this effect was present in ducts. Michiyoshi and Serizawa postulated that when the bubble moved close to the wall, any displacement would be reflected and cause additional agitation [79]. The authors defined the region where this would occur as $d_b/R < r/R < 1$ [79]. Dongjian *et al.* suggested that this 'saddle' distribution of IAC was caused by a combination of the lift, wall lubrication and turbulent dispersion forces [31]. This theory is discussed in detail in section 2.4.1.2, since a separate effort in modelling interfacial area transport is based on it. Kalkach-Navarro et. al. suggested this peak was due to measurement error caused by the statistical assumptions inherent in the two-probe method [34]. Specifically, they postulated that the wall causes the trajectory which the probe traces through the bubble to no longer be random, although Takamasa *et. al.* indirectly refuted the point by confirming the wall-peak distribution using stereo-cameras [34, 48].

The experimental results reviewed indicate that if both the superficial gas or liquid velocity are increased, and the flow regime approaches the bubbly-slug transition, the region of the tube with the highest interfacial area concentration relocates to the center of the channel [32]. Hibiki and Ishii noted that the formation of cap bubbles began at $\alpha \approx 15\%$ [37].

Using the mechanistic models derived in literature, Hibiki and Ishii [66] found that as j_f was increased, the probability of random collisions between bubbles also increased, causing additional coalescence interactions [66]. The coalescence interactions are more likely to occur in the center of the tube, thus reducing the overall interfacial area concentration in this region. Further increases to the j_f allows for bubble disintegrations via the turbulent impact mechanism [66]. Since the center-line of the tube will contain the fastest moving fluid, this will also be the region where the bubble fragmentation is most likely to occur, which explains the core IAC peak.

Kataoka and Serizawa conducted experiments where the both the liquid and gas velocities were fixed, and the only the inlet bubble size was varied [38]. After allowing the flow to develop, the radial IAC distribution was measured downstream ($z/D = 83$), and the authors observed that when smaller bubbles ($d_b \approx 3 - 4$ mm) were injected, the interfacial area concentration peak occurred near the walls of the channel

[38]. When larger bubbles ($d_b \approx 5 - 6$ mm) were injected, the IAC peak started to migrate towards the center-line of the channel [38].

2.4.1.2 Lift Force Hypothesis

In an upwards co-current flow, the bubble will be subject to 'lift' forces due to the radial velocity gradients in the pipe. These lift forces act perpendicular to the direction of the flow and therefore either push bubbles towards the wall or the centerline of the pipe. The location of these void peaks depends on the flow conditions and the size of the bubbles, and this was demonstrated by Tomiyama *et al.* who studied the motion of the air bubbles in a glycerol-water mixture subjected to shear flows [80]. The authors posulated that the lateral motion of a bubble in a vertical co-current flow is governed the balance of a 'transverse lift force', $\vec{F}_{TL}$ and a 'shear-induced lift force', $\vec{F}_{LF}$ [80].

The authors assumed that $\vec{F}_{TL}$ is caused by some complex interaction between the wake of the bubble and the shear field, and suggest that it takes the form of equation (39) [80]. In the equation, C_{TL} is the transverse lift coefficient, d is the diameter of the bubble, and curl $\vec{u_l}$ is the curl of the velocity vector [80]. In the author's experiment, the bubbles were released into a stagnant tank, with a moving belt installed on one of the walls, allowing them to reduce the curl term to $|\text{curl } \vec{u_l}| = \left|\frac{du_l}{dx}\right|$ [80][4]. The authors postulate that this mechanism pushes the bubbles away from the wall and towards the center of the channel.

$$\vec{F}_{TL} = -C_{TL}\rho_l \frac{\pi d^3}{6} \left(\vec{u_g} - \vec{u_l}\right) \times \text{curl } \vec{u_l} \tag{39}$$

Similarly, the shear-induced lift force is given by equation (40), where C_{LF} represents the shear-lift coefficient [80]. The authors indicate this force is responsible for causing the smaller bubbles to migrate towards the walls of a channel [80].

$$\vec{F}_{LF} = C_{LF}\rho_l \frac{\pi d^3}{6} \left(\vec{u_g} - \vec{u_l}\right) \times \text{curl } \vec{u_l} \tag{40}$$

[4] In this case, $\frac{du_l}{dx}$ represents the change in velocity with respect to the change in distance to the belt

The authors found experimental evidence[5] to suggest that for bubbles with a horizontal dimension smaller than $d < 4.4\ mm$, the dominant mechanism was the shear-induced force, which pushes bubbles towards the walls [80]. For bubbles larger than 4.4 mm, the shape of the bubble plays a much larger role, and the interaction between the wall and the bubble wake tends to push it towards the center of the pipe [80].

Using experimental data obtained with high speed photography Tomiyama *et al.* derived a relationship for the lift coefficients as a function of the Eötvös Number, Eo [80]. Krepper *et al.* extended this work by implementing the correlation into the CFD programs Neptune-CFD and ANSYS-CFX and testing against experimental data from the TOPFLOW facility [81]. This force balance forms the basis of the MUSIG model which tracks the transport and interaction of bubbles in up to 32 different 'size-groups' [3].

2.4.2 Axial IAC Distribution

Takamasa *et al.* observed that the bubble diameter, d, increases as the flow travels up through the pipe, and attributed this to both bubble coalescence and expansion [48]. The work of Hibiki *et al.* [70] found similar trends, although they noted that once the liquid superficial velocity was increased past a certain point, the bubbles began to fragment, and the measured d stayed relatively constant along the length of the tube.

Hibiki and Ishii [66] shed some insight into this phenomena by comparing axial IAC measurements against predictions made by the one-group IATE. The authors found that at low $u_{l,s}$, the major driver of change in a_i was the pressure-expansion term [66]. As the bubbles rose up the column, the reduction in hydrostatic pressure caused the void to occupy a greater volume, thus the interfacial area was also increased [66].

2.4.3 Boiling

[5] Experiments were conducted in glycol

Most of the experiments reviewed involved air-water pipe flows although one line of experiments started by Bartel *et al.* investigated the interfacial area concentration distributions in steam-water flow through an annulus [69]. This work, along with that of Situ *et al.* [71, 72] utilized the 2 conductivity probe technique, while Ozar *et al.* [76] conducted their experiments using the 4 probe method. Bartel *et al.* measured the radial and axial distributions of IAC near the point of net vapour generation (PNVG) [69]. They observed bubbles with a small Sauter mean diameter and flow with a relatively large IAC in the regions near the heated wall upstream of the PNVG [69]. Further work by Situ *et al.* demonstrated similar results, and the drop off of a_i with distance from the heater was attributed to the bubbles collapsing from exposure to the subcooled fluid [71, 72]. More advanced experiments involving the study of interfacial area concentration in a 3×3 rod bundle under subcooled boiling conditions were conduced by Yun *et al.* [73]. Under void conditions of $< 15\%$, the authors reported a local interfacial area concentration peak near the walls of the heated rods, which is a result consistent with the previous work done in annular geometries [73].

2.4.4 Other Experiments

Several sets of experiments measuring the IAC were conducted using techniques other than electrical conductivity probes. A line of experiments by Takamasa *et al.* [48] and Hibiki *et al.* [49] used stereo imaging due to the constraints posed by the flow geometry being studied.

In the most-recent literature, the development of the 4-probe sensors has allowed researchers to classify the detected bubbles as part of either Group I or Group II. This has contributed in part towards conducting research in more complex geometries. Ozar *et al.* examined the transport of interfacial area concentration during subcooled boiling in an annular geometry [76]. Schlegel *et al.* noted that the flow dynamics are vastly different in geometries where the maximum cap bubble size is not constrained by the pipe geometry, and so has conducted studies using much larger pipes [77]. Hazuku *et al.* [53, 78] has conducted recent work on the IAC in thin liquid films at very high superficial gas velocities ($u_{g,s} < 75.0$ m/s).

The work of Paranjape *et al.* and Yang *et al.* began to examine the transport of interfacial area concentration in rod bundles [13, 75]. Yang studied the axial evolution of the interfacial area and found that the spacer grids holding the bundles in place caused significant increases in a_i [13]. Such a result demonstrates the need for additional work in this area.

2.5 Summary

2.5.1 IATE Development

1. The two-group IATE represents the current state-of-the-art in terms of modeling the behaviour of a_i in flows. It tracks the transport of both Group I (spherical) and Group II (cap/slug) type bubbles, and allows for interaction between the two groups.

2. There are numerous coalescence and fragmentation mechanisms which influence how a_i develops along a flow. These are represented by the source and sink terms, which while extensive are still incomplete.

3. Authors such as Ishii, Hibiki, Kim and Kataoka have conducted extensive work in the development of the IATE and its source terms. An overwhelming portion of their work utilizes a mechanistically derived model of the source term backed by experimental data.

2.5.2 Bubble Fragmentation

1. Bubble fragmentation has been studied for over 80 years, yet is still not entirely understood. The general consensus is that three disintegration mechanisms exist: shear-based, turbulent-driven and interfacial instability. Kolev suggests acceleration based fragmentation exists, but no studies were located to support this theory [21].

2. In turbulent fragmentation, the dimensionless Weber number is used to characterize the conditions surrounding the bubble at a given instant. Fundamentally the Weber number represents the ratio of the inertial forces to the surface tension forces acting on the interface. However, its derivation varies considerably depending on the author or the scenario being examined.

3. Some critical Weber number should exist, below which bubbles are unlikely to fragment. This is used interchangeably in literature with the term 'maximum stable bubble size'.
4. Shear based fragmentation is characterized by the Capillary number which is the ratio of the velocity and viscosity to the surface tension.

2.5.3 Measurement Techniques

1. The most commonly used technique to measure a_i is the conductivity probe, which uses an array of thin wires to determine when bubbles are passing. In flows with a significiant lateral component, bubbles may be missed or rejected due to not touching both probes - which rules them out for the purposes of the current work.
2. In order to infer the interfacial area from the "pulses" observed by the conductivity probes, assumptions as to their orientation relative to the probes must be made.
3. In every measurement, the a_i is not directly measured, but rather bubble velocities are sampled, and using assumptions on the spherical "shape" of the bubble, an value for a_i is estimated.
4. Optical methods such as LFD and stereoscopic cameras have also been used, although not nearly as frequently as the conductivity probes.

2.5.4 Interfacial Area Experiments

1. Almost all experiments conducted have been air/water at near atmospheric conditions. Very few works deal with steam water flows.
2. The radial distribution of the a_i was observed to have a wall-peaked, transistion or core-peaked configuration. This is postulated to be due to a balance between the lift forces acting on the bubbles. Both the magnitude and direction of these lift forces are functions of the bubble size and shape.

Measurement Techniques

In this study, several measurement techniques are utilized to qualitatively understand the governing mechanisms as well as to quantify the local fluid conditions as a bubble passes through a flow restriction. Laser Doppler Anemometry (LDA) is used to capture characteristics of the single phase flow field such as the local velocity and turbulence intensity. While this information is useful when examining the behaviour of the fluid as it is diverted around an obstruction, it provides little information about what is happening with the discontinous phase. A high speed camera is used in conjunction with shadowography based image processing techniques in order to ascertain the chord length, size and aspect ratio of the bubbles.

3.1 Laser Doppler Anemometry

Laser Doppler Anemometry (LDA) is a non-invasive means of obtaining the velocity at a point in fluid flow or spray. These fluid flows may occur in either open space or in a confined vessel, so long as the point of interest is optically accessible to both the transmitter and receiver optics of the system. This section documents the basic operating principles of a generic LDA system and the details how the LDA system was implemented in this experiment.

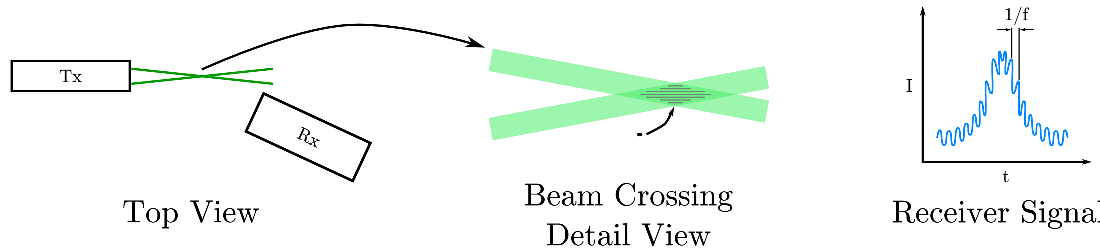

Figure 5: Schematic of the operating principle of the LDA.

3.1.1 Background Theory

In a simple laser anemometry system, a coherent (in phase) beam of monochromatic light is generated by a laser and then passed through a beam splitter. A 'reference' beam and a 'daughter' beam exit the beam splitter and are passed through a focusing optic which redirects the two lines to a convergence point. The diameter of the 'region' where the beams intersect is a function of the beam width or waist, and the angle at which the beams cross. This size of this 'region' is typically on the order of $0.1 - 1.0\ mm$. Due to the wave nature of the photons and the superposition principle, within the beam intersection region there will be a series of interference fringes. Points within the crossing region where the difference in the optical distance travelled by the 'daughter beam' and the 'reference beam' is some integer multiple (k) of the wavelength (λ) will constructively interfere. Similarly, destructive interference occurs at points where the difference in optical distance is equal to $\left(k + \frac{1}{2}\right)\lambda$.

$$\Delta_{constructive} = k\lambda \tag{41}$$

$$\Delta_{destructive} = \left(k + \frac{1}{2}\right)\lambda \tag{42}$$

These conditions cause an alternating fringe pattern of 'brighter' and 'darker' lines to be formed as illustrated in figure 5. Particles such as debris entrained in the fluid or specifically engineered seed particles will intermittently transit the region where the beams intersect. As they flow through the beam crossing, they scatter light which may be observed by an appropriate receiving optic. The intensity of the light scattered will vary depending on whether the particle is in a 'bright' fringe or a 'dark' fringe. From the point of view of the receiving optics, a sinusoidal waveform will be observed. Since the spacing of these fringes Δs, is strictly a function of the wavelength of the laser (which is very precisely defined), the frequency of the sinusoid observed by the receiver ($f_{observed}$), is directly proportional to the velocity of the particle crossing through the beam crossing region.

$$u_{particle} = (\Delta s)\,(f_{observed}) \tag{43}$$

This is the fundamental basis of a basic laser anemometer. The major limitations of this type of system are that it cannot determine the direction which the particle is traveling in, nor can it identify the presence of stationary particles.

Feeding the 'daughter' beam into a Bragg cell can overcome both of these problems. The Bragg cell oscillates at a fixed frequency, f_{Bragg}, and causes the beam which passes through it to be Doppler shifted by this frequency. The result is that when the beams cross, the fringe pattern is no longer stationary in time, but rather appears to be 'moving'. A stationary particle residing in the beam crossing will scatter light at f_{Bragg} due to the apparent motion of the fringes. If the particle is moving in the same direction as the fringe 'motion', the frequency observed by the photo-detector will be slightly less than f_{Bragg}. Similarly, if the particle is moving in the opposite direction as the fringes, then it will cross each interference peak more rapidly, and thus the observed frequency will be slightly greater than f_{Bragg}. By subtracting - or 'downmixing' as it is commonly referred to - the Bragg cell frequency from the frequency observed by the photo-detector, both the velocity and trajectory of the particle can be derived.

3.1.2 System Implementation

A water cooled Innova®70 Series Argon-ion laser serves as the coherent light source in this work. The laser generates three spectral peaks of interest at $\lambda = 514.5$ nm, $\lambda = 488.0$ nm, and $\lambda = 476.5$ nm. Key characteristics of the hardware are supplied in table 13.

Table 13: Key characteristics of the source laser. The beam diameter refers to the distance between the $1/e^2$ points

Laser		Supply	
d_{beam} (mm)	1.5	Voltage (V)	3ϕ, 208
λ_{pk} (nm)	$514.5, 488.0, 476.5$	I_{max} (A)	40
$P_{opt,max}$ (W)	≈ 3.5	q_{max} (kW)	20

The Bragg cell used oscillates at 40 MHz, and the $\lambda = 514.5\ nm$ and $\lambda = 488.0\ nm$ beams are used to measure the axial and transverse flows respectively. The system is setup in a 30° off-axis forward scatter configuration, meaning that the transmitter and receiver pair are pointed facing one another. The configuration of the transmitting lens is listed in table 14.

Table 14: Transmission lens properties. Adapted from [82]

Parameter	514.5 nm	488.0 nm	476.5 nm
Probe Beam Diameter (mm)	1.77	1.77	1.77
Probe Beam Spacing (mm)	20.0	20.0	20.0
Lens Focal Length (mm)	250	250	250
Lens Diameter (mm)	50.0	50.0	50.0
Fringe Spacing (μm)	6.43	6.10	5.96
Meas. Volume Diam. (μm)	93	88	86
Number of Visible Fringes	14	14	14

3.1.2.1 Position Correction Function

A preliminary measurement taken revealed an issue where the distance between the axial velocity maximum and the point where the signal was lost near the wall was significantly less than the radius of the tube, and this is illustrated in figure 6. The reason behind this discrepancy stems from the beam having to pass through three different materials before 'crossing'. At each material interface, the angle of the beam to the optical axis changes, and so the true crossing point is altered. Furthermore, since the distance the beam travels in each material varies every time the traverse is moved, the relationship is technically non-linear. In order to account for this, a correction factor must be derived and applied to the documented traverse position of all measurements.

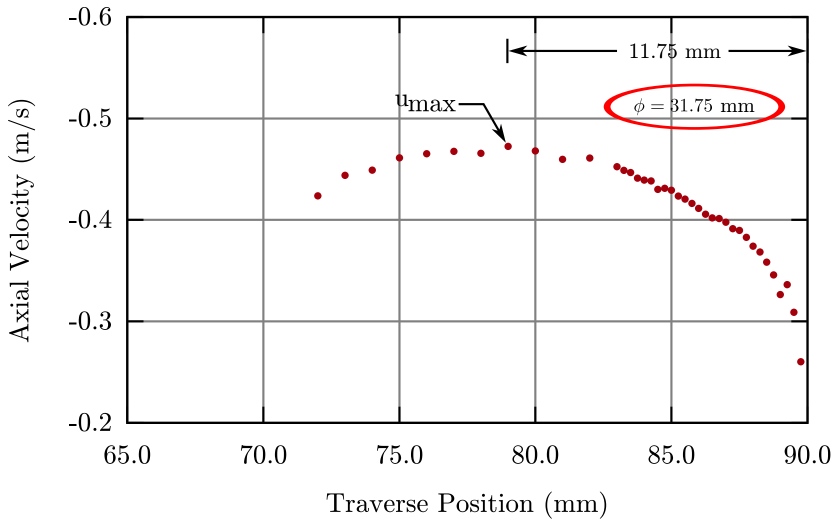

Figure 6: Raw axial velocity data plotted against the traverse position for a superficial fluid velocity of $j_f = 0.376\ m/s$.

When the two beams are used to measure sprays, the beams pass through only one material. The half-angle of the beam crossing is defined only as a function of the initial beam separation at the lens face Δy, and the focal length, F as illustrated in figure 7. The half angle is defined as:

$$\theta_0 = tan^{-1}\left(\frac{\Delta y/2}{F}\right) \tag{44}$$

If the beam passes through multiple materials, the angle of the beams with respect to the center-line will change at each interface. The end result is that the beams will no longer cross at the focal length of the transmitter lens, and this is illustrated in an exaggerated fashion in the right half of figure 7. The distance between the lens face and the true beam crossing (F') as well as the half-angle of intersection (θ') will be a function of both the refractive indices of the materials and the distance the beam travels in each.

The beam leaves the lens at an angle of θ_0, and when it reaches the air-acrylic

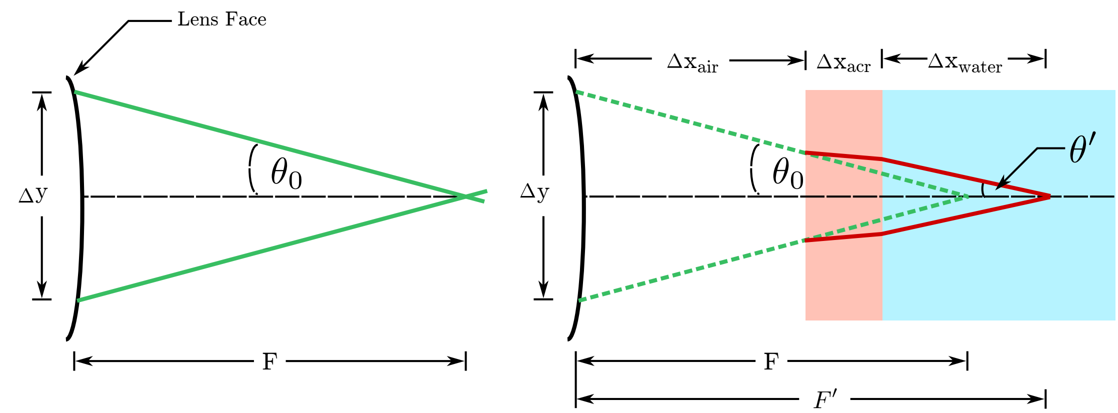

Figure 7: Focal length and half-angle of the beam crossing in air (left) and in water behind an acrylic wall (right)

interface, the distance between the beam and the optical axis (Δy_1) is:

$$\Delta y_1 = \frac{\Delta y}{2} - \Delta x_{air} tan\theta_0 \tag{45}$$

At the interface, the beam is refracted according to Snell's law which depends on the indices of refraction of air (n_{air}) and acrylic (n_{acr}). The new angle (θ_{acr}) with respect to the optical axis is:

$$\theta_{acr} = sin^{-1}\left[\frac{n_{air}}{n_{acr}} sin\left(\theta_0\right)\right] \tag{46}$$

The thickness of the acrylic is fixed and therefore will remain constant regardless of the position of the lens and beam crossing. The distance the beam drops through the acrylic is:

$$\Delta y_{acr} = \Delta x_{acr} tan\theta_{acr} \tag{47}$$

Therefore when the beam reaches the acrylic-water interface, the new distance between the beam and the optical axis is:

$$\Delta y_2 = \Delta y_1 - \Delta x_{acr} tan\left(\theta_{acr}\right) \tag{48}$$

Again, the change in material means that the beam is bent according to Snell's law:

$$\theta_{water} = sin^{-1}\left(\frac{n_{acr}}{n_{water}} sin\left(\theta_{acr}\right)\right) \tag{49}$$

The remaining distance that the beam has to travel before converging is:

$$\Delta x_{water} = \frac{\Delta y_2}{tan\theta_{water}} \tag{50}$$

Combining the equations above, true position of the beam crossing with respect to the distance between the lens and the front face of the acrylic (Δx_{air}) is:

$$\boxed{\Delta x_{water} = \frac{\frac{\Delta y_0}{2} - \Delta x_{air} tan\left(\theta_{air}\right) - \Delta x_{acr} tan\left(\theta_{acr}\right)}{tan\left[sin^{-1}\left(\frac{n_{acr}}{n_{water}} sin\left\{sin^{-1}\left(\frac{n_{air}}{n_{acr}} sin\theta_{air}\right)\right\}\right)\right]}} \tag{51}$$

3.1.2.2 Traversing Mechanism

The transmitter and receiver are mounted on optical rails which are attached to a 3-axis traverse. The traverse is controlled by a stepper motors capable of moving the arm in 0.0125 *mm* increments along the X and Y directions (horizontal), and in 0.00625 *mm* increments along the Z direction (vertical). These values represent the maximum theoretical spatial resolution of the measurements, however in practice owing to the manual adjustments required to locate the beam crossing, along with the beam angle variation due to material changes, the uncertainty of the position is estimated to be on the order of ± 0.1 *mm*.

3.2 High Speed Video & Image Processing

3.2.1 Video System Implementation

High speed imaging was conducted using a Photron FASTCAM SA5 capable of sampling in excess of one million frames per second. Images are captured by the camera by an array of 20 $\mu m \times 20$ μm charged coupled devices (CCD). Each image represents sampling the intensity of every CCD element and converting signal to 12-bit integer. This number represents the greyscale intensity of the pixel, with values of 0 indicating that no light is being received, and values of $2^{12} - 1$ indicating that the pixel is saturated.

Two types of measurements are taken using the imaging system. Qualitative observations of the bubbles fragmenting in the orifice are obtained by setting the camera to high frame rates ($12,000 - 60,000$ frames per second) and high shutter speeds (1000 ns per frame). Images from these tests are used to gain insight into the mechanisms causing the bubbles to fragment. Quantitative measurements are made by setting the camera to a low frame rate ($20 - 30$ frames per second) and very high shutter speeds (363 ns per frame). These images are run through image processing software to extract statistical data on the size, shape and concentration of the bubbles.

The bubbles are not individually tracked since past experience demonstrates that such methods yield very poor statistical distributions [1]. Instead, a large number of frames are taken with the frame rate set so that any one bubble will not appear in more than one frame. In the current work, a series of 1024×512 pixel images were captured to the camera's volatile memory buffer at a rate of $20-30$ frames per second. In each run between $8,000-10,000$ frames are captured, with up to 4 or 5 runs being conducted when the flow conditions cause the bubble number density to be low.

[1] Tracking the motion of each individual bubble is possible by cross-correlating the intensities of two pixels located along the same axis as the flow. However, the error is proportional to 1/framerate, and in our experience, frame rates of $70,000$ frames per second are required to reduce this to reasonable ($\approx 2\%$) levels. At such high frame rates, even with a reduction in the resolution of the camera, only $3-4$ seconds of video may be taken yielding $\approx 250,000$ frames to be processed for each run. Within each run, typically 50-100 bubbles are captured, which yields a very poor statistical distribution of bubble sizes and velocities. By comparison, a single run taking a large number of images spaced far enough apart (in time) can yield upwards of $> 1,000$ bubbles.

The test section is backlit using 1000 W halogen lights, while the camera is outfitted with a 60 mm AF Micro Nikkor lens. The lens has a 1 : 1 magnification ratio, meaning that the size of each pixel in an image is the same size as the CCD element, thus the 1024×512 pixel image represents an area of $20.48\ mm \times 10.24\ mm$. Frames are taken with a shutter speed of 1/1000000 s to reduce motion blurring.

Two types of image processing are conducted: chordal measurements in the vertical direction, and bubble aspect ratio measurements. Non-uniform lighting caused by the curvature of the test section created steep background lighting gradients in the horizontal direction as demonstrated in figure 8. Chordal measurements made by sampling only along vertical lines in the image can overcome this as they do not depend on the horizontal gradient, and this technique is discussed in depth in section 3.2.2.

In the regions of the image where the lighting is roughly uniform (e.g. the middle of the image in figure 8), a more general image processing technique can be used to determine the bounds of the bubble in both the horizontal and vertical direction. This aspect ratio analysis is described in section 3.2.3.

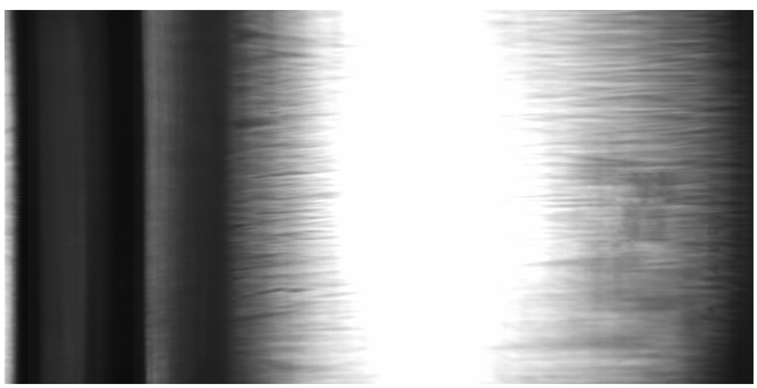

Figure 8: Sample image of the test section filled with water. Note that the edge of the test section clearly visible (bright line) at the far left of the image.

3.2.2 Image Processing - Chordal Measurements

For each test run up to 16 GB of images are acquired and processed in order to extract chord and void fraction data. A series of processing steps as illustrated in figure 9 is conducted on each set of images. In summary, the process involves:

1. A set of 'background' images (without void present) is taken and averaged.

2. For each of the images with void, the average background image is subtracted from each frame in order to reduce the effects of the non-uniform lighting.

3. Each subtracted image is sampled along a column of pixels of interest.

4. The column sample is transformed into its Fourier components and convolved with a low pass filter.

5. The 'cleaned' data is passed through a detection algorithm which detects "rising" and "falling" edges on the basis of:

    - The magnitude of the intensity at a given point.
    - The spatial derivative (in the vertical direction) of the intensity at a given point.
    - Whether or not a rising edge has been detected nearby.

6. The pixel distance between each rising and falling edge pair is calculated, and converted to a spatial measurement using a conversion factor based on the size of each CCD sensor in the camera.

7. A final check is performed to ensure that the bubble candidate is within the focal plane of the camera by verifying the maximum intensity difference is above a certain threshold.

8. Once all of the frames in a data set have been processed, void fraction information is computed.

9. Steps 3 - 8 are repeated along multiple columns, spanning the width of the test section.

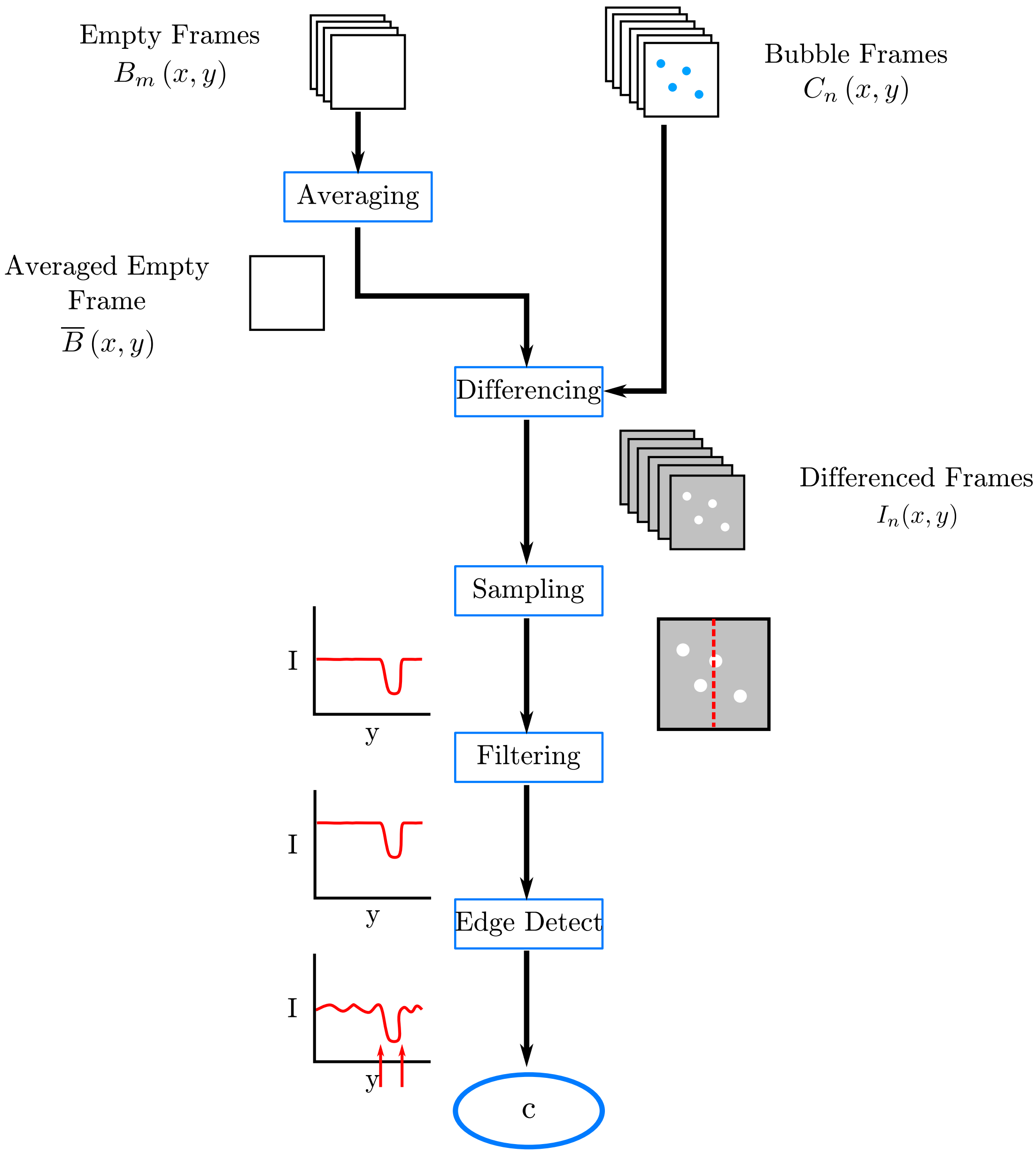

Figure 9: Image processing data flow chart.

3.2.2.1 Background Averaging

In order to remove the background light a set of n images of the test section without air flow was taken, where n is typically in the range of $500 < n \leq 600$. Within this set of images, denoted B_m, the average value of the intensity over the set is calculated and stored. The resulting composite image, $\bar{B}(x, y)$, is subsequently used to determine whether or not a bubble is present. This averaging step was performed any time the lighting conditions, camera position, camera settings, lens arrangement or test section was altered.

$$\bar{B}(x, y) = \frac{\sum_{m=1}^{n} B_m(x, y)}{n} \tag{52}$$

3.2.2.2 Image Differencing

The 'average image' is then subtracted off of each bubble frame, $C_n(x, y)$, forming a new image representing the intensity difference between the original two. In the difference image, $I_n(x, y)$, negative values represent regions where the light intensity is lower that the background value, and this is assumed to be caused by bubbles transiting the area.

$$I_n(x, y) = -\bar{B}(x, y) + C_n(x, y) \tag{53}$$

3.2.2.3 Spatial Sampling

For each of the differenced bubble frames, an intensity sample is taken at a fixed radial coordinate to form a vector of intensity as a function of vertical location. In this work, this sample consists of 512 points, meaning that the maximum bubble size which may be detected is on the order of 10 mm. The data sample from each frame is then individually passed onto the post-processing algorithm.

3.2.2.4 Filtering

The sensitivity of the camera CCD is high enough such that shot noise affects the ability for subsequent processing steps to properly detect passing bubbles. These random intensity fluctuations are removed in Fourier space using a low pass filter which removes portions of the spectra above 450 Hz. The end result is a comparatively 'cleaner' signal with distinct peaks representing the frames where a bubble is passing through the sampling point.

Figure 10 demonstrates the effect the applicaton of the filter has on the sampled data. The video frame at the top of the figure is sampled along its centerline and compared to the averaged blank file. The raw data and its first derivative are plotted on the two graphs on the left side of the plot, and it is evident that very little useful information may be derived from the derivative plot (bottom left) due to the minute fluctuations in the data intensity. On the right hand side of figure 10, the raw data is fed through a low pass filter prior to the derivative being taken. This results in considerably smoother derivative curves which is useful in the edge detection step.

3.2.2.5 Edge Detection

In order for a bubble to be 'detected', the post-processing code scans the column of filtered pixel data looking for the first point that matches both the absolute value threshhold and the first derivative threshhold criteria set in equations (54) and (55). This point is considered the 'rising edge' of the bubble, and can be clearly seen in figure 11. Once such a point is located, the code seeks the next pixel along the line which matches the falling edge criteria in equations (56) and (57). The derivatives used in both cases are calculated via central differencing.

$$I\left(x,y\right) \geq 250 \tag{54}$$

$$\frac{dI\left(x,y\right)}{dy} \geq 70 \tag{55}$$

$$I\left(x,y\right) \leq 250 \tag{56}$$

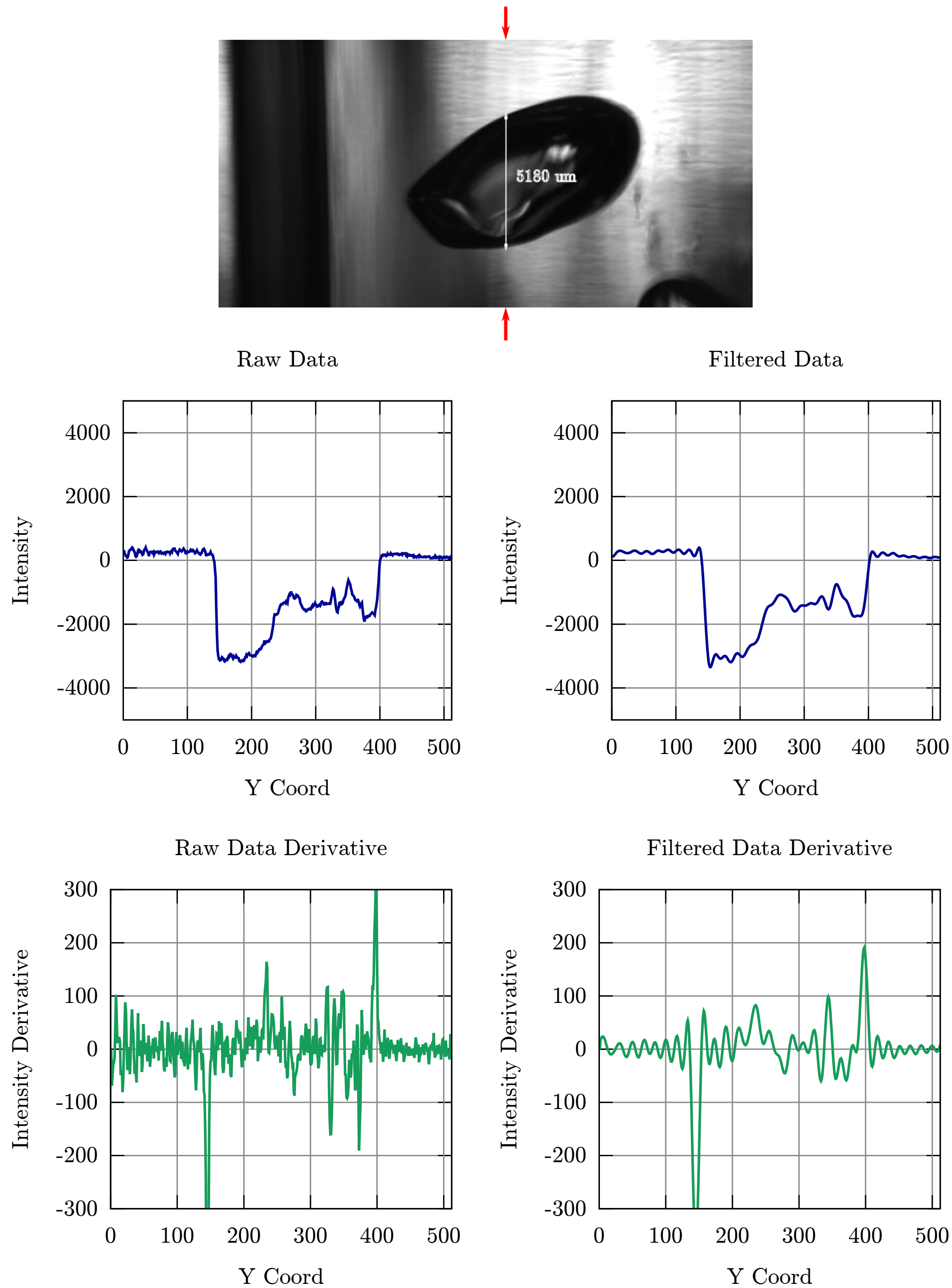

Figure 10: Example of the post-processing output for at $j_g = 2.105\ mm/s$ and $j_f = 0.191\ m/s$. Graphs on the left plot the raw pixel differences and their spatial derivative along the centerline of the picture. Graphs on the right plot the filtered difference and derivative data. Note the considerable improvement in the quality of the filtered derivative plot.

$$\frac{dI\left(x,y\right)}{dy} \leq -70 \tag{57}$$

Figure 11 illustrates two examples of bubble candidates which have passed both the intensity and the first derivative tests. In both cases, the image is sampled along the centerline, and this data is passed to the edge detection algorithm. The shaded portion of the graph corresponds to the location in the image where the code thinks the bubble is, and this information is used to composite the arrow onto the images at the top of the figure. At the lighting conditions used for these specific test, this demonstrates that the threshholding criteria in the above equations are adequate to detect the bubbles.

Figure 12 illustrates two examples of bubbles which have passed the intensity level thresholding test, however the values of the derivatives at these points were too low to classify them as 'good data points'. These 'fuzzy' images are the result of the bubble passing outside of the depth-of-field of the camera, and so they candidates are rejected. The two particular examples were rejected on the basis of the magnitude of the first derivatives being too low when the pixel intensity dipped below the zero-threshold.

Note that both figures 11 and 12 are automatically generated outputs of the bubble detection program.

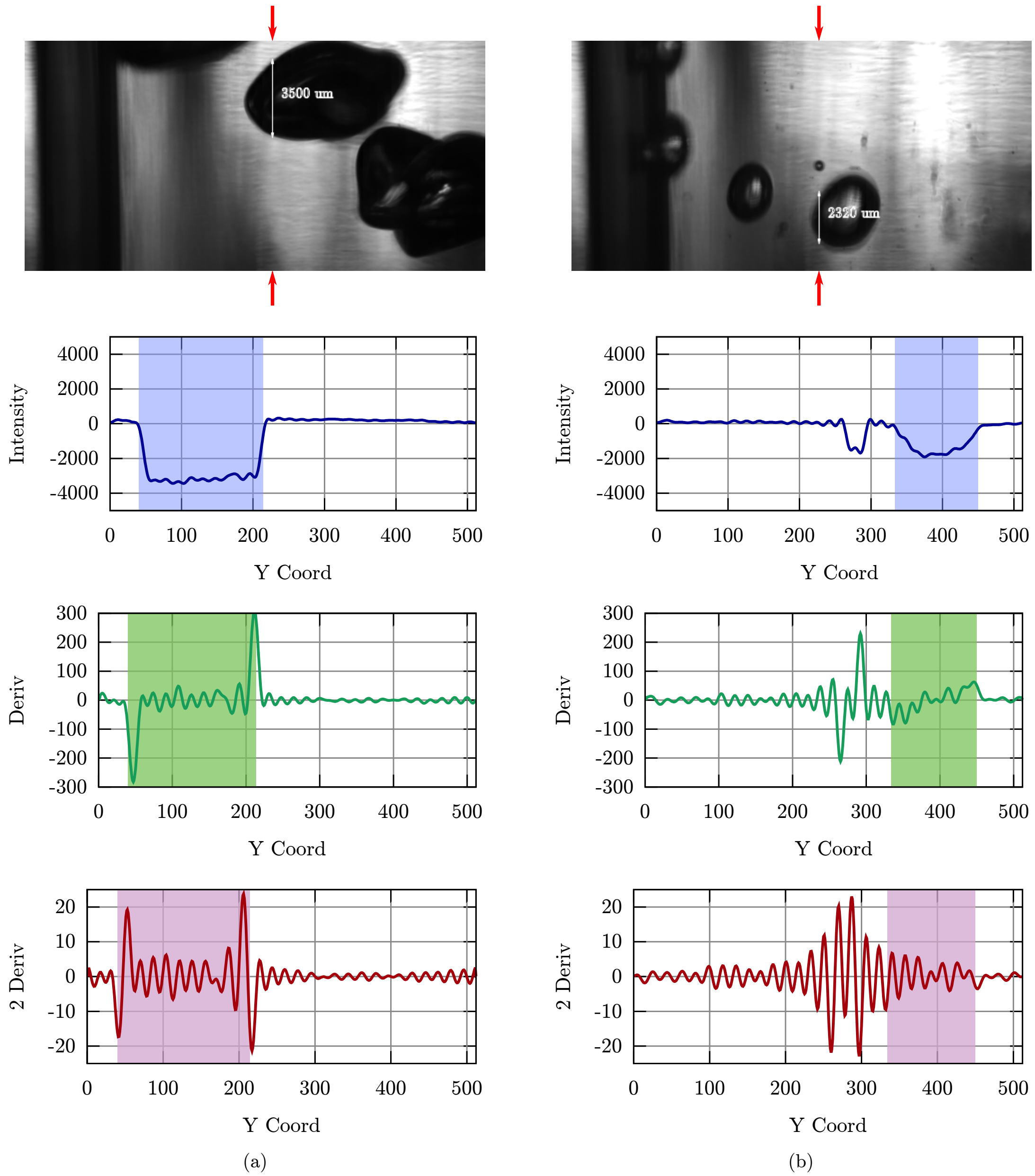

Figure 11: Example of the post-processing output where bubbles have passed the focal plane verification checks under conditions of $j_g = 0.0125\ m/s$ with liquid superficial velocities of (a) $j_f = 0.191\ m/s$ and (b) $j_f = 0.702\ m/s$.

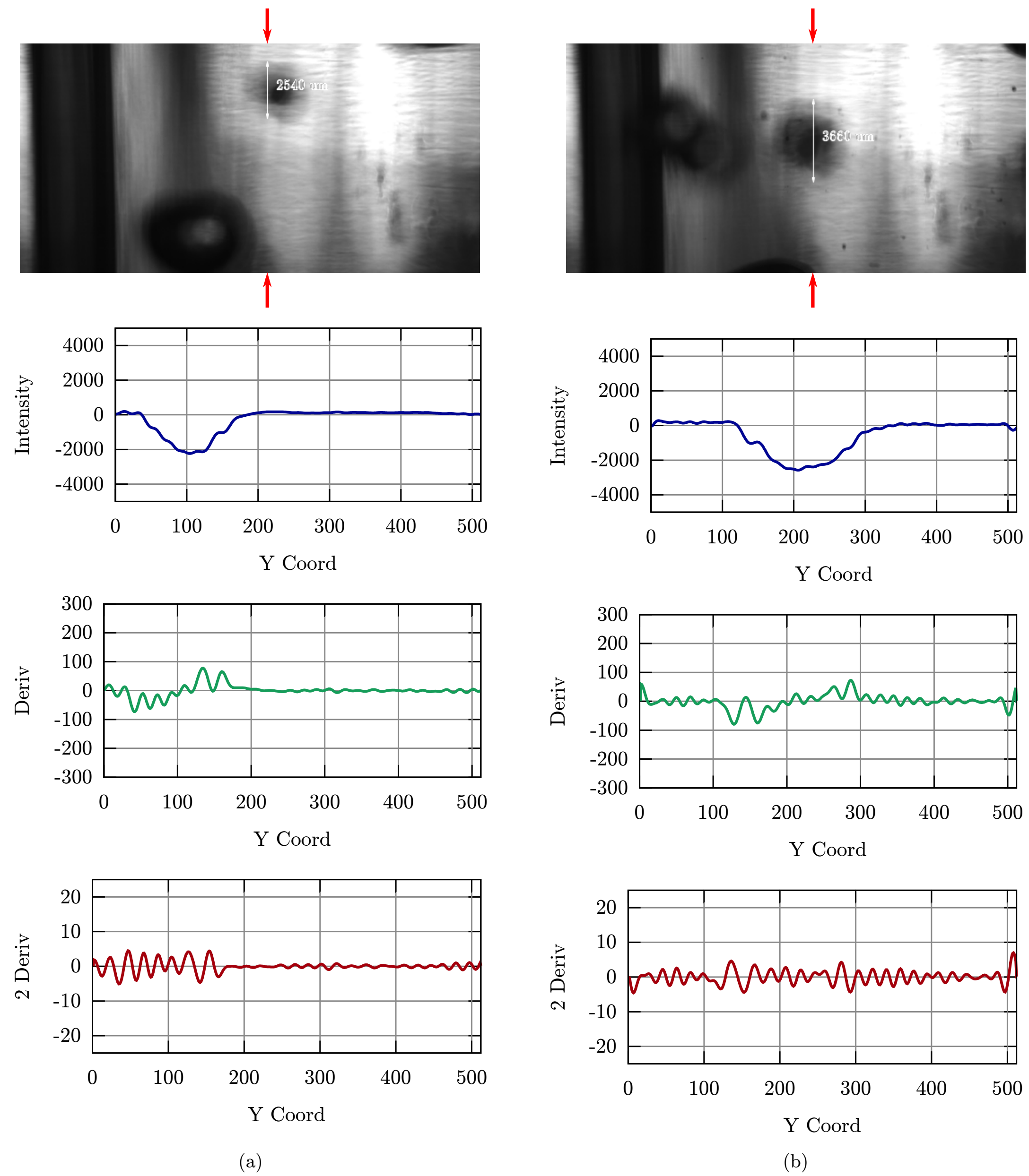

Figure 12: Example of the post-processing output where bubbles have failed the focal plane verification checks under conditions of $j_g = 0.0311\ m/s$ with liquid superficial velocities of (a) $j_f = 0.191\ m/s$ and (b) $j_f = 0.702\ m/s$.

3.2.2.6 Chordal Void Fraction Calculation

The total 'length' sampled for each set of images is calculated as equation (58).

$$L_{total} = (\text{Image Height}) \times (\text{Number of Frames}) \tag{58}$$

By extension, the void fraction may be defined as the percentage of the pixels occupied by a bubble as in equation (59).

$$\alpha = \frac{\sum_{n=0}^{n=N_{bubbles}} L_{bubble,n}}{L_{total}} \tag{59}$$

3.2.2.7 Limits and Uncertainty

Bubble chords detected must be at least 4 pixels in length, yielding a minimum measurable chord size of 80 μm. In the current work, the images acquired are 1024×512 pixels which sets the limits for the maximum size of detectable bubbles. Assuming that the rising edge occurs between the first two pixels in the column, and that the falling edge is found between the last two pixels of the column (510 total pixels), the maximum detectable bubble chord is 10200 μm.

The locations of both the rising and falling edges are estimated to be accurate within ± 1 pixel, corresponding to a chord size accuracy of ± 40 μm.

3.2.3 Image Processing - Aspect Ratio

In regions where the lighting was relatively uniform in both the vertical and horizontal directions, more advanced image processing techniques may be employed to determine the aspect ratio of the bubbles. The same sets of images may be processed by both techniques. In this technique the raw bubble images are taken, and the background is subtracted in much the same way in the previous section. After that the images are processed by applying:

1. A Sobel transform is applied the differenced image to seek regions where there

are suspected object edges. These are defined as steep local lighting gradients.

2. A thresholding operation is conducted on the differenced image to binarize the image into "dark" areas and "light" areas.

3. A watershed operation [2] is applied to the Sobel filtered image to determine the boundaries of individual objects. The binarized image is overlaid to determine which objects represent bubbles.

4. Each distinct object remaining is checked against a set of criteria to determine if it is a valid bubble.

Since many of these operations are very complex in nature, extensive use of SciPy's "ndimage" image processing library and the "scikit-image" set of extensions is used [3].

3.2.3.1 Sobel Filter

The Sobel transform is an edge detection transformation which takes an input image and locates regions where the spatial intensity gradient is high. A new image is created using the gradient data. In the current work, the Sobel transform is applied to each differenced image, $I_n(x, y)$.

For each pixel not sitting on the outer edge of the image, the horizontal and vertical spatial intensity gradients are calculated using the kernels [4] in equations (60) and (61) [83]. For each point in the new image, the absolute magnitude of the gradient is calculated as equation (62) [83]. Figure 13 illustrates the result of the Sobel transform applied to a image where the background lighting has been subtracted.

[2] The watershed operation is very similar to the familiar "flood fill" operation found in basic image editing software.

[3] The work in this section is programmed entirely in Python and makes extensive use of the pre-existing functions in SciPy, which is a set of Python extensions geared towards scientific data processing.

[4] The value of each pixel in the new image is generated by applying the kernel to the corresponding pixel in the original image. The center value on the right side of the kernel definition corresponds with the pixel being computed. By convention, the kernel represents a multiplier applied to the neighbouring pixels of the original image. For example, assume $I(x, y)$ is the original image and $I'(x, y)$ is the transformed image. The value of $\mathbf{G}_x$ at coordinates (5,9) is $I'(5, 9) = -I(4, 8) + I(6, 8) - 2I(4, 9) + 2I(6, 9) - I(7, 10) + I(9, 10)$

$$\mathbf{G}_x = \begin{bmatrix} -1 & 0 & 1 \\ -2 & 0 & 2 \\ -1 & 0 & 1 \end{bmatrix} \tag{60}$$

$$\mathbf{G}_y = \begin{bmatrix} 1 & 2 & 1 \\ 0 & 0 & 0 \\ -1 & -2 & -1 \end{bmatrix} \tag{61}$$

$$\mathbf{G} = |\mathbf{G}_x| + |\mathbf{G}_y| \tag{62}$$

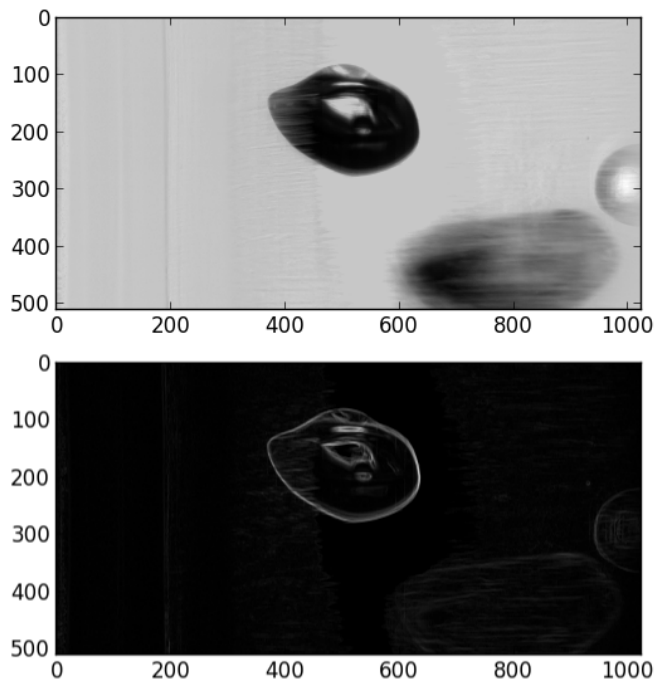

Figure 13: Example of a differenced image (top) and the result of the Sobel transform (bottom)

3.2.3.2 Thresholding

A thresholding operation is conducted on each pixel of $I_n(x, y)$ in order to create a new binary image representing possible bubble locations. In this work, a value of

−1700 was found to work well based repeated testing. This value will vary depending on lighting conditions, material and fluid opacity, camera sensor sensitivity and the lens configuration.

Figure 14 illustrates the result of the thresholding operation applied to the top image of figure 13. Clusters of pixels passing the threshold check are tagged as potential bubble candidates.

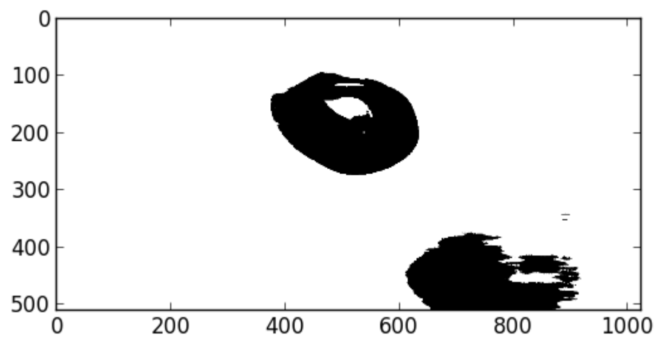

Figure 14: Example of a thresholded image

3.2.3.3 Watershed

In the Sobel transformed image from figure 13, the boundary of the bubble is not clearly defined - in fact it is several pixels thick. The binary image in figure 14 was constructed with a simple thresholding operation. It just so happens in this case, that it is very close to the size and shape of the bubble - in other images it may be somewhat smaller due to lighting fluctuations.

The watershed transform is an image segmentation transformation which is used to separate objects in an image. It takes the Sobel transformed image as well as the thresholded image and outputs the boundaries between the individual objects in the image. It functions by interpreting the Sobel image as a height map (where areas of high gradient are considered "ridges" and areas of low gradient are considered "valleys") and the regions thresholded as bubbles as a "water source" (hence the name watershed transform) [84]. The algorithm "floods" the valleys until the boundaries neighbour either a background pixel or another bubble - essentially detecting the local maxima in the Sobel image.

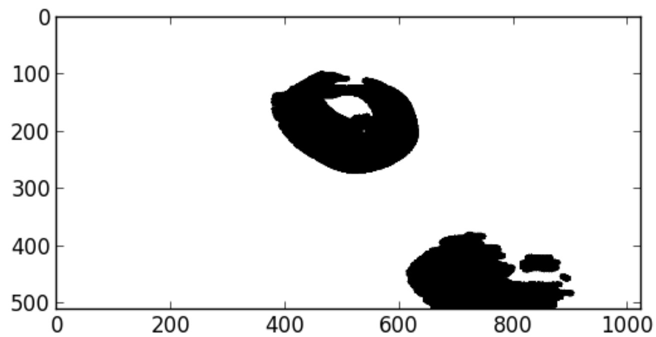

Figure 15: Image after the watershed transform has been applied

3.2.3.4 Logic Check

After all of the bubble candidates in the image have been identified and 'filled' to the nearest boundaries, six checks are performed on each candidate to determine if it is actually a valid bubble.

1. A boundary check is performed to remove any bubble candidates who have bounding boxes which touch the outer edges of the image. These bubbles are not entirely captured by the image, and should be removed.
2. A bubble intensity check is performed to remove any bubbles which may be severely out of focus. The intensity check takes the average of all of the pixels within the bounding box of each bubble candidate, and compares it to a fixed value. This value may vary depending on the lighting conditions, but is typically set to -1700 (a value of 0 represents a pixel intensity in the bubble image equal to that of the same pixel in the background image. This value of -1700 means that the average of all of the pixels within the bounding box must be 1700 intensity units "darker" than the background image). See the intensity plots in figures 11 and 12 to understand why this value is appropriate.
3. A size check is conducted to remove any objects smaller than a certain threshold (500 μm). Occasionally the bubble may "bulge" due to the turbulence and the cause light to scatter off the surface somewhat randomly. This scattered light is sometimes identified as a bubble, and this check removes those false candidates.

While this also impairs the ability of this program to detect very small bubbles, the aspect ratio of these is almost always ≈ 1.

4. A enclosure check is performed to remove any bubble candidates which are completely enclosed by another candidate. Occasionally reflections off the surface of a bubble may be misinterpreted as a smaller structure inside a larger object. This check eliminates the smaller object.

5. A position check is performed to only consider bubbles located entirely within the region where the background lighting is expected to be uniform.

6. The final check verifies that the aspect ratio of the bubble is within expectations. The measured aspect ratio of the bubble must be between $0.25 < AR < 2.25$ [5] which as section 5.2.3 demonstrates, encloses the entire distribution of bubbles by a considerable margin. Bubbles candidates with aspect ratios falling outside this range are likely clusters of overlapping bubbles.

Figure 16 illustrates the final output of the program, which is simply a bounding box in the region where it believes the bubble to exist. The bounding box is composited onto the original image for illustrative purposes. Note that the bubble candidates on the bottom right hand side of the image were rejected due to being outside the zone with the uniform lighting (check #5). Additionally, had this region been defined as part of the zone with uniform lighting, the bubble candidates would have been rejected due to being out of the focal plane.

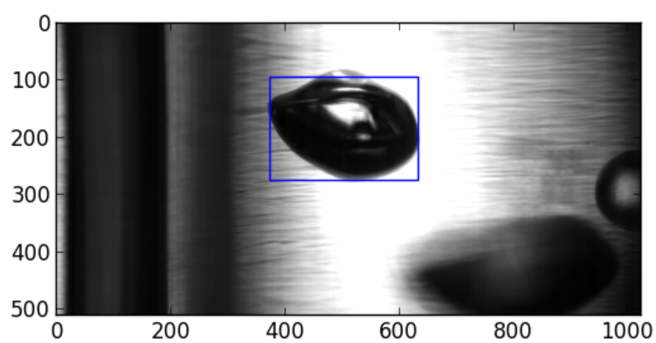

Figure 16: Bubble successfully identified by the program. The bounding box where the program believes the bubble to reside is composited onto the original image

[5] $AR = \frac{\Delta X}{\Delta Y}$

3.3 Summary

Laser Doppler Anemometry is used to measure the velocity and turbulence intensity of the single phase flow in the axial direction. The key points from the discussion are:

1. The position of the beam crossing is manipulated by moving a traverse in any one of the three spatial directions.
2. The position of the beam crossing is not known. It is inferred by 'touching' the crossing point against one of the test section walls.
3. Moving the traverse does not result in a 1:1 movement of the beam crossing position. To account for the multiple materials which the laser passes through, a position correction function has been derived.
4. Use of the Phase Doppler Particle Analyzer mode to measure the chord lengths of the bubbles is possible, but not a realistic option due to the weak signal strength of the laser when scattered light reaches the receiver.

High speed video is used to both qualitatively understand the mechanisms behind the bubble fragmentation process, and to quantitatively compute the change in the interfacial area before and after bubbles pass through the obstruction.

A suite of image processing scripts and programs were created in order to obtain characteristic information about the bubbles.

1. Bubble chord sizes are determined at multiple locations along the width of the image by seeking decreases in the image intensity.
2. Aspect ratio and size information may be acquired near the center of the tube where the lighting intensity is most uniform.

Experimental Setup

4.1 Facility

In order to perform the proposed experiments, a brand new facility was designed, procured, constructed and commissioned. A schematic of the facility is illustrated in figure 17, while general characteristics are listed in table 15. Instrumentation was also acquired and installed, and this is discussed in section 4.2.

Tap water at 20°C is decalcified, filtered and stored in a reservoir tank with a 120 L capacity. A 38.1 mm (1.5") ID suction line supplies water from this tank to a 2.24 kW (3 hp) pump which is controlled via a variable frequency drive (VFD). The pump discharges into a 2.5 m (99") horizontal length of 25.4 mm (1") ID stainless steel tubing which is instrumented for both mass flow rate and temperature, the details of which are described in section 4.2. After the piping run, the flow enters a machined aluminium 'inlet block' as illustrated in figure 18 containing a penetration

Table 15: Operating Characteristics of the Loop

	Water Side	Air Side
Working Fluid	Decalcified Water	Compressed Air
Fluid Temperature (°C)	20 - 25	20
Maximum Flow Rate ($kg \cdot s^{-1}$)	2.00	(3.2)(10^{-5})
Maximum Superficial Velocity ($m \cdot s^{-1}$)	2.55	0.037
Operating Pressure (kPa)	101.3	400.0

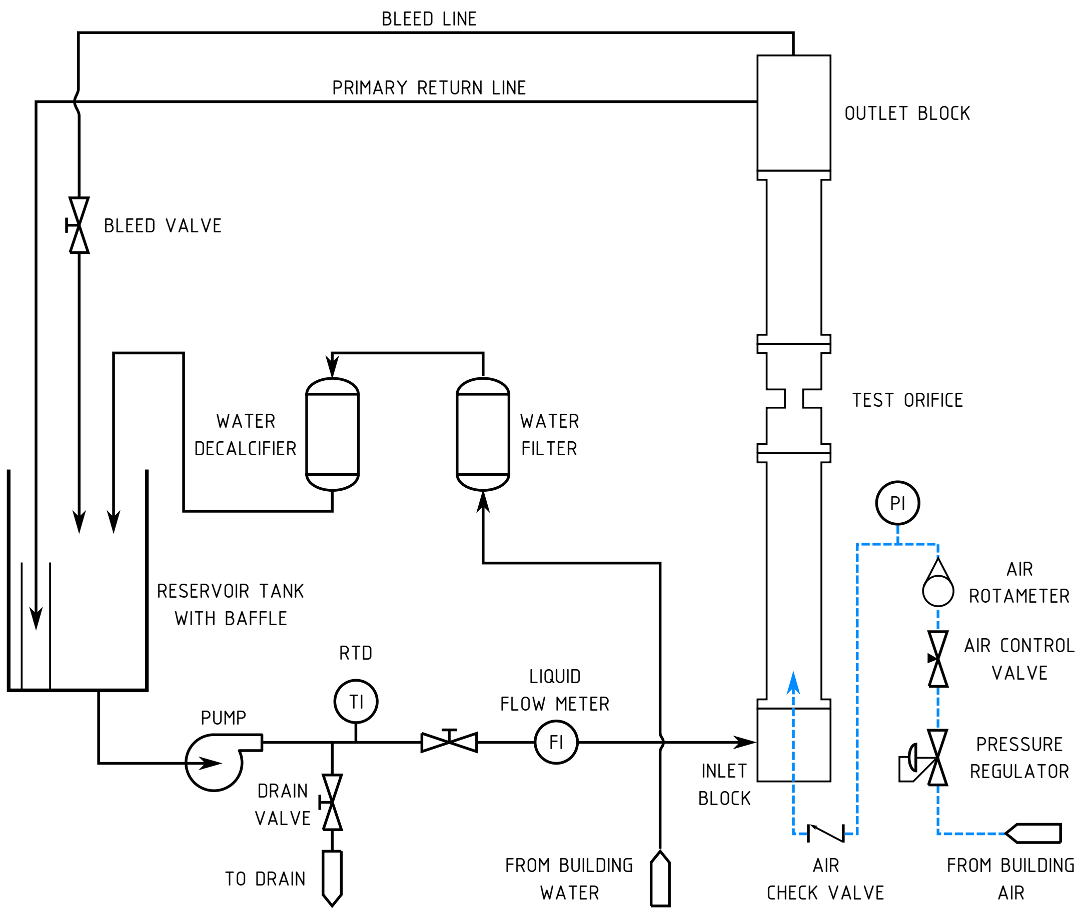

Figure 17: Schematic of the flow loop

for an air injector, and couples the loop to the vertical acrylic test section via a flange. The test section discharges into an aluminum 'outlet block' which allows connections to both the bleed line and the return line. Instrumentation for the flow rate is also available on the return line. The test sections are discussed in section 4.1.1.

Compressed air is supplied to the loop from the building taps, and is regulated and filtered for oil and debris. A 20-turn precision needle valve allows fine control of the air flow, while a rotameter and pressure transducer report the volumetric flow rate and the gauge pressure. The air line is connected to the loop at the inlet block using a quick disconnect fitting with a built in check-valve to prevent back flow.

A length of 3.175 mm (1/8") ID stainless steel tubing is inserted into a feed-through fitting in the inlet block and acts as a hydrodynamic sheath. The end of the sheath is fed several centimeters past the flange connection in order to reduce the influence of the turbulence on bubble departure. A piece of hypodermic tubing with an ID of 0.512 mm (0.020") is epoxied onto the end of the sheath, and allows bubbles to be gradually injected into the flow.

4.1.1 Test Section

The "test section" consists of the pieces between the inlet block and the outlet block. It consists of 3 parts: an approach run, an orifice and a discharge run. The flanges and the orifice components are made of cast acrylic, while extruded acrylic is used for the tubing.

The approach run consists of a vertical, 813 mm (32") long extruded acrylic tube with an ID of 31.75 mm (1.25"). The length of the tube allows for the flow to develop for some distance after passing through the inlet block, however the distance only represents 25.6 D_{hyd} which is insufficient for the fluid to reach a 'fully developed' state. Typically a flow is considered fully developed after traveling $80-100$ D_{hyd} downstream from any flow area change, however height limitations in the room prevent such a facility from being constructed. Additionally, as the results section will demonstrate, the incidences of bubble fragmentation in the inlet run is negligible relative to the occurrences in the orifice.

The orifice segment consists of a hole milled in a 19.05 mm (3/4") thick piece of

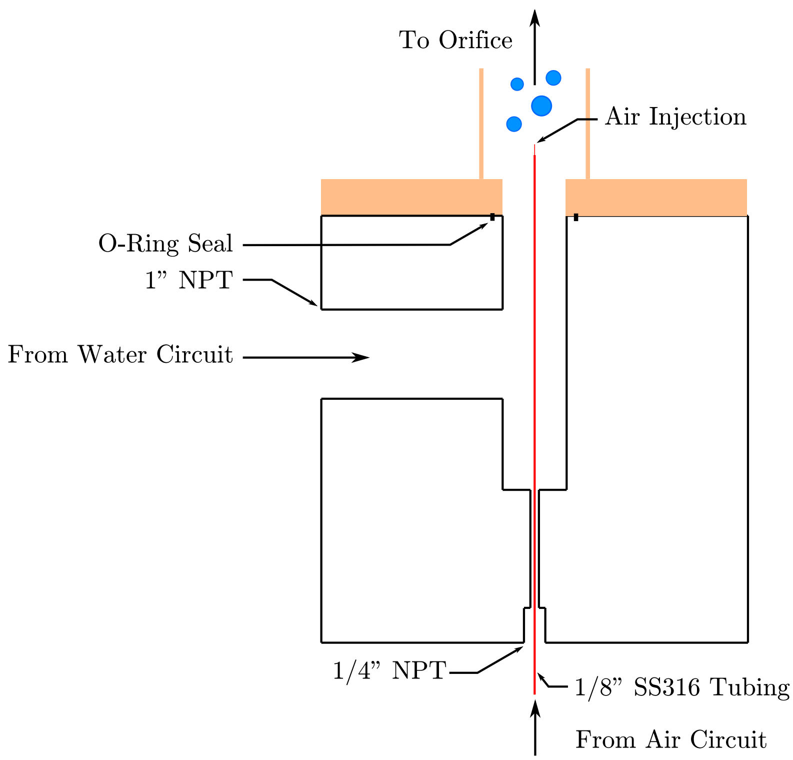

Figure 18: Cutaway view of the inlet block and air injection point

Table 16: Orifice Segment Characteristics

Parameter	Test Section 1	Test Section 2	Test Section 3
Tube ID	31.75 mm	31.75 mm	31.75 mm
A_{tube}	791.7 mm^2	791.7 mm^2	791.7 mm^2
Orifice ID	25.40 mm	19.05 mm	12.70 mm
$A_{orifice}$	506.7 mm^2	285.0 mm^2	126.7 mm^2
$\frac{A_{tube}}{A_{orifice}}$	1.56	2.78	6.25
Blockage Ratio	0.36	0.64	0.84

cast acrylic. Spool pieces are solvent welded onto either face of the orifice, allowing the segment to be flanged onto the inlet and outlet runs. In this work, 3 orifice diameters are investigated and these are listed in table 16. Blockage Ratios are calculated as: Blockage Ratio $= 1 - \left(\frac{d_{orifice}}{d_{tube}}\right)^2$.

A rendered view of the 12.7 mm (1/2") orifice assembly is illustrated in figure 19. Detailed CAD drawings for the test section and orifices are supplied in Appendix A.

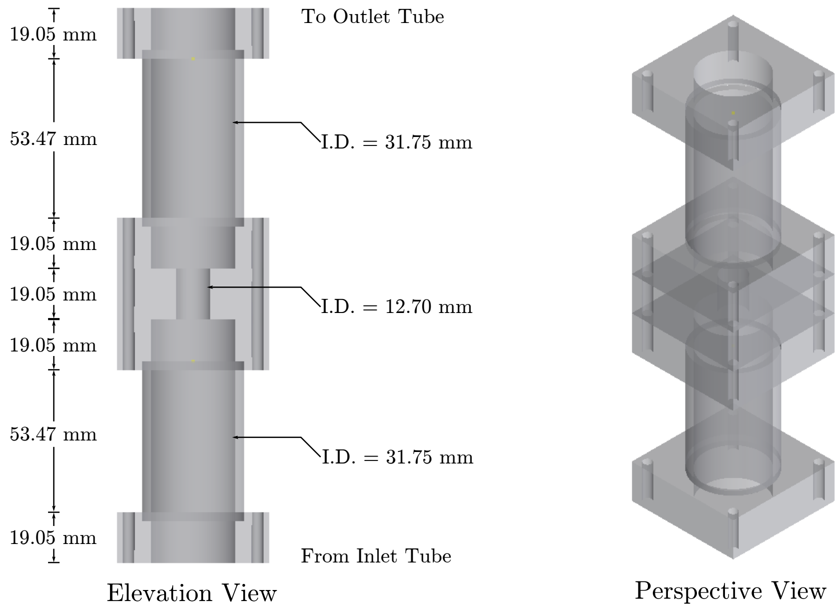

Figure 19: Top and Perspective view of the 1/2" orifice segment

4.2 Instrumentation

4.2.1 Liquid Flow Measurement

The mass flow rate into and out of each of the two channels is measured using Rosemount 8732E magnetic flow meters. The instruments are contained within a 'wafer' type housing and connected to the loop via flange connections. General technical specifications for the devices are listed in table 17, while uncertainties are quantified in table 18. Additional device specific details are listed in Appendix A.

4.2.2 Air Flow Measurement

The volumetric flow rate of air into the test section was measured using a Gilmont Instruments GF-2160 float type air flow meter with parameters specified in table 19. Flow rates were determined by visually observing the height at which the ball float was suspended within the tube while control was achieved using a ultra high-precision 20-turn needle valve with a flow coefficient of $Cv = 0.02$. The manufacturer's specified

Table 17: Specifications for the magnetic flow meters

Parameter	Value
Line Size (ID)	25.4 mm
Liner Material	PTFE
Low Flow Cutoff	0.012 m/s
Maximum Flow Rate	12.00 m/s
Configured Range	0 - 5 m/s
Output Range	4 - 20 mA
Operating Temperature Range	-29 to $+177$ (°C)

Table 18: Accuracy and uncertainties for the magnetic flow meters

Parameter	Value
Base Accuracy	±0.25% of flow rate
Analog Output Accuracy	±4μA
Repeatability	±0.1% of reading
Stability	±0.1% of rate over 6 months
Ambient Temperature Effect	±0.25% over temperature range

uncertainty for the flow meter is the greater of ±5% of the value read or ±2 mm.

Since the air is supplied from the building taps 'at pressure' and the air flow meter is calibrated at STP, a conversion is done in order to account for the higher density passing through the rotameter. Details of the conversion as well as how the gas superficial velocity is determined are supplied Appendix A.3.1 and A.3.2.

4.2.3 Air Pressure Measurement

Air is supplied from the building compressed air lines and fed to a ControlAir Inc. Type 300 precision air regulator and filter installed immediately downstream. The manufacturer claims a supply pressure variation of 172 kPa will result in an output pressure change of 1.4 kPa [85].

The air pressure is reported downstream of the rotameter using a Rosemount

Table 19: Specifications for the air flow meter

Parameter	Value
Line Size (ID)	6.35 mm (1/4")
Body Material	Glass Tube
Flow Range (at STP)	1.00 to 280 (mL/min)
Flow Range (at 355 kPa(a))	1.87 to 469 (mL/min)
Maximum Pressure	861 (kPa)
Operating Temperature Range	-26 to 65 ($°C$)
Uncertainty	$max\,(\pm 5\%, \pm 2\ mm)$
Repeatability	$max\,(\pm 1\%, \pm 0.5$ scale division)

1144G pressure transmitter. At the lowest air flow rates used in the tests, a pressure of 256.4 $kPa(g)$ was recorded, while the pressure at the highest air flow rate was 253.7 $kPa(g)$. At 25$°C$, according to the Ideal Gas Law, the variation of pressure between the two gas flow rates causes a density change of 0.7% (between 4.15 and 4.18 kg/m^3).

Table 20: Specifications for the Pressure Regulator

Parameter	Value
Maximum Supply Pressure	1723 (kPa(g))
Output Pressure Range	0–827 (kPa(g))
Filter	40 (μm)

Table 21: Specifications for the Pressure Transducer

Parameter	Value
Pressure Range	0–552 (kPa(g))
Base Accuracy	±0.5%

4.2.4 Temperature Measurement

Temperature measurements are conducted using a platinum Resistive Temperature Device (RTD) housed within stainless steel thermowell and connected to the loop using an NPT fitting. The RTD is driven by a Omega DP-18 temperature indicator and power supply, and the general characteristics for both are listed in table 22 while accuracy and uncertainty information is supplied in table 23.

Table 22: Specifications for the RTD

Parameter	Value
Temeperature Range ($°C$)	0–200
Type	Thin Film Platinum
Connection	$\frac{1}{4}$" MNPT
Thermowell Material	Stainless Steel 316

Table 23: Accuracy and uncertainties for the RTD

Parameter	Value
Base Accuracy	±0.15°C at 20°C
Temperature Coefficient of Resistance	0.00385 $\Omega/\frac{\Omega}{°C}$

Results

The results chapter is divided into the following parts:

- Section 5.1 documents the fragmentation process occuring inside an orifice. High frame rate video provides qualitative evidence of the mechanisms which are occuring, while LDA measurements provide supplemental velocity and turbulence information about the flow.
- Section 5.2 discusses how the bubbles were sized. The work in the section examines the validity of some of the shape assumptions made, as well as how the bubbles are deformed due to variations in the liquid velocity and as they are forced through blockages.
- Section 5.3 deals with the interfacial area. Results taken sufficiently upstream of the orifice are considered unaffected by it, and so the a_i values are first compared against values in literature to verify that the post-processing algorithm is supplying acceptable results. After the accuracy has been established, the a_i measured upstream of the orifice is compared to the values obtained downstream.

For the LDA measurements, seven elevations along the length of the test section were selected as illustrated in figure 20. At each elevation, axial velocity data was acquired at between 35 and 45 radial locations, with each point consisting of 10,000 velocity measurements. The data is taken at a spatial resolution of 1 mm when near the centerline, and increasing to 0.25 mm when close to the wall. Data is acquired for mass flow rates of between 0.150 kg/s and 0.950 kg/s with the equivalent liquid superficial velocities and bulk Reynolds number (as measured in the tube) listed in table 24. The full set of results is supplied in Appendix B. All references to the superficial liquid or gas velocities are calculated with the tube diameter ($\phi = 31.75\ mm$).

High shutter speed photography is conducted at an 'upper' and 'lower' elevation as illustrated in figure 21. High speed video for qualitative study is also taken of the bubbles fragmenting in the orifice at the location indicated in the figure.

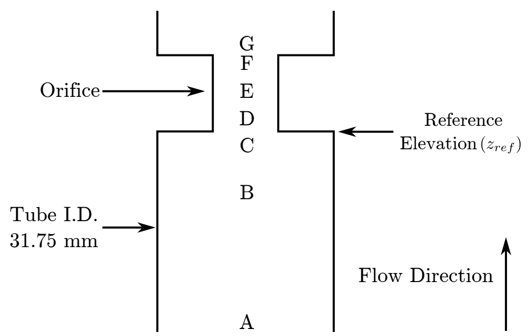

Measurement Position	Dist to Ref. Elev. ($\Delta z_{ref}, mm$)	Rel. Dist. to Ref. Elev. ($\frac{\Delta z_{ref}}{d_{hyd}}$)
A	-83.67	-2.64
B	-7.67	-0.24
C	-2.23	-0.07
D	3.77	0.12
E	10.27	0.32
F	16.77	0.53
G	23.27	0.73

Figure 20: LDA measurement elevations.

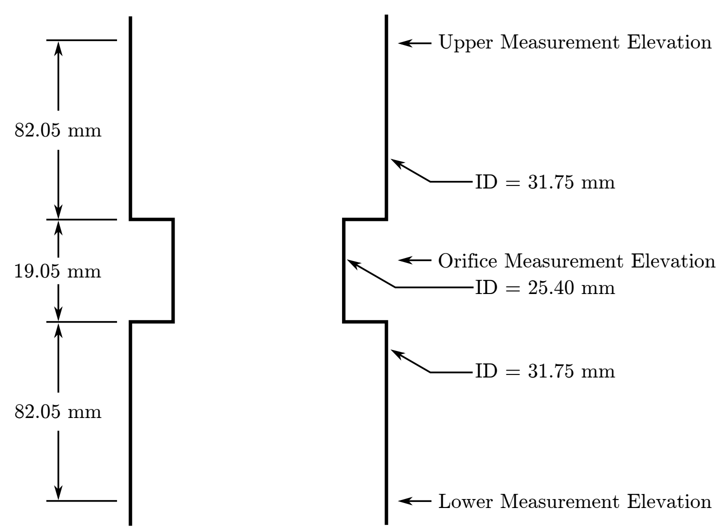

Figure 21: Side view schematic of the 25.4 mm diameter orifice test section with video and photography elevations indicated.

Table 24: Liquid Flow Conditions

$\dot{m}$ (kg/s)	j_f (m/s)	Re $(-)$
0.150	0.191	6759
0.350	0.447	15770
0.550	0.702	24782
0.750	0.957	33794
0.950	1.212	42806

5.1 Fragmentation Process

In the tests in this section, two types of measurements were conducted using high speed photography. A preliminary set of videos was taken to qualitatively determine the mechanisms and the process behind the fragmentation as the bubble is accelerated through the orifice. A brief discussion on the observations from these videos is conducted in section 5.1. In the section, the camera was set to a high frame rate and high shutter speed to capture the qualitative details of the bubbles breaking up.

Additional quantitative work was also completed by using a low frame rate and taking advantage of the camera's large memory buffer. In this manner, a large number of images were captured of the bubbles both before and after they passed through the orifice. Using these images, a statistical description of the bubble chord sizes and aspect ratios could be determined.

A set of preliminary videos taken suggest that several fragmentation mechanisms are occuring as bubbles pass through the orifice. Figure 22 is a composite view of the orifice section with air-water flows passing under "bubbly flow" conditions.

From the images in the figure, it is difficult to discern precisely what is occuring in the orifice. Multiple fragmentation events are occuring in the region simultaneously, and so a set of tests run at a very low gas flow rate ($j_g = 0.004$ m/s, near the bottom of the operating range of the flow meter) were conducted. The goal of these tests was to isolate a single bubble breaking up in the orifice region for qualatative study. In these isolation tests, the camera was set to acquire data at 12500 frames per second with a shutter speed of 368.5 ns.

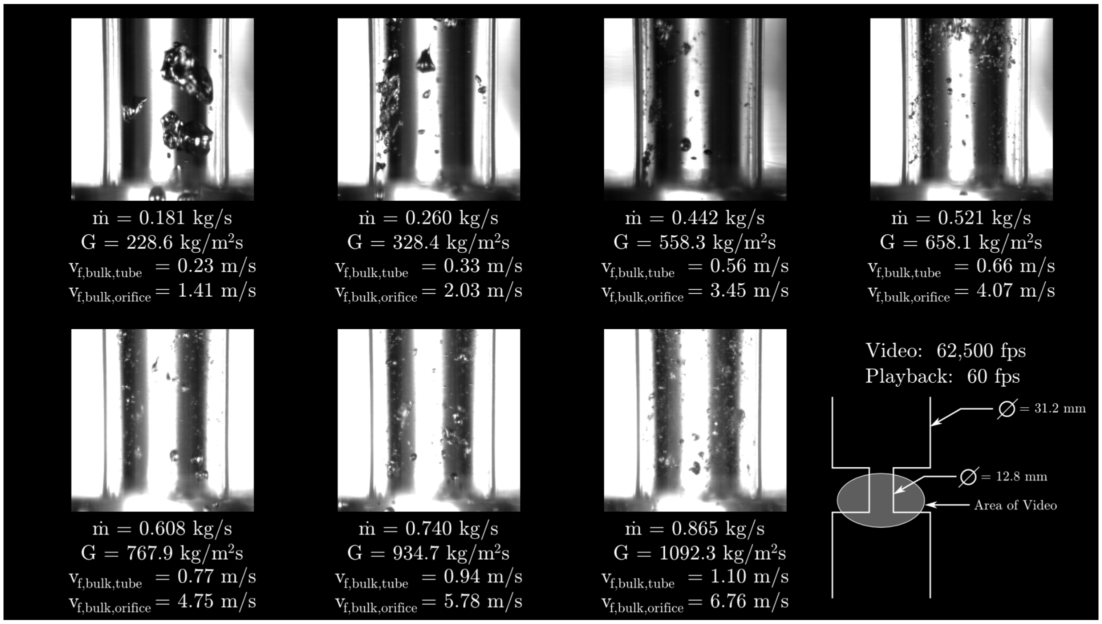

Figure 22: Fragmentation occuring in the $\phi = 12.7\ mm$ orifice at different mass flow rates.

The video shows two distinct fragmentation mechanisms occuring in the flow obstruction - one caused by the shearing of the bubble due to a velocity gradients, and one caused by the fluctuation of the fluid velocity field. In addition, a special case of the turbulent fragmentation was observed to occur when the parent bubble becomes entrained in the re-circulation zone of the orifice and gets stripped apart by the passing fluid.

In observations of bubbles fragmenting after being injected into a water jet, Martínez-Bazán *et al.* [23] discounted interfacial instability as a cause of disintegration on the grounds that the time scale required for this mechanism is far larger than the bubble residence time within the turbulent region. In these tests, orifice liquid velocities of between 0.3 m/s to 8 m/s were reported. At these speeds, the bubble is expected to spend between 0.0024 s to 0.0647 s within the flow restriction.

5.1.1 Shear Dominant

The shear mechanism exists due to velocity gradients which exist in and around the orifice, and fragmentation was observed to occur due to differences in velocity along the surface of the bubble. This mechanism tends to occur at lower fluid velocities when the magnitude of the turbulence in the orifice is too low to break apart the bubble on its own.

An example of a bubble undergoing this type of fragmentation is illustrated in figure 23 which consists of a series of images taken $\Delta t = 4\ ms$ apart. Axial velocity measurements obtained in the orifice using the LDA at $j_f = 0.191\ m/s$ are illustrated in figure 24. The measurements were taken under single phase conditions due to the tendency of the bubbles to scatter the beam or block the receiver.

The LDA measurements demonstrate that near the entrance of the orifice (at measurement elevation D), the velocity profile is relatively flat. However, further downstream from the entrance by measurement elevation E, a steep gradient develops with respect to the wall. Between $r/R_{orf} = 0.80$ and $r/R_{orf} = 0.97$ (a distance of 1.6 mm), the mean measured axial velocity decreases from $u = 0.72\ m/s$ to $u = 0.10\ m/s$. In the data points closest to the orifice wall, part of the measured velocity distribution is negative, suggesting that a recirculation region is forming.

An illustration of the breakup process is illustrated in figure 25. In the figure a spherical bubble approaches the blockage at position Q. It reaches the blockage at position R, and is stretched laterally as it is sucked into the flow restriction. At position T, the side of the bubble closest to the wall will be subjected to a lower velocity than the side of the bubble nearest to the center of the orifice. As a result of the velocity difference, the faster moving fluid may pull a relatively large daughter bubble off of the parent bubble.

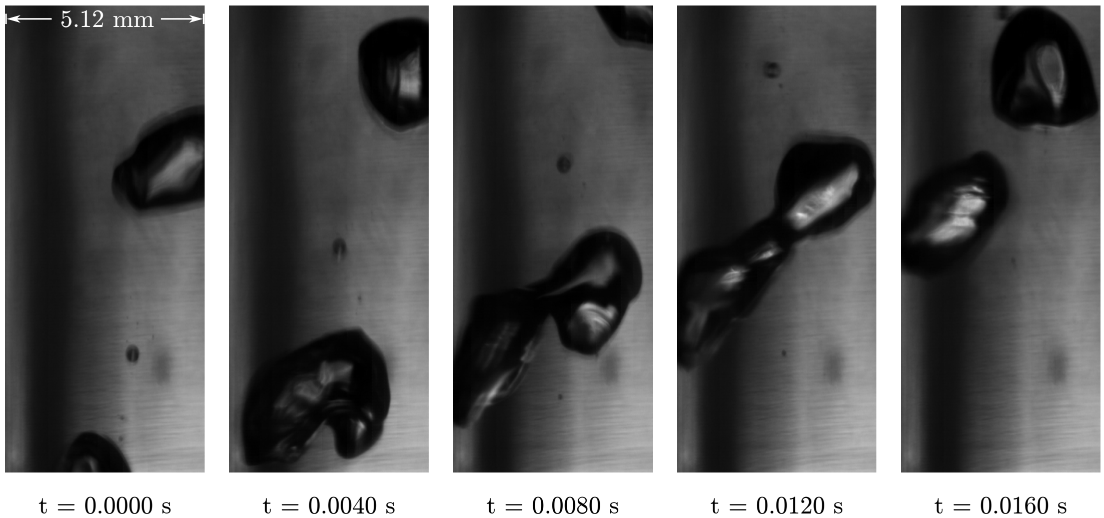

Figure 23: Observed shear fragmentation occuring through the $\phi = 19.1$ mm orifice at $j_f = 0.191$ m/s and $j_g = 0.004$ m/s. The bottom of each image is cropped at about 1 mm from the entrance of the orifice, while the left edge is about 2 mm from the orifice wall. Δt between each frame illustrated is 4 ms.

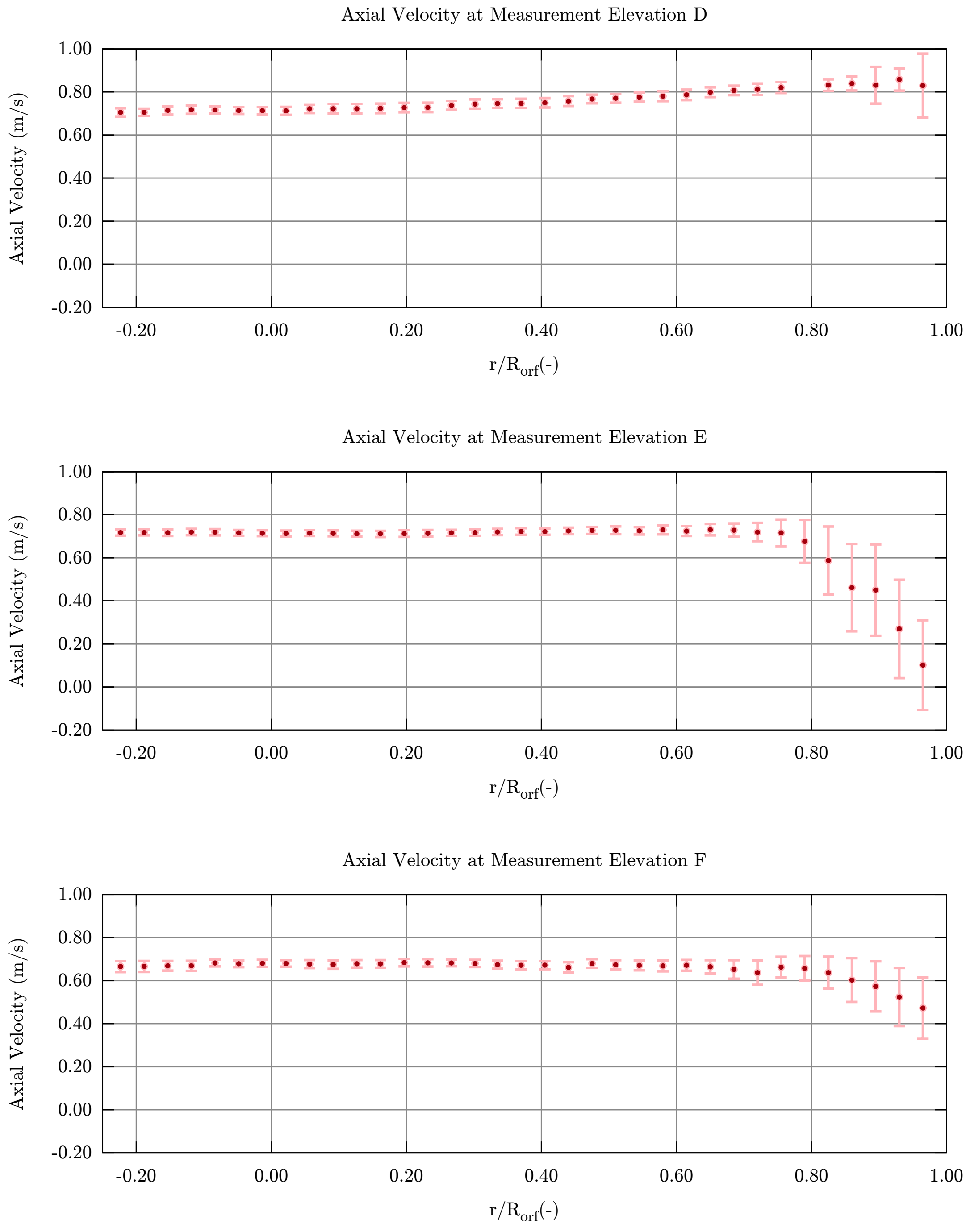

Figure 24: Single phase axial velocity measurements, taken at measurement elevations D (top), E (middle) and F (bottom) in the $\phi = 19.1\ mm$ orifice at $j_f = 0.191\ m/s$. Positive velocities indicate upwards flow. Error bars represent the root mean square of the turbulent fluctuation.

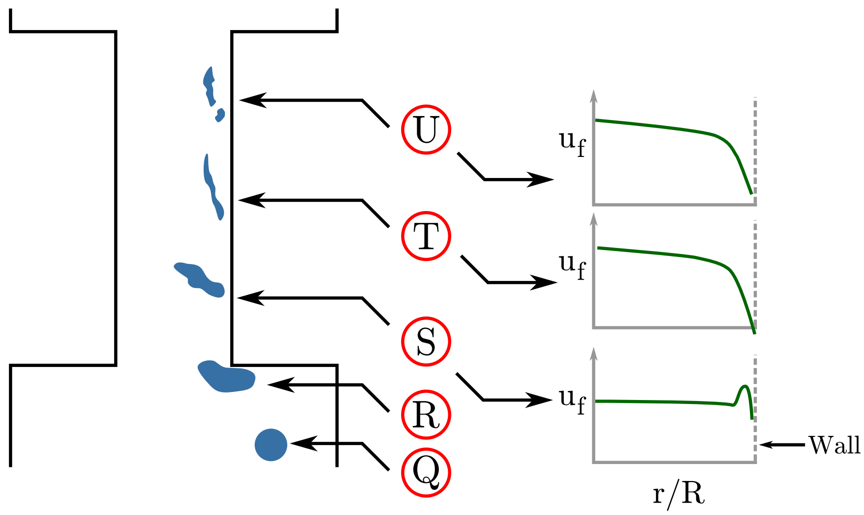

Figure 25: Stylized representation of the shear-type bubble fragmentation mechanism and fluid velocity profiles

This mechanism may also exist due to the velocity gradients in the axial direction. As the flow approaches and enters the orifice, it will be subjected to a large change in velocity over a short distance. A bubble travelling along the centerline of the tube may be pulled apart by this sudden velocity change. As an example, Figure 26 illustrates the measured axial velocities along the centerline of the test section at $j_f = 0.447\ m/s$. The plot demonstrates that the majority of the fluid acceleration takes place between measurement elevations C and D (third and fourth points from the left on each graph) which are seperated by about 6 mm [1].

A key characteristic of this mechanism is that the turbulent fluctuations are insufficient by themselves to overcome the surface tension. From the qualitative study, this is evidenced by the lack of perturbations on the surface of the bubble (as compared to the fragmentation events illustrated in the subsequent sections), which in turn causes relatively few daughter bubbles to be created.

[1]Measurements could not be made at a higher spatial resolution between these two points due to the difference in the optical path length which would have occured had one beam entered the test section through the orifice, while the other entered through the tube.

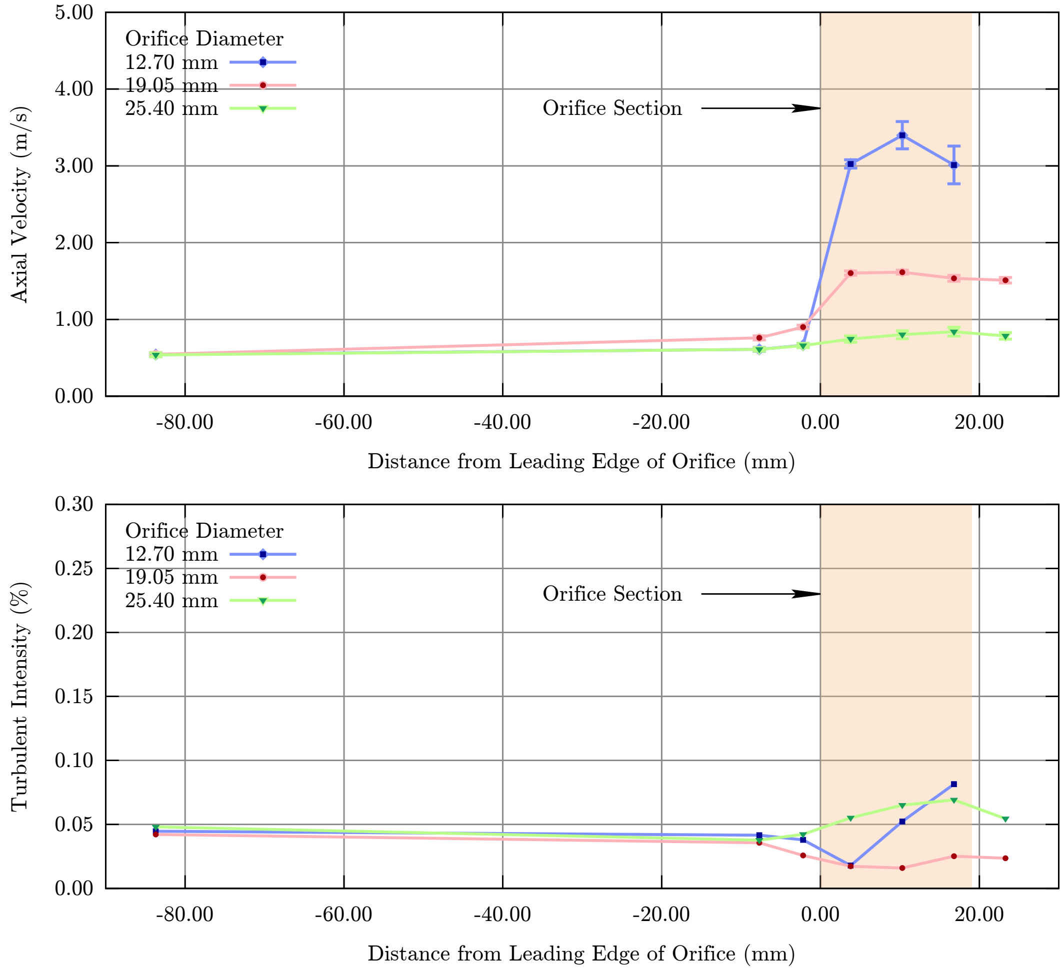

Figure 26: Single phase fluid velocity (top) and relative turbulent intensity (bottom) at $j_f = 0.45\ m/s$.

5.1.2 Turbulent Dominant

Figures 27 and 28 are examples of the observed turbulent fragmentation process taken from frames captured in the $\phi = 19.1\ mm$ orifice at $j_f = 0.702\ m/s$ and $j_f = 0.957\ m/s$ respectively. In the figures, the fragmentation process is distinct from the shear mechanism since the entire surface of the bubble is highly perturbed throughout the process. Additionally, the end result of both of these cases is the detachment of a cluster of very small bubbles (with a diameter of $d < 500\ \mu m$) on the top side of the bubble.

The time scale at which this process takes place is also significantly shorter than that of the shear process. In the shear fragmentation mechanism, it takes on the order of 10 ms for the bubble to break apart, whereas the turbulent fragmentation process tends to occur on the order of 1 ms in the conditions investigated.

A stylized illustration of the process is supplied in figure 29. Once again, a spherical bubble approaches the orifice from position Q, and is stretched laterally as it enters the restriction at point R. A velocity gradient causes some elongation and rotation as the bubble passes through position S, however the turbulent fluctuations are much higher in this case, and the surface of the bubble begins to deform. Some of the deformations may be significant enough to cause small fragments of the bubble to be pulled off of the bubble. At higher flow rates it is possible for the bubble to undergo multiple turbulent fragmentations events while passing through the orifice.

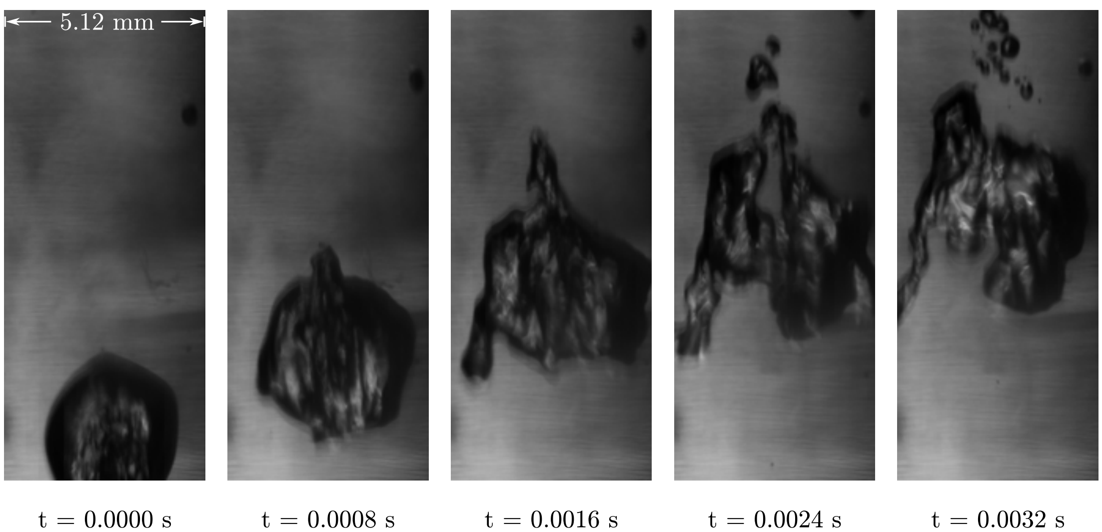

Figure 27: Observed turbulent fragmentation occuring through the $\phi = 19.1$ mm orifice at $j_f = 0.702$ m/s and $j_g = 0.004$ m/s. The bottom of each image is cropped at about 3 mm from the entrance of the orifice. Δt between each frame illustrated is 0.8 ms.

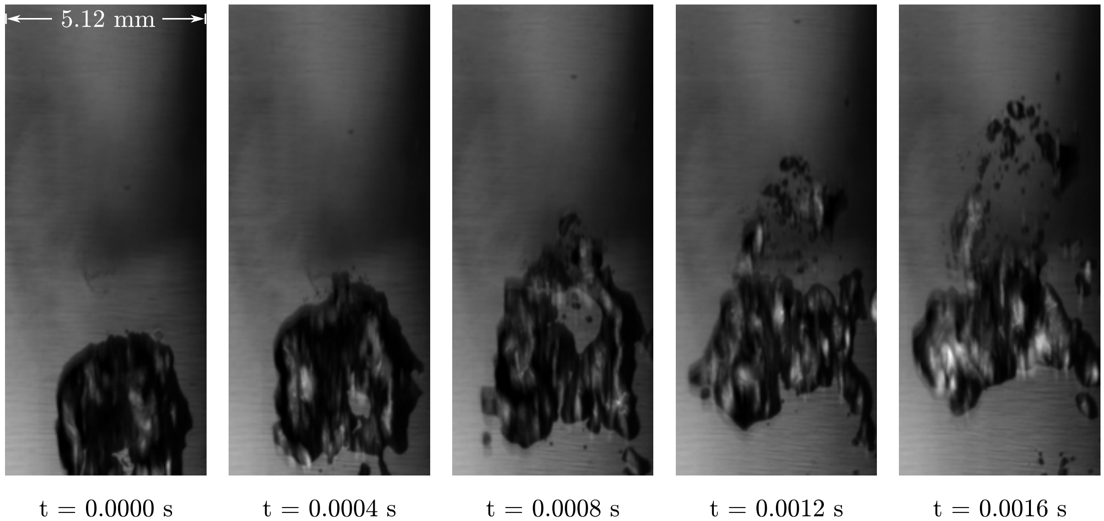

Figure 28: Observed turbulent fragmentation occuring through the ϕ = 19.1 mm orifice at $j_f = 0.957\ m/s$ and $j_g = 0.004\ m/s$. The bottom of each image is cropped at about 3 mm from the entrance of the orifice. Δt between each frame illustrated is 0.4 ms.

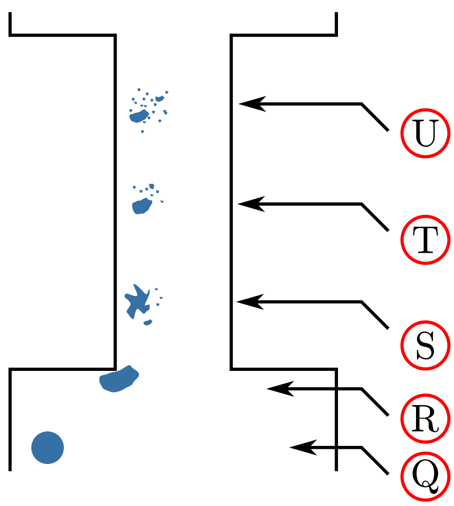

Figure 29: Stylized representation of the turbulence type bubble fragmentation mechanism

5.1.3 Entrainment in the Recirculation Region

When the fluid is forced through a sudden change in flow area, the formation of a recirculation region may occur. As illustrated in figure 30, a bubble enters the orifice at point R, and shortly downstream of entrance is captured by the recirculation region at point S. When this occurs, the fluid moving past may strip off small fragments of the main bubble. In many of the observed cases, the main bubble remains stuck in the recirculation region, while smaller daughter bubbles are continually being pulled off of it. Eventually, the main bubble either completely disintegrates or is dislodged by the wake of another bubble. The large number of daughter bubbles formed by this mechanism means it is likely a major source of interfacial area generation unique to situations where there are changes in the flow area. No previous literature has cited such phenomena.

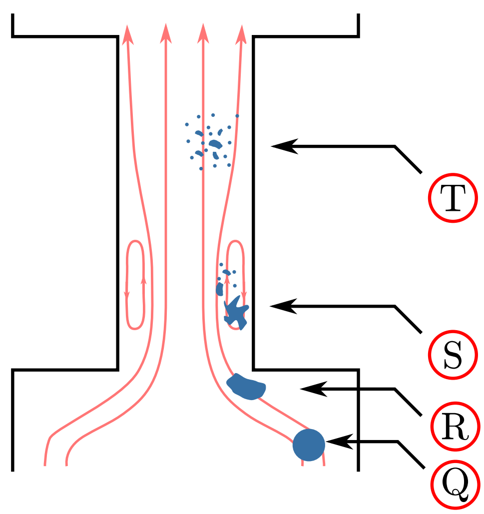

Figure 30: Stylized representation of the entrainment-turbulence type bubble fragmentation mechanism

Figures 31 and 32 are example sequences where a larger bubble is captured in the recirculation region in the $\phi = 19.1\ mm$ orifice and completely broken into much smaller bubbles. The two figures are taken at conditions of $j_f = 0.702\ m/s$ and $j_f = 0.957\ m/s$, with the gas superficial velocity held constant at $j_g = 0.004\ m/s$. The corresponding axial velocity measurements through the orifice under single phase conditions are supplied in figures 33 and 34. In the $j_f = 0.702\ m/s$ case at elevation E, part of the measured velocity distribution at the point closest to the wall was negative, suggesting that there may be some recirculation happening. This is not observed at $j_f = 0.957\ m/s$ - although the measurements do not get as close to the wall as the $j_f = 0.702\ m/s$ case [2].

The frames from figure 31 are taken under the same flow conditions, scaling and time intervals as figure 27. In the turbulent fragmentation only case (figure 27), the main bubble enters the orifice and after $t = 3.2\ ms$ has elapsed in the sequence, has fragmented and moved up half-way through the frame. The top row of the entrainment-turbulent fragmentation example (figure 31) illustrates the bubble over the same elapsed time. It is clear that in this case the main bubble has not moved axially, and a steady stream of small ($d < 1\ mm$) bubbles is being removed from its surface. The highly perturbed surface of the main bubble suggests that this is a turbulent fragmentation mechanism. By the end of the sequence, at $t = 15.2\ ms$, the initial bubble has been completely converted into a large population of sub-millimeter bubbles.

A similar comparison can be made between figures 28 and 32 where the former illustrates a bubble fragmenting due to turbulence but escaping downstream, and the latter clearly shows a large bubble being caught in the recirculation region and being completely reduced to sub-millimeter daughter bubbles. The main bubble in figure 32 is not only prevented from rising by the recirculating flow, but appears to pushed downwards in the second row of images. The higher flow rate relative to figure 31 also causes the formation of smaller bubbles.

It is postulated that this breakup mechanism is most effective when the sze of the recirculation region is larger than the size of the bubbles. Traditionally, the *vena contracta* is defined as the narrowest point of the fluid jet (where the local velocity is approximately equal to the maximum velocity), and its size is commonly approximated as $d_{vc} = 0.64\ d_{orifice}$. This is observed in the velocity measurements in figures 33 and 34 at measurement elevations E and F where the turbulent intensity (size of the uncertainty bands) beings to increase between the radial coordinates $0.60 < r/R_{orifice} < 0.70$, with the velocity beginning to drop off significantly after $r/R_{orifice} > 0.70$.

[2] The figures report the mean measured axial velocity (points) and the root mean square (error bars). While the mean velocity is not measured to be negative, parts of the velocity distribution may still exist at $u < 0$. It is speculated that had one more measurement been made closer to the wall in the $j_f = 0.957\ m/s$ case, part of the velocity distribution would have been negative.

For the $\phi = 19.1$ mm orifice, the *vena contracta* has a diameter of 12.2 mm, meaning that the recirculating region on each side is about 3.5 mm, which is roughly the same size as the bubbles. It would be reasonable to assume that in smaller diameter orifices, the size of the recirculation is also smaller. Under similar conditions, it is postulated that bubbles larger than the reciruclation region are less likely to escape and fragment due to other mechanisms. The likelihood of capture in these regions should be the topic of further studies.

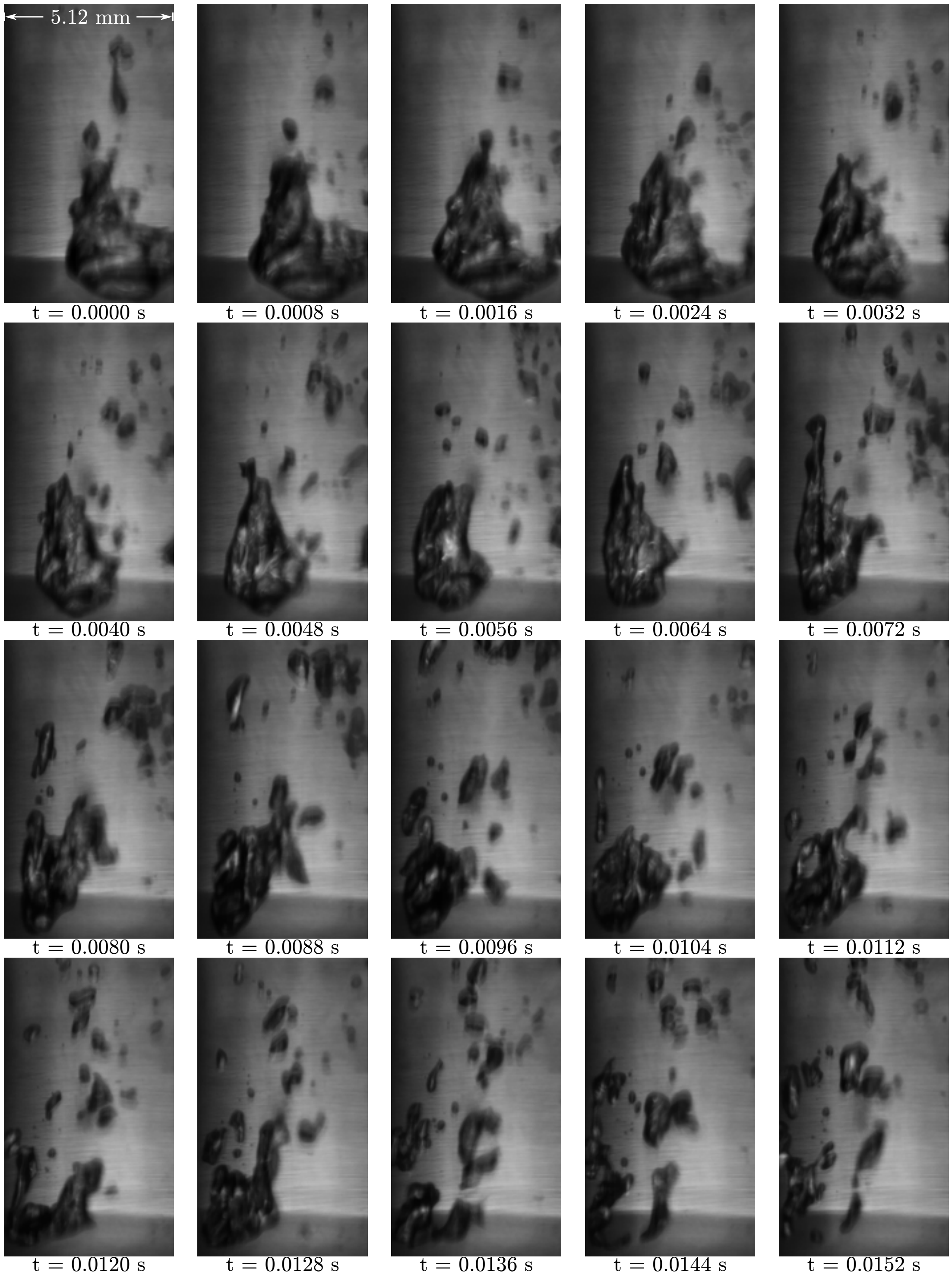

Figure 31: Observed entrained-turbulent fragmentation occuring through the ϕ = 19.1 mm orifice at $j_f = 0.702\ m/s$ and $j_g = 0.004\ m/s$. The bottom of each image is cropped at about 1 mm from the entrance of the orifice. Δt between each frame illustrated is 0.8 ms.

Figure 32: Observed entrained-turbulent fragmentation occuring through the $\phi =$ 19.1 mm orifice at $j_f = 0.957$ m/s and $j_g = 0.004$ m/s. The bottom of each image is cropped at about 1 mm from the entrance of the orifice. Δt between each frame illustrated is 0.4 ms.

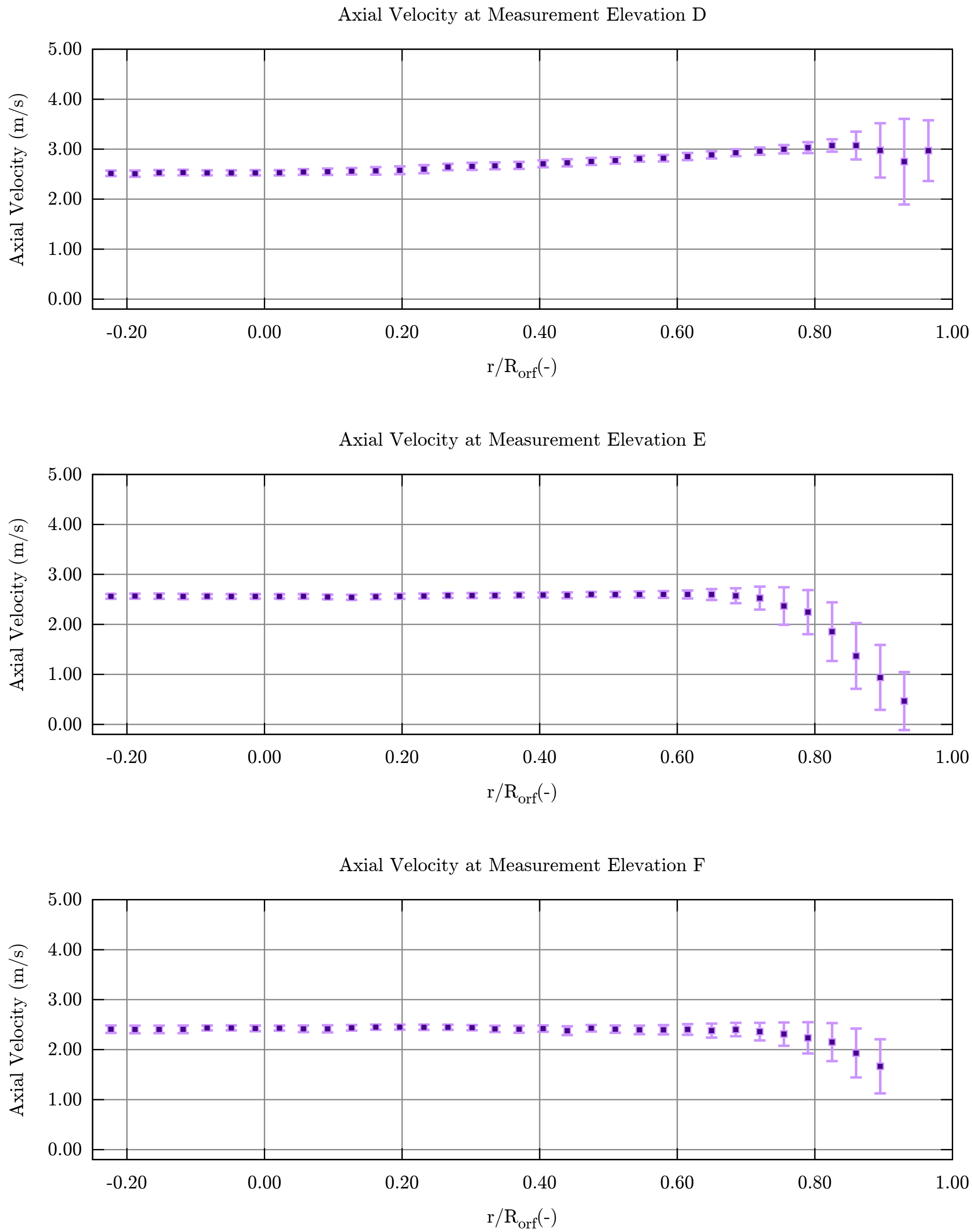

Figure 33: Single phase axial velocity measurements, taken at measurement elevations D (top), E (middle) and F (bottom) in the $\phi = 19.1$ mm orifice at $j_f = 0.702$ m/s. Positive velocities indicate upwards flow. Error bars represent the root mean square of the turbulent fluctuation.

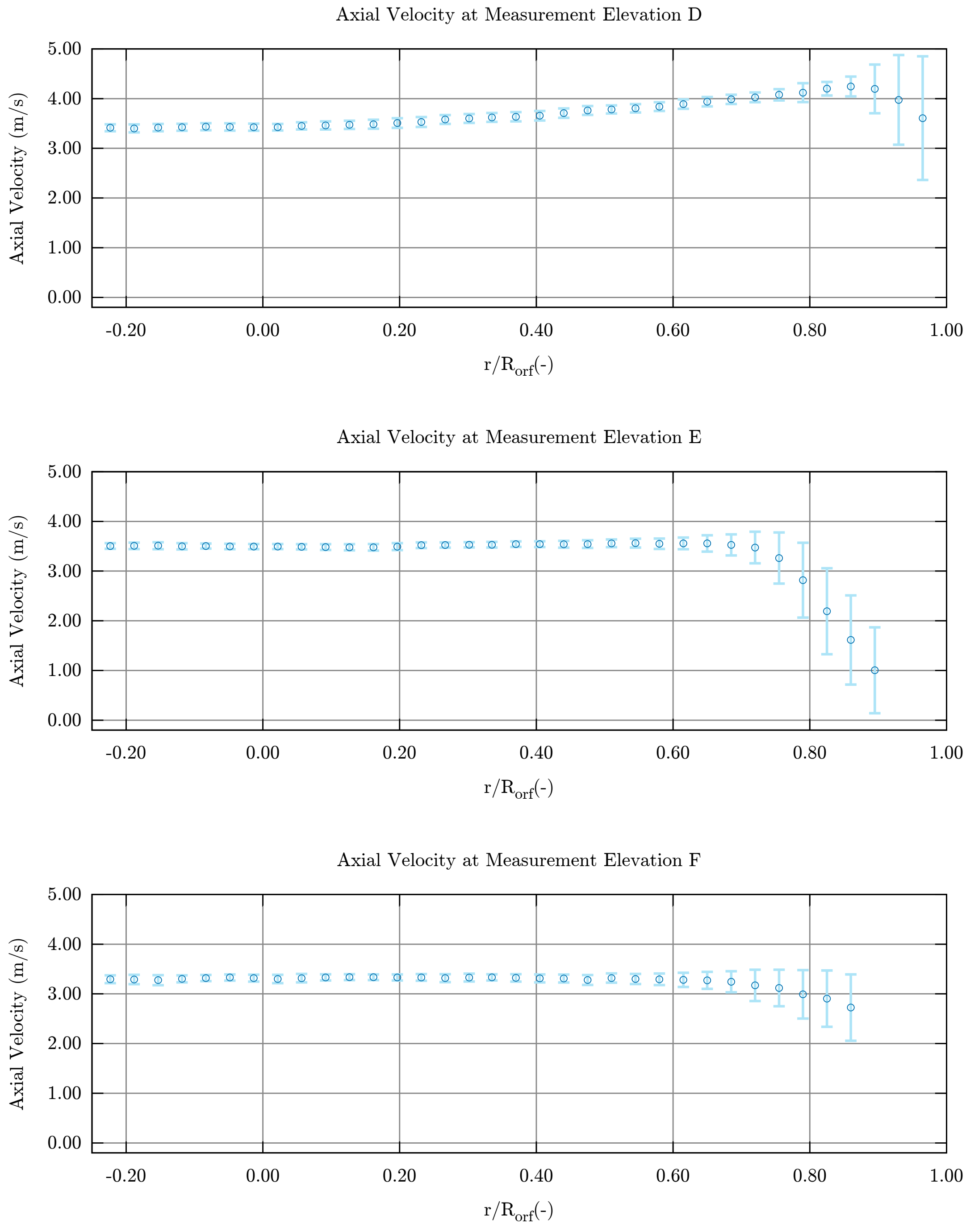

Figure 34: Single phase axial velocity measurements, taken at measurement elevations D (top), E (middle) and F (bottom) in the $\phi = 19.1\ mm$ orifice at $j_f = 0.957\ m/s$. Positive velocities indicate upwards flow. Error bars represent the root mean square of the turbulent fluctuation.

5.1.4 Summary

Two distinct breakup mechanisms have been identified in this section: a shear based breakup and turbulent fragmentation. In cases where the flow rate was high enough to cause a significant recirculation region to form, large bubbles were observed to enter the orifice and become entrained. Fluid flowing past these bubbles would periodically rip off small fragments of the larger bubble. This entrainment-turbulent type of breakup mechanism was observed to generate many more smaller bubbles than a single turbulent or shear fragmentation event, and is postulated to be a major source of a_i.

The literature review in section 2.2 indicates that both breakup mechanisms observed are consistent with literature. Specifically, bubbles being broken up by turbulence did appear very 'bulgy' (in agreement with the observations by Hinze [20]) while those being pulled apart by shear appeared to deform in a 'lenticular' manner (again, in agreement with Hinze).

The special case where the bubbles broke up after being entrained in the recirculation region represents something unique that does not appear to have been previously considered. The number of new smaller bubbles created suggests that this may be a major source of interfacial area. The only studies of bubble fragmentation due to obstructions found in literature were the TOPFLOW experiments which used wire mesh sensors which were not capable of measuring bubbles smaller than 2 mm [81].

5.2 Bubble Sizing

Obtaining accurate data on the size of the bubbles is perhaps the most difficult task in interfacial area studies. While the most common methods to measure bubble sizes include electrical conductivity probes and wire mesh sensors, the minimum bubble sizes detectable by these techniques is constrained by the finite spacing between the probes (typically on the order of $1-2\ mm$). The previous chapter has demonstrated that the bubble fragmentation process in the orifice may cause a large population of bubbles to form which are smaller than this size, and so camera based methods are used for bubble sizing in the current work.

Camera methods are well suited for measurement of flows at low void fractions, such as in this study. Higher void fractions ($\alpha > 0.10$) lead the bubbles overlapping in the frame frequently which reduces the accuracy of the sizing. However, at very low void fractions, the size of the bubbles becomes dependent on the gas superficial velocity. Although the air supply used in the experiment is regulated, it is still desirable to operate in a region where the bubble size is relatively insensitive to the air pressure. The work in section 5.2.1 seeks to establish flow conditions where the bubble sizes are relatively stable with respect to the air injection rate, as well as examine the effects of the gas superficial velocity on measured bubble chord size distribution.

As indicated in chapter 3.2.2, the measurement technique measured bubble chords along a selected vertical columns of the image. This was done to reduce the computational processing requirements, obtain data for the radial interfacial area profile, as well as to gather a statistical distribution of the bubble sizes. Since bubble chords are measured instead of bubble diameters, section 5.2.2 discusses how the bubble diameter distribution may be estimated from the chord data by making some assumptions about the bubble shape.

Images obtained in section 5.1 indicated that the larger bubbles ($d > 1000\ \mu m$) were non-spherical. Since a key assumption of the work of many authors is that the bubbles are spherical, section 5.2.3 quantifies the degree of non-sphericalness of the bubbles, as well as how the aspect ratio changes with flow condition.

Finally, since a wide range of bubble sizes are observed, it would be useful to track the relative contributions to the interfacial area as a function of bubbles of size.

Section 5.2.4 discusses the use of an area distribution function (ADF) in order to determine the overall contributions to the interfacial area.

5.2.1 Establishing a Stable Bubble Size

Quantitative bubble sizing in these tests were conducted using the high speed camera operating at high shutter speeds (but with low frame rates). For the purposes of this comparison, the maximum bubble size "observed" in the tests is defined as the chord size corresponding with the 95^{th} percentile, $c_{95\%}$, of the bubble population's cumulative distribution function (CDF). In this section the chord size is assumed (for the purposes of discussion) to approximate the diameter of the bubble [3].

Air flow rates between $j_g = 0.0019\ m/s$ and $j_g = 0.0373\ m/s$ [4] were used. The chord size of the bubbles were measured at position A, upstream of the leading face of the orifice. All reported values in this section are taken from measurements along the centerline of the test section.

Figure 35 is a stylistic representation of the expected evolution of $d_{95\%}$ as the superficial gas velocity is increased, when the fluid flow rate remains constant.

At extremely low gas flow rates ($j_g = 0.0019\ m/s$), air is forced out of the hypodermic needle slowly and the bubbles are swept up by the flow before they have an opportunity to develop into larger structures. In this scenario, $d_{bub} << d_{crit}$, so the bubbles are easily held together by surface tension and typically do not fragment further. Since very little air is being injected into the flow, the bubble number density is also low enough that the bubble collision probability is negligible - thus coalescence is infrequent.

Increasing the air flow rate allows the bubbles to grow larger before being carried off by the flow. Occasionally a bubble will grow such that $d_{bub} > d_{crit}$, which leads to fragmentation. However, since the bubble coalesence is still occuring infrequently, the maximum diameter of the bubbles will be approximated by the critical diameter. This region represents the ideal region for the current study since the d_{crit} is observable,

[3] The validity of this assumption is discussed in detail in section 5.2.2

[4] Values of j_g were purposely selected to be within this range to avoid the bubbly-slug transition region which typically starts at $j_g \approx 0.010\ m/s$ for this tube diameter, and to reduce the number density of the bubbles to a suitable value for the optical technique.

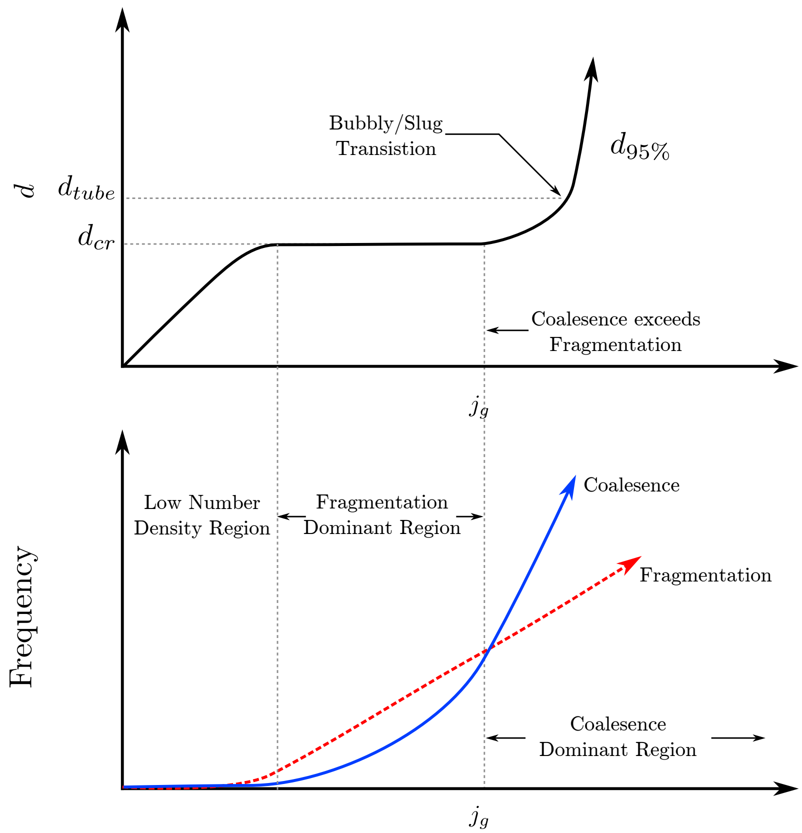

Figure 35: Expected evolution of $c_{95\%}$ at a constant j_f (top) along with the expected relative frequencies of the bubble interaction mechanisms (bottom).

while at the same time the number density is still low enough to allow for optical sizing techniques to be used.

Further increasing the flow causes the bubble density to increase such that bubble collisions are commonplace, and occur more frequently than turbulent fragmentation. This causes the maximum bubble size to increase until it approaches the diameter of the tube, at which point the bubbly/slug transistion occurs. The bubble “diameter” increases rapidly in this region since the diameter in the current work is defined as the chord of the bubble as measured parallel to the direction of the bulk flow. The cap or slug bubbles which form in this region are characterized by being much longer than they are wide.

Figure 36 illustrates both the PDFs and the CDFs for 3 different values of j_f when the air flow is set to a constant of $j_g = 0.0019\ m/s$. Fragmentation does not appear to be occuring in the lower liquid flow cases ($j_f = 0.191\ m/s$ and $j_f = 0.447\ m/s$) since the distribution of bubble sizes contains a single peak. In the PDF of the $j_f = 0.702\ m/s$ case, the increased bulk fluid velocity represents a larger amount of turbulent energy available, and as a result the critical diameter of the flow is lower. In this case, it is evident from the secondary peak at in the $c < 500\ \mu m$ range that some fragmentation events are occuring. The existence and significance of these secondary peaks is discussed in depth in section 5.2.4.

Figures 37 and 38 are the chord distributions for $j_g = 0.0125\ m/s$ and $j_g = 0.0311\ m/s$ respectively. In comparison to the very low gas flow rate cases, the bubble distribution PDFs have become flattened, and contain long tails. These two flow rates represent points along the flat part of figure 35 since even with the j_g increasing by a factor of 2.5 between the two figures, the distribution does not change significantly. Some fragmentation occurs in the $j_f = 0.447\ m/s$ and $j_f = 0.702\ m/s$ cases as evidenced by presence of a significant number of bubbles in the $c < 500\ \mu m$ range.

The number of frames sampled and the number of bubbles detected along the centerline for each case in figures 36, 37, and 38 is presented in table 25. At higher gas flow rates, the bubble density increases which is why some of those cases use fewer frames to achieve similar statistics.

Table 25: Number of frames sampled and bubbles detected

j_g (m/s)	$j_f = 0.191$ m/s		$j_f = 0.447$ m/s		$j_f = 0.702$ m/s	
	n_{frames}	$n_{bubbles}$	n_{frames}	$n_{bubbles}$	n_{frames}	$n_{bubbles}$
0.0019	43676	2497	43676	2186	43674	2709
0.0125	43676	8294	43676	5204	43674	10080
0.0311	43676	14653	32757	9404	21837	5333

A second set of data was acquired using fewer frames (and consequently, fewer detected bubbles) over a larger number of gas superficial velocities. These data were used to study the relationship between the gas flow rate and the bubble size. The bubble chord distribution medians and 95^{th} percentiles for these cases are plotted against the superficial gas flow velocity in figures 39 and 40. As illustrated in figure 39, the region where the bubble chord diameter is dependent on the air flow rate is very limited. For the conditions examined, the bubble size distributions are most sensitive to the air injection rate for superficial gas velocities of $j_g < 0.0125$ m/s. Above this flow rate, the median of the chord diameters are not strongly affected by changes in the air rate - although it is expected to increase once the bubble density increases to levels where coalesence exceeds the fragmentation.

The maximum bubble size is considered to approximate d_{crit} between gas superficial velocities of 0.0125 $m/s \leq j_g < 0.0311$ m/s.

The fragmentation upstream of the orifice starts to contribute significantly to the bubble size distribution at $j_f > 0.447$ m/s (corresponding to $Re_f \approx 16,000$)

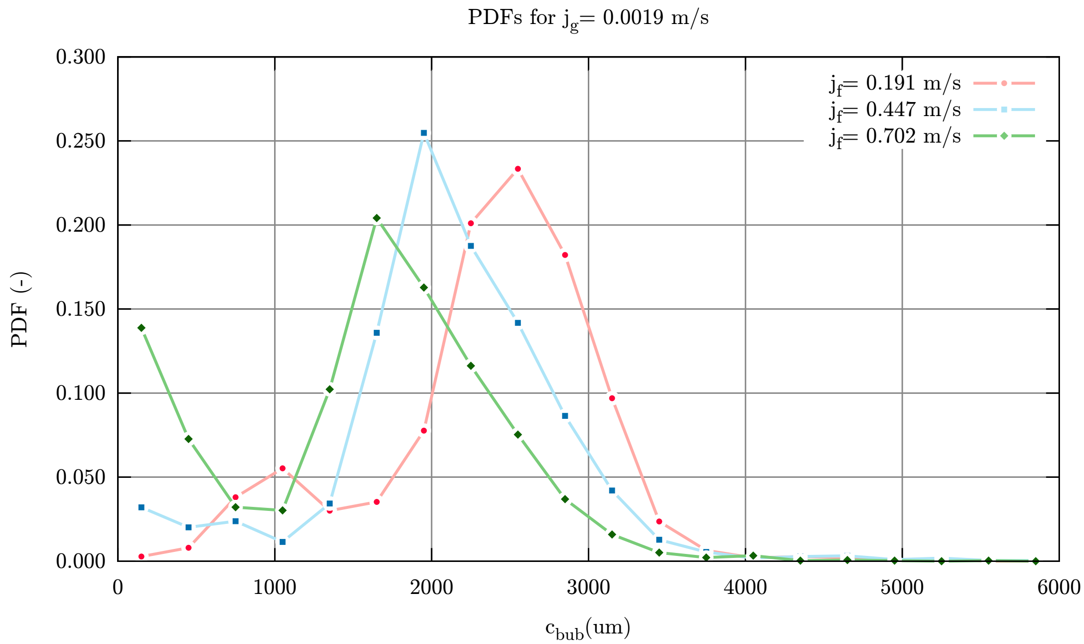

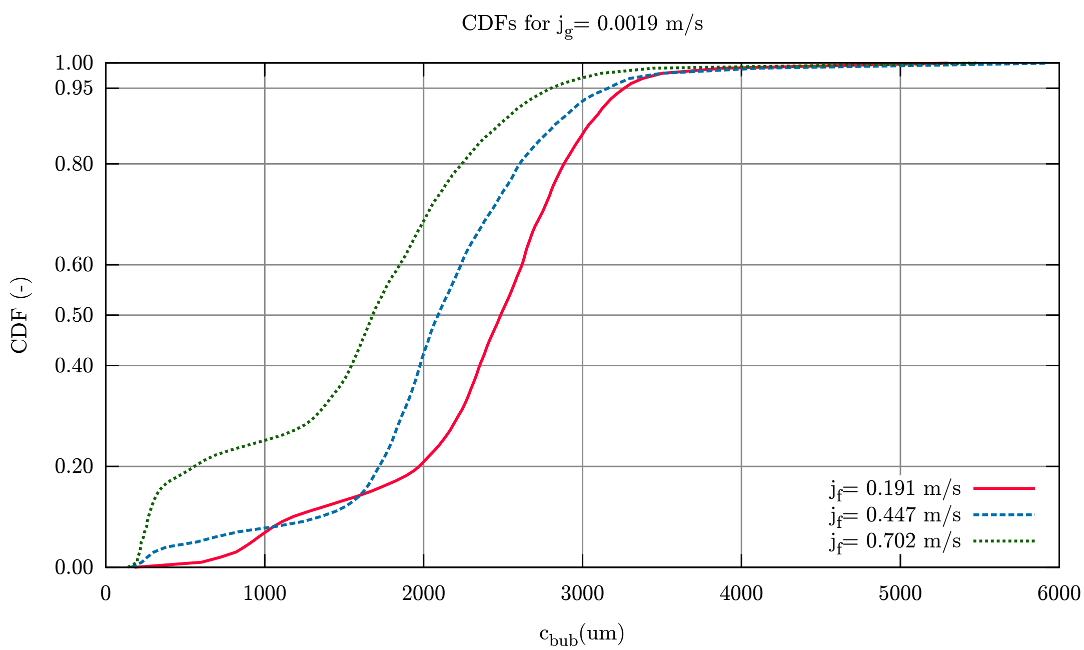

Figure 36: Bubble chord PDFs (top) and CDFs (bottom) at $j_g = 0.0019\ m/s$.

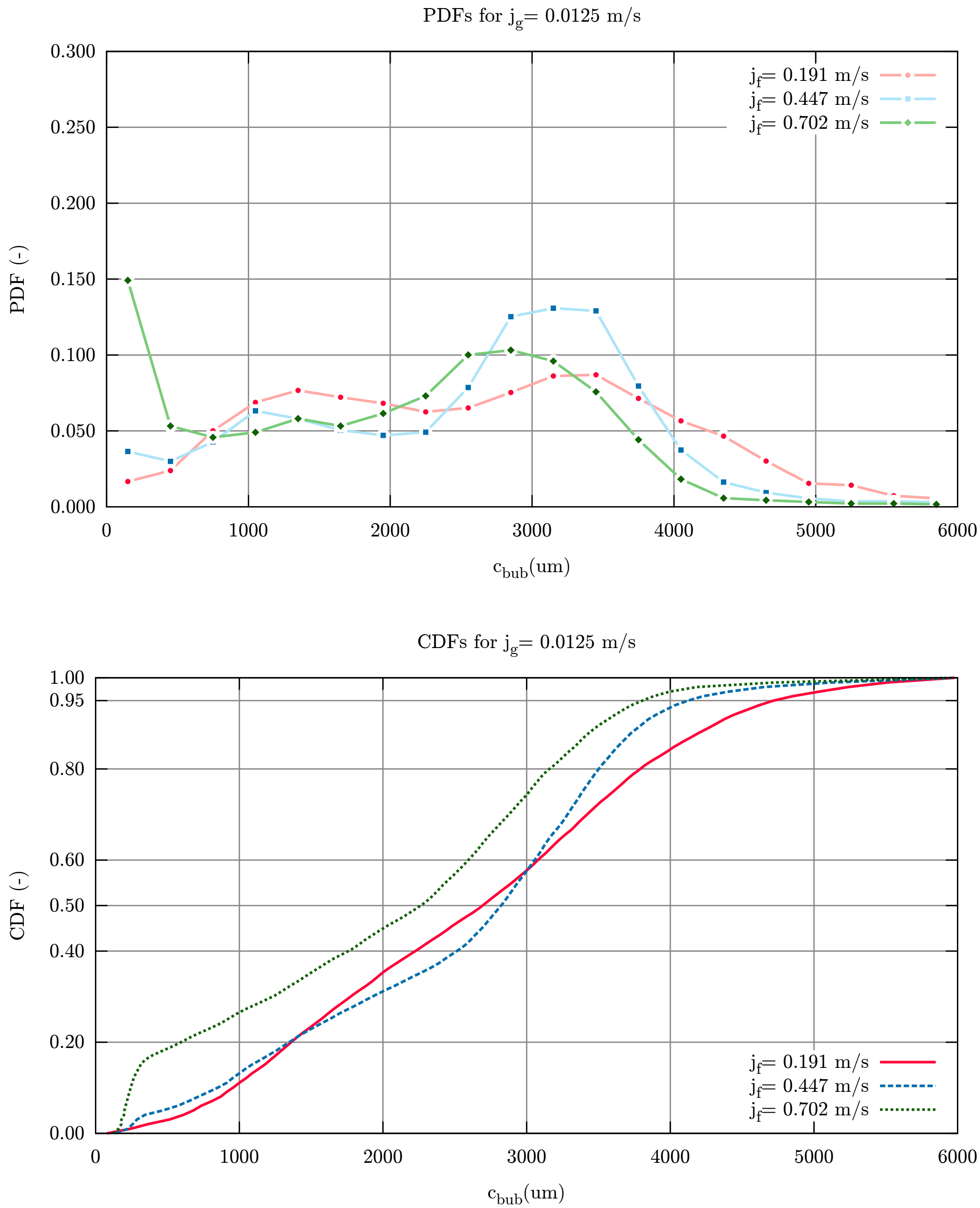

Figure 37: Bubble chord PDFs (top) and CDFs (bottom) at $j_g = 0.0125\ m/s$.

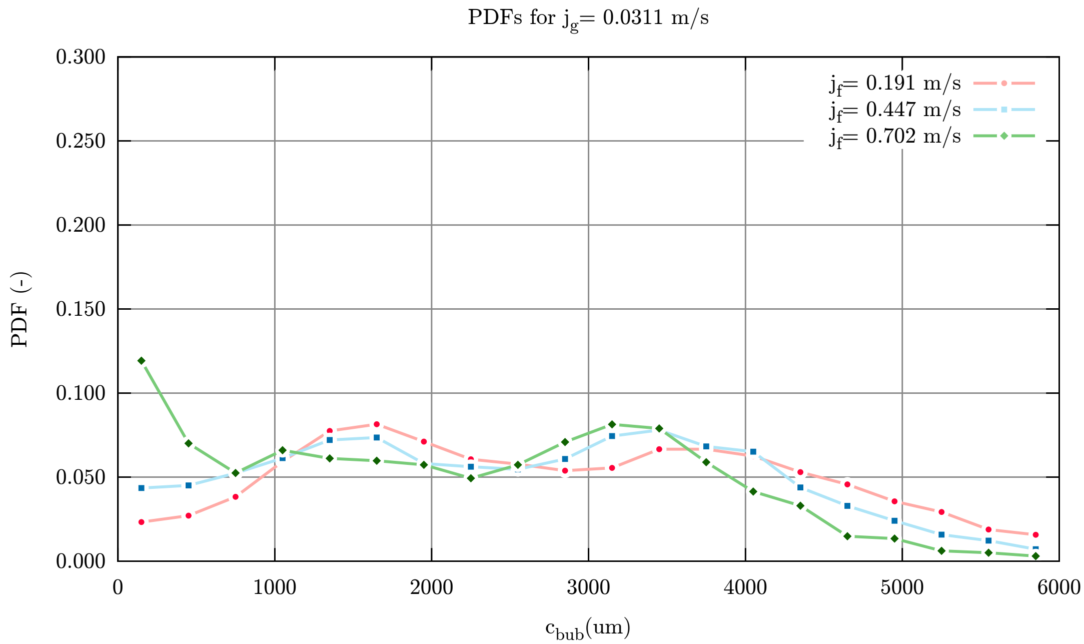

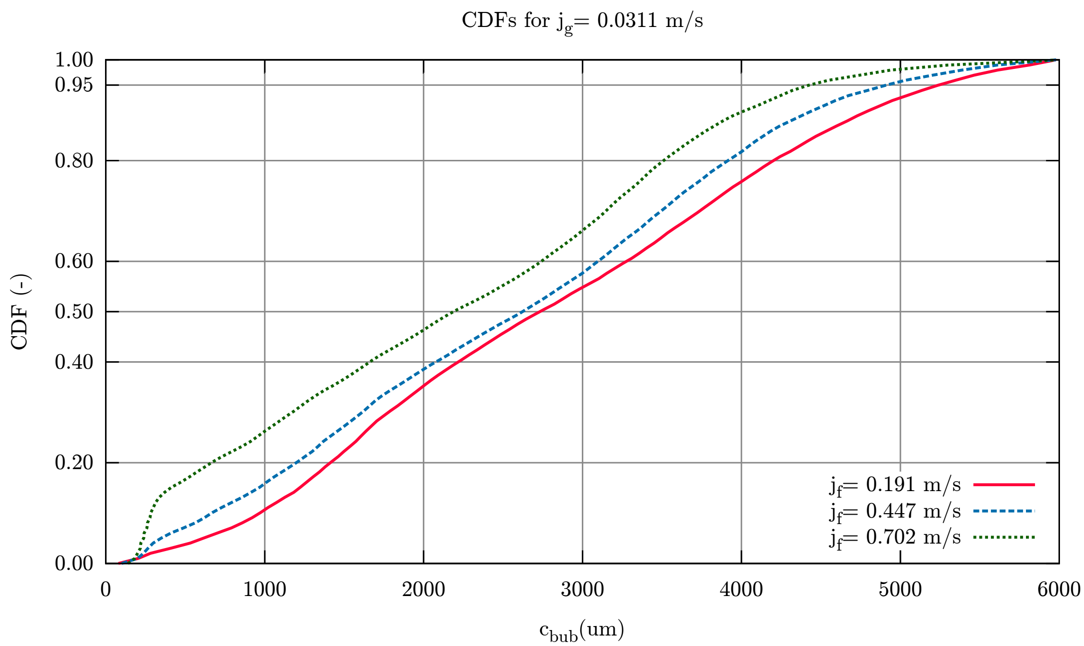

Figure 38: Bubble chord PDFs (top) and CDFs (bottom) at $j_g = 0.0311\ m/s$.

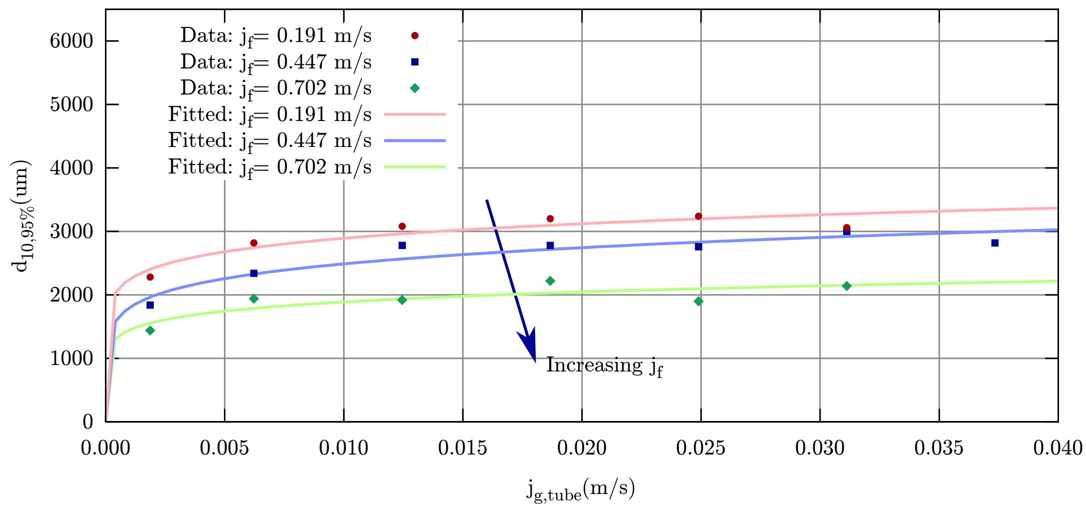

Figure 39: Bubble chord medians at selected gas and liquid flow rates as measured at position A.

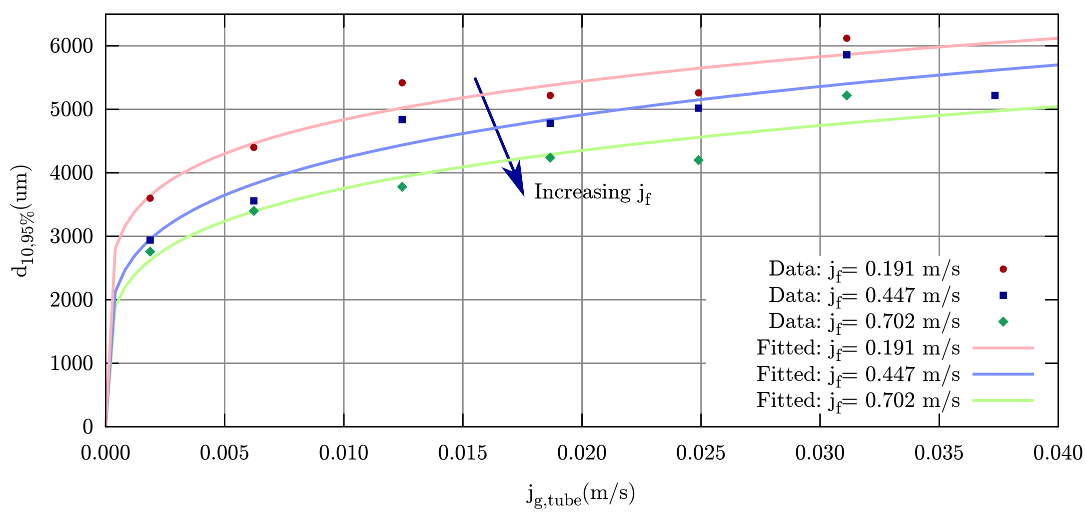

Figure 40: 95^{th} percentile of bubble chords at selected gas and liquid flow rates as measured at position A.

5.2.2 Chord vs. Diameter Sampling

In the results presented in section 5.2.1, all bubble sizes reported are obtained from chordal measurements taken from the high speed video. The simplicity of sampling chord lengths is offset by some degree of ambiguity as to what these values represent. Figure 41 illustrates how a single chord measurement of length y can represent either the entire diameter of the bubble or just a portion of it. The only thing which may be inferred from the raw chord data is that true diameter of the bubbles will be equal to or larger than the measurement. The purpose of the work in this section is to quantify the extent of this bias. The raw chord size distribution may be transformed into an estimate of the parent diameter distribution of the bubbles given that some assumptions are made about the bubble shape.

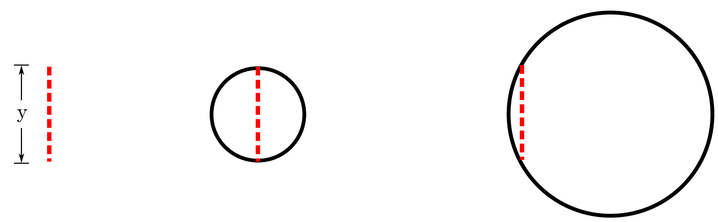

Figure 41: Ambiguity of the chordal measurements

5.2.2.1 Background and Geometric Considerations

Back calculation of particle size distributions from chord size distributions is a task which is commonly conducted in studies of powders [86, 87, 88] - although the mathematical derivation was originally developed for the study of gas-liquid flows [89]. Kalkach-Navarro *et al.* demonstrated that this technique could be applied to conductivity probes to study size distributions [34].

According to Herringe, the probability of measuring a chord of length y, denoted by $P(y, D)$, is the product of the probability of a bubble having a diameter of D, $P(D)$, and the probability of measuring a chord length of y given that a bubble of diameter D was sampled, $P(y \mid D)$, as indicated in equation (63).

$$P(y, D) = P(y \mid D)\, P(D) \tag{63}$$

In practice a distribution of chord lengths is typically measured whereas the diameter distribution is sought. Herringe demonstrates how the joint probability $P(y \mid D)$ may derived via assumptions made on the shape of the bubbles, and this is explained in further detail in appendix C.5. The current work utilizes a camera to take numerous pictures of bubbles which in theory should contain information about the bubble shape. However the curvature of the test section means image processing algorithms have great difficutly distinguishing bubbles from the background near the edges of the test section, and so this topic is separately investigated in section 5.2.3.

Li and Wilkinson compiled a list of expressions for $P(y \mid D)$ for various shapes projected in 2-dimensions [90] [5]. In the current study, both spherical and ellipsoid bubbles were observed in the test section, projected as circles and ellipses in the camera image. However, as section 5.2.3 will demonstrate, smaller bubbles tend to be spherical, while larger bubbles (at low flow rates) have an ellipsoid shape. These ellipsoid bubbles are almost always observed to be wider than they are tall ($R > \beta R$ according to figure 42). When this occurs, a chord randomly sampled in the y direction somewhere between $0 < r < R$ is likely to be closer to the size of the semi-minor axis, than in the spherical case (the size of the semi-major axis size can be backed out by dividing by β).

$$P(y \mid D)_{circle} = \frac{ydy}{R\sqrt{R^2 - y^2}} \tag{64}$$

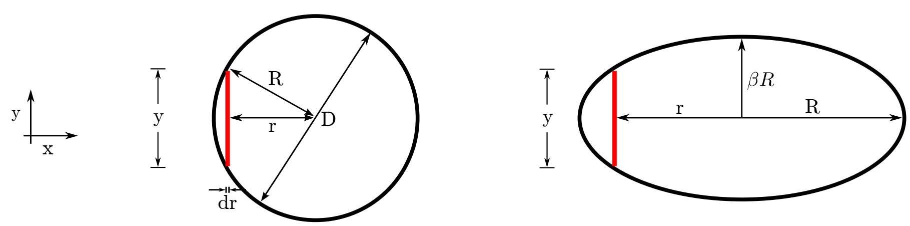

Figure 42: Definition of chord symbols

One of the problems with this method is that the exact functional form of the chord size probability distribution are rarely known. At best, using numerous measurements

[5] Clark and Turton's work is often cited in these types of studies - however they examined the sizes of 3-dimensional bubbles passing through a point (conductivity probe) [91].

an approximation to the chord size distribution may be made. By binning data from a large set of chord size measurements, Clark and Turton demonstrated that a backwards transform may be applied to the data to recover an approximation to the diameter distribution [91]. According to the authors, the number of chord measurements in a bin bounded by lengths y_i and y_{i+1} (i.e. $y_i < y < y_{i+1}$) and denoted as $c\left(y_i, y_{i+1}\right)$ in equation 65, where subscript i refers to the index of a size bin, is equal to the integral of equation (63) over that size range [91] [6].

$$\begin{aligned} c\left(y_i, y_{i+1}\right) &= \int_{y_i}^{y_{i+1}} P\left(y\right) \\ &= \int_{y_i}^{y_{i+1}} \int_{0}^{D_{max}} P\left(y \mid D\right) P\left(D\right) dDdy \end{aligned} \tag{65}$$

If the range of chord measurements is divided into n segments and the data is binned accordingly, then the reduced chord data may be represented as the vector $\mathbf{c}$ according to equation (66). The goal of the work is then to find the corresponding vector representing the distribution of diameters, $\mathbf{D}$ (as in equation 67).

$$\mathbf{c} = \begin{pmatrix} c(y_1, y_2) \\ \vdots \\ c(y_n, y_{n+1}) \end{pmatrix} \tag{66}$$

$$\mathbf{D} = \begin{pmatrix} D(y_1, y_2) \\ \vdots \\ D(y_n, y_{n+1}) \end{pmatrix} \tag{67}$$

The relationship between $\mathbf{c}$ and $\mathbf{D}$ is governed by equation (68), where $\mathbf{P}$ is an $n \times n$ matrix. Each element of $\mathbf{P}$ (denoted $P_{i,j}$) represents the probability that a chord belonging to size bin i is measured from a bubble with a diameter belonging

[6] The equation is presented as the authors have - which is technically correct. In practice, the integral over dD only needs to be taken between y_i and D_{max}, since the measurement of a chord of size y can only occur if the bubble has a diameter equal to or greater than y.

to size bin j. Since the maximum size of a chord through a bubble is equal to its diameter, all elements where $i > j$ are set equal to 0, leaving a triangular matrix. An example is included in appendix C.5 for clarity.

$$\mathbf{c} = \mathbf{P}\mathbf{D} \tag{68}$$

Each element of matrix $\mathbf{P}$ is calculated using the integral of equations (64) [91]. This is evaluated by Li to be equation (69), over the lower and upper size bounds (y_i and y_{i+1}) of some arbitrary bin [90]. In the equations, it is assumed that the bubbles in each size bin all have a diameter equal to the midpoint of the bin [7].

$$P_{i,j,sphere} = \sqrt{1 - \left(\frac{y_i}{D_j}\right)^2} - \sqrt{1 - \left(\frac{y_{i+1}}{D_j}\right)^2} \tag{69}$$

Hukkanen and Braatz indicate that in an ideal scenario, the diameter distribution may be calculated using a backwards transform obtained by inverting $\mathbf{P}$ with equation (70) [86]. However the authors suggest that noise in the data may cause non-physical fluctuations which are best suppressed by using ridge regression or Tikhonov regularization as indicated in equation (71) [86]. In the equation, γ is some small positive number (which for this work is always selected to be $\gamma = 0.1$ [8]), $\mathbf{I}$ is the $n \times n$ identity matrix, and $\mathbf{P}^T$ is the transpose of the matrix $\mathbf{P}$ [86].

$$\mathbf{D} = \mathbf{P^{-1}c} \tag{70}$$

$$\mathbf{D} = \left(\gamma\mathbf{I} + \mathbf{P}^T\mathbf{P}\right)^{-1}\mathbf{P}^T\mathbf{c} \tag{71}$$

[7] The work of Hukkanen demonstrates that the diameter calculation may be more accurate if some form of distribution interpolation were done within each bin [86]. However the additional complexity is beyond what is required in the scope of this work.

[8] This value is selected on the basis of the recommendation by [86].

5.2.2.2 Transform Application

In general, the transform aims to redistribute some of the chord samples from the smaller size bins into the larger size bins in order to account for the probability that the edge of a bubble has been measured. For the purposes of illustrating its application on actual data, three cases from section 5.2.1 are used to demonstrate the effect of the transform. The three cases examined were run at a constant gas superficial velocity of $j_g = 0.0125\ m/s$, with liquid superficial velocities of $j_f = 0.191$, 0.442, and 0.702 m/s.

Figures 43, 44 and 45 illustrate the measured chord distributions (red squares) along with the transformed distribution (blue circles) assuming that the bubbles are all spheres. The means of both the chord distributions as well as transformed distributions are evaluated and supplied in table 26 [9]. The table also summarizes a set of tests to determine the sensitivity to bin size selection.

Numerically, this redistribution has the most significant effect on the cases where a large portion of the chord samples are found in the smaller size. In the $j_f = 0.702\ m/s$ case, a large peak in the sub 500 μm region exists in the chord data, and is significantly reduced by the diameter transform. The result is the mean of the transformed distribution in the $j_f = 0.702\ m/s$ case is about 24% greater than the chord size distribution mean. This is compared to about $14 - 16\%$ greater for the $j_f = 0.191$ and 0.442 m/s cases where a peak does not exist.

The reduction of this peak however may not represent what is actually occuring in the test section. Images at these conditions (see section 5.2.4) show that these chord measurements are actually of a population of small bubbles which have broken off of larger bubbles. Clark and Turton suggest that these types of multimodal distributions may not be easily treated with this type of backwards transformation [91]. For this reason, the interfacial area results in section 5.3 are <u>not</u> transformed.

[9] The expected value of the distribution is estimated by taking the product of the probability of a measurement in a bin and the weight of the bin (defined as the bin midpoint). The sum of these values over all of the bins yields the expected value. This is an estimate based on the reduced data.

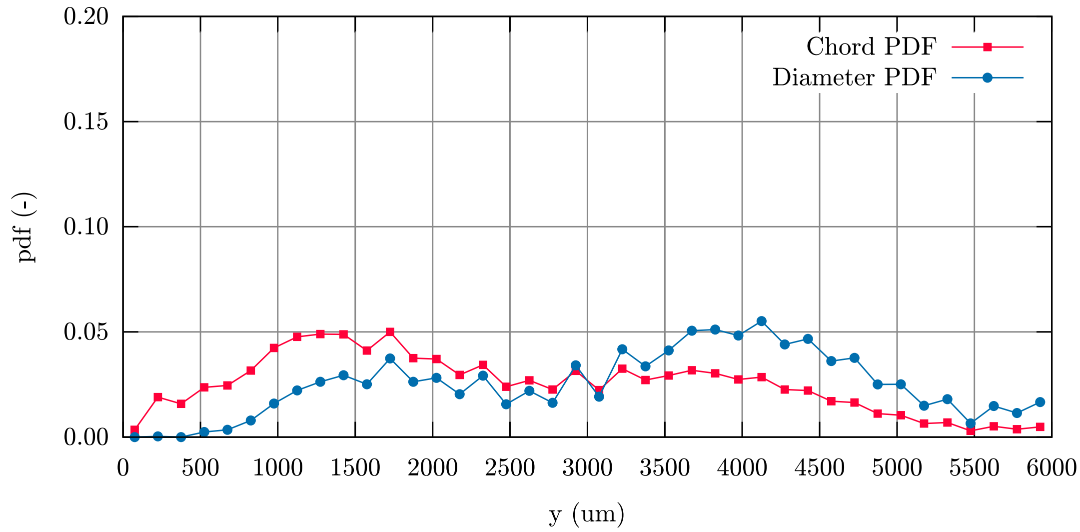

Figure 43: Chord size distribution plotted against the estimated diameter distribution based on the assumption all bubbles were spherical. Flow conditions of $j_f = 0.191\ m/s$ and $j_g = 0.0125\ m/s$ were used.

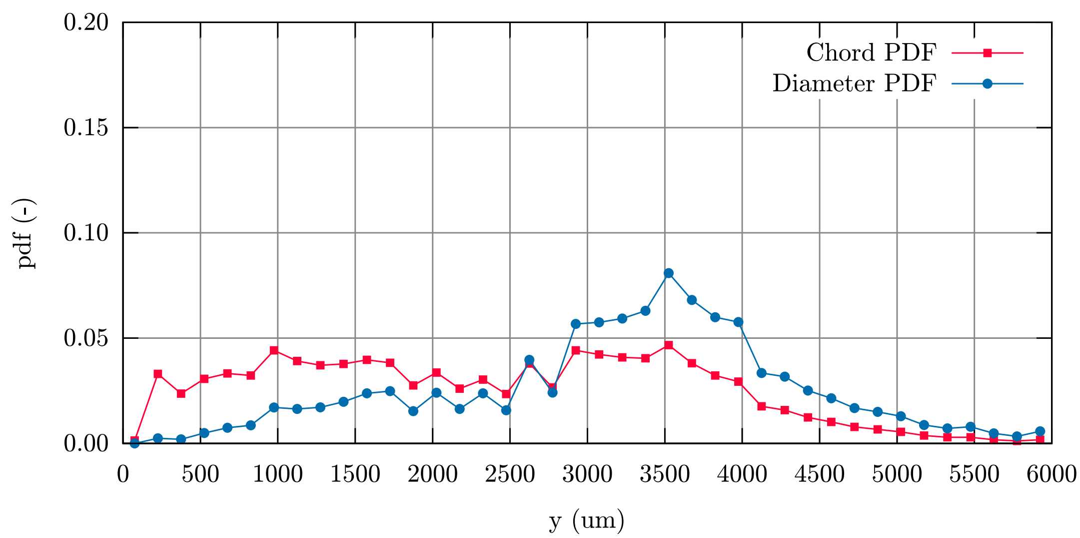

Figure 44: Chord size distribution plotted against the estimated diameter distribution based on the assumption all bubbles were spherical. Flow conditions of $j_f = 0.442\ m/s$ and $j_g = 0.0125\ m/s$ were used.

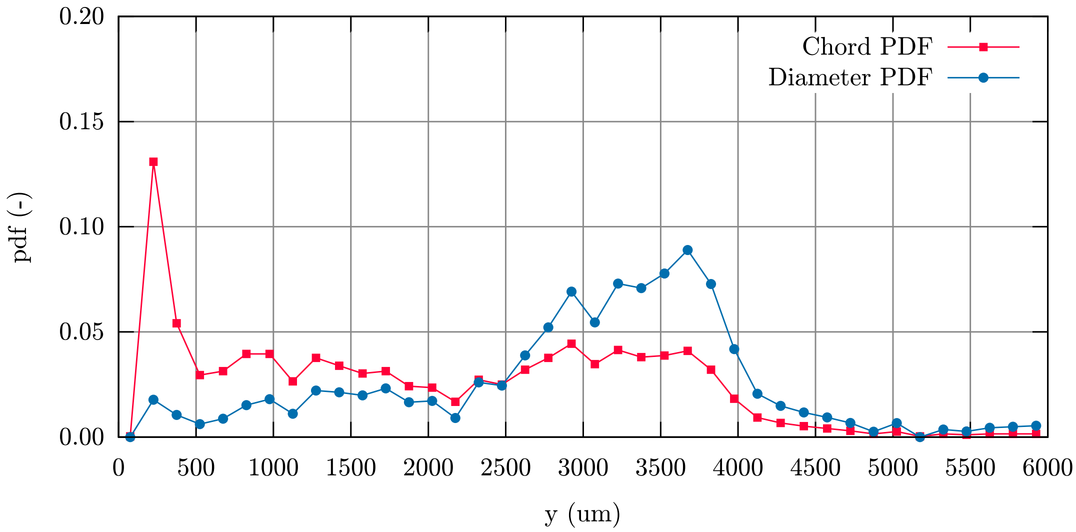

Figure 45: Chord size distribution plotted against the estimated diameter distribution based on the assumption all bubbles were spherical. Flow conditions of $j_f = 0.702\ m/s$ and $j_g = 0.0125\ m/s$ were used

Table 26: Sensitivity of the mean chord size and transformed diameter size to the number of bins. All measurements in μm, with Δ defined as the ratio of the transformed size distribution mean to the measured chord size distribution mean. All transformed values are calculated under the assumption that the bubbles are spherical. All tests were conducted at $j_g = 0.0125\ m/s$.

$j_f\ (m/s)$	Chord	20 Bins		40 Bins		80 Bins	
	$\overline{y}$	$\overline{y}$	Δ	$\overline{y}$	Δ	$\overline{y}$	Δ
0.191	2469	2835	1.148	2851	1.155	2863	1.160
0.447	2364	2723	1.151	2736	1.157	2746	1.162
0.702	1996	2455	1.223	2478	1.241	2492	1.248

5.2.3 Bubble Shape and Aspect Ratio

Although in the current work a camera is used to photograph hundreds of thousands of bubbles, the curved geometry of the test section creates an uneven background light. Most image processing routines require both finding the spatial derivative of each pixel to determine the location of the edges of objects such as bubbles, and some degree of light intensity thresholding to 'classify' regions of the image as either part of the background or an object. This means that the area in the image where the bubble detection algorithm will work well is limited to the center of the test section where the lighting is relatively constant.

The measurements in the previous sections were based on the assumption that each bubble is a sphere. This is a key assumption in most of the literature reviewed, since the deformation of a bubble will cause it to form a complex shape (such as a oblate spheroid) where the surface area is difficult to calculate [10]. The goal of this section is to assess the validity of the spherical assumption in the current work.

In order to quantify the bubble shape, the aspect ratio of the bubble is defined as in equation (72). This quantity is measured by drawing a bounding box around any object detected in a frame by the algorithm described in section 3.2.3, and letting Δx represent the horizontal size of the box, and Δy describe the vertical size of the box. A sphere (projected as a circle in the image) will have an aspect ratio of $AR = 1$. The effects of the liquid superfical velocity and orifice size on the aspect ratio of the bubbles are examined in sections 5.2.3.1 and 5.2.3.2 respectively.

$$AR = \frac{\Delta x}{\Delta y} \tag{72}$$

[10] The volume for a oblate spheroid is easily found, however the surface area for such a shape is non-trivial and requires knowledge of the aspect ratio. It is not typically considered in literature.

5.2.3.1 Effect of Liquid Flow Rate

The aspect ratio of the bubbles were examined at three different liquid superifical velocities: $j_f = 0.191$, 0.442, and 0.702 m/s. At each flow rate, 2500 images were analyzed, and bubbles in the region where the background lighting intensity was roughly constant were sized and counted. This region corresponds approximately with $0 < r/R < 0.5$. The images are taken at the 'Lower' elevation marked in figure 21.

The x and y sizes of the first 500 bubbles at each flow rate are plotted in figure 46, with the y direction understood to be parallel with the bulk flow. The distribution of aspect ratios at each flow rate are illustrated in figure 47, while key statistical parameters are documented in table 27. Sample frames are provided in figure 48. Limitations in the aspect ratio algorithm make it difficult to size bubbles smaller than $d \approx 0.5$ mm, so few points are captured in this region. The results from the previous sections demonstrate that relatively few bubbles exist in this size range at the lower liquid velocities. However when $j_f > 0.702$ m/s, turbulent fragmentation begins to generate large numbers of small bubbles, which may mean that the number of bubbles missed becomes significant. Fortunately, the data trends suggest that the AR tends get closer to $AR = 1$ when the bubble sizes are small.

At the lowest flow rate, the aspect ratio of the bubbles is typically greater than 1 when one of the dimensions is greater than 3 mm. Bubbles smaller than 3 mm tend have an aspect ratio of $AR \approx 1$. As the flow rate increases the $d > 3$ mm bubbles begin to breakup as illustrated by the shift in the population towards smaller sizes illustrated in figure 46. By $j_f = 0.702$ m/s, the majority of the population is distributed around $AR = 1$. As both figure 47 and table 27 indicate, the standard deviation of the distribution also decreases with increasing j_f, indicating a greater degree of uniformity in the bubbles. At $j_f = 0.702$ m/s, figure 47 shows a large population of bubbles with an aspect ratio slightly less than 1, and figure 46 indicates that these are mostly bubbles between about $2 < d < 3$ mm. The slightly larger y dimension may be a result of the drag forces pulling the sides of the bubble back.

The spherical assumption is valid for $j_f > 0.702$ m/s where $AR \approx 1$. At the lowest flow rate examined, the mean aspect ratio was $AR = 1.204$ indicating only a minor shape distortion.

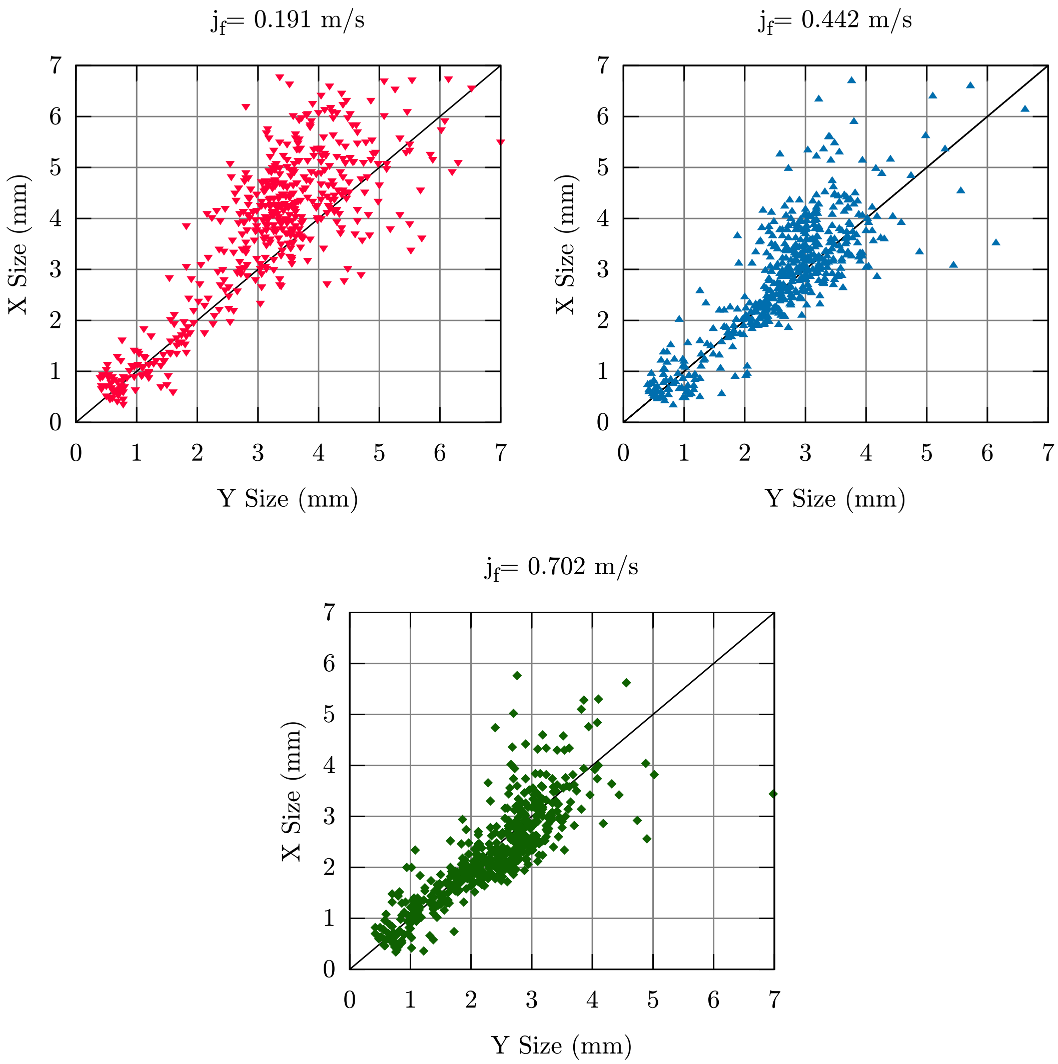

Figure 46: Effect of j_f on the bubble x and y dimensions. Data are taken at the lower elevation at a fixed gas superficial velocity of $j_g = 0.0125\ m/s$ and j_f of $0.191\ m/s$ (top left), $0.442\ m/s$ (top right), and $0.702\ m/s$ (bottom). The diagonal line in each plot represents $AR = 1$. Only the first 500 points in each sample are shown.

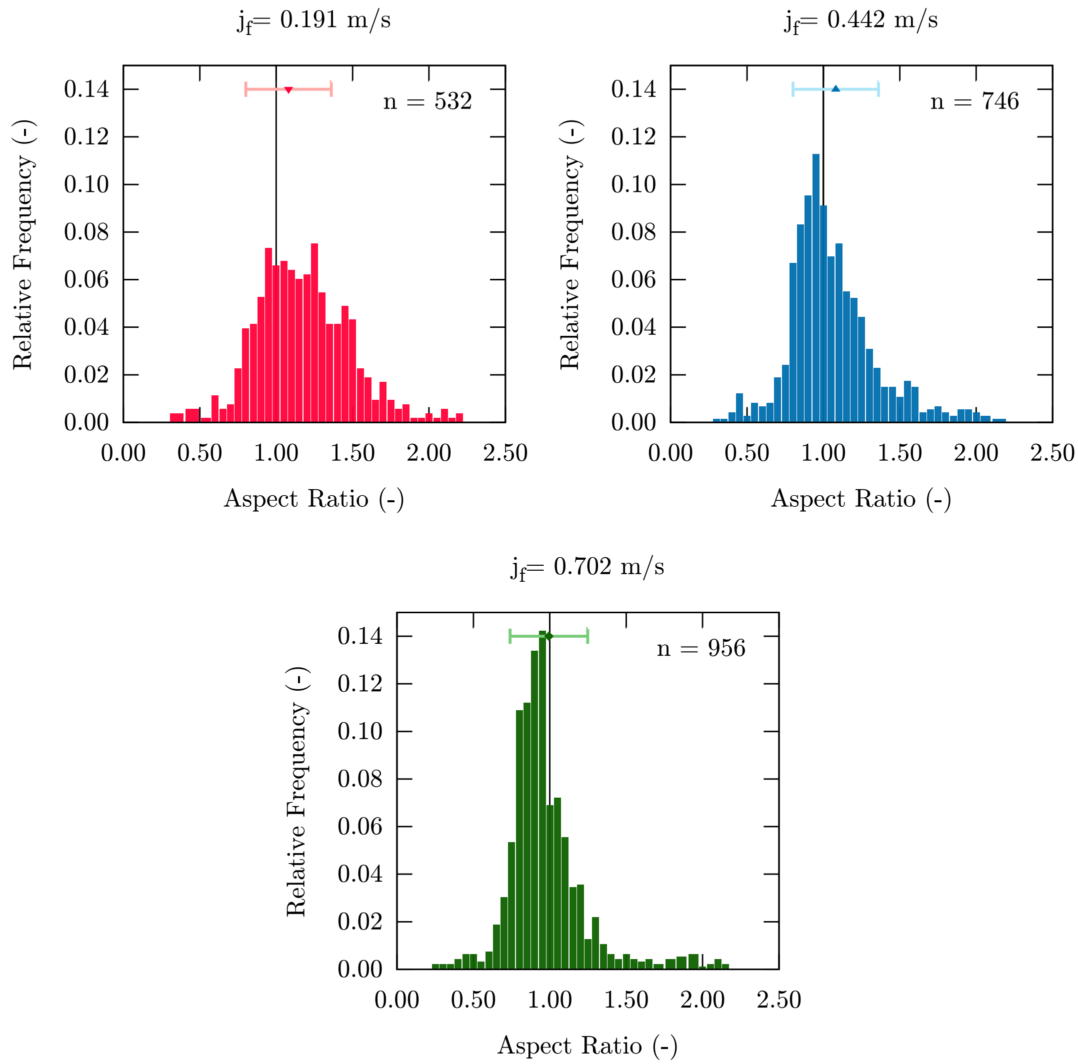

Figure 47: Effect of j_f on the bubble aspect ratio distribution. Data are taken at the lower elevation at a fixed gas superficial velocity of $j_g = 0.0125\ m/s$ and j_f of 0.191 m/s (top left), 0.442 m/s (top right), and 0.702 m/s (bottom). Points at the top of each graph mark the mean of each distribution, with error bars extending to 1σ. The vertical line in each graph marks $AR = 1$.

Table 27: Influence of j_f on aspect ratio.

$j_f(m/s)$	n_{bub}	$\overline{\Delta x}$ (mm)	$\sigma_{\Delta x}$	$\overline{\Delta y}$ (mm)	$\sigma_{\Delta y}$	AR	σ_{AR}
0.191	532	3.789	1.620	3.180	1.294	1.204	0.301
0.442	746	2.884	1.178	2.693	0.977	1.081	0.280
0.702	956	2.243	0.956	2.302	0.917	0.994	0.254

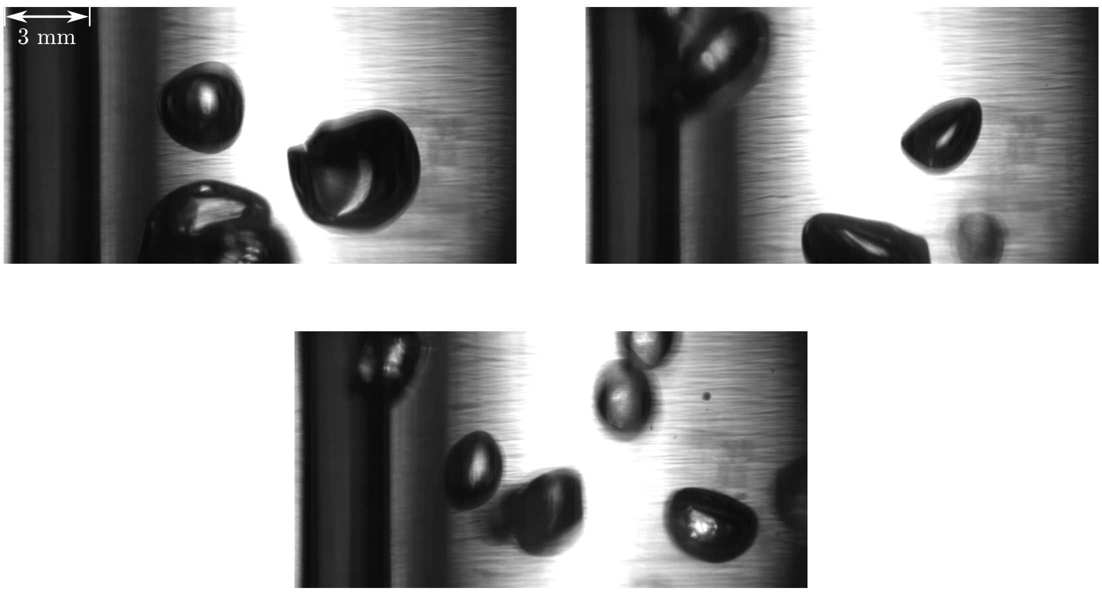

Figure 48: Sample frames from the aspect ratio tests at $j_f = 0.191\ m/s$ (top left), $j_f = 0.442\ m/s$ (top right), and $j_f = 0.702\ m/s$ (bottom).

5.2.3.2 Effect of Orifices

At the lowest liquid superficial velocity ($j_f = 0.191\ m/s$) most of the bubbles are large enough to be sampled by the aspect ratio measurement algorithm. Since the subsequent chapters deal with the increase in interfacial area due to fragmentation of bubbles as they are forced through an orifice, this section examines both the change in aspect ratio and size caused by the flow blockage at $j_f = 0.191\ m/s$ and $j_g = 0.0125\ m/s$. No higher flow rates were tested since the additional turbulent fragmentation would cause a large portion of the bubbles to be smaller than what can be detected by the aspect ratio measurement algorithm.

Bubbles sizes are captured upstream of the orifice (at the 'lower' elevation), and compared to images taken at the 'upper' elevation point for orifice diameters of $\phi =$ 25.4, 19.1, and 12.7 mm. Once again, 2500 images at each position were taken and bubbles characteristics between roughly $0 < r/R < 0.5$ were measured.

Figures 49 and 50 illustrated the dimensions of the first 500 points of each test case and the aspect ratio distributions respectively. Figure 51 are sample frames from each of the tests conducted in this section. Table 28 lists the statistical properties of each case, while table 29 presents the results of a simple sizing test. In the test, for each set of data, the number of bubbles with an x dimension greater than 3.0 mm were counted and their percentage of the total population they represent is calculated. This metric should indicate the significance of fragmentation in the orifice.

A comparison of the tabulated bubble characteristics at the lower elevation and after the bubbles have passed through the $\phi = 25.4$ mm orifice reveals that the average size in both the x and y directions has increased. This unexpected result was verified by running the algorithm on an additional 2500 images taken at the same conditions. This result would suggest that as the bubbles pass through this orifice, no fragmentation is occuring (the estimated bulk Reynolds number in the orifice is $Re \approx 8500$) - but rather since the local concentration of bubbles has increased, coalescence is occuring. This is supported by the results in table 29 where the percentage of bubbles with an x dimension greater than 3 mm has increased from 73.3% to 81.6%

Decreasing the diameter of the orifice causes more fragmentation, and this is particularly evident in the $\phi = 12.7$ mm case where the aspect ratio is reduced to $AR = 0.932$. In the other cases, a large cluster of points sit above the $AR = 1$ line in figure 49, but in the case they have almost all been eliminated.

A comparsion of the $j_f = 0.442$ m/s case from the previous section and the $j_f = 0.191$ m/s through the $\phi = 12.7$ mm orifice case in the current section may demonstrate how fragmentation occuring due to a flow blockage is distinct from solely turbulent fragmentation. In the former case, the bulk Reynolds number in the unobstructed tube is $Re \approx 15800$. In the flow that passes through the restriction, the bulk Reynolds number in the orifice was calculated to be $Re \approx 16900$. While the difference in these two values is relatively small (about a 7% difference), the mean bubble size in both the x and y directions decreases by 35.6% and 24.4% respectively when the flow passes through the orifice. This result may be interpreted to mean that the flow restriction can cause conditions where the likelihood of bubble fragmenting is much higher (perhaps due to being entrained in the recirculation zone).

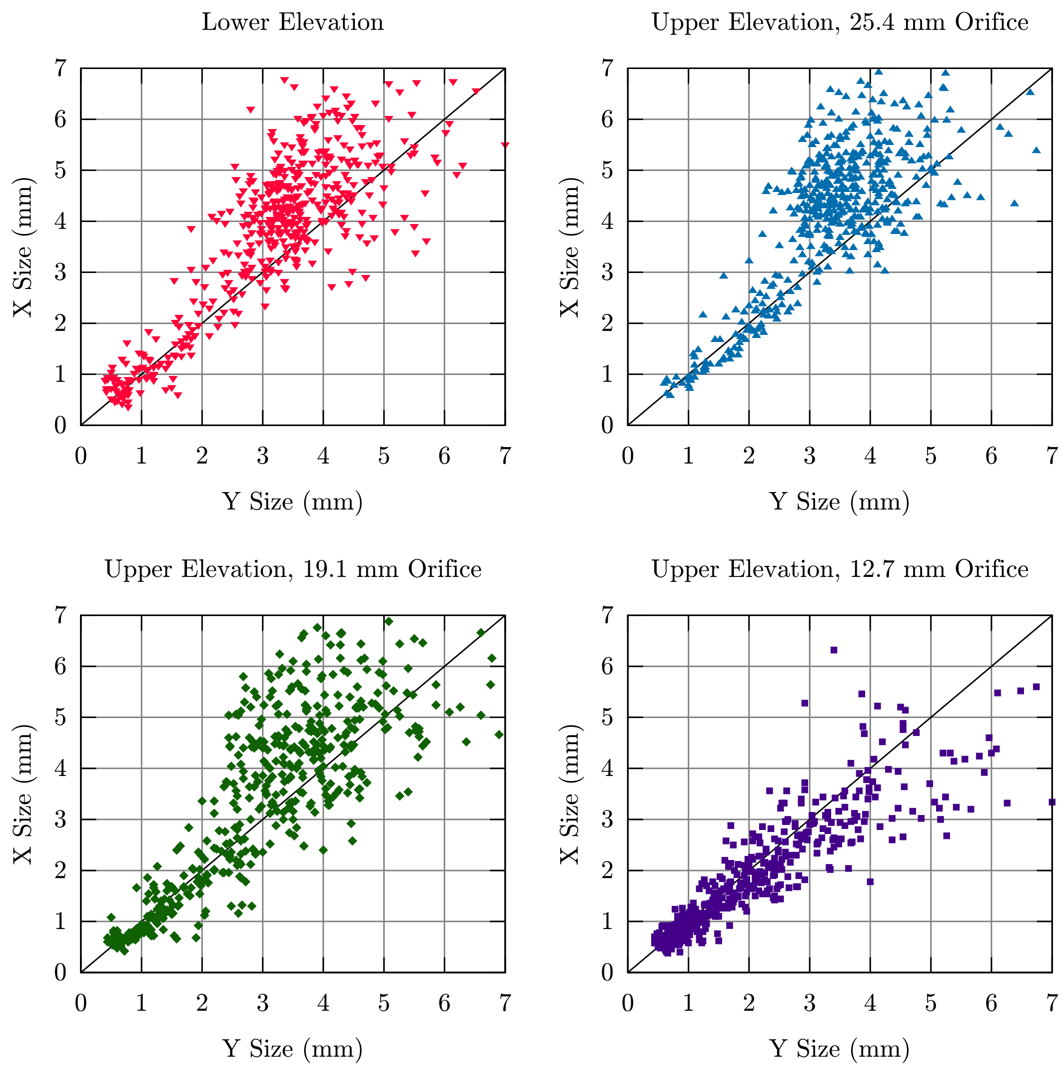

Figure 49: Effect of the orifice sizes on the bubble x and y dimensions. Data are taken at the lower elevation (top left) and compared against data taken at the upper measurement point of the $\phi = 25.4$ mm orifice section (top right), the $\phi = 19.1$ mm section (bottom left) and the $\phi = 12.7$ mm section (bottom right). The diagonal line in each graph marks $AR = 1$. All data are taken at $j_f = 0.191$ m/s and $j_g = 0.0125$ m/s. Only the first 500 points in each sample are shown.

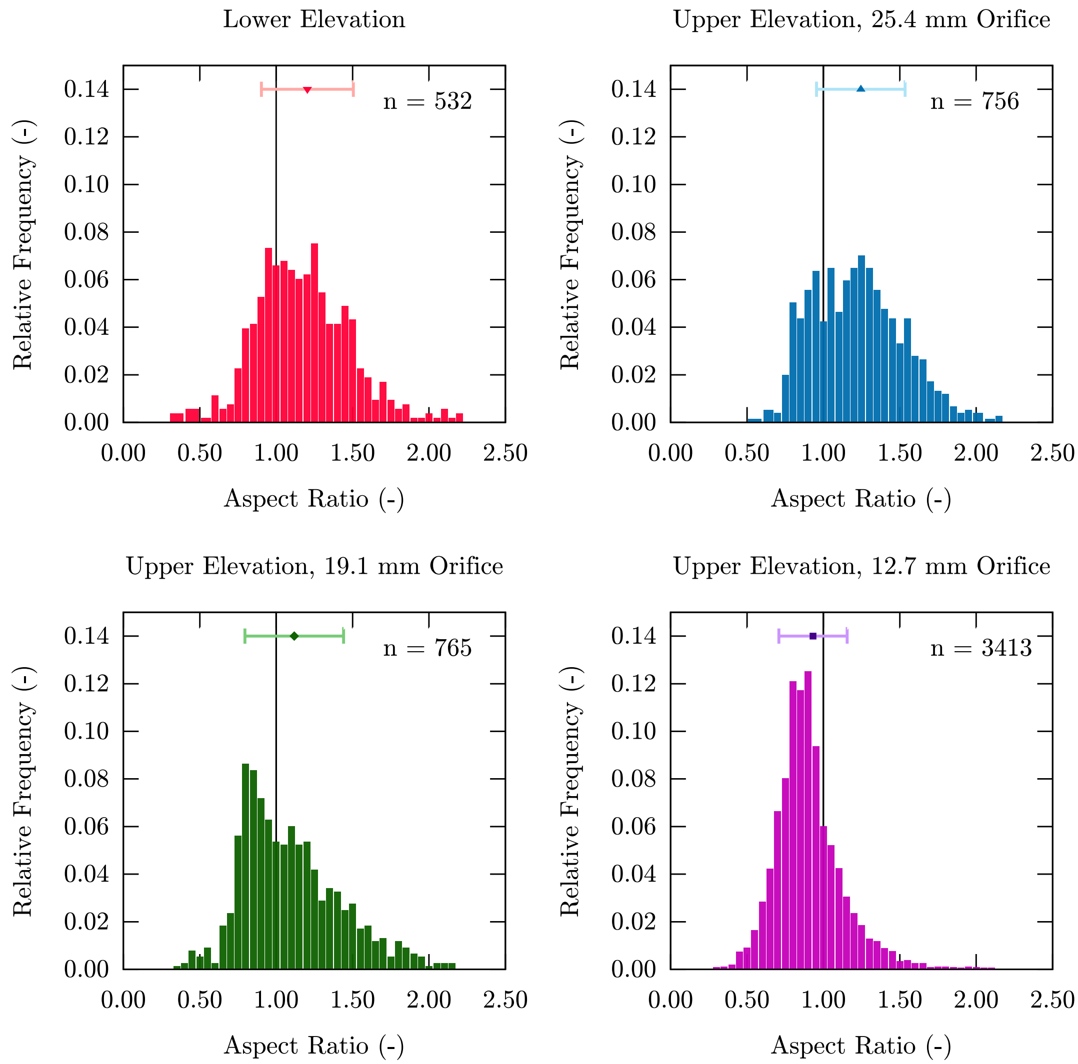

Figure 50: Effect of the orifice sizes on the bubble aspect ratio distribution. Data are taken at the lower elevation (top left) and compared against data taken at the upper measurement point of the $\phi = 25.4\ mm$ orifice section (top right), the $\phi = 19.1\ mm$ section (bottom left) and the $\phi = 12.7\ mm$ section (bottom right). Points at the top of each graph mark the mean of each distribution, with error bars extending to 1σ. The vertical line in each graph marks $AR = 1$. All data are taken at $j_f = 0.191\ m/s$ and $j_g = 0.0125\ m/s$.

Table 28: Aspect ratio results at $j_f = 0.191\ m/s$ through different orifices.

Location / Orifice	n_{bub}	$\overline{\Delta x}$ (mm)	$\sigma_{\Delta x}$	$\overline{\Delta y}$ (mm)	$\sigma_{\Delta y}$	AR	σ_{AR}
Lower Elevation	532	3.789	1.620	3.180	1.294	1.204	0.301
Upper, $\phi = 25.4\ mm$	756	4.257	1.507	3.427	1.093	1.245	0.290
Upper, $\phi = 19.1\ mm$	765	3.423	1.789	3.027	1.443	1.118	0.323
Upper, $\phi = 12.7\ mm$	3413	1.855	1.280	2.037	1.389	0.932	0.223

Table 29: Portion of the bubble size measurements where $\Delta x > 3.0\ mm$.

Location / Orifice	n_{bub}	$n_{\Delta x > 3.0\ mm}$	%
Lower Elevation	532	390	73.3%
Upper, $\phi = 25.4\ mm$	756	617	81.6%
Upper, $\phi = 19.1\ mm$	765	466	60.9%
Upper, $\phi = 12.7\ mm$	3413	576	17.9%

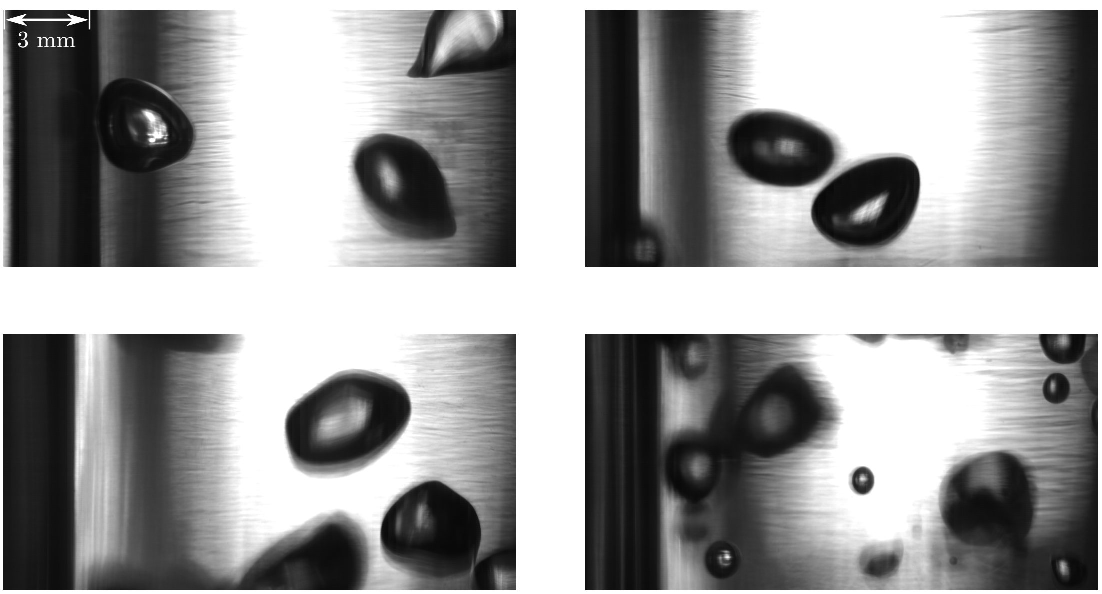

Figure 51: Sample frames from the aspect ratio tests at $j_f = 0.191\ m/s$. Frames are taken upstream of the blockage (top left), downstream of the $\phi = 25.4\ mm$ orifice (top right), downstream of the $\phi = 19.1\ mm$ orifice (bottom left) and downstream of the $\phi = 12.7\ mm$ orifice (bottom right).

5.2.4 Statistical Reporting & Area-Weighting

Preliminary results indicated that in some cases a large population of small bubbles with a chord length, c, of less than 1000 μm were observed. Analysis of sample frames (see figure 53) from these cases revealed that the bubbles are not an artifact of the image processing routine, and do in fact physically exist in the system. The quantity of these bubbles stems from the fact that a single large bubble may fragment into many smaller bubbles. This creates a significant problem when attempting to examine the PDFs under these conditions, since in a standard PDF each sample is given an equal weighting. Since the 'small bubbles' outnumber the larger ones in some cases by factors of 5:1 or 10:1, the PDF becomes highly skewed towards smaller diameters as illustrated in figure 52, even though they may not necessarily contribute significantly to the interfacial area.

In order to work around this problem, a weighting system was used so that bubbles which contribute more to the overall interfacial area are emphasized. Since the quantity of interest in the subsequent chapters is the interfacial area, the distribution is weighted by a factor of c^2.

When the data collected is reduced to a regular or unweighted discrete PDF, the range of the data set is divided into a series of diameter subranges or bins. The number of points falling into each bin ($n_{c_{min},c_{max}}$) is counted and normalized against the total number of points in the entire data set (c_{total}). If a specific bin is bounded by $c_{min} \leq c < c_{max}$, then the probability of the random sample falling into this subrange is indicated in equation (73). The PDF itself is approximated by evaluating the probability of a random sample falling into each bin over the entire range. It follows that the unweighted CDF is simply the sum of the probabilities up until a certain bin or diameter as indciated in equation (74).

$$P\left(c_{min} \leq c < c_{max}\right) = \frac{n_{c_{min},c_{max}}}{n_{total}} \tag{73}$$

$$CDF\left(c\right) = \int_{0}^{c} PDF(c) \tag{74}$$

In the Area-weighted Distribution Function (ADF), the range of diameters is once again split into a series of bins. However rather than counting the number of bubbles falling in each bin, the surface area of each particle in the bin is calculated and

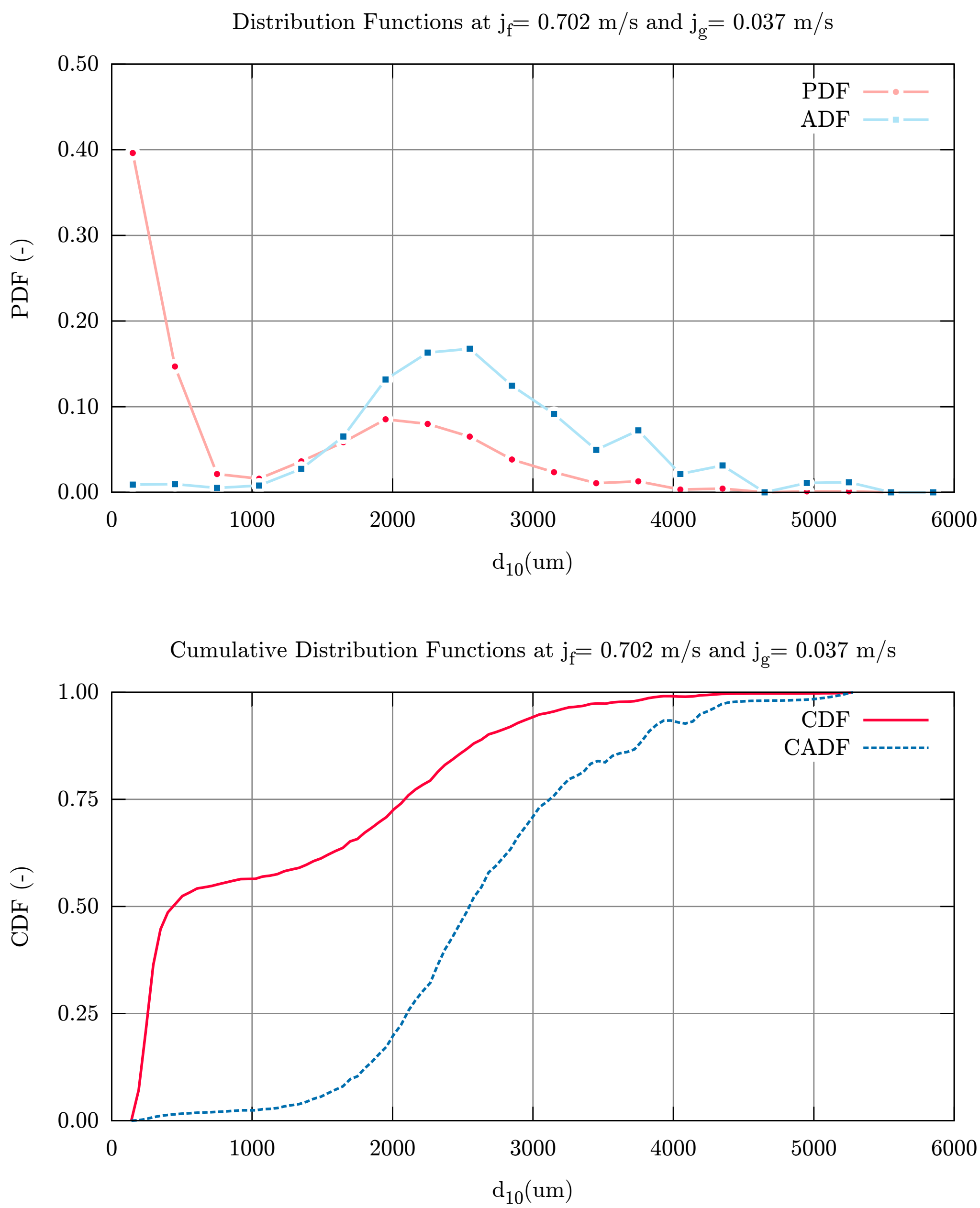

Figure 52: Difference between the standard probability distribution function and the area-weighted probability distribution function (top) as well as the related cumulative and area-weighted cumulative distribution functions (bottom). Test conditions of $j_f = 0.702\ m/s$ and $j_g = 0.037\ m/s$ were used, and data was taken upstream of the orifice. The image sets were sampled along the centerline of the image.

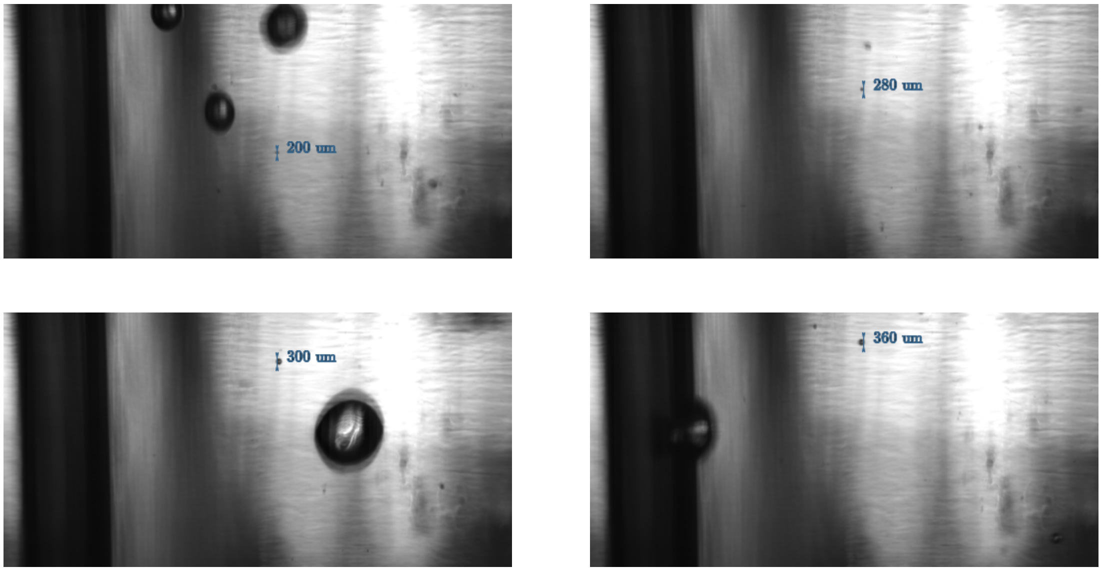

Figure 53: Sample frames upstream of the orifice with test conditions of $j_f = 0.702\ m/s$ and $j_g = 0.037\ m/s$ where the bubble sizing algorithm has identififed the existence of a substantial population of bubbles with $c \approx 300\mu m$.

summed. This value is then normalized against the total surface area among all bubble sizes sampled. The contribution to the total interfacial area of a bin bounded by $c_{min} \leq c < c_{max}$ is evaluated as equation (75) noting that c_i represents the chord sizes of only the bubbles which fall into the bin.

$$ADF\left(c_{min} \leq c < c_{max}\right) = \frac{\pi \sum_{i=1}^{n_{c_{min},c_{max}}} c_i^2}{\pi \sum_{k=1}^{n_{bub}} c_k^2} \tag{75}$$

The top portion of Figure 52 plots the PDF and ADF for a set of data taken upstream of the orifice, under conditions where fragmentation was occuring. The PDF (red circles) indicates that over 55% of the bubbles counted had chords of $c < 500\ \mu m$, however the ADF (blue squares) indicates that the contribution to the interfacial area from the first two bins amounts to less than 3% of the total a_i. The ADF indicates that the majority of interfacial area is contributed by bubbles betwen $1600\ \mu m \leq c < 3200\ \mu m$.

The Area-weighted distribution function is used to represent the contribution to the total interfacial area by the bubbles in each diameter bin.

Unweighted probability distribution functions should still be used to determine bubble chord distribution characteristics such as $c_{95\%}$.

5.2.5 Summary

By varying the gas flow rate and sampling the bubble chord size distribution along the center of the tube, the work in section 5.2.1 demonstrated that the bubble chord size distributions are very sensitive to the air superficial velocity at $j_g < 0.0125\ m/s$. Above this rate, the median sizes of the bubble distributions tended to stay roughly constant, and so the subsequent tests in the interfacial area portion of the work will be conducted at this flow rate.

The work in the section also demonstrated that as the fluid superifical velocity increased, the turbulent fragmentation mechanism started to play a role in shaping the size distribution of the bubbles. Between $j_f = 0.447$ and $0.702\ m/s$ (corresponding to $Re = 15770$ and 24782), a sharp peak in the size distribution formed at $d < 1000\ \mu m$. The chord samples in this size region are likely from small bubble fragments off of larger objects.

One of the problems with sampling only bubble chords is that they will almost always be smaller than the diameter of the bubble. Section 5.2.2 addressed this problem by quantifying the extent of this under-representation by performing a transformation on the chord size distribution based on the geometric relationship between the chord size and the diameter. The results demonstrated that the estimated diameter mean is about 15% higher than the measured chord size mean. This value was higher when the chord distribution was bimodal, however the accuracy of the transform in this scenario is questionable. Hence it is not applied in the work in the subsequent sections since the bubble size distributions are expected to be highly bimodal.

The aspect ratio work in section 5.2.3 addresses whether or not the spherical assumption made in the previous section is correct. The results demonstrated that the aspect ratio of the bubbles is $AR \approx 1$ when the diameter of the bubble is $d < 3\ mm$. For diameters larger than 3 mm, the aspect ratio was typically $AR > 1$ indicating that the bubble was an ellipsoid wider than it was tall. However, bubbles of this size were only present at low fluid velocities where turbulent breakup was not occuring. Nevertheless as an example, a sphere with a diameter of 3 mm will have a surface area ($A_i = 4\pi r^2$) of 28.27 mm^2 and occupy a volume of ($V = \frac{4\pi r^3}{3}$) 14.13 mm^3.

The results in section 5.2.3 indicate that at the lowest liquid velocity, the aspect ratio will be roughly $AR = 1.2$. If volume is conserved, the corresponding oblate ellipsoid would have dimensions of $\Delta Y = 1.328\ mm$ and $\Delta X = 1.594\ mm$, where ΔY represents the semi-minor axis of the bubble (half of its total height) and ΔX is the semi-major axis (half of its total width).

An oblate ellipsoid has a surface area which may be calculated as:

$$A_i = 2\pi \Delta X^2 \left(1 + \frac{1-e^2}{e} tanh^{-1} e\right) \tag{76}$$

Where the ellipticity, e is defined as:

$$e = \sqrt{1 - \frac{\Delta Y^2}{\Delta X^2}} \tag{77}$$

The corresponding surface area of a bubble of such dimensions is 30.90 mm, which is only 9.3% greater than the surface area of the sphere. Since every other case has bubbles which have aspect ratios closer to $AR = 1$ (especially at higher velocities), this is assumed to be the worst case. From this, it would be reasonable to state that the spherical assumption is valid, noting that at $j_f = 0.191\ m/s$ in the unobstructed flow, the assumption may underpredict the surface area by at most, $\approx 9\%$.

The work in section 5.2.4 presents and demonstrates a method to determine the contribution to the interfacial area from each bubble size bin. When applied to a test case, the method demonstrated that even with a relatively large population of small bubbles, the overall contribution to the interfacial area from these bubbles is minor.

5.3 Interfacial Area

The interfacial results chapter is split into four sections: calculation of the interfacial area, void fraction verification, orifice effects and a discussion.

The interfacial area concentration is not directly measured, but rather inferred from chordal size measurements. A discussion on how it is estimated based on the video measurements is supplied in section 5.3.1.

Verification of both the measured void fraction and the preliminary interfacial area concentration measurements against literature is performed in section 5.3.2

The goal of the verification tests is to lend credibility to the results presented in section 5.3.3 where the effects of the orifice on the a_i are ultimately examined.

A discussion and interpretation of the results is found in section 5.3.4.

5.3.1 Interfacial Area Calculation

As demonstrated in section 5.2.3, the bubbles are generally spherical in shape except at the lowest liquid superficial velocities. At lower j_f, the bubbles are oblate ellipsoids, however it is a non-trival task to calculate the surface area of the ellipsoid based on chordal measurements alone. Thus for the purposes of this section, the bubbles will be assumed to be spherical - although the under-prediction in surface area at low j_f is fully acknowledged [11].

Kataoka *et al.* state that the linearly averaged interfacial area may be derived as a function of the number of bubbles per unit length and the harmonic average of the angle between the surface normal and the line along which the sample is made [32]. While the authors indicate that this technique would be well suited for photographic methods, the accurate determination of a surface normal from a 2-dimensional image is a non-trivial task.

[11] Hibiki and Ishii have claimed that mathematically, even if the bubble were deformed to an aspect ratio of $AR = 2$, the variation in the interfacial area concentration is less than 10% [37]. Ultimately, the spherical assumption is made in any study involving two-sensor conductivity probes [32].

In more recent literature, most studies involving electrical conductivity probes are verified in some manner against photographic studies. Hibiki *et al.* took several images, assumed a constant Sauter mean diameter of $d_{32} = 3\ mm$, calculated the void fraction occupied by bubbles in the image, and backed out the a_i for the entire picture using equation (78) [36]. A derivation of why the Sauter mean diameter (which is nothing more than the ratio of the mean bubble surface area to the mean bubble volume) is used is supplied in appendix C.6.

$$a_i = \frac{6\alpha_g}{d_{32}} \tag{78}$$

Authors such as Dongjian *et al.* manually measured the minor and major axes of each bubble in a wide-field image. Assuming each bubble was an ellipsoid, the authors calculated the image-averaged interfacial area and compared that value to the results of their conductivity probe.

In the current work, columns of pixels are sampled, and bubble chords are measured as described in section 3.2.2. Each bubble chord is assumed to represent the diameter of the bubble it comes from. The work in section 5.2.2 demonstrated that on average, this will cause the size to be under reported by at most 15%. However, since this is a global bias, all measurements are affected in the same way and so qualitative trends are preserved. Additionally, since a_i is linearlly related to d_{32}, applying a correction is possible if the chord size distribution is known (so long as the distribution is not bimodal). The advantage to this method is that the radial distribution of a_i may be estimated, and it is not particularly sensitive to the lighting gradients caused by the curvature of the test section.

5.3.2 Verification of Results

5.3.2.1 Void Fraction Comparison to Correlation

In order to estimate the interfacial area, the local void fraction of the flow must be known. In this work, the void fraction is estimated by determining the portion of each chord sample which is occupied by a bubble, and this was described in detail in section 3.2.2.6. The chord samples in this section are obtained along the centerline of the tube. The data obtained are compared against values in literature as a verification of both the method.

Since void fraction is a commonly chracteristic of two phase flows, there exists a substantial body of work on the topic. Recent reviews by Godbole [92], Woldesemayat [93], and Coddington [94] each determined that the drift flux type relationships tended to be the most accurate in assessing the void fraction. Such relationships take the form of (79), and relate the void fraction primarily to the superficial gas and liquid velocities.

$$\alpha = \frac{j_g}{C_0\left(j_g + j_f\right) + u_{slip}} \tag{79}$$

Among the drift-flux relationships examined, studies by both Woldesemayat and Coddington found the correlation proposed by Dix to be among the most accurate [93, 94]. Woldesemayat noted that the accuracy of the Dix predictions seemed to be affected by the system pressure, and proposed a correction based on such [93]. In the data examined, the authors found that the corrected Dix correlation predicted the void fraction of the experimental points to within 10% of the true value over 75% of the time. For these reasons the Woldesemayat-Dix correlation is used as the basis of the comparison in this work, with the coefficients for the relationship given as equations (80) and (81).

$$C_0 = \frac{j_g}{j_g + j_f}\left[1 + \left(\frac{j_f}{j_g}\right)^b\right] \tag{80}$$

$$b = \left(\frac{\rho_g}{\rho_f}\right)^{0.1}$$

$$u_{slip} = 2.9\left[g\sigma\left(\frac{\rho_f - \rho_g}{\rho_f^2}\right)\right]^{0.25} \tag{81}$$

Figure 54 plots the void fractions measured in the current work against the values predicted by the Woldesemayat-Dix relationship. Generally, the measured void fraction was slightly less than the predicted void fraction. However quantitatively, over 80% of the experimental points fell within ±0.02 of the values predicted by the correlation, which is a good result in two phase studies.

> The void fraction calculated by the post-processing technique is consistent with expected values from the Dix-Woldesemayat correlation.

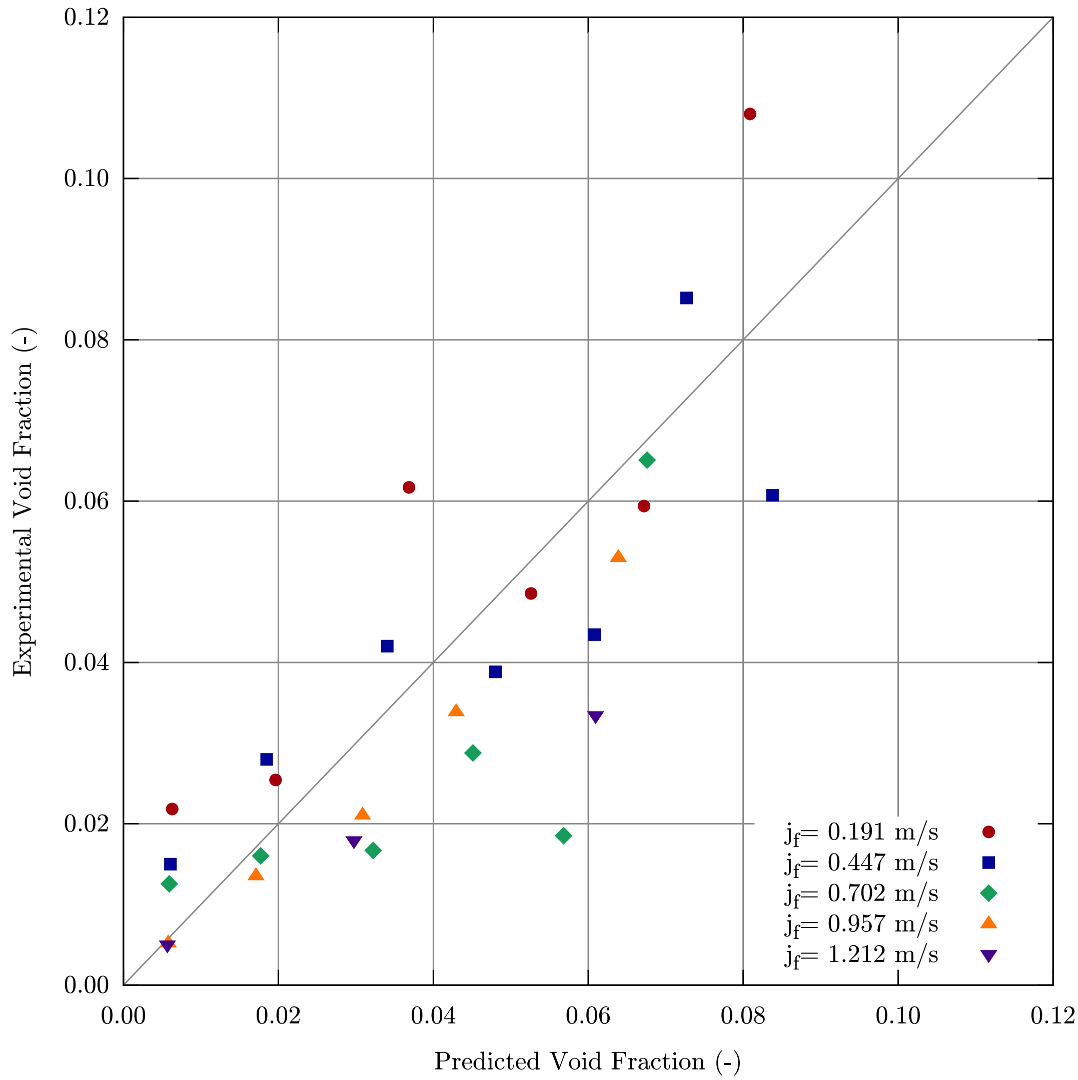

Figure 54: Measured void fraction vs. Woldesemayat-Dix Correlation. Points represent the void fraction as measured through the centerline of the tube at position ‘A’, 2.7 d_{hyd} upstream of the blockage location.

5.3.2.2 Radial Upstream a_i Measurements

One of the major advantages of the video frame analysis technique is that multiple points may be simultaneously sampled. In this section, measurements of d_{32}, α_g and a_i were conducted at 1 mm intervals upstream of the orifice section, and these results are compared against those found in literature. Figures 55, 56 and 57 are plots of radial distributions of these three properties at superficial liquid velocities between $0.191\ m/s \leq j_f \leq 1.212\ m/s$.

In bubbly flows, previous literature indicates that three types of void and a_i distributions exist: center-peaked, transitional and wall-peaked. The initial distribution of void is dependent on the superficial liquid and gas velocities, as well as the radial position of the air injector. Kondo *et al.* demonstrated that the radial position of the air inlet becomes irrelevant very quickly, and that beyond $z/d_{hyd} > 5$ downstream from the injection point, the radial void distribution stabilizes and becomes independent of the air injector configuration [74]. Since the measurements in the current work take place at $z/d_{hyd} = 30$, it is assumed the comparison to other works is not signficantly impacted by the differences in the geometry of the air injectors.

In the current work, in the low j_f cases plotted in figure 55, both the a_i and void decrease past $r/R > 0.50$. This center-peaked distribution is consistent with the observed results by Hibiki reproduced in figure 58 (left most plot) [12]. In the Hibiki work, the lowest curves in each plot represent gas superficial velocities of $j_g \approx 0.05\ m/s$, which is almost double the highest gas flow rates in the current work, however, the qualitative trends remain consistent.

As the fluid velocity is increased, the radial distribution of the a_i flattens out as illustrated in figure 56. The variation in a_i is primarily due to the radial redistribution of the void rather than a change in the bubble size since the Sauter mean diameter remains roughly the same between figures 55 and 56. This result is reflected in the Hibiki results (second plot from the left in figure 58) where an increase from $j_f = 0.262\ m/s$ to $j_f = 0.872\ m/s$ causes a similar flattening of the radial a_i distribution.

The Hibiki results also show a wall-peak in the a_i beginning to develop at $j_f = 0.872\ m/s$ and becoming more prominent at $j_f = 1.75\ m/s$ (middle plot in figure

[12] Reprinted from Int. J. Heat Mass Transfer, vol 42, T. Hibiki and M. Ishii, Experimental study on interfacial area transport in bubbly two-phase flow, 3019–3035, 1999, with permission from Elsevier.

58. In the present work, this characteristic is not present at $j_f = 0.702$ m/s as the radial profile is still flattening and transitioning from the center-peaked distribution. However, when the fluid superficial velocity is increased to $j_f = 1.212$ m/s (figure 57), the a_i in the region between $0.70 \leq r/R \leq 1.00$ begins to increase and demonstrate signs of a wall-peak forming. The wall-peaks in figure 57 are not as prominent as those observed in literature, and it is speculated that this discrepency may be simply due to the lower gas velocities used in the current work.

> The observed transition from a center-peaked to a wall-peaked a_i distribution at around $j_f = 0.70$ m/s is consistent with results reported in literature by Hibiki [37].

While the previous verification work has demonstrated good qualitative agreement with the results in literature, the test conditions differed enough that the magnitude of the a_i measurements could not be confirmed. In order to check the magnitude of the a_i being reported by the post-processing code, the distribution of a_i is compared to results obtained by Revankar which are at similar flow conditions [33].

The right half of figure 59[13] displays the radial a_i distribution measured by Revankar and Ishii in a 5.08 cm (ID) tube at constant gas flow rates [33]. The left half of figure 59 plots the results obtained in the current work (on the same scale) at similar flow rates. While the Revankar data does not demonstrate (perhaps owing to a larger tube diameter) the center-line peaking effects as in the current result, the magnitude of the a_i between $0.00 \leq r/R \leq 0.50$ is nearly identical to the results obtained by the video analysis performed here.

> The magnitude of the reported a_i in the current work is consistent with the results reported by Revankar and Ishii at similar conditions [33].

[13]Reprinted from Int. J. Heat Mass Transfer, vol 35, S.T. Revankar and M. Ishii, Local interfacial area measurement in bubbly flow, 913–925, 1992, with permission from Elsevier.

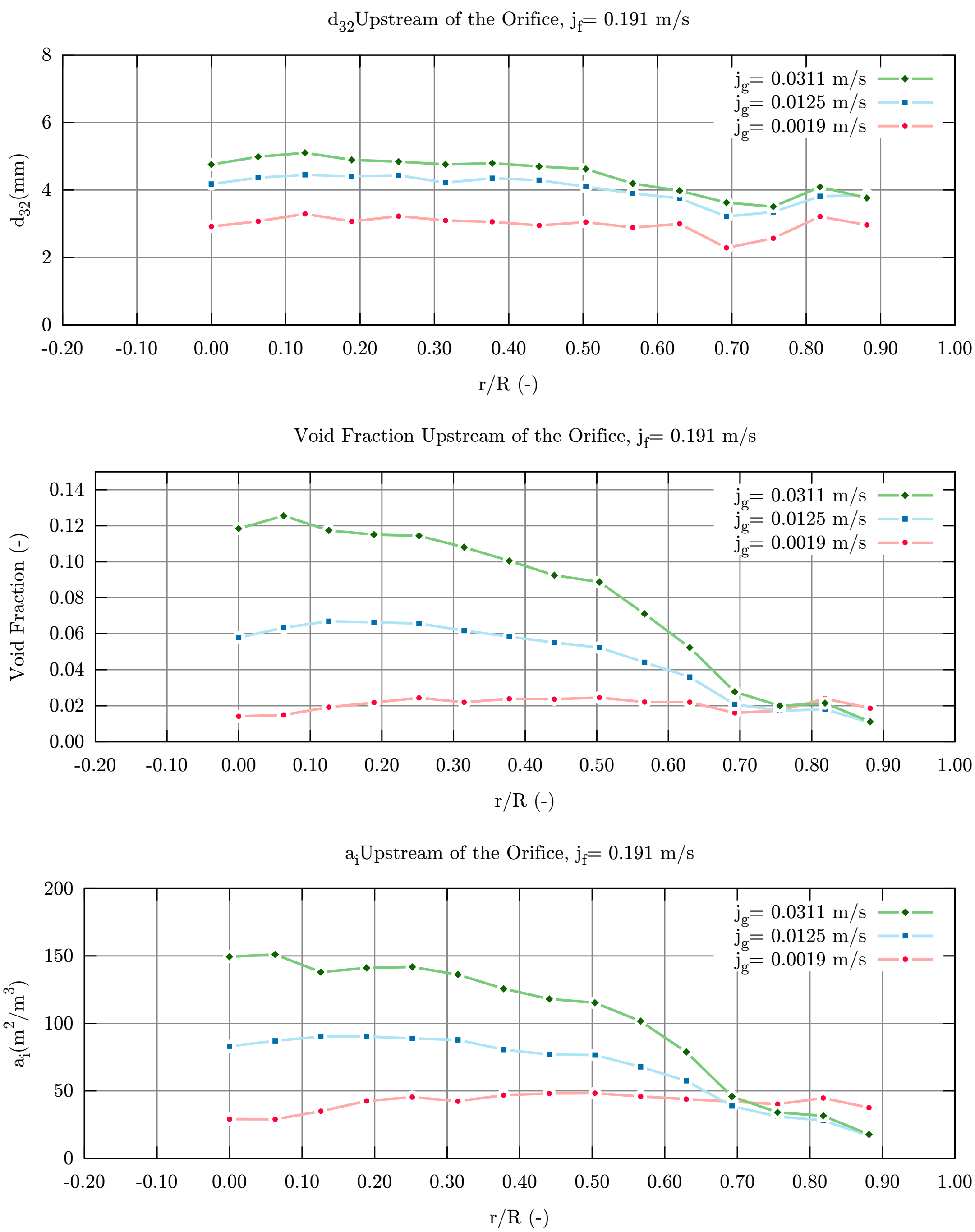

Figure 55: Radial distribution of the d_{32} (top), α (middle) and a_i (bottom) at different gas flow rates for a superficial velocity of $j_f = 0.191\ m/s$.

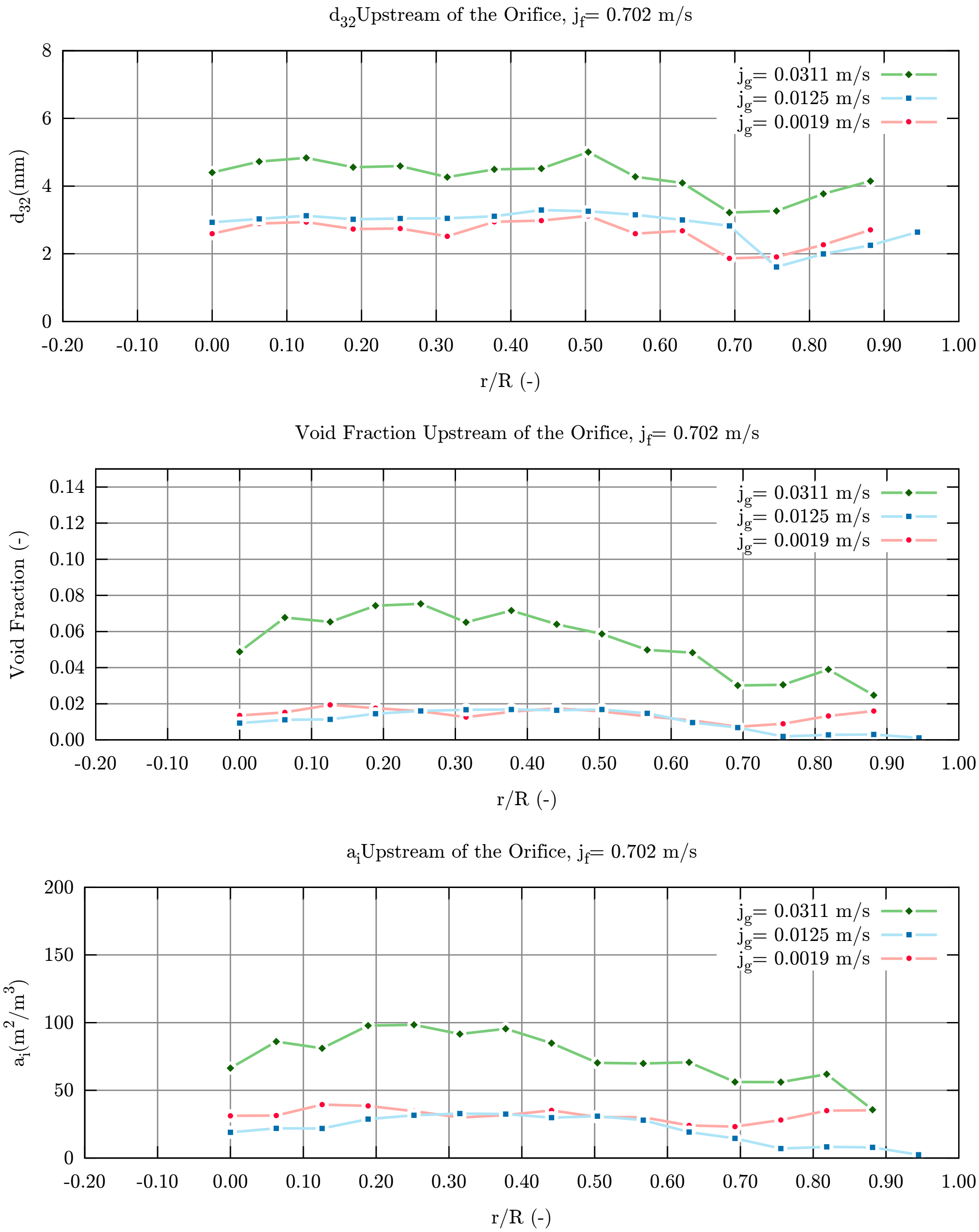

Figure 56: Radial distribution of the d_{32} (top), α (middle) and a_i (bottom) at different gas flow rates for a superficial velocity of $j_f = 0.702\ m/s$.

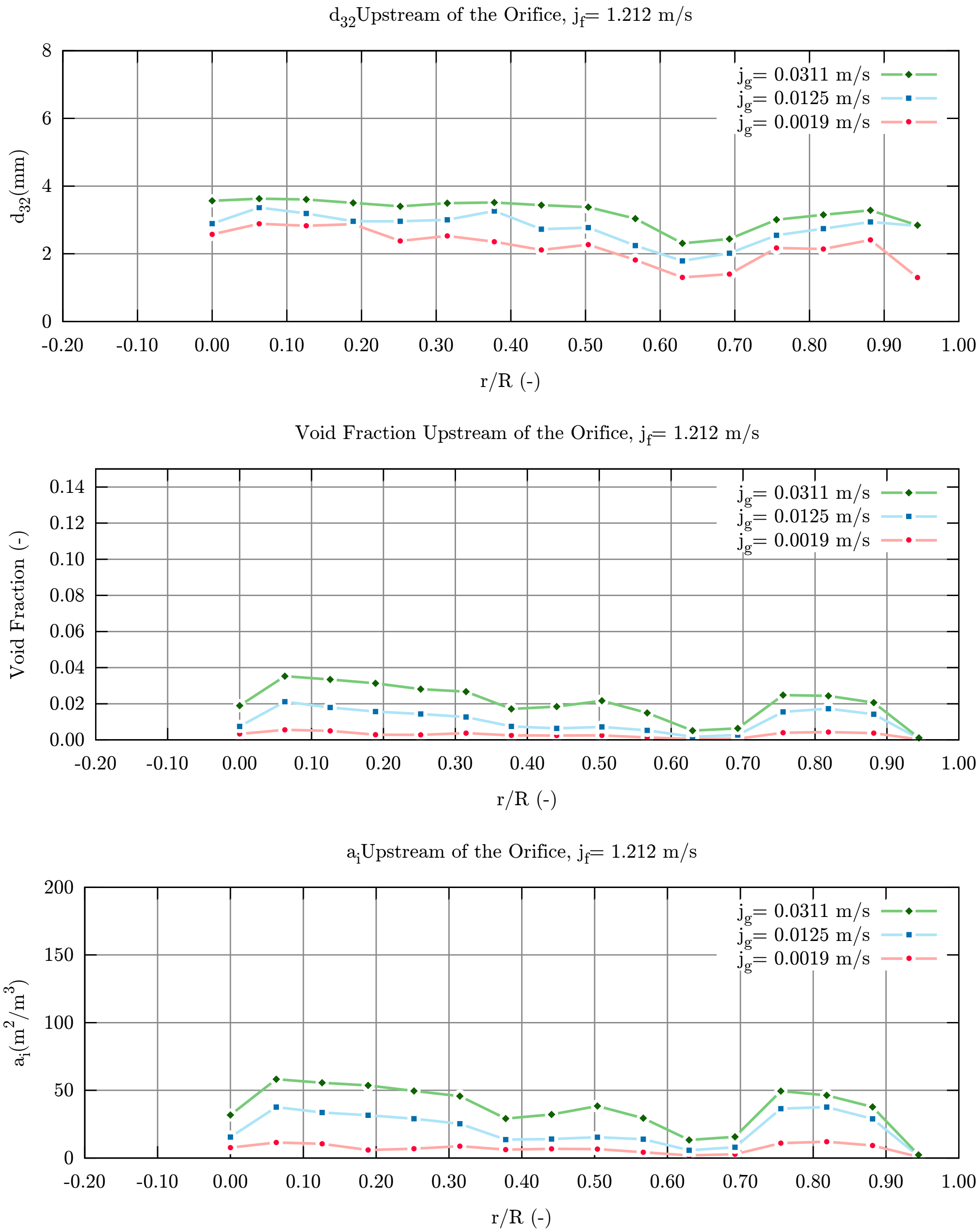

Figure 57: Radial distribution of the d_{32} (top), α (middle) and a_i (bottom) at different gas flow rates for a superficial velocity of $j_f = 1.212\ m/s$.

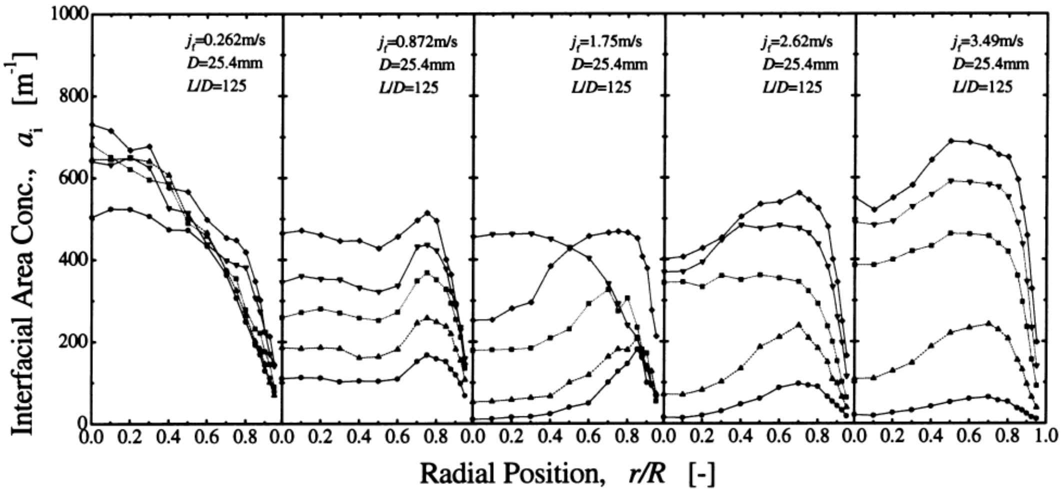

Figure 58: Radial a_i distributions obtained by Hibiki and Ishii under various j_f [37]. Note that comparisons made to the current work are done with the lowest curves in each plot which correspond to $j_g \approx 0.05\ m/s$.

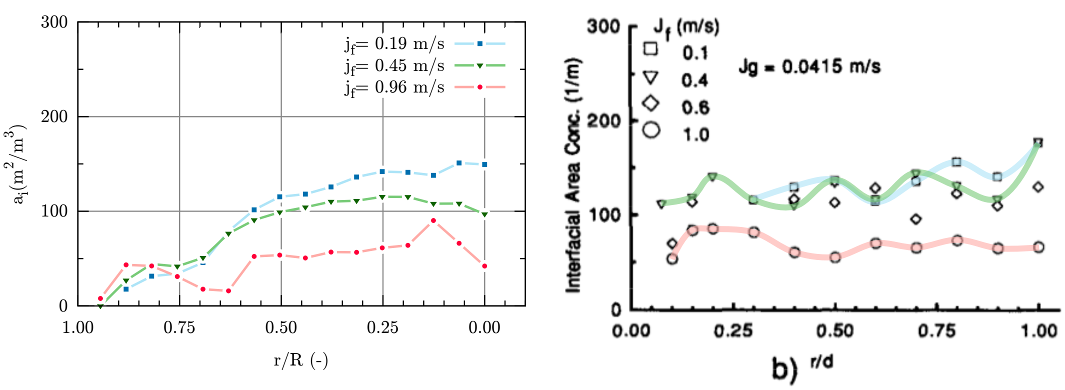

Figure 59: Radial a_i distribution results obtained in the current work with $j_g = 0.031\ m/s$ (left) compared to that of Revankar and Ishii (right). A $0.0508\ m$ (ID) tube and $49 \times 0.12\ mm\ (ID)$ needle type air injection nozzles were used in the Revankar work [33]. The r/d on the x-axis of the right figure is interpreted (based on other figures in the work) to actually represent the radial coordinate (r/R), with $r/d = 0.00$ located at the tube wall, and $r/d = 1.00$ coinciding with the tube centerline position.

5.3.3 Fragmentation Through The Orifice

Having measured and confirmed the accuracy of the interfacial area concentration measurements upstream of the orifice in section 5.3.2.2, the goals of this section are to examine the effects which flow blockages have on the a_i. When the bubbles are forced through the flow restriction, there is an expectation that the increased local turbulence and the acceleration of the fluid phase will increase the likelihood of fragmentation. The change in fragmentation rate should correspond with an increase in a_i, however the extent of this increase remains unknown.

When the bubbles pass through the orifice, a single large bubble may disintegrate into many smaller bubbles. In order to evaluate how these contribute to the increase in a_i, section 5.2.4 discusses how an area-weighted PDF may be applied. Sections 5.3.3.1, 5.3.3.2 and 5.3.3.3 plot and discuss the results obtained when the air is forced through the three orifice geometries.

Table 30: Number of frames sampled and bubbles detected

j_f (m/s)	$r/R = 0.0$		$r/R = 0.5$	
	n_{frames}	$n_{bubbles}$	n_{frames}	$n_{bubbles}$
Lower Elevation				
0.191 m/s	43676	8779	43676	7411
0.702 m/s	43676	4657	43676	4137
1.212 m/s	21837	4064	21837	2761
Upper Elevation, $\phi = 25.4$ mm				
0.191 m/s	43676	5625	43676	6909
0.702 m/s	43676	6175	43676	6909
1.212 m/s	21837	9875	21837	9457
Upper Elevation, $\phi = 19.1$ mm				
0.191 m/s	43676	8458	43676	5908
0.702 m/s	43676	50320	43676	30882
1.212 m/s	21837	49522	21837	27841
Upper Elevation, $\phi = 12.7$ mm				
0.191 m/s	29116	35918	29116	9866
0.702 m/s	43676	108919	43676	59942
1.212 m/s	21837	41363	21837	31419

5.3.3.1 25.4 mm ID Orifice, Blockage Ratio = 0.36

The d_{32}, α_g and a_i are measured before and after the orifice at the elevations indicated in figure 21. The radial distributions of these properties are plotted under liquid superficial velocities of j_f = 0.191, 0.702, and 1.212 m/s in figures 60, 62 and 64 respectively. Detailed PDFs and ADFs for these cases are plotted in figures 61, 63 and 65 at the centerline position ($r/R_{tube} = 0.0$) and halfway between the centerline and the wall ($r/R_{tube} = 0.5$). Sample frames from the runs are supplied in figure 66.

Each of the data sets marked 'Lower' in this section as well as sections 5.3.3.2 and 5.3.3.3 use a common set of data acquired using multiple runs. The use of a common data set for each of the three orifice designs is justified based on the single phase results. Figure 26 has demonstrated that at the lower measurement elevation, both the velocity and turbulent intensity are essentially identical between the three orifice test sections.

At the lowest flow rate, figure 60 indicates that no significant change in the bubble diameters occurs when they pass through the orifice. At both $r/R_{tube} = 0.0$ and 0.5 there is very little difference between the bubble PDFs upstream and downstream of the orifice. The conclusion is that fragmentation is not occuring under these conditions. The shift of the chord size distribution to a higher value in figure 61 tends to support this claim, although from the data in the PDFs alone it is not clear whether the bubbles are coalescing or simply being streteched by the velocity gradient in the orifice. The data in section 5.2.3.2 indicates that at these conditions the average bubble size (in both the x and y directions) near the centerline of the tube increases supportng the claim that coalesence was occuring.

As the superficial liquid velocity is increased to $j_f = 0.702\ m/s$, the PDFs in figure 63 indicate that a population of bubbles with a diameter $d_{10} < 600\ \mu m$ has started to form after the flow has passed the orifice, suggesting that there is some fragmenting occuring. The ADFs indicate that the contributions to the interfacial area by these smaller bubbles is insignificant, and that most of the a_i is still due to the larger bubbles $3000 < d_{10} < 4000\ \mu m$.

Further increasing the fluid superficial velocity to $j_f = 1.212\ m/s$ causes a reduction in the d_{32} downstream of the orifice as the bubbles begin to disintegrate with increasing frequency, and this is illustrated in figure 64. These conditions also mark the first time that the peaks in the PDFs and ADFs appear to shift towards smaller diameters as the daughter bubble population begins to make a significant contribution to the a_i as demonstrated in figure 65. It is also evident from these figures that the relative number of these smaller bubbles is slightly higher at $r/R = 0.5$ than at $r/R = 0.0$. This would infer that the bubbles are breaking up more frequently near orifice walls than they are along the centerline, which is consistent with the measured turbulence and turbulent dissipation rate profiles.

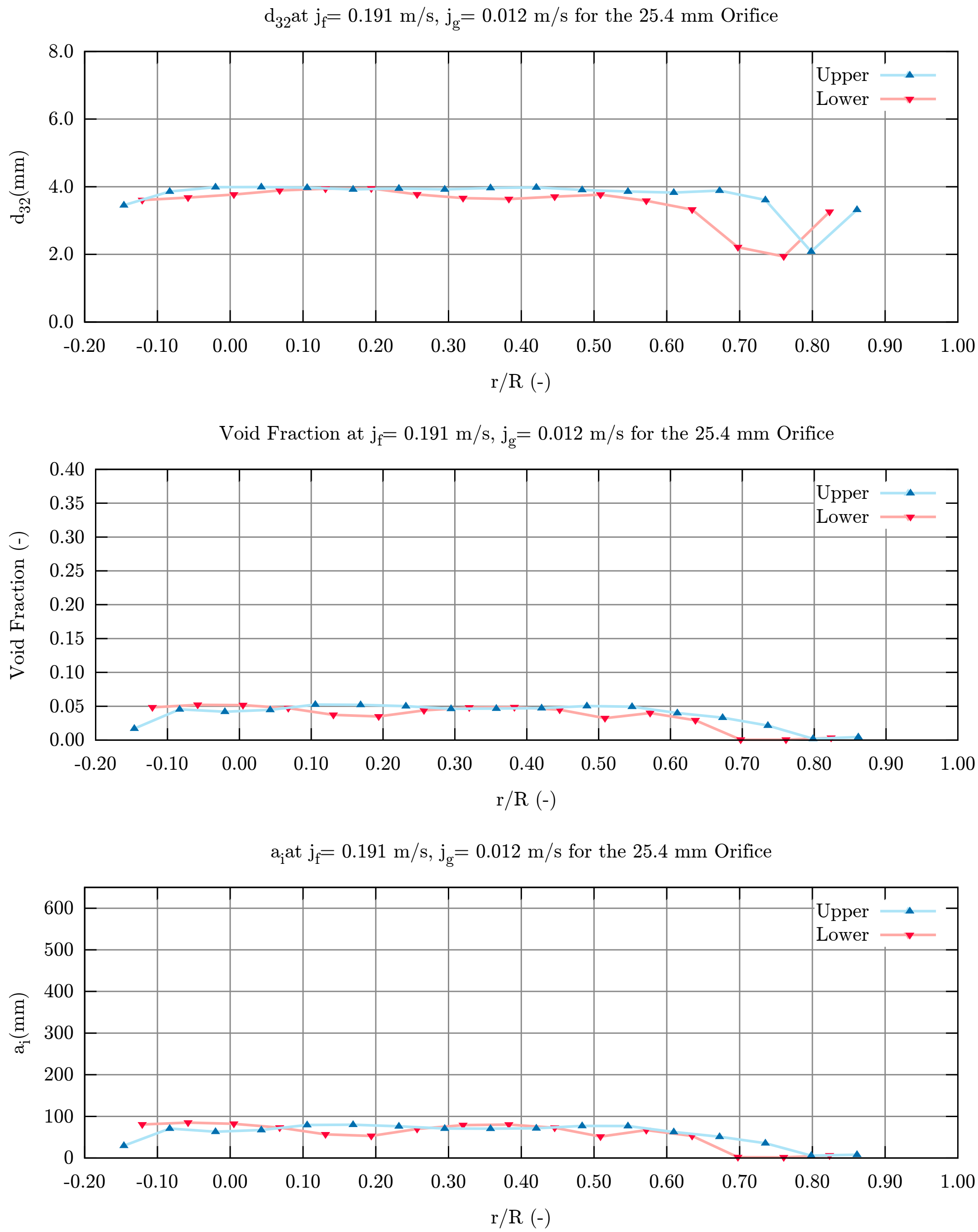

Figure 60: Radial Distribution for $\phi = 25.4\ mm$ at $j_f = 0.191\ m/s$.

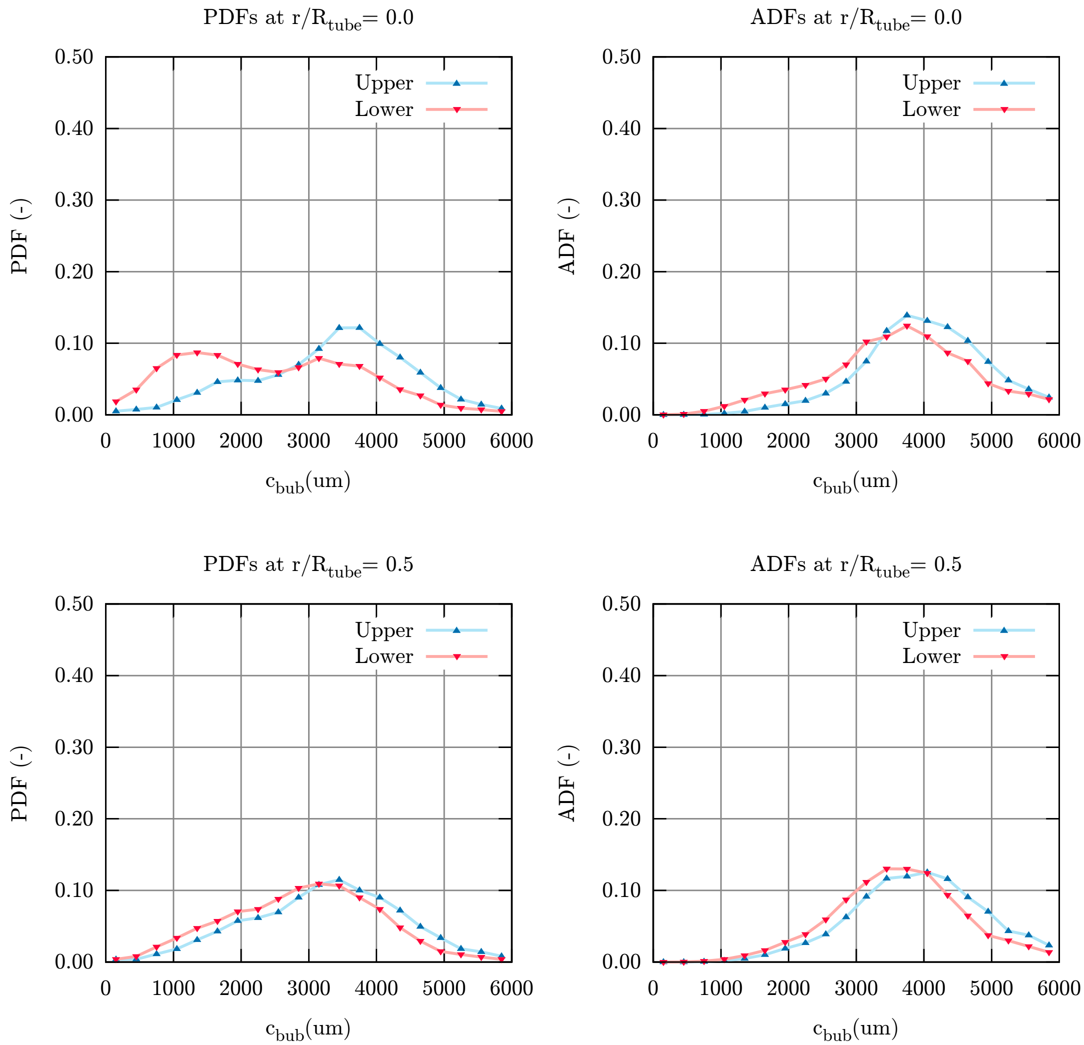

Figure 61: Size distribution functions for flow through an orifice of $\phi = 25.4\ mm$ at $j_f = 0.191\ m/s$. Distributions are sampled at $r/R_{tube} = 0.0$ (top) and $r/R_{tube} = 0.5$ (bottom).

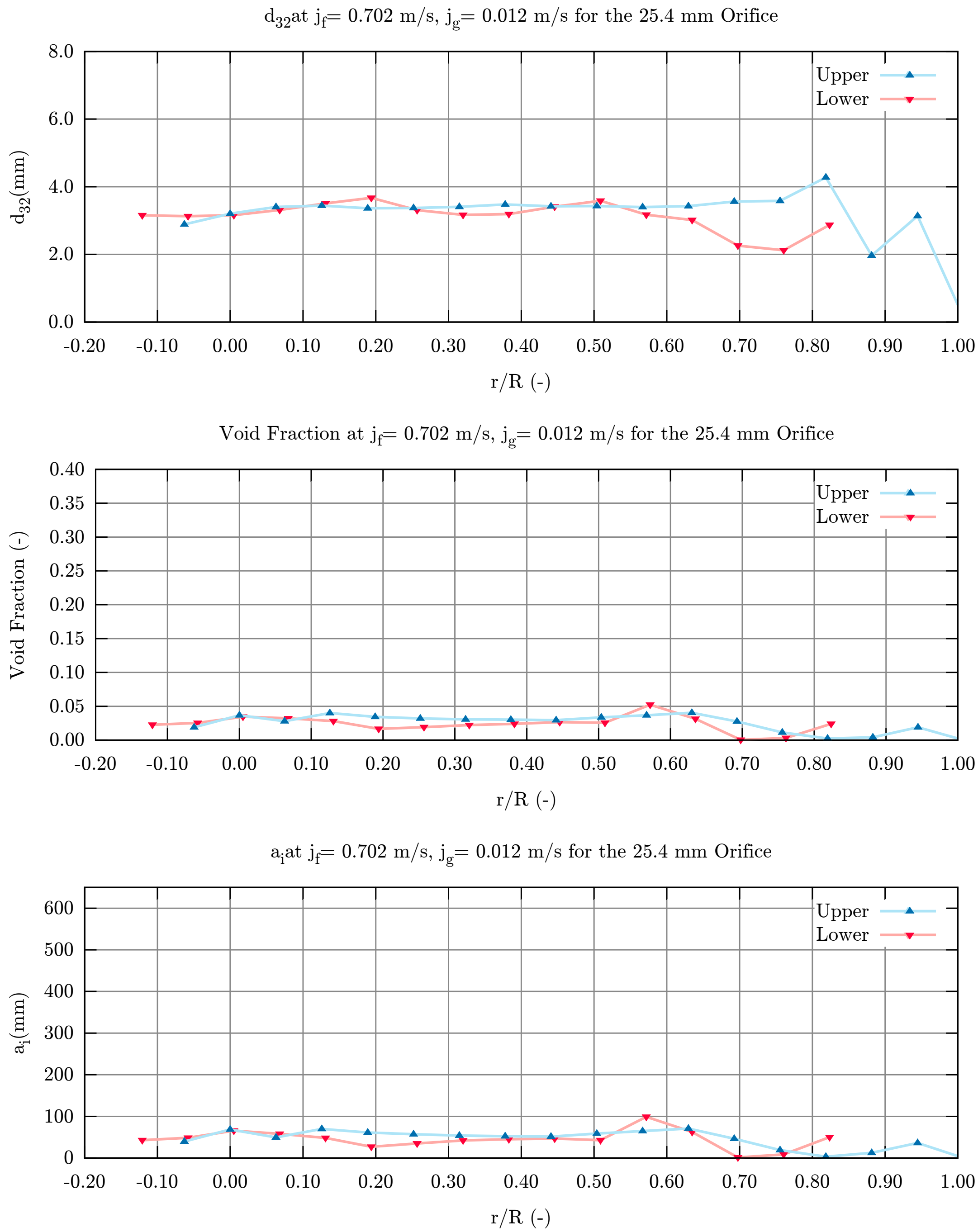

Figure 62: Radial Distribution for $\phi = 25.4\ mm$ at $j_f = 0.702\ m/s$.

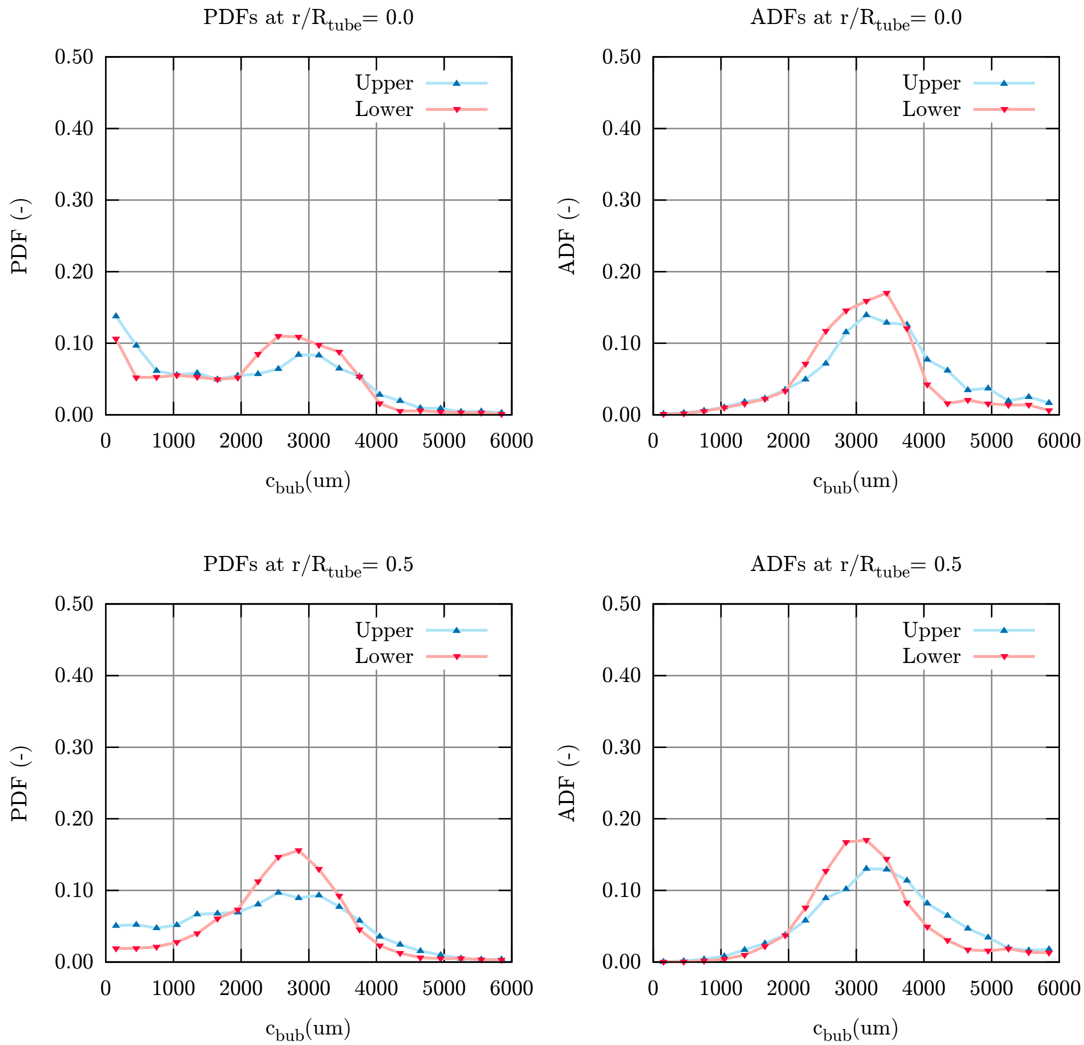

Figure 63: Size distribution functions for flow through an orifice of $\phi = 25.4\ mm$ at $j_f = 0.702\ m/s$. Distributions are sampled at $r/R_{tube} = 0.0$ (top) and $r/R_{tube} = 0.5$ (bottom).

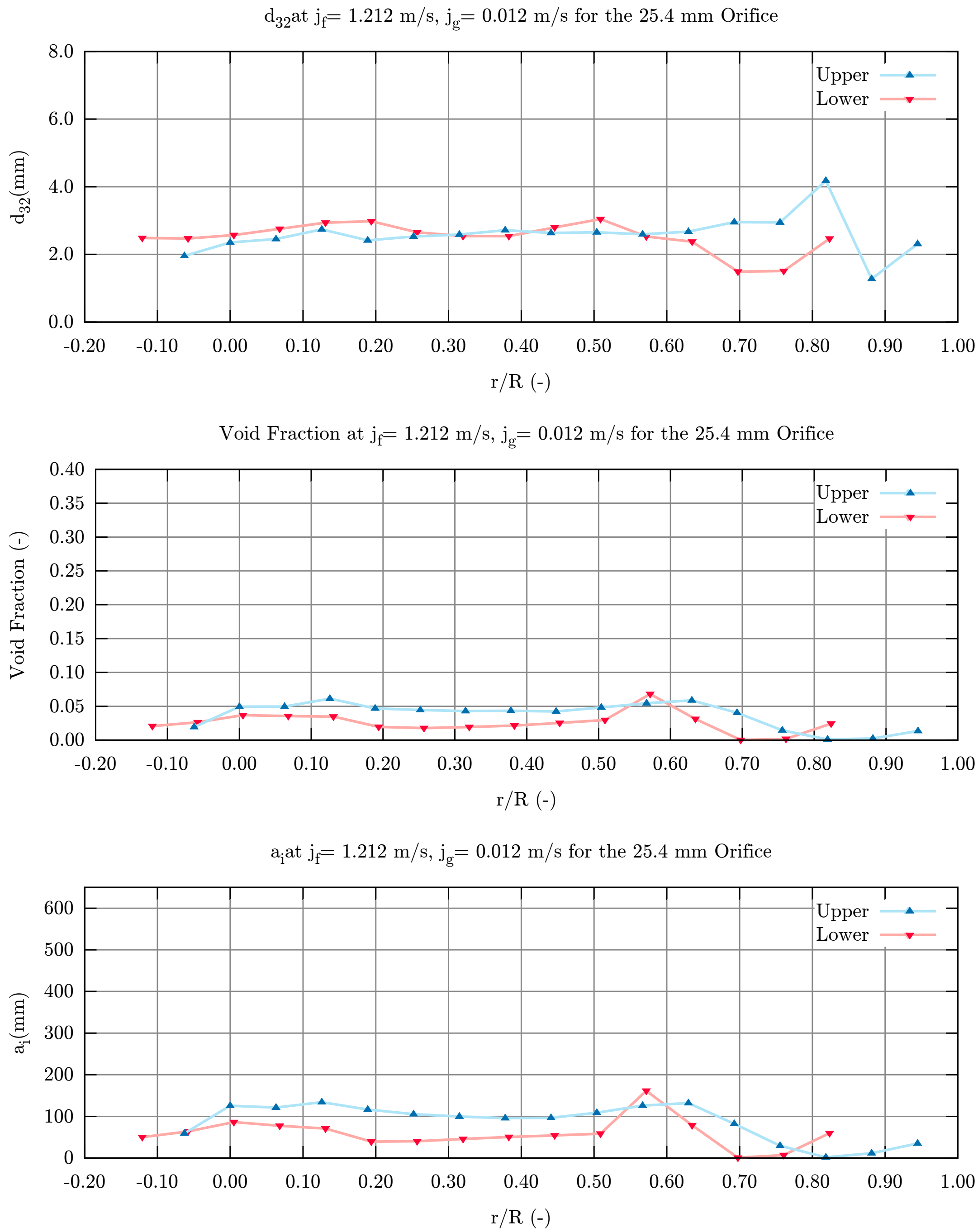

Figure 64: Radial Distribution for $\phi = 25.4\ mm$ at $j_f = 1.212\ m/s$.

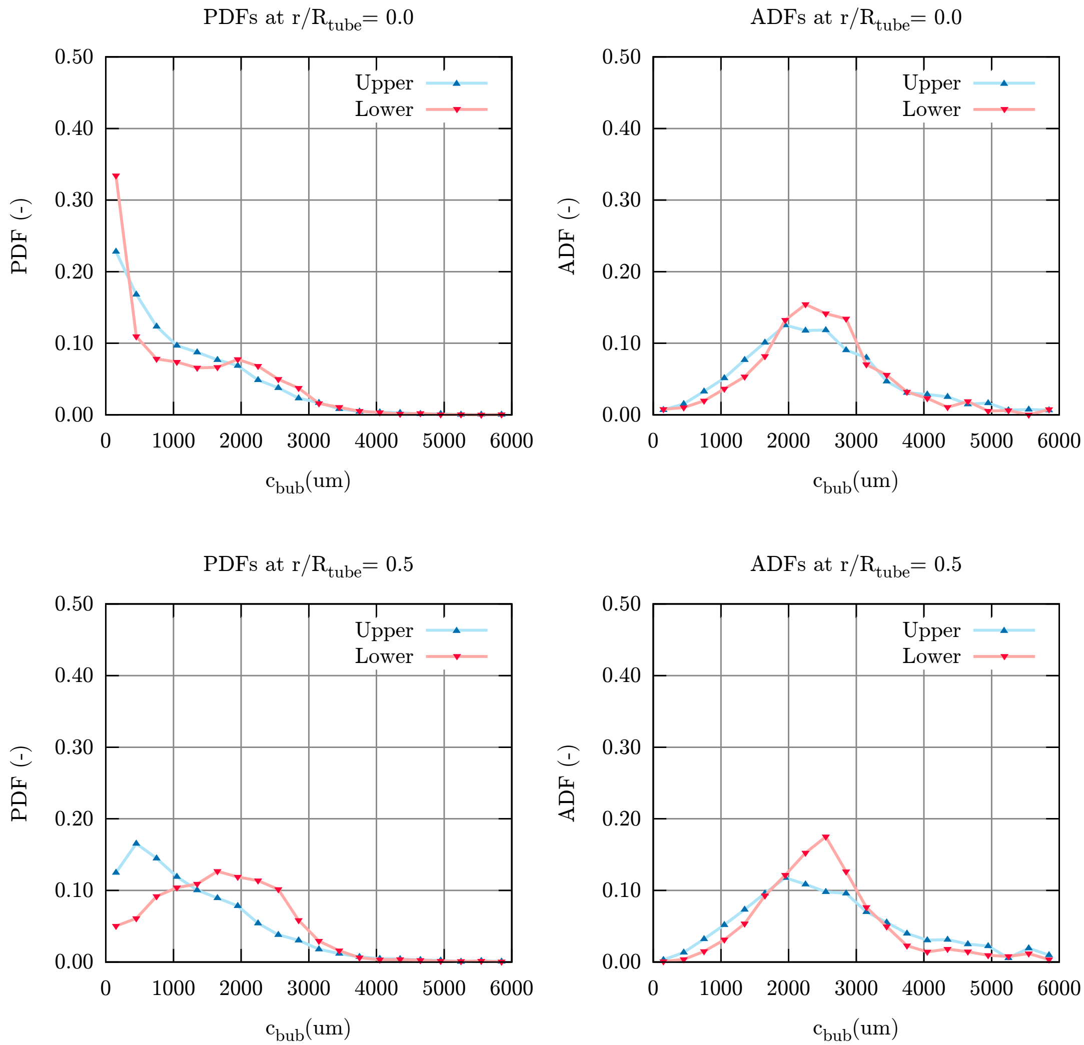

Figure 65: Size distribution functions for flow through an orifice of $\phi = 25.4\ mm$ at $j_f = 1.212\ m/s$. Distributions are sampled at $r/R_{tube} = 0.0$ (top) and $r/R_{tube} = 0.5$ (bottom).

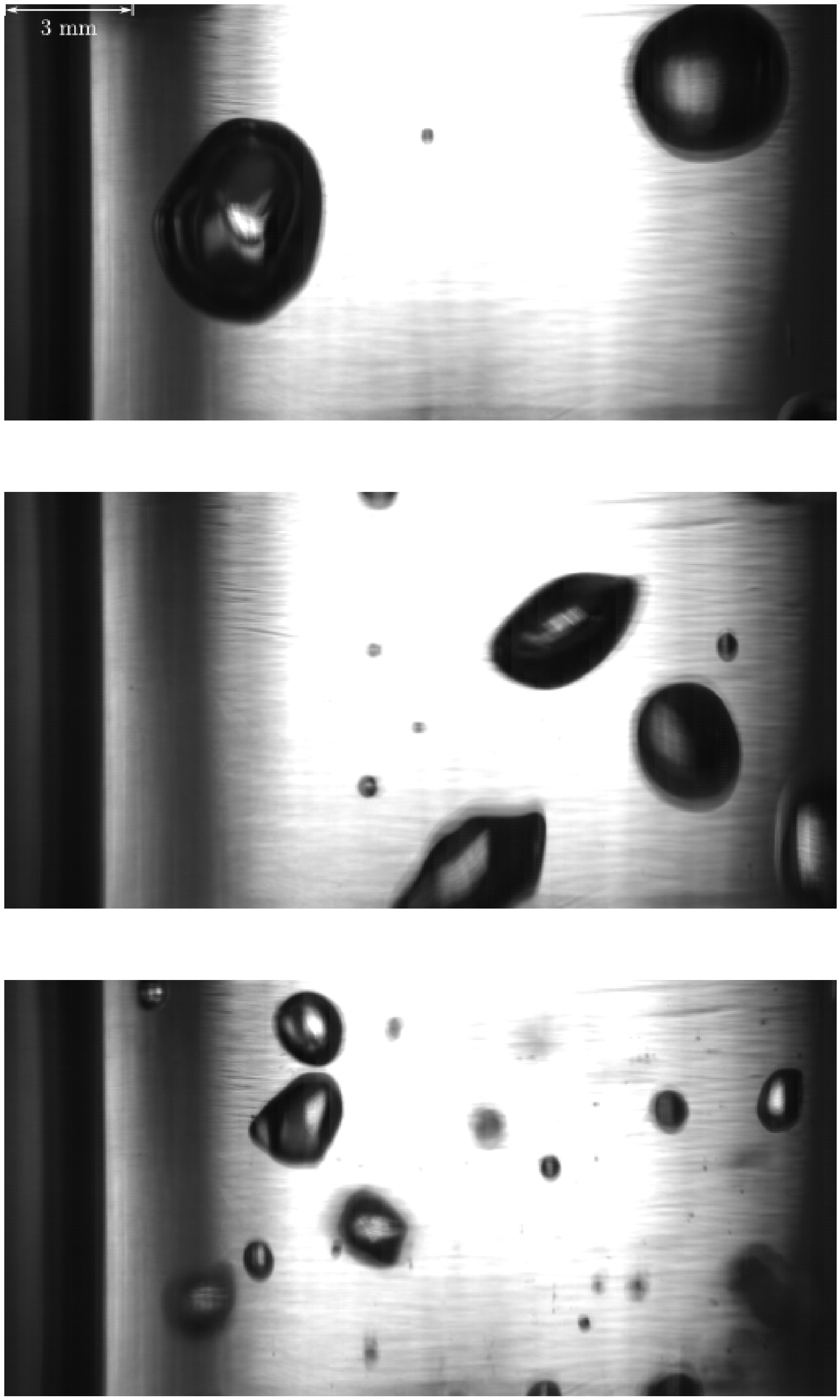

Figure 66: Sample frames where $\phi = 25.4\ mm$, $j_g = 0.0125\ m/s$, and $j_f = 0.191\ m/s$ (top), $j_f = 0.702\ m/s$, and $j_f = 1.212\ m/s$.

5.3.3.2 19.1 mm ID Orifice, Blockage Ratio = 0.64

The a_i results for the $\phi = 19.1$ mm orifice are illustrated in figures 67, 69 and 71, with the corresponding PDF and ADFs in figures 68, 70, and 72. Sample frames from the runs are supplied in figure 73.

In figures 69 and 71, the void fraction is noticably higher at the upper elevation than it is at the lower measurement point. This is an effect which was not observed in the $\phi = 25.4$ mm results. This void fraction increase is a local effect due to the bubbles being concentrated into a smaller portion of the flow area by the restriction. As they exit the restriction, most of the bubbles remain entrained by the liquid jet in the center of the flow area for several d_{hyd} which prevents them from quickly moving back out towards the tube wall. This would in turn cause the void fraction near the centerline of the upper measurement point to be higher than at the lower measurement point. Those bubbles that do 'escape' the jet may be entrained in the recirculation zone just downstream of the orifice outlet, and end up being counted multiple times. Again, this would give the impression that a higher void fraction exists.

This result is not observed at the low fluid velocity case (figure 67) since the jet in the core of the flow is not as strong.

At $r/R_{tube} = 0.0$ in the $j_f = 0.191$ m/s PDFs for both the $\phi = 25.4$ and $\phi = 19.1$ orifices (figures 61 and 68), the bubble chord diameter increases slightly after passing through the orifice. This is likely caused by a change in the aspect ratio of each bubble, and is examined in further detail in section 5.2.3. This effect is significant in these cases since the flow through the orifice is insufficient to cause fragmentation which would otherwise reduce the measured diameters (the lack of bubbles in the $d < 1000$ μm region would support this claim). At $r/R_{tube} = 0.5$ under the same conditions, some limited fragmentation is occuring which suppresses the diameter peak from shifting. Coalesence is not expected and is not qualitatively observed.

At $j_f = 0.702$ m/s, the PDFs in figure 68 exhibit a distinct shift before and after the orifice. The downstream results along both the centerline and at $r/R = 0.5$ show a large population of bubble fragments at $d \approx 1000$ μm.

Further increasing the liquid superficial velocity to $j_f = 1.212$ m/s causes the majority of the daughter bubbles to fall in the range of $d \leq 600$ μm.

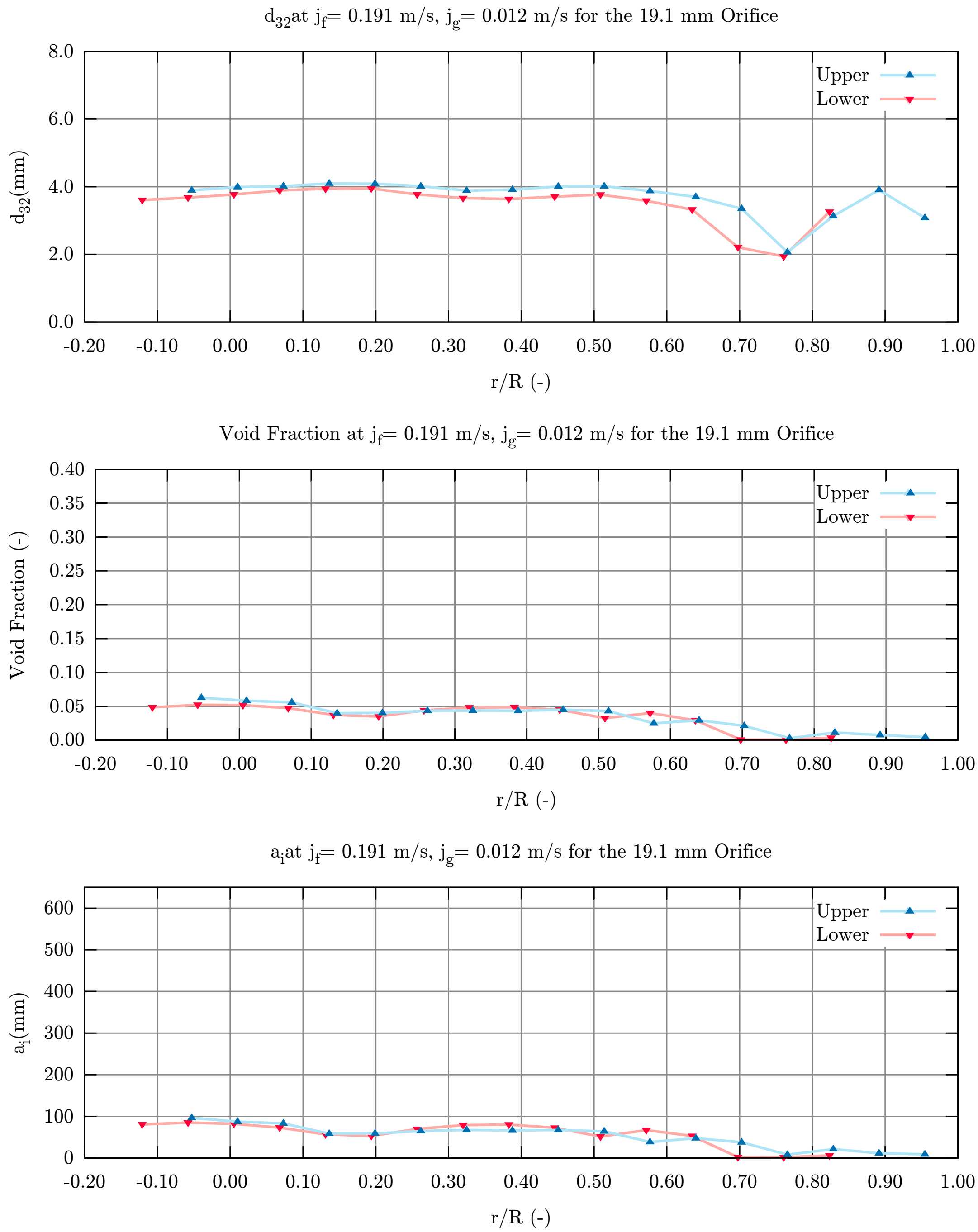

Figure 67: Radial Distribution for $\phi = 19.1\ mm$ at $j_f = 0.191\ m/s$.

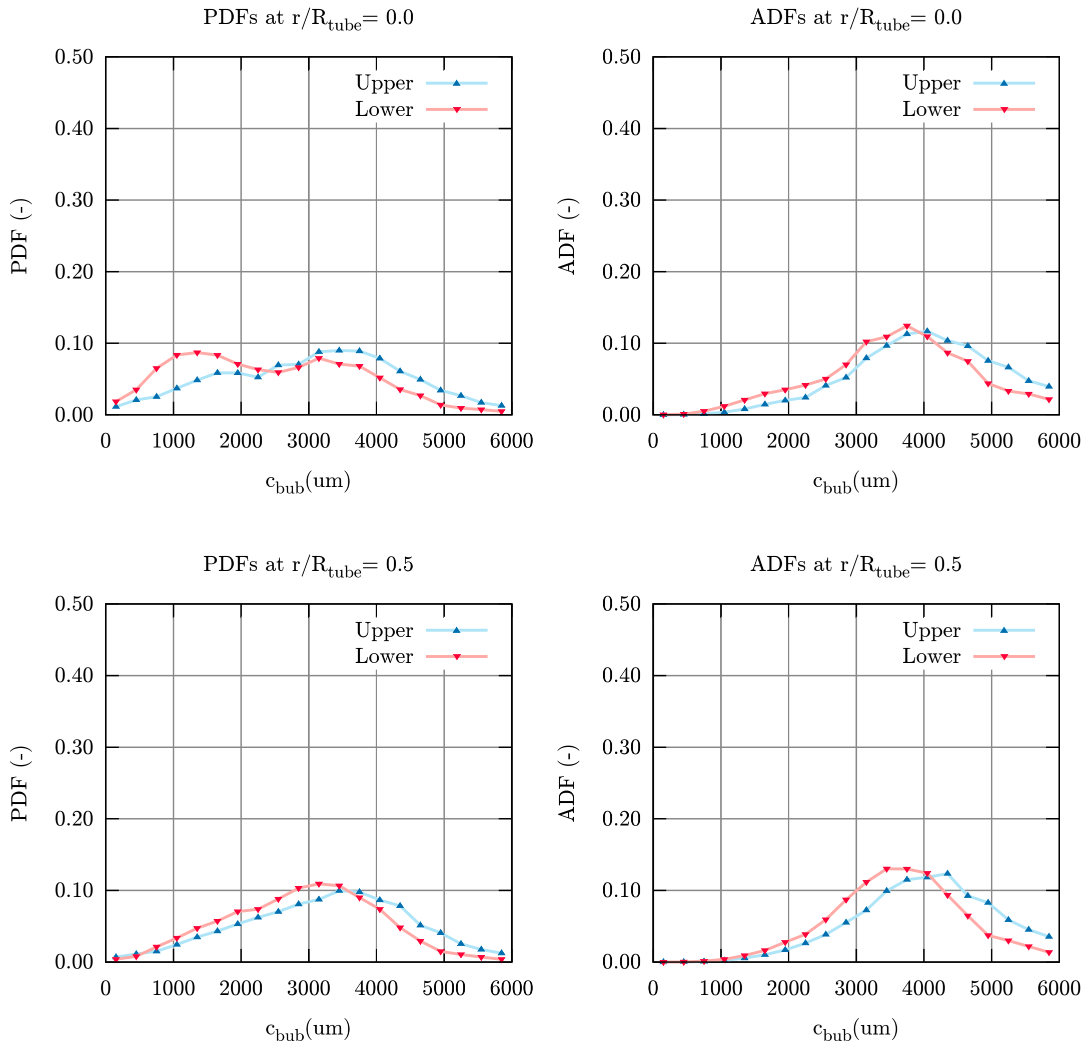

Figure 68: Size distribution functions for flow through an orifice of $\phi = 19.1\ mm$ at $j_f = 0.191\ m/s$. Distributions are sampled at $r/R_{tube} = 0.0$ (top) and $r/R_{tube} = 0.5$ (bottom).

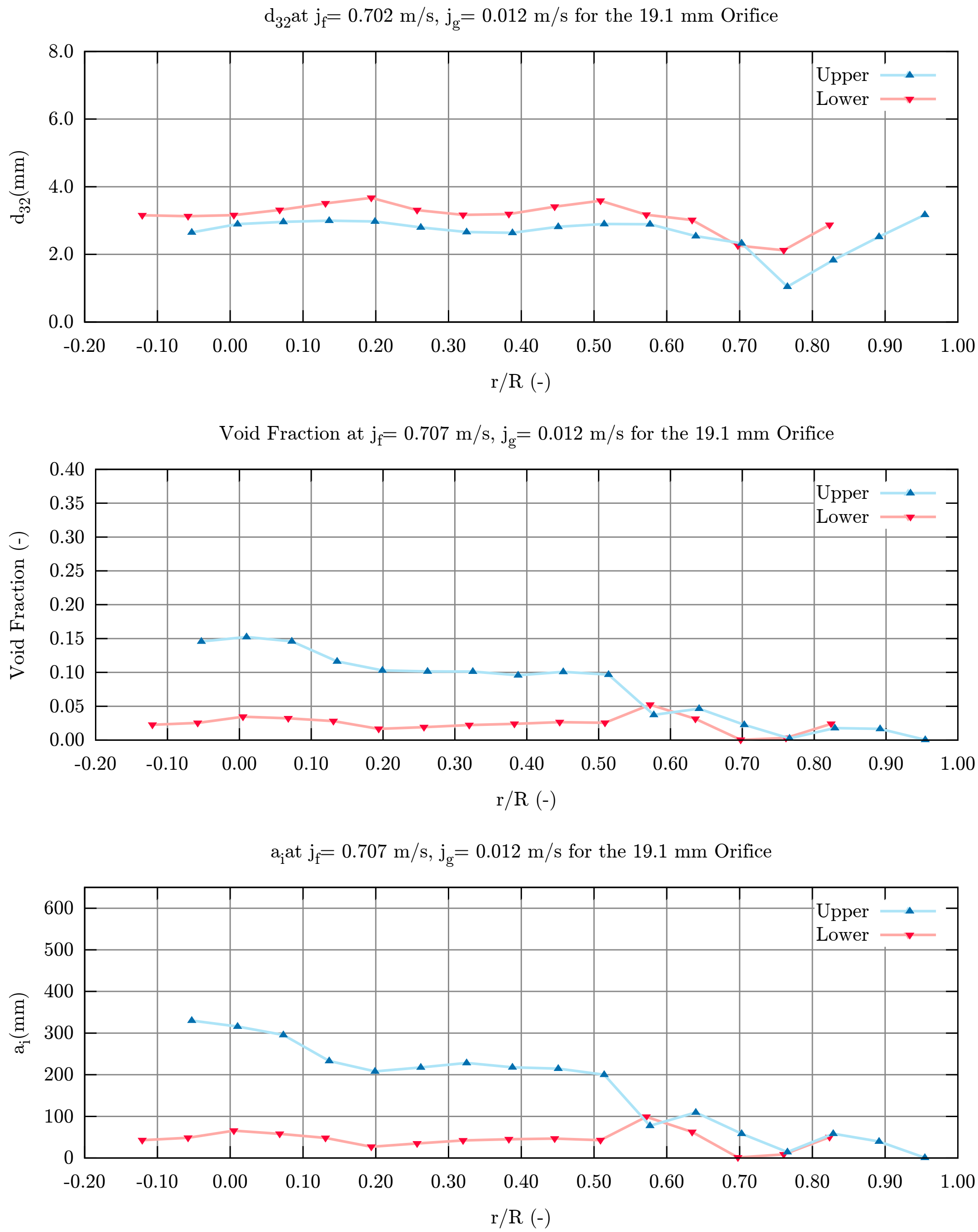

Figure 69: Radial Distribution for $\phi = 19.1\ mm$ at $j_f = 0.702\ m/s$.

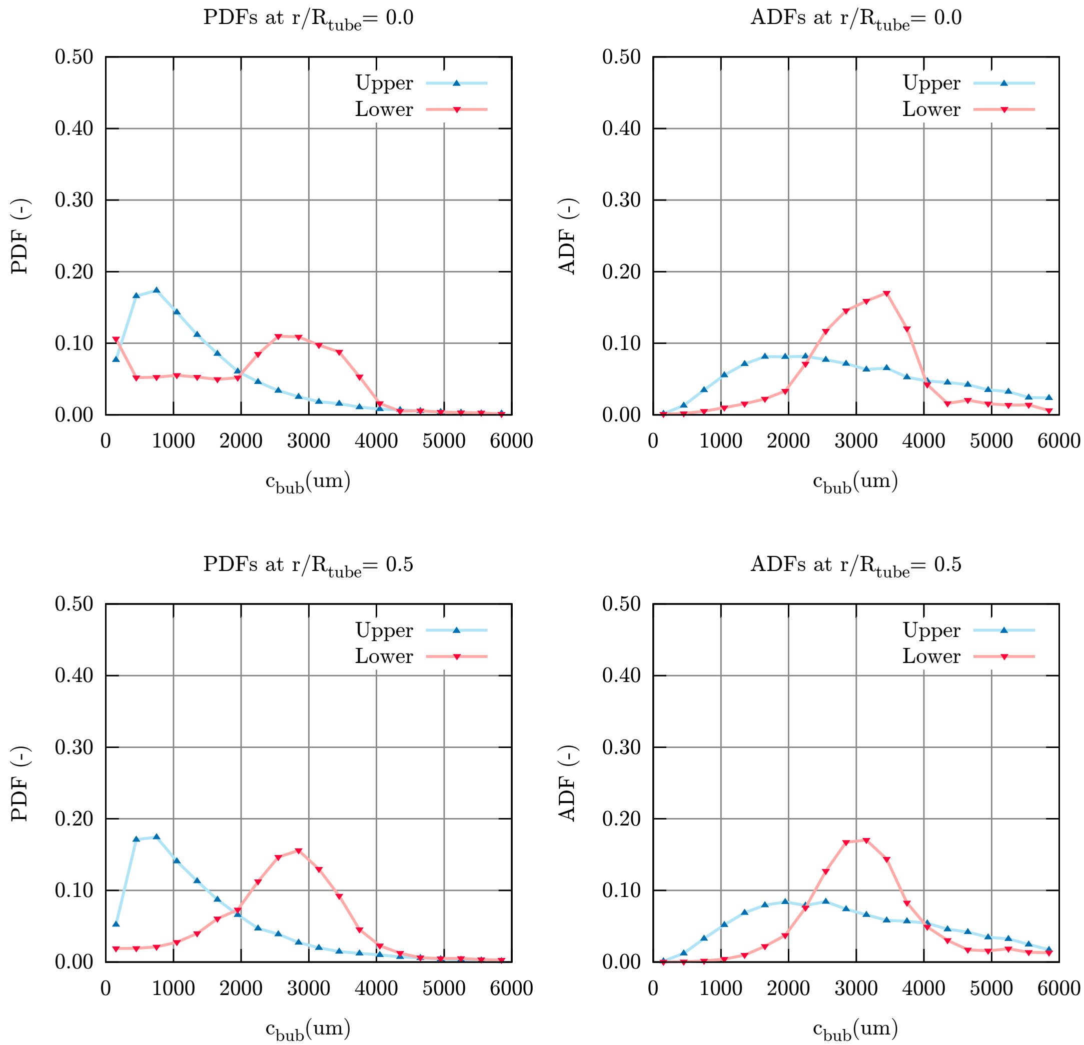

Figure 70: Size distribution functions for flow through an orifice of $\phi = 19.1\ mm$ at $j_f = 0.702\ m/s$. Distributions are sampled at $r/R_{tube} = 0.0$ (top) and $r/R_{tube} = 0.5$ (bottom).

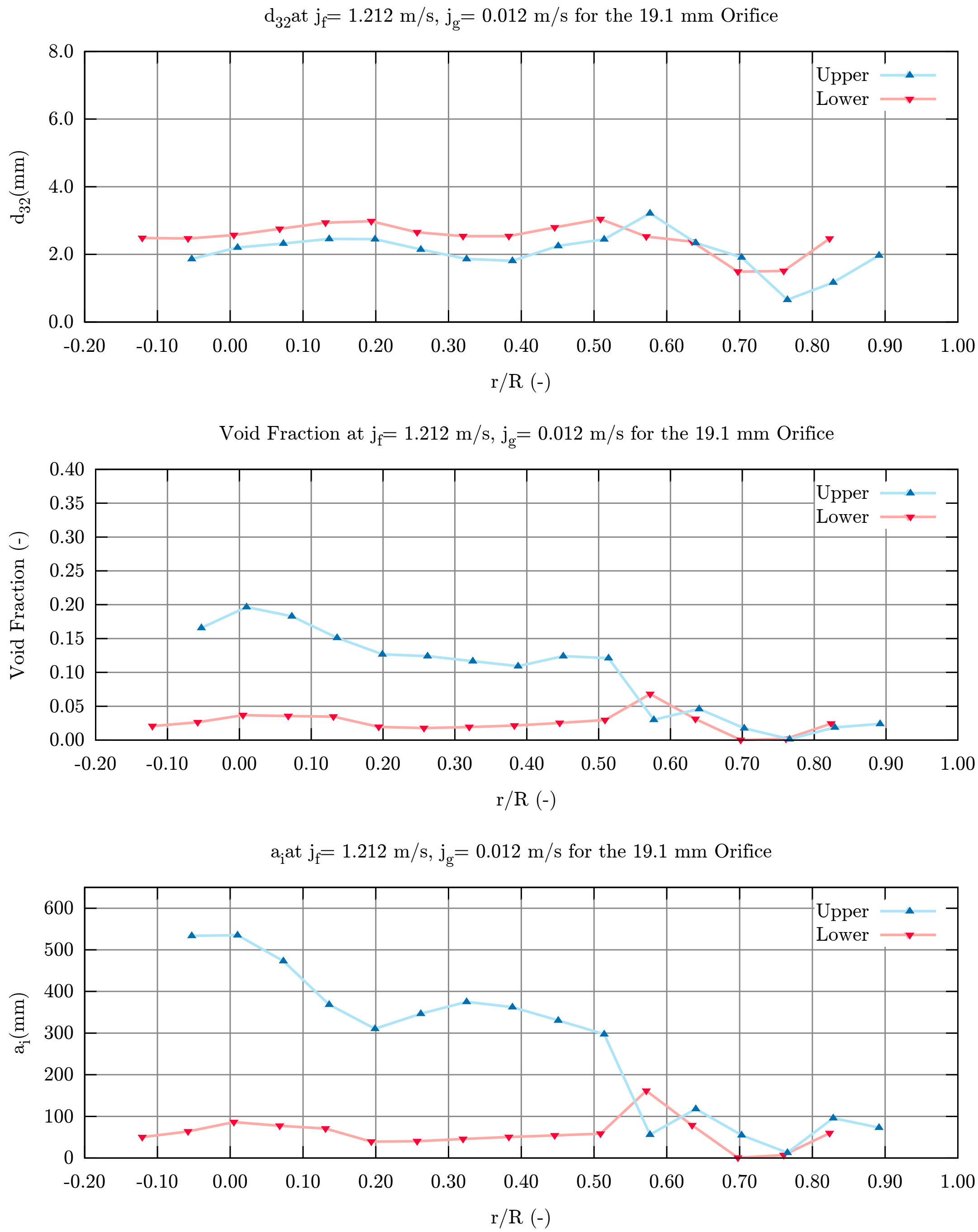

Figure 71: Radial Distribution for $\phi = 19.1\ mm$ at $j_f = 1.212\ m/s$.

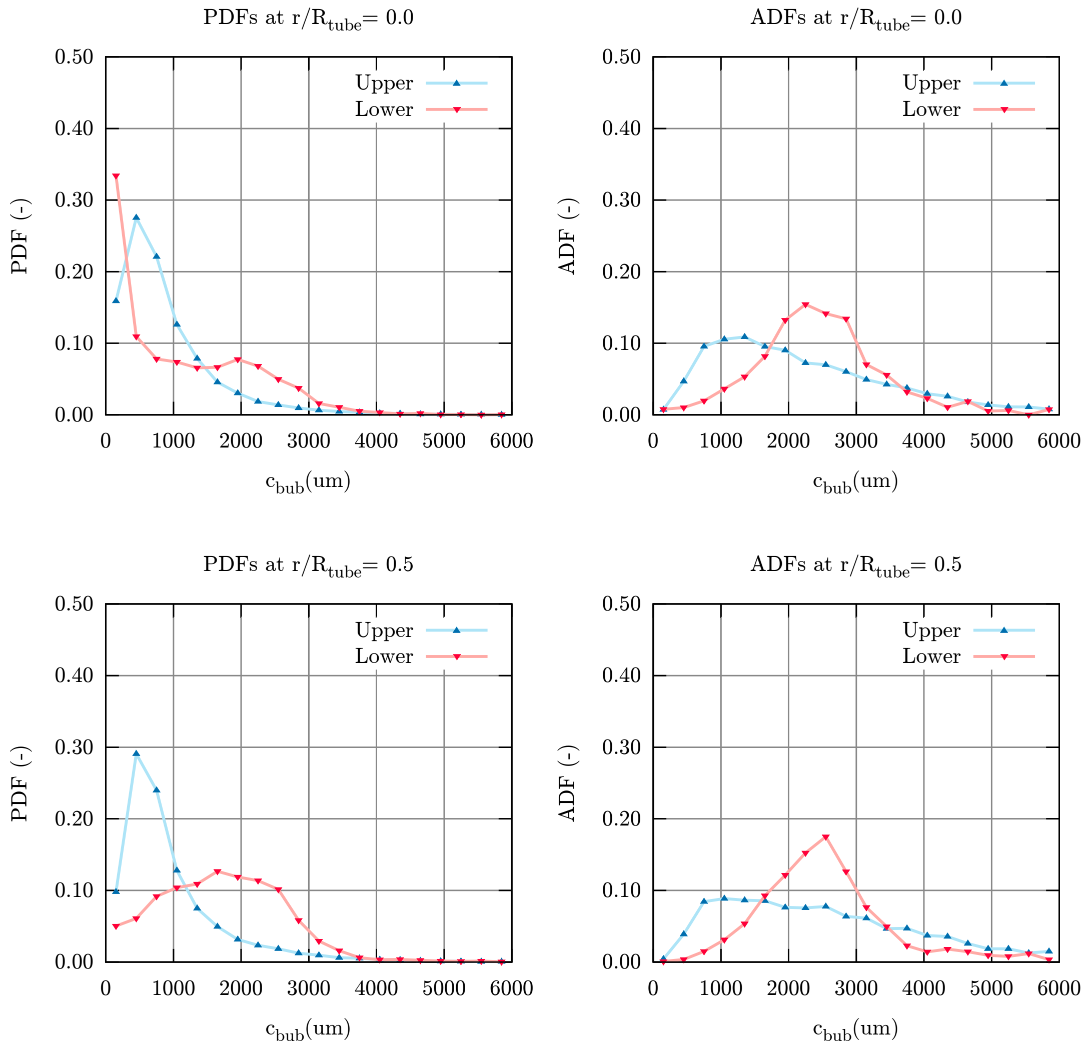

Figure 72: Size distribution functions for flow through an orifice of $\phi = 19.1\ mm$ at $j_f = 1.212\ m/s$. Distributions are sampled at $r/R_{tube} = 0.0$ (top) and $r/R_{tube} = 0.5$ (bottom).

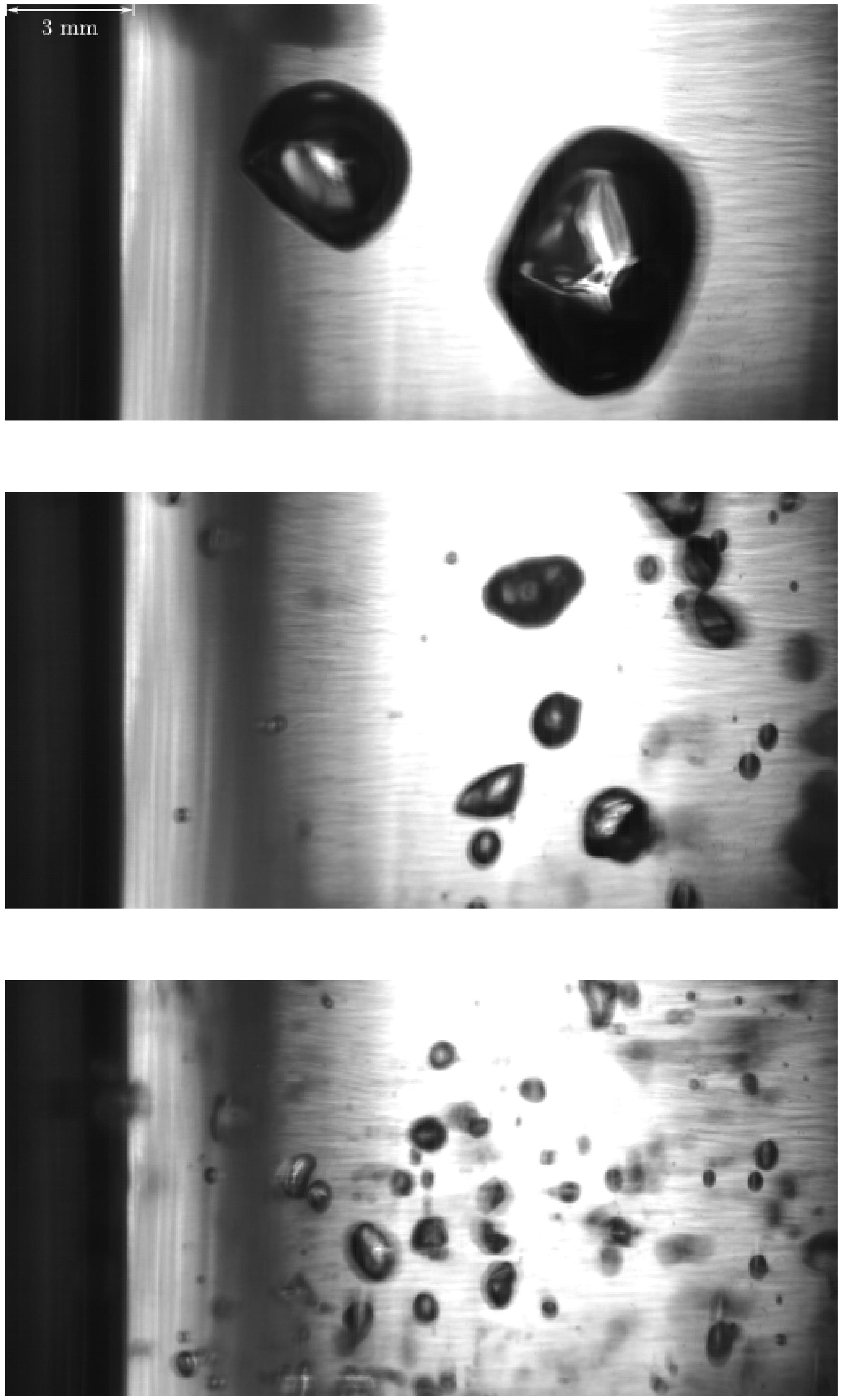

Figure 73: Sample frames where $\phi = 19.1\ mm$, $j_g = 0.0125\ m/s$, and $j_f = 0.191\ m/s$ (top), $j_f = 0.702\ m/s$, and $j_f = 1.212\ m/s$.

5.3.3.3 12.7 mm ID Orifice, Blockage Ratio = 0.84

Radial distributions of the d_{32}, α_g and a_i both upstream and downstream of the 12.7 mm orifice are plotted under liquid superficial velocities of j_f = 0.191, 0.702, and 1.212 m/s in figures 74, 76 and 78. Detailed PDFs and ADFs for these cases are plotted in figures 75, 77 and 79 at the centerline position ($r/R_{tube} = 0.0$) and halfway between the centerline and the wall ($r/R_{tube} = 0.5$). Sample frames from the runs are supplied in figure 80.

Owing to the much smaller ratio between the tube diameter and the orifice diameter ($R_{tube}/R_{orifice}$ = 6.25), the likelihood of fragmentation is expected to be substantially higher.

The PDFs in the j_f = 0.191 m/s case (figure 75) are very different from those measured in the 25.4 mm and 19.1 mm orifice diameter cases. No distinct peak occurs in the upper PDFs in the current measurements, but rather the entire curve is distributed across all diameters. This is interpreted to mean that when the bubbles are accelerated through the orifice they are stretched axially. However turbulence levels are inadequate to break apart many of the bubbles and so they exit the flow restriction highly deformed.

When the liquid flows are increased to j_f = 0.702 m/s and j_f = 1.212 m/s, the distinct peaks are restored in the PDFs (the PDFs (figures 77 and 79). However, the void fraction for these cases also appears to be grossly over measured. As the middle and bottom images of figure 80 show, there are very high densities of small bubbles downstream of the orifice. The increased number density is caused by a combination of the very high fragmentation probability and bubbles being stuck in a recirculation region near the outlet. The reported results in these cases are likely incorrect.

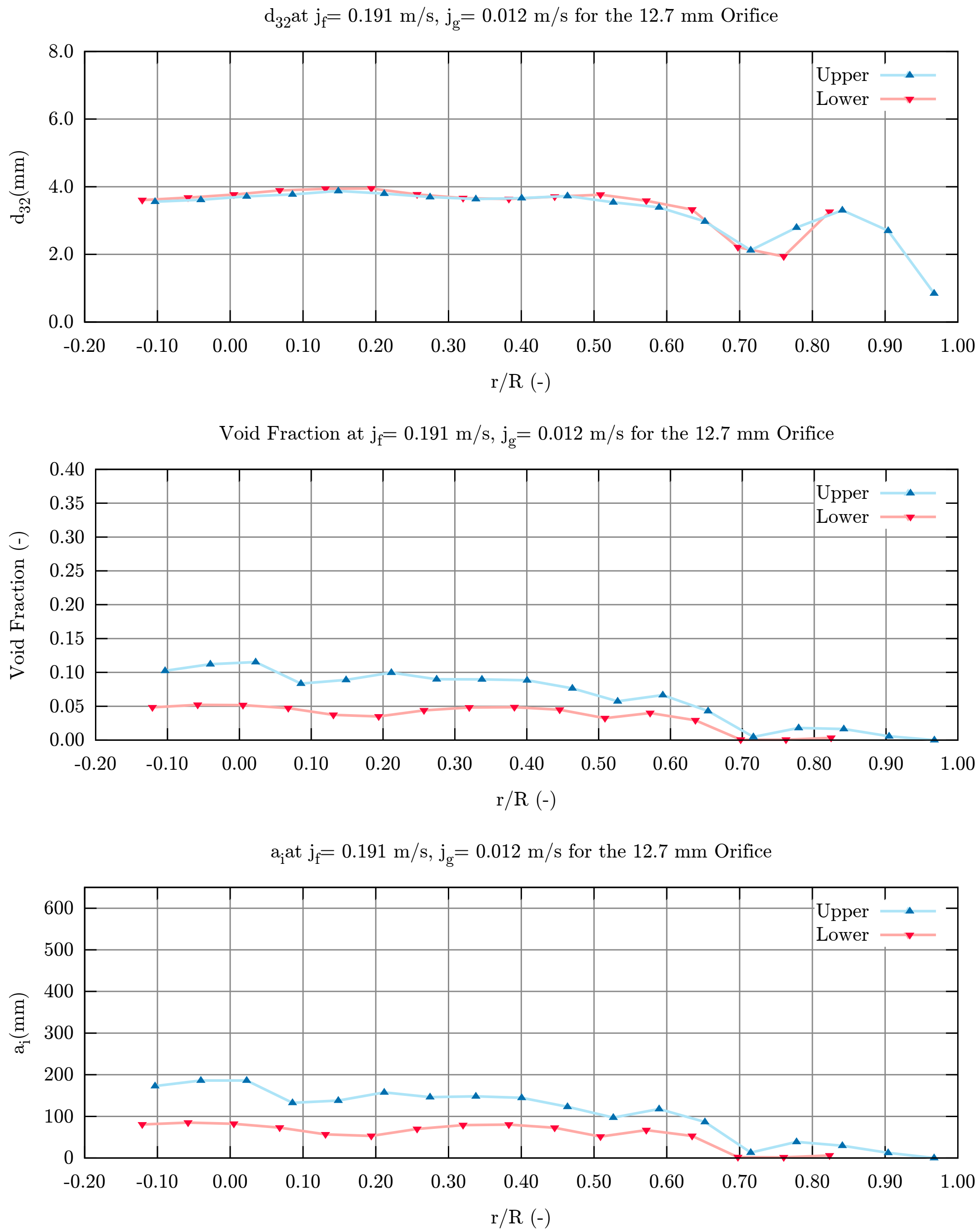

Figure 74: Radial Distribution for $\phi = 12.7\ mm$ at $j_f = 0.191\ m/s$.

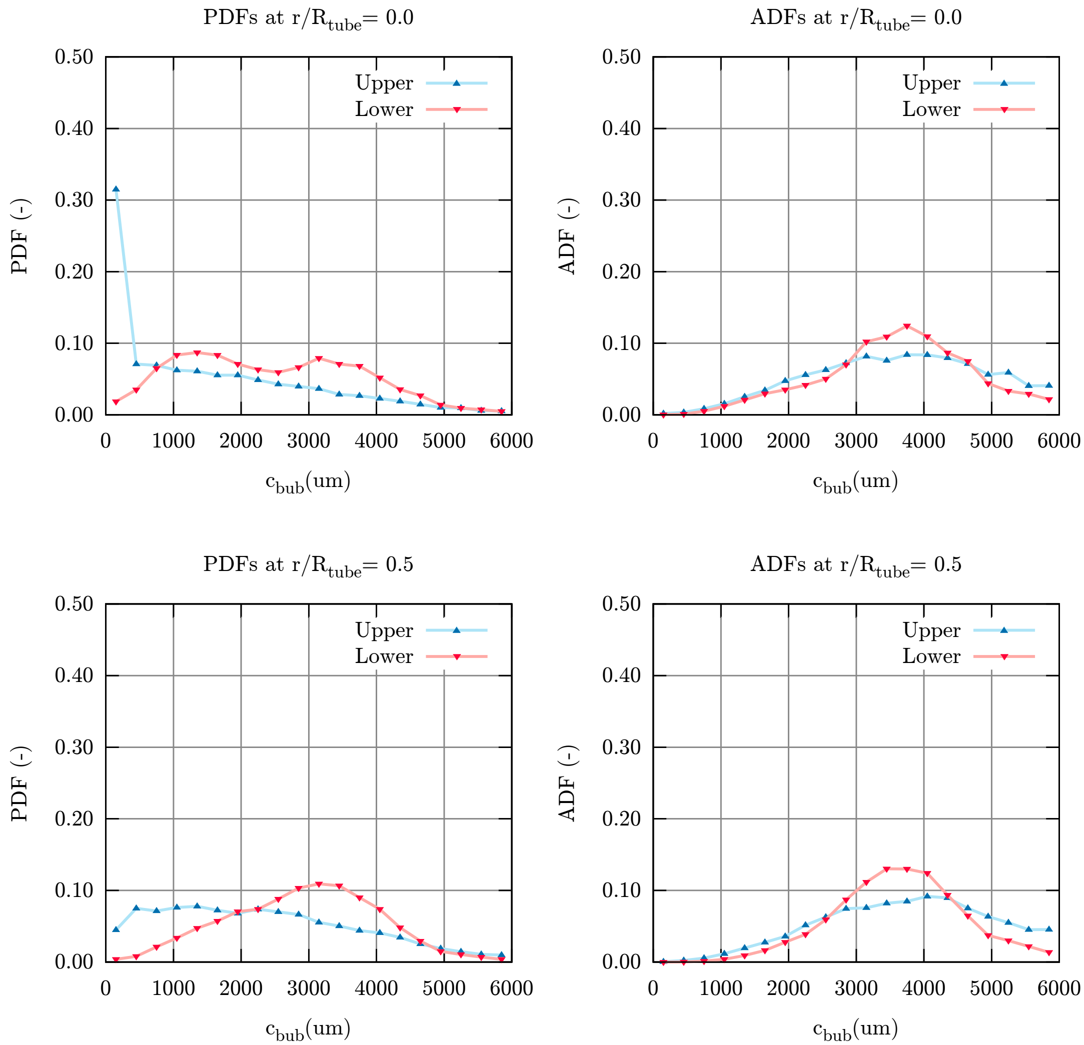

Figure 75: Size distribution functions for flow through an orifice of $\phi = 12.7\ mm$ at $j_f = 0.191\ m/s$. Distributions are sampled at $r/R_{tube} = 0.0$ (top) and $r/R_{tube} = 0.5$ (bottom).

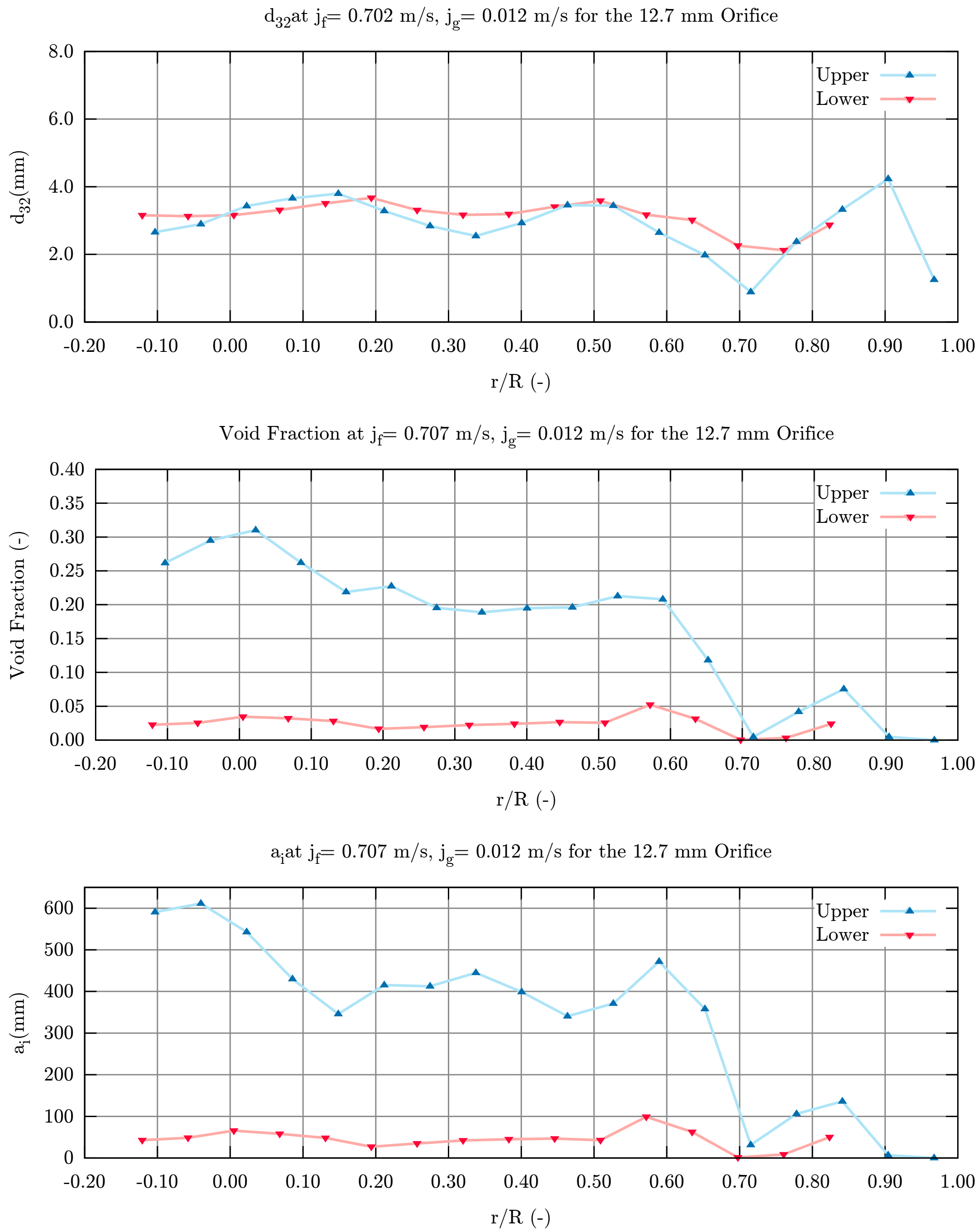

Figure 76: Radial Distribution for $\phi = 12.7\ mm$ at $j_f = 0.707\ m/s$.

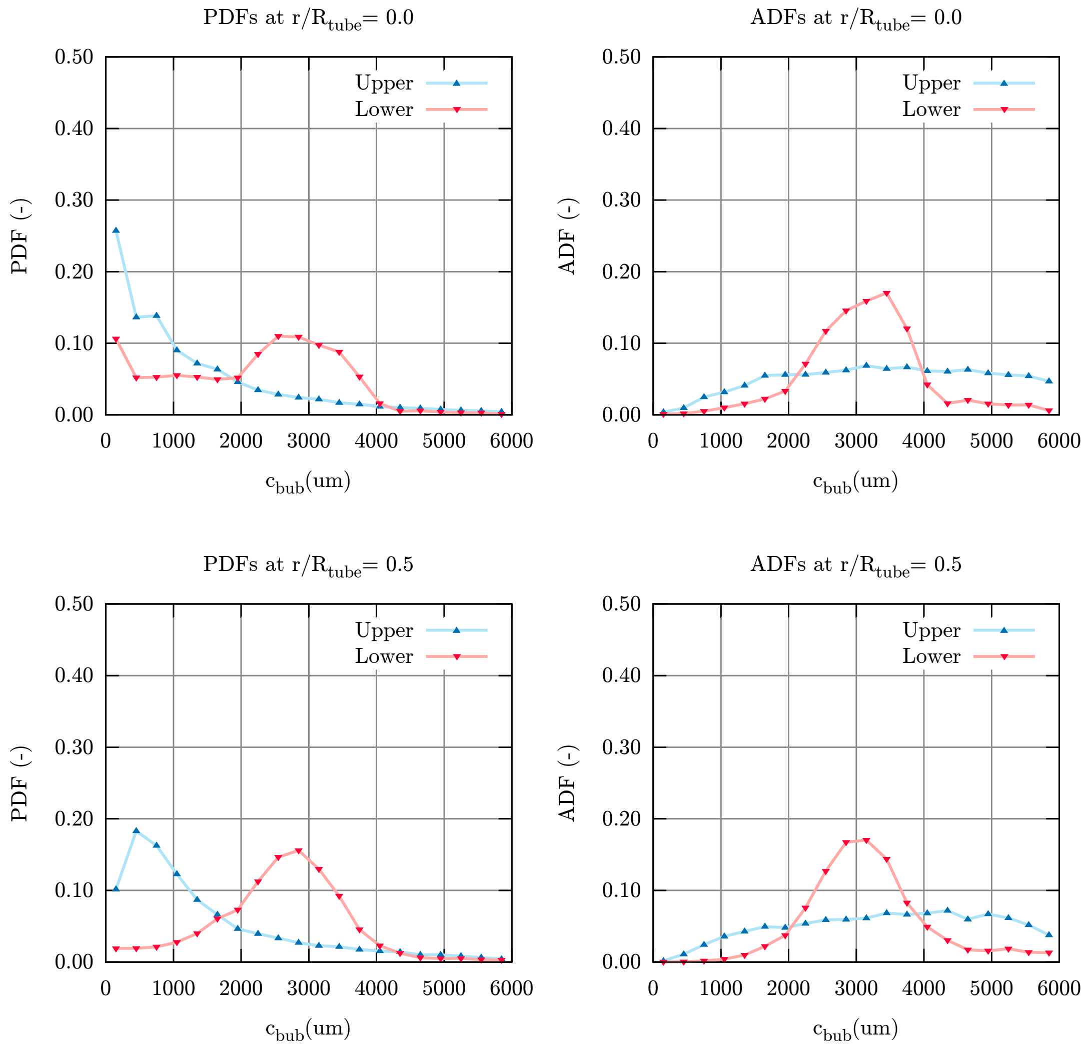

Figure 77: Size distribution functions for flow through an orifice of $\phi = 12.7\ mm$ at $j_f = 0.702\ m/s$. Distributions are sampled at $r/R_{tube} = 0.0$ (top) and $r/R_{tube} = 0.5$ (bottom).

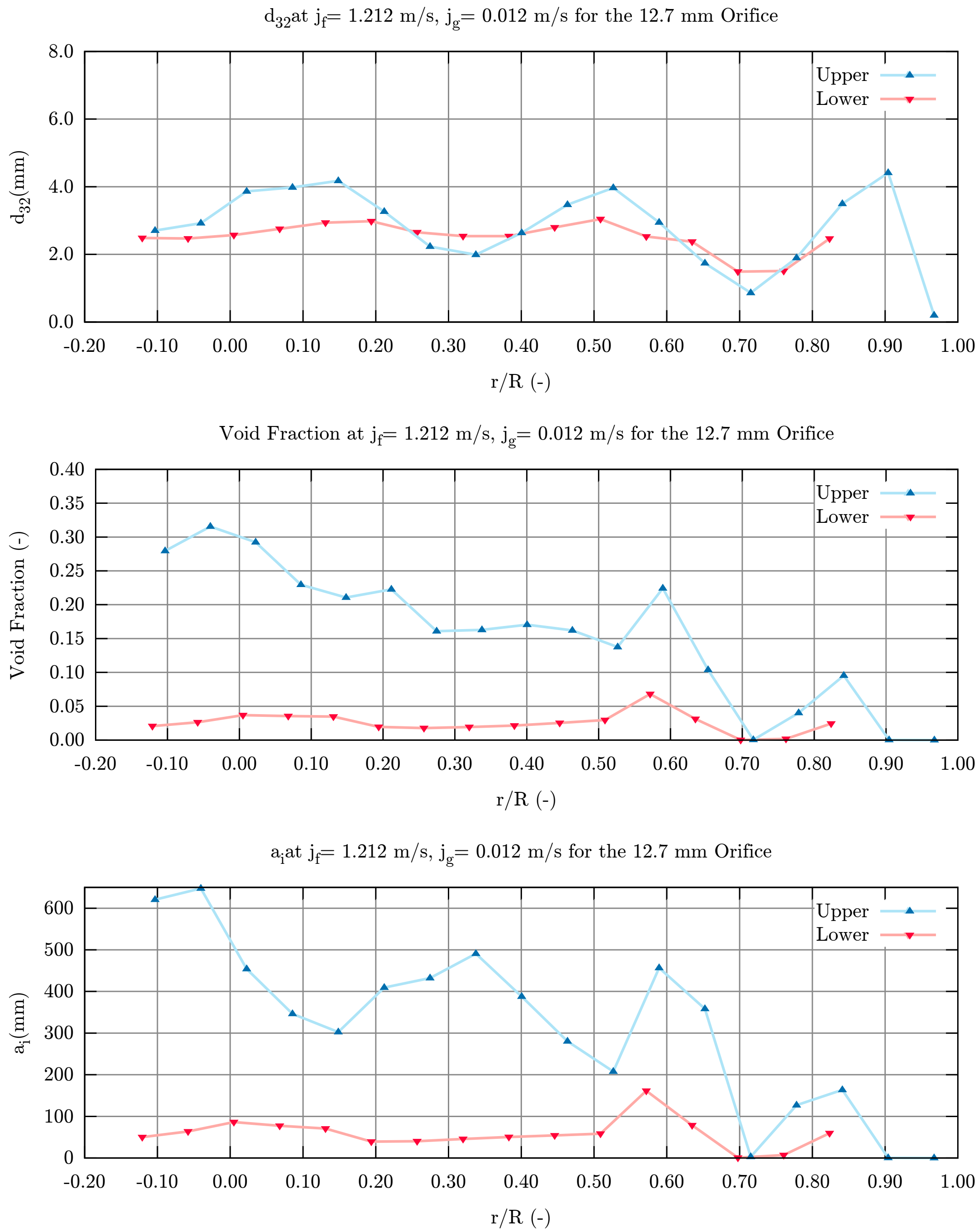

Figure 78: Radial Distribution for $\phi = 12.7\ mm$ at $j_f = 1.212\ m/s$.

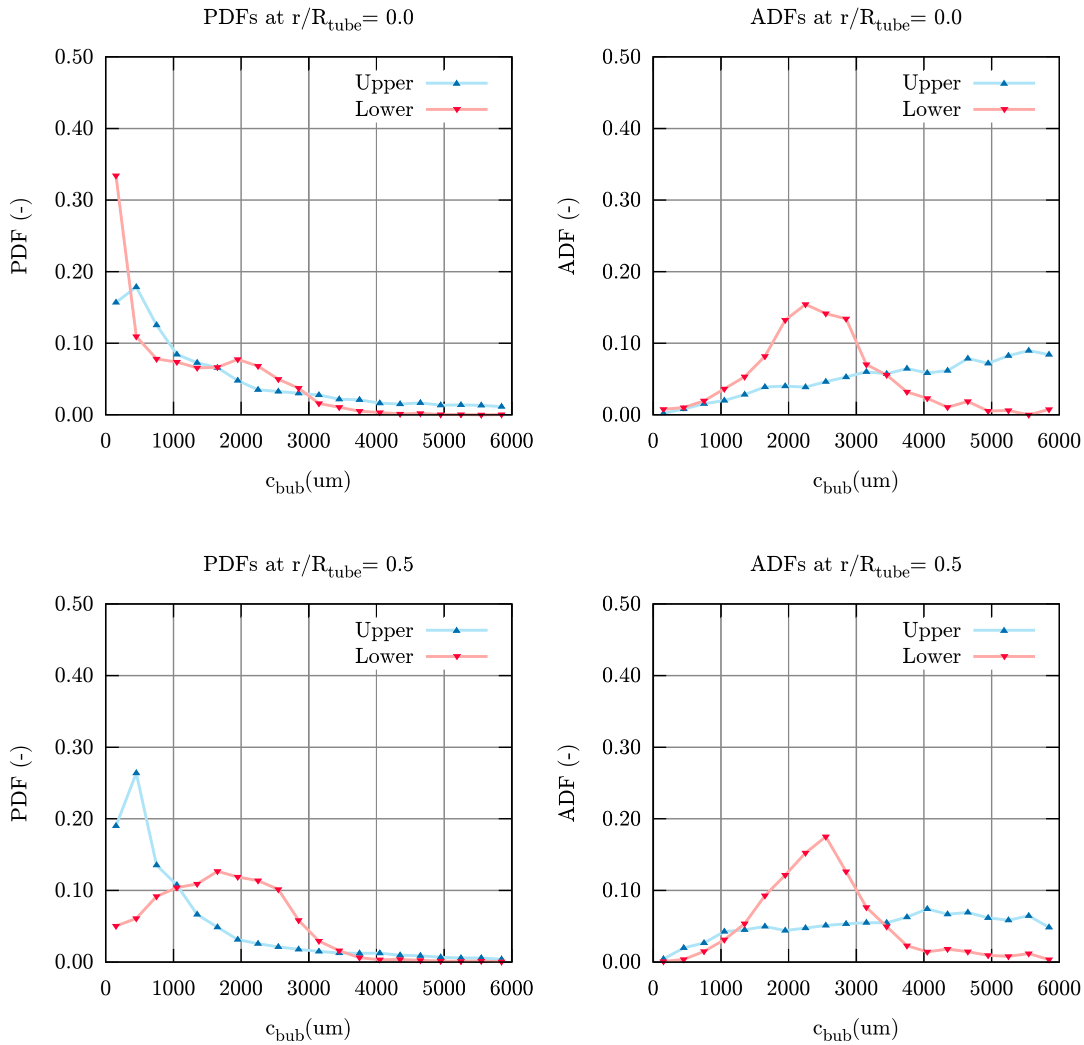

Figure 79: Size distribution functions for flow through an orifice of $\phi = 12.7\ mm$ at $j_f = 1.212\ m/s$. Distributions are sampled at $r/R_{tube} = 0.0$ (top) and $r/R_{tube} = 0.5$ (bottom).

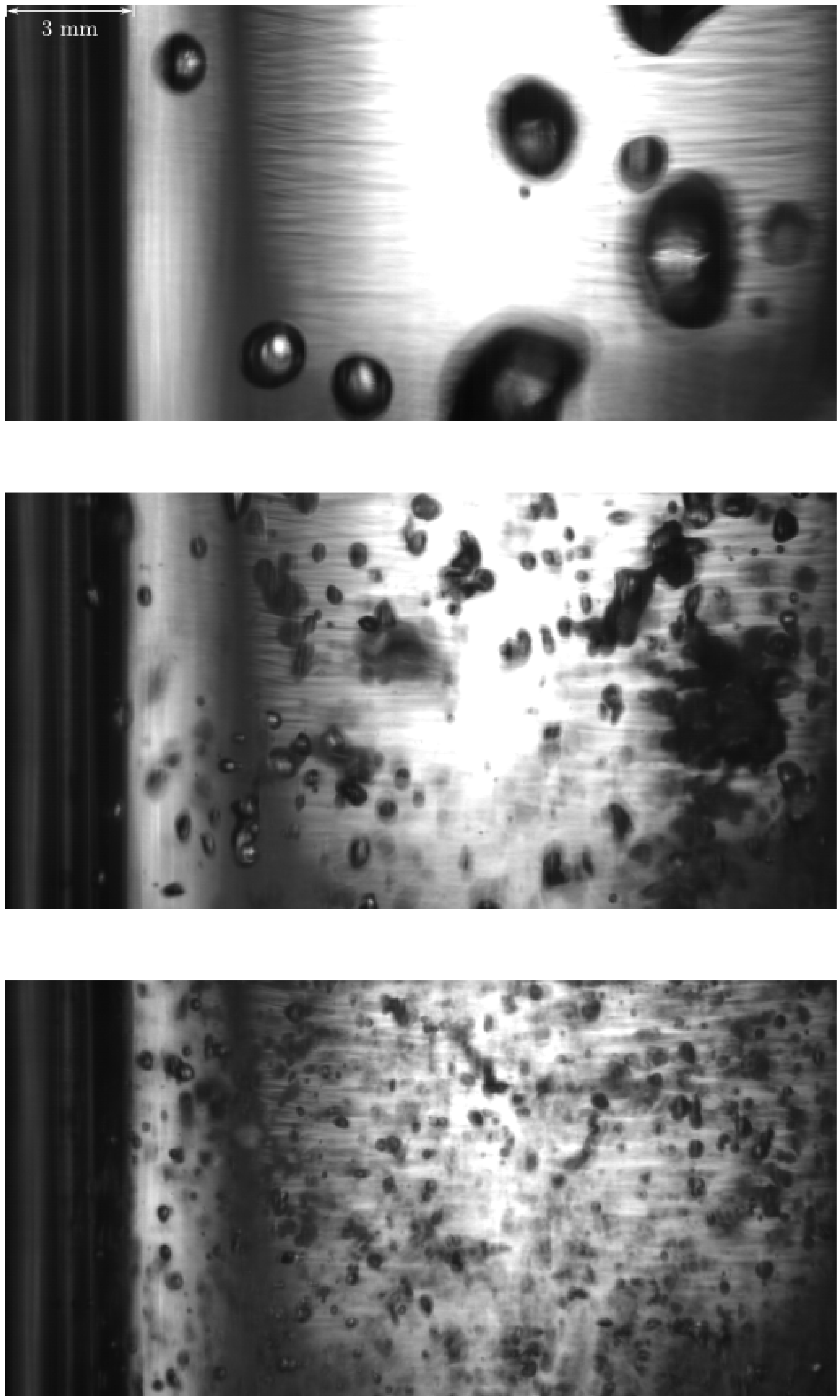

Figure 80: Sample frames where $\phi = 12.7\ mm$, $j_g = 0.0125\ m/s$, and $j_f = 0.191\ m/s$ (top), $j_f = 0.702\ m/s$, and $j_f = 1.212\ m/s$.

5.3.4 Discussion and Summary

When bubbles are forced through the orifice, up to four effects may be simultaneously occuring. These are summarized as:

1. The reduction of the flow area causes the bubbles to concentrate in a region near the centerline of the test section. This increases the local void fraction, and subsequently increases the local interfacial area concentration. Even after the flow has discharged from the orifice for $2 - 3d_{hyd}$, none of the bubbles have migrated back out towards the walls (i.e. they are entrained in the jet).
2. The increase in fragmentation rate will cause the bubbles to break up - in some cases into many smaller bubbles. This causes a decrease in the Sauter mean diameter, which in turn causes the a_i to increase. This effect is more pronounced as j_f increased or the diameter of the orifice decreased.
3. The increase in the number density of bubbles in the flow restriction causes the likelihood of coalesence to increase. This increases the Sauter mean diameter of the bubble population, which causes a decrease in the a_i. This was observed to occur in the low j_f cases when the reduction in flow area was small (e.g. the $\phi = 25.4\ mm$ case).
4. The change in the aspect ratio of the bubbles (they become stretched in the direction of the flow) causes the reported chord lengths to increase. This increases the d_{32} which causes a decrease in the a_i (again observed primarily in the $\phi = 25.4\ mm$ case).

Additionally, from the ADF plots, it is evident that in $\phi = 25.4\ mm$ cases, the smaller bubbles ($c < 1000\ \mu m$) generally do not contribute significantly to the interfacial area, even at the highest flow rate tested. Some fragmentation does take place, however many of the larger bubbles survive the passage through the orifice and are not broken up completely. As a result, while there are a number of these smaller bubbles in the flow, their interfacial area contribution is relatively insignificant.

Under the same flow conditions, reducing the diameter of the orifice increases the efficiency of the fragmentation. This causes more of the large bubbles to be broken up. Since fewer large bubbles survive, the relative contribution to the interfacial area by the smaller bubbles increases.

Conclusions

6.1 Summary

The overarching goal of the current work was to examine how blockages in an air-water flow affect the interfacial area. To accomplish this, a brand new test facility was designed, procured, constructed and instrumented. Flow conditions were carefully selected in order to keep the number density of the bubbles in the flow relatively low to prevent coalescence. Superficial liquid velocities of between $0.191\ m/s \leq j_f \leq 1.212\ m/s$ were examined in a round vertical tube with an inner diameter of $\phi = 31.75\ mm$. Air was supplied at superficial velocities of $0.0019\ m/s \leq j_g \leq 0.0373\ m/s$ through a $\phi = 0.5\ mm$ needle. Flow obstructions consisted of a 19.1 mm long circular orifice with blockage ratios of 0.36, 0.64, and 0.84.

Void fractions of $0.005 \leq \alpha_g \leq 0.080$ were examined. The low void fraction conditions of the test allowed for high speed video to be used to observe the bubbles breaking up in the orifice. Additionally, a large set of digital images taken at ultra high shutter speeds (363 ns) and at spatial resolutions of 0.02 mm were acquired and analyzed to supply quantitative measurements. A suite of image processing tools was developed in order to extract the void fraction and bubble size information, and to take advantage of modern parallel processing tools.

While photographic / image processing techniques are limited in the conditions which they may be used in (i.e. bubbles overlapping is a problem at higher void fractions), they are used extensively to validate meausrements made by the other techniques [31, 37, 45, 55]. Furthermore, data on bubble properties such as their aspect ratios may be collected - something which is not possible with the other techniques. Additionally this technique is non-intrusive.

6.2 Conclusions

6.2.1 Fragmentation Mechanisms

In the current work, bubble fragmentation was observed to occur due to either shearing or turbulence. Shearing was observed to occur at low flow rates and resulted in the parent bubble being split into two similarly sized daughter particles. This class of events was observed to occur over time scales of $t \approx 10 - 20\ ms$ under the conditions investigated. When the flow rate was increased, turbulent fragmentation was observed to occur in the orifice, and this was characterized by multiple smaller daughter particles being pulled off of the larger bubble. Under this scenario, the original 'parent bubble' survives, and a large numberof bubbles with $d < 1000\ \mu m$, are created. The time scales for this breakup mechanism were observed to be on the order of $t \approx 1 - 2\ ms$. Both types of observed fragmentation were consistent with descriptions reported in literature.

A unique case of breakup was also observed which is specific to the geometry in the current work, and does not appear to have been previously reported in literature. Occasionally, bubbles in the test section were observed to be entrained in the reciruclation zone downstream of the leading edge of the orifice. When this occured the bubbles were continually bombarded by turbulent eddies, and undergo multiple successive turbulent fragmentation events. The result of this process is the complete destruction of the parent bubble into smaller ($d < 1000\ \mu m$) daughter bubbles. It is postulated that the region in the orifice where this mechanism is most likely to occur is anywhere outside of the *vena contracta*, with the location of this recirculating region being commonly estimated as $0.64 < r/R_{orifice} < 1.00$ (and having been verified by LDA measurements). Furthermore since it is possible for this fragmentation mechanism to occur along the trailing edges of other types of obstructions such as mixing vanes or end plates, additional study with relevant geometries would be invaluable.

6.2.2 Bubble Characteristics

Upstream of any flow blockages, the median bubble chord diameter was found to be highly sensitive to the superficial gas velocity for low values of j_g. For velocities of $j_g > 0.0125$ m/s, the distribution medians were relatively stable. The measured chord size distributions exhibited a single peak for values of $j_f < 0.447$ m/s which corresponded to a bulk Reynolds number of $Re \approx 16,000$. Increasing the liquid flow rate above this threshold caused bubble fragmentation to begin occuring due to turbulence, and a secondary peak in the $d < 1000$ μm range formed. The bimodal distribution was determined to represent populations of both parent bubbles and their fragments. This type of distribution is not reported in interfacial area studies due to the physical limitations of the measurement techniques used, and represents a contribution to knowledge.

Aspect ratio measurements were conducted both upstream and downstream of the orifice. At low j_f, the upstream measurements indicated that the bubbles were shaped like oblate ellipsoids with a mean aspect ratio of $\overline{AR} \approx 1.2$ when the major axis was larger than 3 mm. Increasing the liquid flow rate to $j_f = 0.702$ m/s, beyond the onset of turbulent fragmentation, reduced the overall size of the bubbles, and decreased the mean aspect ratio to $\overline{AR} \approx 0.99$, and reduced the scatter of the data from $\sigma_{AR} = 0.301$ when $j_f = 0.191$ m/s, to $\sigma_{AR} = 0.254$. This is interpreted to mean that approximating the bubbles as spheres is valid at higher values of j_f.

Additional work was conducted evaluating the bubble shape before and after passing through the different orifice diameters. The study found that at low liquid superficial velocities ($j_f = 0.191$ m/s) when fragmentation was not taking place, after passing through the $\phi = 25.4$ mm orifice, the mean size of the bubbles increased (as compared to the upstream measurements). This suggested that the reduction in flow area served to concentrate the bubble number density and enhance the coalesence mechanism. Under the same flow rate, when the diameter of the orifice was decreased, the local fluid velocities increased and turbulent fragmentation started to become the dominant mechanism, breaking up the bubble population as demonstrated by the reduction of the mean aspect ratio. While several studies on the shape of bubbles have been previously conducted for stagnant columns, few have been conducted on vertical cocurrent flows. No studies on bubble shape after passing through a flow blockage have been located, and thus the work in this section represents a further additional to the knowledge base.

The relationship between the bubble chord lengths and their diameters was also examined using a geometric transform. In normal bubble distributions as low flow rates ($j_f = 0.191\ m/s$), the mean chord lenght was calculated to be about 15% smaller than the calculated diameter of the bubbles. However, the accuracy of this transform was reduced once the bubble population began to fragment creating a bimodal distribution of chords. While the use of this technique itself is not novel, its application in conjunction with visually obtained data offers insight into its validity which has not previously been addressed in literature. Specifically, Kalkach-Navarro [34] applied a similar transform to bubble chord size data obtained using electrical conductivity probes. In the current work it has been demonstrated that the use of the transform becomes increasingly inaccurate as the fluid velocity increases.

6.2.3 Interfacial Area

One of the major facets of the current work is the large scale acqusition of bubble size and shape distribution data - something which is not commonly found in literature. The selection of the lensing (and the ultra fast shutter speed) also allowed bubble size information to be reported at much higher spatial resolutions than typically found in literature. The measurement of size and shape information for the very small daughter bubbles ($d < 1000\ \mu m$) created due to some form of turbulent fragmentation represents a significant contribution to knowledge. Due to physical limitations, advanced interfacial area measurement techniques such as 4-point conductivity probes and wire-mesh sensors cannot measure bubbles smaller than about 1 mm and 2 mm respectively [42, 54]. The current work has demonstrated that fragmentation - especially after passing through and orifice - creates significant bubble populations smaller than these limits, and they may in fact contribute significantly to the interfacial area.

In the test cases at higher liquid flow rates, large peaks in the chord size distribution were observed in the smaller size bins. These bubbles were determined to be daughter bubbles caused by the fragmentation of a larger structure. Area distribution functions were derived to determine whether these small bubbles were making a significant contribution to the interfacial area. The data from these distributions found that in some cases even while bubbles smaller than 1.0 mm made up over 50% of the population, their contribution to the interfacial area was less than 10%. The majority of the interfacial area in each population still comes from the larger bubbles. However, when the fragmentation was thorough (i.e. when few large bubbles survived) the contribution of the small bubbles became significant. It is postulated that this effect plays a major role when the entrainment-turbulent fragmentation mechanism occurs, such as in flow geometries where a flow obstruction is present.

6.3 Future Work

- While the chord distribution method provided some insight into the interfacial area change through the orifice, it is still only an approximation. Using the aspect ratio measurement algorithm could provide more accurate data - however its inability to distinguish between smaller bubbles and noise is its major drawback, especially in a fragmentation study. A natural extension of the current work would be to improve the algorithm to allow for smaller bubbles.

- If the aspect ratio tracking algorithm could be improved to detect the smaller bubbles, it would be of tremendous benefit to apply it to the images captured of the bubbles breaking up in the orifice. Such work would significantly improve the current understanding of the fragmentation process. Alternatively, a lens with a higher magnification power could be employed.

- The non-uniform background lighting intensity across the image also restricted the area where both the bubble chord sizes and the aspect ratio could be sampled. This may be fixed by using both a larger array of lighting or conducting future experiments in ducts rather than tubes.

- The current work focused on orifices where the area change was significant. Since little to no existing literature on the topic was found, this design descision was made to ensure that the bubbles would break up due to the blockage. With the facility constructed and groundwork laid, the next logical step in this line of study would be to examine geometries which are relevant to fuel channel components (e.g. end plates, bearing pads, bundle misalignment, mixing vanes or spacer grids).

- Horizontal flow configurations should also be explored since it introduces a degree of asymmetry due to either flow stratification or buoyancy effects. Such an arrangement would be of particular interest to studies involving reactors with horizontal fuel channels.

Bibliography

[1] M. Ishii, "Development of interfacial area transport equation - modeling and experimental benchmark," in *Proc. of the* 14^{th} *Int. Top. Meeting on Nuclear Reactor Thermal Hydraulics*, 2011.

[2] G. Kocamustafaogullari and M. Ishii, "Foundation of the interfacial area transport equation and its closure relations," *Int. J. Heat Mass Transfer*, vol. 38, no. 3, pp. 481–493, 1995.

[3] E. Krepper, D. Lucas, T. Frank, H.-M. Prasser, and P. J. Zwart, "The inhomogeneous MUSIG model for the simulation of polydispersed flows," *Nuc. Eng. Des.*, vol. 7, pp. 1690–1702, 2008.

[4] E. Krepper, T. Frank, D. Lucas, H.-M. Prasser, and P. J. Zwart, "Inhomogeneous MUSIG model - a population balance approach for polydispersed bubbly flows," in *Proc. of the* 12^{th} *Int. Top. Meeting on Nuclear Reactor Thermal Hydraulics*, 2007.

[5] M. Ishii and T. Hibiki, *Thermo-Fluid Dynamics of Two-Phase Flow.* Springer Link New York, second ed., 2011.

[6] M. Ishii, S. Kim, and J. Uhle, "Interfacial area transport equation: model development and benchmark experiments," *Int. J. of Heat and Mass Transfer*, vol. 45, no. 15, pp. 3111–3123, 2002.

[7] P. Emonot, A. Souyri, J. L. Gandrille, and F. Barre, "CATHARE-3: A new system code for thermal-hydraulics in the context of the NEPTUNE project," *Nuc. Eng. Des.*, vol. 241, no. 11, pp. 4476–4481, 2011.

[8] Idaho National Laboratory, Idaho Falls, USA, *RELAP5-3D©Code Manual Volume IV: Models and Correlations*, 2.4 ed., June 2005.

[9] U.S. Nuclear Regulatory Commission, Washington, DC, USA, *TRACE V5.0 Theory Manual*, draft ed.

[10] Atomic Energy of Canada Limited, Mississauga, Canada, *ASSERT-PV IST V3R1:Software Theory Manual*, r0 ed., January 2007.

[11] J. D. Talley, S. Kim, J. Mahaffy, S. M. Bajorek, and K. Tien, "Implementation and evaluation of one-group interfacial area transport equation in TRACE," *Nuc. Eng. Des.*, vol. 241, no. 3, pp. 865–873, 2011.

[12] J. D. Talley, T. Worosz, S. Kim, S. M. Bajorek, and K. Tien, "Effect of bubble interactions on the prediction of interfacial area in TRACE," *Nuc. Eng. Des.*, vol. 264, no. 1, pp. 135–145, 2013.

[13] X. Yang, J. P. Schlegel, S. Paranjape, Y. Liu, S. W. Chen, T. Hibiki, and M. Ishii, "Interfacial area transport in two-phase flows in a scaled 8 × 8 rod bundle geometry at elevated pressures," in *Proc. of the* 14^{th} *Int. Top. Meeting on Nuclear Reactor Thermal Hydraulics*, 2011.

[14] Q. Wu, S. Kim, M. Ishii, and S. G. Beus, "One-group interfacial area transport in vertical bubbly flow," *Int. J. Heat Mass Transfer*, vol. 41, no. 8–9, pp. 1103–1112, 1998.

[15] T. Hibiki and M. Ishii, "Two-group interfacial area transport equations at bubbly-to-slug flow transistion," *Nuc. Eng. Des.*, vol. 202, no. 1, pp. 39–76, 2000.

[16] M. Ishii and S. Kim, "Development of one-group and two-group interfacial area transport equation," *Nucl. Science and Eng.*, vol. 146, no. 3, pp. 257–273, 2004.

[17] M. Ishii, S. Kim, and J. Kelly, "Development of interfacial area transport equation," *Nuc. Eng. Tech.*, vol. 37, no. 6, pp. 525–536, 2005.

[18] T. Hibiki, T. H. Lee, J. Y. Lee, and M. Ishii, "Interfacial area concentration in boiling bubbly flow systems," *Chem. Eng. Sci.*, vol. 61, no. 24, pp. 7979–7990, 2006.

[19] G. I. Taylor, "The formation of emulsions in definable fields," *Proc. R. Soc. Lond.*

A, vol. 146, no. 858, pp. 501–523, 1934.

[20] J. O. Hinze, “Fundamentals of the hydrodynamic mechanism of splitting in dispersion processes,” *AIChE J.*, vol. 1, no. 3, pp. 289–295, 1955.

[21] N. I. Kolev, “Fragmentation and coalescence dynamics in multiphase flows,” *Exp. Thermal and Fluid Sci.*, vol. 6, no. 3, pp. 211–251, 1993.

[22] H. Luo and H. F. Svendsen, “Theoretical model for drop and bubble breakup in turbulent dispersions,” *AIChE J.*, vol. 42, no. 5, pp. 1225–1233, 1996.

[23] C. Martínez-Bazán, J. L. Montañés, and J. C. Lasheras, “On the breakup of an air bubble injected into a fully developed turbulent flow. Part 1. Breakup frequency,” *J. Fluid Mech.*, vol. 401, pp. 157–182, 1999.

[24] C. Martínez-Bazán, J. L. Montañés, and J. C. Lasheras, “On the breakup of an air bubble injected into a fully developed turbulent flow. Part 2. Size PDF of the resulting daughter bubbles,” *J. Fluid Mech.*, vol. 401, pp. 183–207, 1999.

[25] G. K. Batchelor, *The Theory of Homogeneous Turbulence*. Cambridge University Press, second ed., 1959.

[26] M. J. Prince and H. W. Blanch, “Bubble coalescence and break-up in air-sparge bubble columns,” *AIChE J.*, vol. 36, no. 10, pp. 1485–1499, 1990.

[27] F. Risso and J. Fabre, “Oscillations and breakup of a bubble immersed in a turbulent field,” *J. Fluid Mech.*, vol. 372, pp. 323–355, 1998.

[28] M. A. Delichatsios, “Model for the breakup rate of spherical drops in isotropic turbulent flows,” *Phys. Fluids*, vol. 18, pp. 622–623, 1975.

[29] H. A. Stone and L. G. Leal, “The influence of initial deformation on drop breakup in subcritical time-dependent flows at low Reynolds numbers,” *J. Fluid Mech.*, vol. 206, pp. 223–263, 1989.

[30] H. A. Stone, “Dynamics of drop deformation and breakup in viscous fluids,” *Annu. Rev. Fluid Mech*, vol. 26, pp. 65–102, 1994.

[31] Z. Dongjian, G. Liejin, L. Changzhi, and Z. Ximin, “An experimental study on local interfacial area concentration using a double-sensor probe,” *Int. J. of Heat and Mass Transfer*, vol. 48, no. 10, pp. 1926–1935, 2005.

[32] I. Kataoka, M. Ishii, and A. Serizawa, "Local formulation of measurements of interfacial area concentration in two-phase flow," *Int. J. Multiphase Flow*, vol. 12, no. 4, pp. 505–529, 1986.

[33] S. T. Revankar and M. Ishii, "Local interfacial area measurement in bubbly flow," *Int. J. Heat Mass Transfer*, vol. 35, no. 4, pp. 913–925, 1992.

[34] S. Kalkach-Navarro, R. T. L. Jr., D. A. Drew, and R. Meyder, "Interfacial area density, mean radius and number density measurements in bubbly two-phase flow," *Nuc. Eng. Des*, vol. 142, no. 2–3, pp. 341–351, 1993.

[35] Q. Wu and M. Ishii, "Sensitivity study on double-sensor conductivity probe for the measurement of interfacial area concentration in bubbly flow," *Int. J. Multiphase Flow*, vol. 25, no. 1, pp. 155–173, 1999.

[36] T. Hibiki, H. Hogsett, and M. Ishii, "Local measurement of interfacial area, interfacial velocity and liquid turbulence in two-phase flow," *Nuc. Eng. Des.*, vol. 184, no. 2–3, pp. 287–304, 1998.

[37] T. Hibiki and M. Ishii, "Experimental study on interfacial area transport in bubbly two-phase flows," *Int. J. of Heat and Mass Transfer*, vol. 42, no. 16, pp. 3019–3035, 1999.

[38] I. Kataoka and A. Serizawa, "Interfacial area concentration in bubbly flow," *Nuc. Eng. Des.*, vol. 120, no. 2–3, pp. 163–180, 1990.

[39] I. Kataoka, M. Ishii, and A. Serizawa, "Sensitivity analysis of bubble size and probe geometry on the measurements of interfacial area concentration in gas-liquid two-phase flow," *Nuc. Eng. Des.*, vol. 146, no. 1–3, pp. 53–70, 1994.

[40] M. Ishii and S. Kim, "Micro four-sensor probe measurement of interfacial area transport for bubbly flow in round pipe," *Nuc. Eng. Des.*, vol. 205, no. 1–2, pp. 123–131, 2001.

[41] S. T. Revankar and M. Ishii, "Theory and measurement of local interfacial area using a four sensor probe in two–phase flow," *Int. J. Heat Mass Transfer*, vol. 36, no. 12, pp. 2997–3007, 1993.

[42] S. Kim, X. Y. Fu, X. Wang, and M. Ishii, "Development of the miniaturized four-sensor conductivity prove and the signal processing scheme," *Int. J. of Heat*

and Mass Transfer, vol. 43, no. 22, pp. 4101–4118, 2000.

[43] S. L. Kiambi, A. M. Duquenne, A. Bascoul, and H. Delmas, "Measurements of local interfacial area: application of bi-optical fibre technique," *Chem. Eng. Sci.*, vol. 56, no. 21, pp. 6447–6453, 2001.

[44] J.-M. L. Corre, E. Hervieu, M. Ishii, and J.-M. Delhaye, "Benchmarking and improvements of measurement techniques for local-time-averaged two-phase flow parameters," *Exp. in Fluids*, vol. 35, no. 5, pp. 448–458, 2003.

[45] S. Kim, M. Ishii, Q. Wu, D. McCreary, and S. G. Beus, "Interfacial structures of confined air-water two-phase bubbly flow," *Exp. Thermal and Fluid Sci.*, vol. 26, no. 5, pp. 461–472, 2002.

[46] G. J. Zhang and M. Ishii, "Isokinetic sampling probe and image processing system for droplet size measurement in two-phase flow," *Int. J. Heat Mass Transfer*, vol. 38, no. 11, pp. 2019–2027, 1995.

[47] E. Fantini, L. Tognotti, and A. Tonazzini, "Drop size distribution in sprays by image processing," *Computers Chem Engng*, vol. 14, no. 211, pages =, 1990.

[48] T. Takamasa, T. Goto, T. Hibiki, and M. Ishii, "Experimental study of interfacial area transport of bubbly flow in small-diameter tube," *Int. J. of Multiphase Flow*, vol. 29, no. 3, pp. 395–409, 2003.

[49] T. Hibiki, T. Hazuku, T. Takamasa, and M. Ishii, "Some characteristics of developing bubbly flow in a vertical mini pipe," *Int. J. of Heat and Fluid Flow*, vol. 28, no. 5, pp. 1034–1048, 2007.

[50] T. Kato, Y. Takata, T. Hazuku, T. Takamasa, and T. Hibiki, "Gas-liquid interfacial configurations of developing bubbly flow in a mini pipe," in *Proc. of the* 13^{th} *Int. Top. Meeting on Nuclear Reactor Thermal Hydraulics*, 2009.

[51] J. L. Wegener and J. A. Drallmeier, "Measruement of thin liquid film characteristics using laser focus displacement instruments for atomization applications," in *Proc. of the* 22^{nd} *Annual Conference on Liquid Atomization and Spray Systems*, 2010.

[52] T. Takamasa and K. Kobayashi, "Measuring interfacial waves on film flowing down tube inner wall using laser focus displacement meter," *Int. J. of Multiphase*

Flow, vol. 26, no. 9, pp. 1493–1507, 2000.

[53] T. Hazuku, N. Fukamachi, T. Takamasa, T. Hibiki, and M. Ishii, "Measurement of liquid film in microchannels using a laser focus displacement meter," *Exp. in Fluids*, vol. 38, no. 6, pp. 780–788, 2005.

[54] H.-M. Prasser, A. Böttger, and J. Zschau, "A new electrode-mesh tomograph for gas-liquid flows," *Flow Measurement and Instrumentation*, vol. 9, no. 2, pp. 111–119, 1998.

[55] H.-M. Prasser, D. Scholz, and C. Zippe, "Bubble size measurement using wire-mesh sensors," *Flow Measurement and Instrumentation*, vol. 12, no. 4, pp. 299–312, 2001.

[56] H.-M. Prasser, M. Misawa, and I. Tiseanu, "Comparison between wire-mesh sensor and ultra-fast x-ray tomograph for an air-water flow in a vertical pipe," *Flow Measurement and Instrumentation*, vol. 16, no. 2–3, pp. 73–83, 2005.

[57] A. Manera, H.-M. Prasser, D. Lucas, and T. van der Hagen, "Three-dimensional flow pattern visualization and bubble size distributions in stationary and transient upward flashing flow," *Int J. Multiphase Flow*, vol. 32, no. 8, pp. 996–1016, 2006.

[58] A. Manera, B. Ozar, S. Paranjape, M. Ishii, and H.-M. Prasser, "Comparison between wire mesh sensors and conductive needle-probes for measurements of two-phase flow parameters," *Nuc. Eng. Des.*, vol. 239, no. 9, pp. 1718–1724, 2009.

[59] H.-M. Prasser, "Evolution of interfacial area concentration in a vertical air-water flow measured by wire-mesh sensors," *Nuc. Eng. Des.*, vol. 237, no. 15–17, pp. 1608–1617, 2007.

[60] D. Lucas, E. Krepper, and H.-M. Prasser, "Development of co-current air-water flow in a vertical pipe," *Int. J. Multiphase Flow*, vol. 31, no. 12, pp. 1304–1328, 2005.

[61] E. Krepper, D. Lucas, and H.-M. Prasser, "On the modelling of bubbly flow in vertical pipes," *Nuc. Eng. Des.*, vol. 5, pp. 597–611, 2005.

[62] D. Lucas, M. Beyer, L. Szalinski, and P. Schütz, "A new database on the evolution of air-water flows along a large vertical pipe," *Int. J. Thermal Sci.*, vol. 49, no. 4, pp. 664–674, 2010.

[63] T. Frank, H.-M. Prasser, M. Beyer, and S. A. Issa, "Gas-liquid flow around an obstacle in a vertical pipe - CFD simulation & comparison to experimental data," in *Proc. of the* 6^{th} *Int. Conf. on Multiphase Flow*, 2007.

[64] J. M. Delhaye and P. Bricard, "Interfacial area in bubbly flow: experimental data and correlations," *Nuc. Eng. Des.*, vol. 151, no. 1, pp. 65–77, 1994.

[65] A. Bandyopadhyay and M. N. Biswas, "Determination of interfacial area in a tapered bubble column," *J Chem. Technol. Biotechnol.*, vol. 86, no. 9, pp. 1211–1225, 2011.

[66] T. Hibiki and M. Ishii, "One-group interfacial area transport of bubbly flows in vertical round tubes," *Int. J. of Heat and Mass Transfer*, vol. 43, no. 15, pp. 2711–2726, 2000.

[67] I. Kataoka, "Development of research on interfacial area transport," *J. of Nuc. Sci. and Tech.*, vol. 47, no. 1, pp. 1–19, 2010.

[68] S. Hogsett and M. Ishii, "Local two-phase measurements using sensor techniques," *Nuc. Eng. Des.*, vol. 175, no. 1–2, pp. 15–24, 1997.

[69] M. D. Bartel, M. Ishii, T. Masukawa, Y. Mi, and R. Situ, "Interfacial area measurements in subcooled flow boiling," *Nuc. Eng. Des.*, vol. 210, no. 1–3, pp. 135–155, 2001.

[70] T. Hibiki, M. Ishii, and Z. Xiao, "Axial interfacial area transport of vertical bubbly flows," *Int. J. of Heat and Mass Transfer*, vol. 44, no. 10, pp. 1869–1888, 2001.

[71] R. Situ, T. Hibiki, X. Sun, Y. Mi, and M. Ishii, "Flow structure of subcooled boiling flow in an internally heated annulus," *Int J. of Heat and Mass Transfer*, vol. 47, no. 24, pp. 5351–5364, 2004.

[72] R. Situ, T. Hibiki, X. Sun, Y. Mi, and M. Ishii, "Axial development of subcooled boiling flow in an internally heated annulus," *Exp. in Fluids*, vol. 37, no. 4, pp. 589–603, 2004.

[73] B.-J. Yun, G.-C. Park, J. E. Julia, and T. Hibiki, "Flow structure of subcooled boiling water flow in a subchannel of 3 × 3 rod bundles," *J. of Nuc. Sci. and Tech.*, vol. 45, no. 5, pp. 402–422, 2008.

[74] K. Kondo, K. Ishiyama, G. Ishikawa, K. Y. an I. Kataoka, M. Naitoh, H. Okada, and T. Morii, "Distribution of void fraction and interfacial area concentration in developing region of vertical pipe," in *Proc. of the* 22^{nd} *Int. Symp. on Transport Phenomena*, 2011.

[75] S. Paranjape, M. Ishii, and T. Hibiki, "Modeling and measurement of interfacial area concentration in two-phase flow," *Nuc. Eng. Des.*, vol. 240, no. 9, pp. 2329–2337, 2010.

[76] B. Ozar, C. S. Brooks, T. Hibiki, and M. Ishii, "Interfacial area transport of steam-water two-phase flow in a vertical annulus at elevated pressures during sub-cooled boiling," in *Proc. of the* 14^{th} *Int. Top. Meeting on Nuclear Reactor Thermal Hydraulics*, 2011.

[77] J. P. Schlegel, S. Miwa, S. W. Chen, T. Hibiki, and M. Ishii, "Interfacial area transport equation evaluation methodology in large diameter pipes," in *Proc. of the* 14^{th} *Int. Top. Meeting on Nuclear Reactor Thermal Hydraulics*, 2011.

[78] T. Hazuku, T. Takamasa, T. Hibiki, and M. Ishii, "Interfacial area concentration in annular two-phase flow," *Int. J. of Heat and Mass Transfer*, vol. 50, no. 15–16, pp. 2986–2995, 2007.

[79] I. Michiyoshi and A. Serizawa, "Turbulence in two-phase bubbly flow," *Nuc. Eng. Des.*, vol. 95, no. 1, pp. 253–267, 1986.

[80] A. Tomiyama, H. Tamai, I. Zun, and S. Hosokawa, "Transverse migration of single bubbles in simple shear flows," *Chem. Eng. Sci.*, vol. 57, no. 11, pp. 1849–1858, 2002.

[81] E. Krepper, P. Ruyer, M. Beyer, D. Lucas, H.-M. Prasser, and N. Seiler, "Cfd simulation of polydispersed bubbly two-phase flow around an obstacle," *Sci. Tech. Nuc. Inst.*, vol. 2009, p. 12, 2009.

[82] TSI Incorporated, 500 Cardigan Road, Shoreview, MN 55126, USA, *TR/TM Series Fiberoptic Probes Owner's Manual*, second ed., November 2005.

[83] R. Fisher, S. Perkins, A. Walker, and E. Wolfart, "The hypermedia image processing reference." website, 2003. http://homepages.inf.ed.ac.uk/rbf/HIPR2/.

[84] S. Beucher, "Image segmentation and mathematical morphology." website, 2010. http://cmm.ensmp.fr/∼beucher/wtshed.html.

[85] ControlAir Inc., 8 Columbia Dr., Amherst, NH 03031, USA, *Type 300 Series Instrument Air Filter and Filter Regulators*, December 2006.

[86] E. J. Hukkanen and R. D. Braatz, "Measurement of particle size distribution in suspension polymerization using in situ laser backscattering," *Sensor Actuat B-Chem*, vol. 96, no. 1–2, pp. 451–459, 2003.

[87] A. Ruf, J. Worlitschek, and M. Mazzotti, "Modeling and experimental analysis of PSD measurments through FBRM," *Part. Part. Syst. Charact.*, vol. 17, no. 4, pp. 167–179, 2000.

[88] M. J. H. Simmons, P. A. Langston, and A. S. Burbidge, "Particle and droplet size analysis from chord distributions," *Powder Tech.*, vol. 102, no. 1, pp. 75–83, 1999.

[89] R. A. Herringe and M. R. Davis, "Structural development of gas-liquid mixture flows," *J. Fluid Mech.*, vol. 73, no. 1, pp. 97–123, 1976.

[90] M. Li and D. Wilkinson, "Determination of non-spherical particle size distribution from chord length measurements. Part 1: Theoretical analysis," *Chem. Eng. Sci.*, vol. 60, no. 12, pp. 3251–3265, 2005.

[91] N. N. Clark and R. Turton, "Chord length distributions related to bubble size distributions in multiphase flows," *Int. J. Multiphase Flow*, vol. 14, no. 4, pp. 413–424, 1988.

[92] P. V. Godbole, C. C. Tang, and A. J. Ghajar, "Comparisons of void fraction correlations for different flow patterns in upward vertical two-phase flow," *Heat Trans. Eng.*, vol. 32, no. 10, pp. 843–860, 2011.

[93] M. A. Woldesemayat and A. J. Ghajar, "Comparison of void fraction correlations for different flow patterns in horizontal and upward inclined pipes," *Int. J. Multiphase Flow*, vol. 33, no. 4, pp. 347–370, 2007.

[94] P. Coddington and R. Macian, "A study of the performance of void fraction

correlations used in the context of drift-flux two-phase flow models," *Nuc. Eng. Des.*, vol. 215, no. 3, pp. 199–216, 2002.

[95] Gilmont Instruments, 28W092 Commercial Avenue, Barrington, IL 60010, USA, *Gilmont Instruments Air Flow Meter Catalog.*

[96] T. J. Liu and S. G. Bankoff, "Structure of air-water bubbly flow in a vertical pipe – i. liquid mean velocity and turbulence measurements," *Int. J. Heat Mass Transfer*, vol. 36, no. 4, pp. 1049–1060, 1993.

Facility

A.1 Drawings

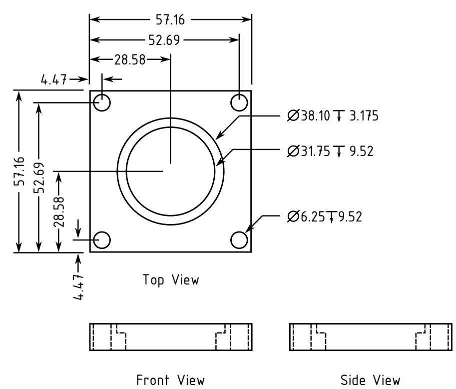

Figure 81: Dimensions of the flange pieces in the test section. All dimensions in mm.

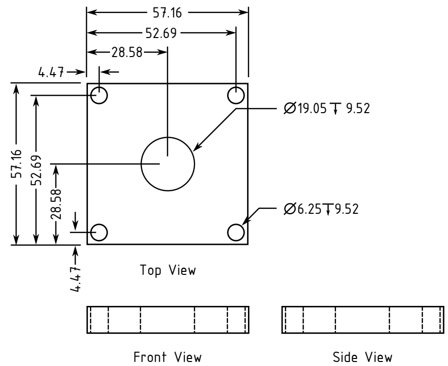

Figure 82: Dimensions of the orifice piece of the test section, $\phi = 19.05\ mm$ version. All dimensions in mm.

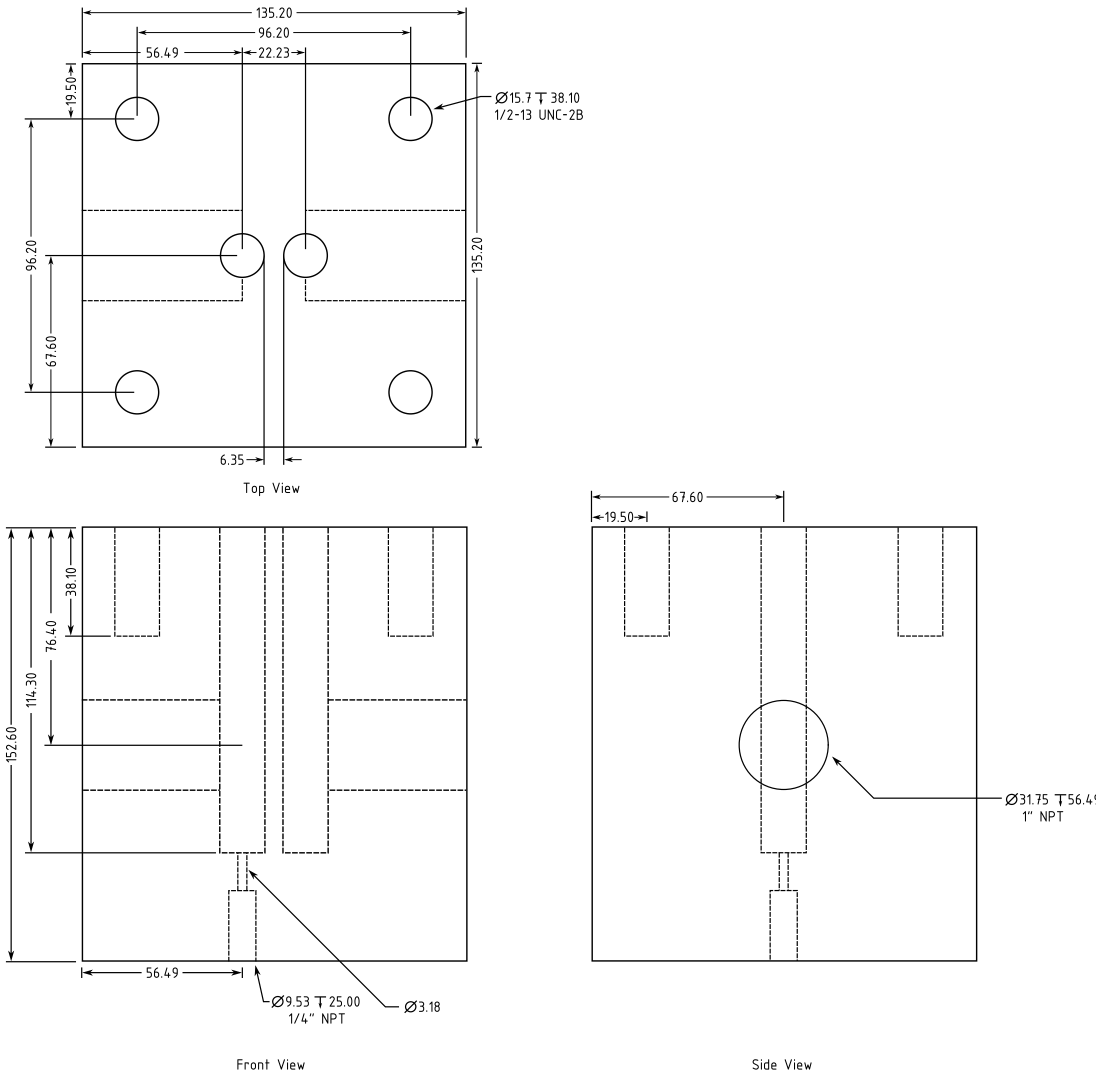

Figure 83: Inlet block drawing. All dimensions in mm.

A.2 Test Section Assembly

Each test section assembly consists of 4× flange pieces (figure 81), 2×53.5 *mm* lengths of 38.1 *mm* O.D., 31.75 *mm* I.D. acrylic tubing, and 1× orifice piece (figure 84). All seams are solvent welded. Alignment is done through bolt holes on each machined acrylic piece, and assembled according to figure 84.

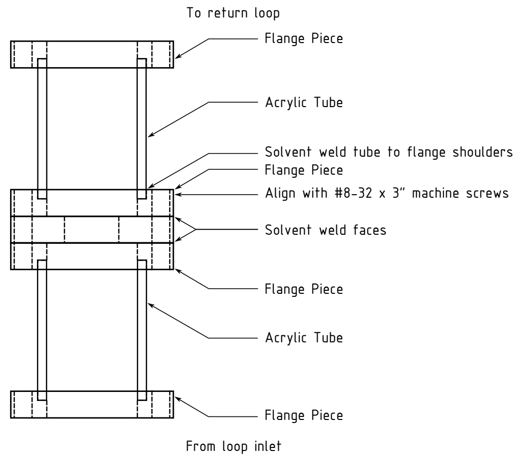

Figure 84: Dimensions of the orifice piece of the test section, $\phi = 19.05\ mm$ version. All dimensions in mm.

A.3 Instrumentation

A.3.1 Air Flow Meter Pressure Conversion

The air flow meter used was marked for air at standard temperature and pressure (STP), however since compressed air was being fed into the meter, the readings need to be adjusted for the higher density of air.

Pressure measurements taken immediately downstream of the air flow meter indicated that the pressure varied between $355.0 \leq P \leq 357.7\ kPa(a)$ over the entire range of gas superficial velocities in this study.

According to the manufacturer's specifications, the actual volumetric flow rate, Q_{actual} is related to the air flow rate indicated on the meter, $Q_{reading}$ by equation (82) [95]. Select values of the equivalent volumetric flow rates are listed in table 31. Since the difference in flow rates between the two pressures is approximately 0.4%, for the purposes of calculations in this study, the volumetric flow rates at $P = 355\ kPa(a)$ is used.

$$Q_{actual} = Q_{reading}\sqrt{\frac{P_{actual}}{P_{STP}}} \tag{82}$$

Table 31: True Air Flow Rates at 355 and 357.7 kPa(a)

$Q_{reading}$ (mL/min)	$Q_{355.0\ kPa}$ (mL/min)	$Q_{357.7\ kPa}$ (mL/min)
15.0	28.1	28.2
50.0	93.6	94.0
100.0	187.2	187.9
150.0	280.8	281.9
200.0	374.4	375.8
250.0	468.0	469.8

A.3.2 Calculation of j_g

Approximating the compressed air as an ideal gas means the system is governed by the equation $PV = nRT$, where P is the system pressure in Pa, V is a volume in m^3, n is the number of moles of air, R is the gas constant in $J/mol \cdot K$, and T is the absolute temperature in K.

By definition the density, ρ, is defined as: $\rho = \frac{m}{V}$ in units of kg/m^3, where m is the mass of the air in kg. Additionally, if M is the molar weight of the air in kg/mol, then n by definition is m/M. The air density is then calculated as:

$$\rho = \frac{PM}{RT} \tag{83}$$

Assuming that the molar weight of air is 28.97 kg/mol, at a temperature of $T = 298.15\ K$ the density of the compressed air at selected pressures of interest are listed in table 32. The variation of the density between $P = 355.0\ kPa(a)$ and $P = 357.7\ kPa(a)$ is only 0.7%, and so to simplify subsequent calculations, a density of $4.149\ kg/m^3$ at the air flow meter is always assumed.

The superficial gas velocity is determined by applying mass conservation principles between the air flow instrumentation and the injection needle in the test section. At the maximum air flow conditions in this study the volumetric flow rate is $Q_{air} = 468.0\ mL/min$ while the density is $\rho_{air} = 4.149\ kg/m^3$. The equivalent air mass flow rate at the air flow instrumentation location is $\dot{m}_{air} = (3.24)\left(10^{-5}\right)\ kg/s$.

Table 32: Densities of air at $T = 298.15\ K$

Pressure $(kPa(a))$	Density (kg/m^3)
101.3	1.183
119.4	1.395
200.0	2.337
300.0	3.506
355.0	4.149
357.7	4.180

At the test section injection point, the air is forced from a $\phi = 3.175\ mm$ tube to into a $\phi = 0.051\ mm$ needle before it discharges into the liquid. This causes significant pressure losses. The internal pressure of the bubbles in the flow is not avaliable, so it is assumed that it is in equilibrium with the liquid at the bottom of the test section. The static pressure at the point of the air injection is $P = 18.1\ kPa(g)$, and so by an air density of $\rho = 1.395\ kg/m^3$ is used to calculate the superficial gas velocity. The superficial gas velocity is calculated as equation (84), where A is the cross sectional flow area of the tube and $\dot{m}_{air}$ is the air mass flow rate as previously determined.

$$j_g = \frac{\dot{m}_{air}}{\rho A} \tag{84}$$

LDV Data

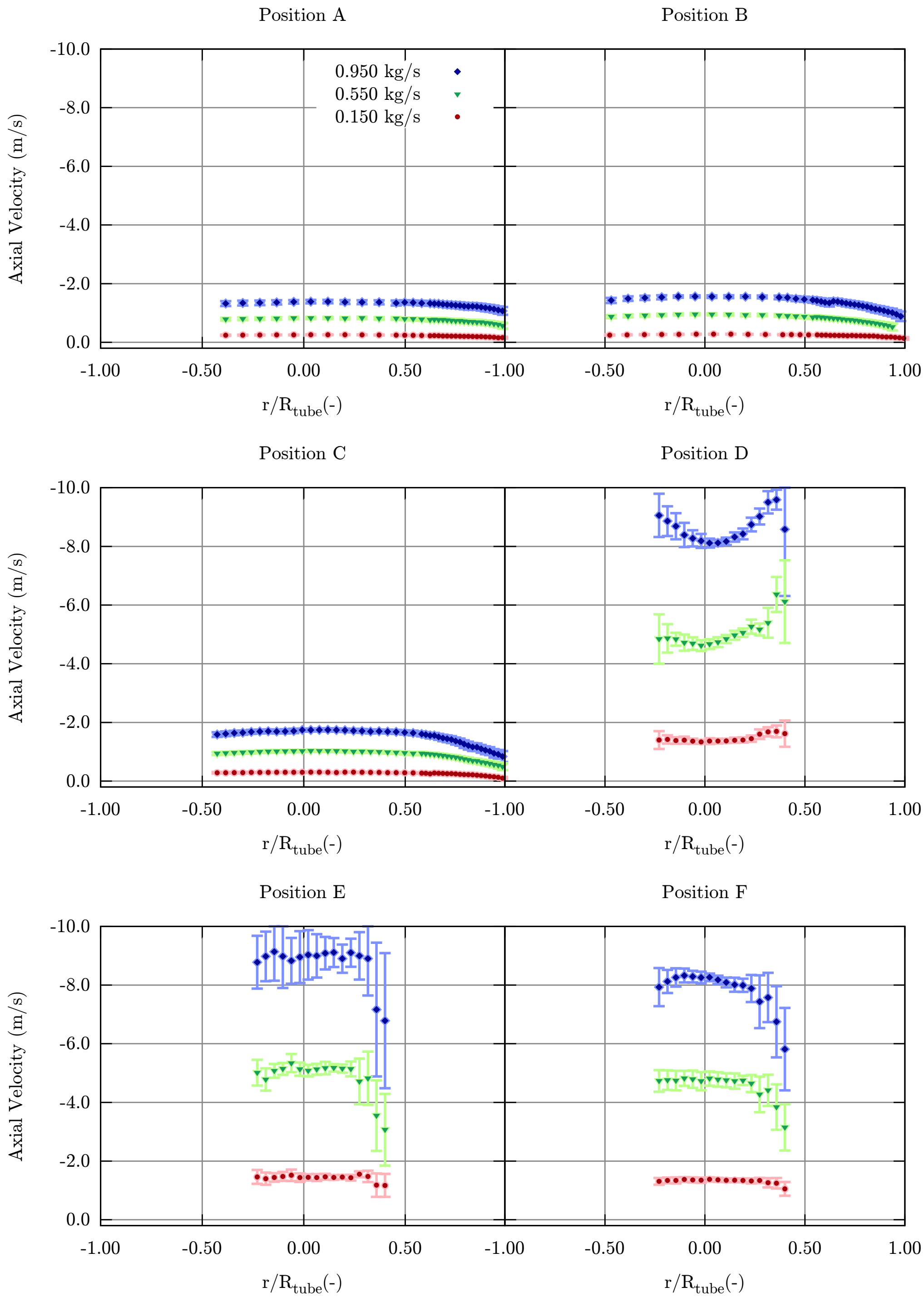

Figure 85: Velocity Data, 12.7 mm Test Section

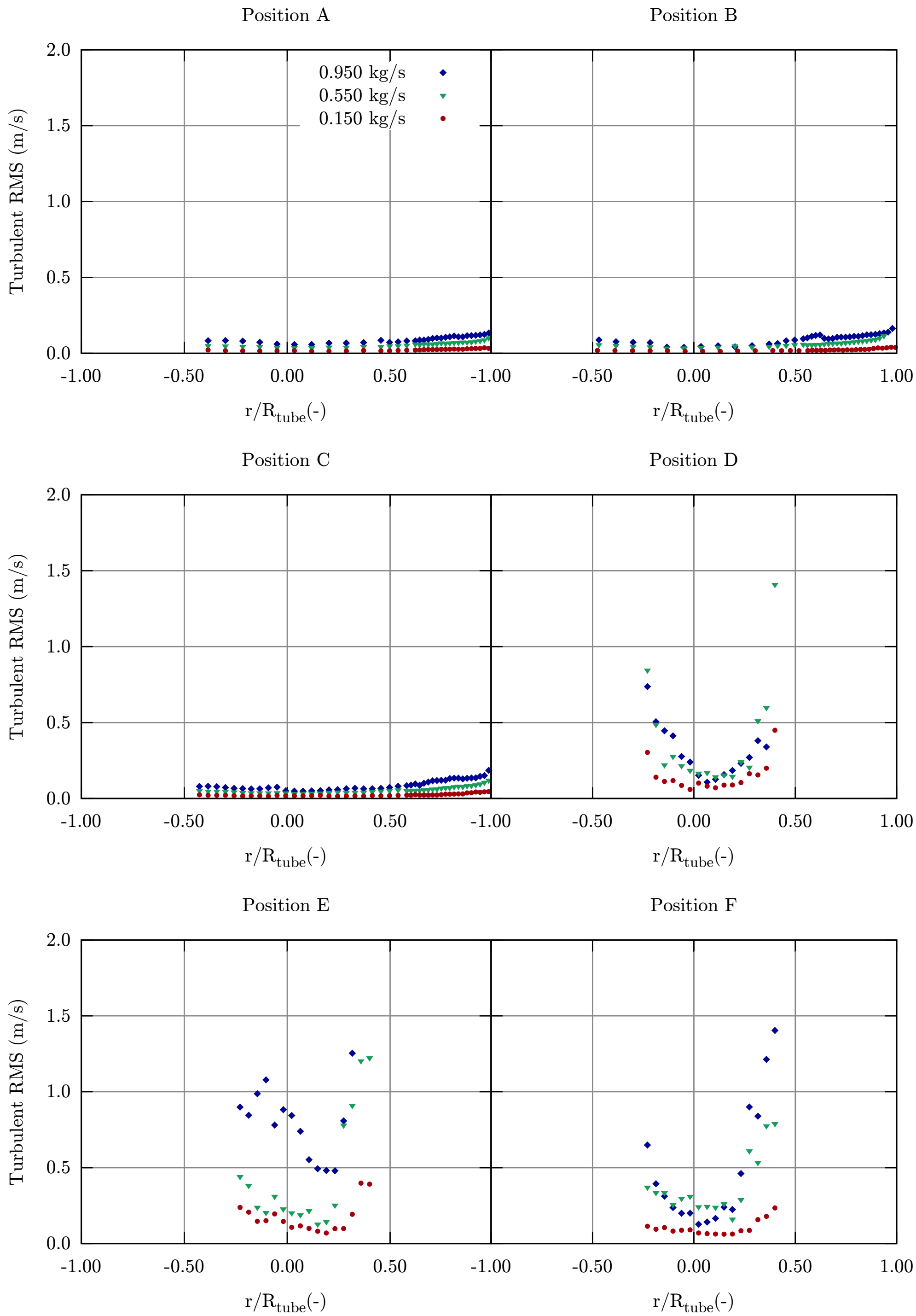

Figure 86: Turbulent RMS Data, 12.7 mm Test Section

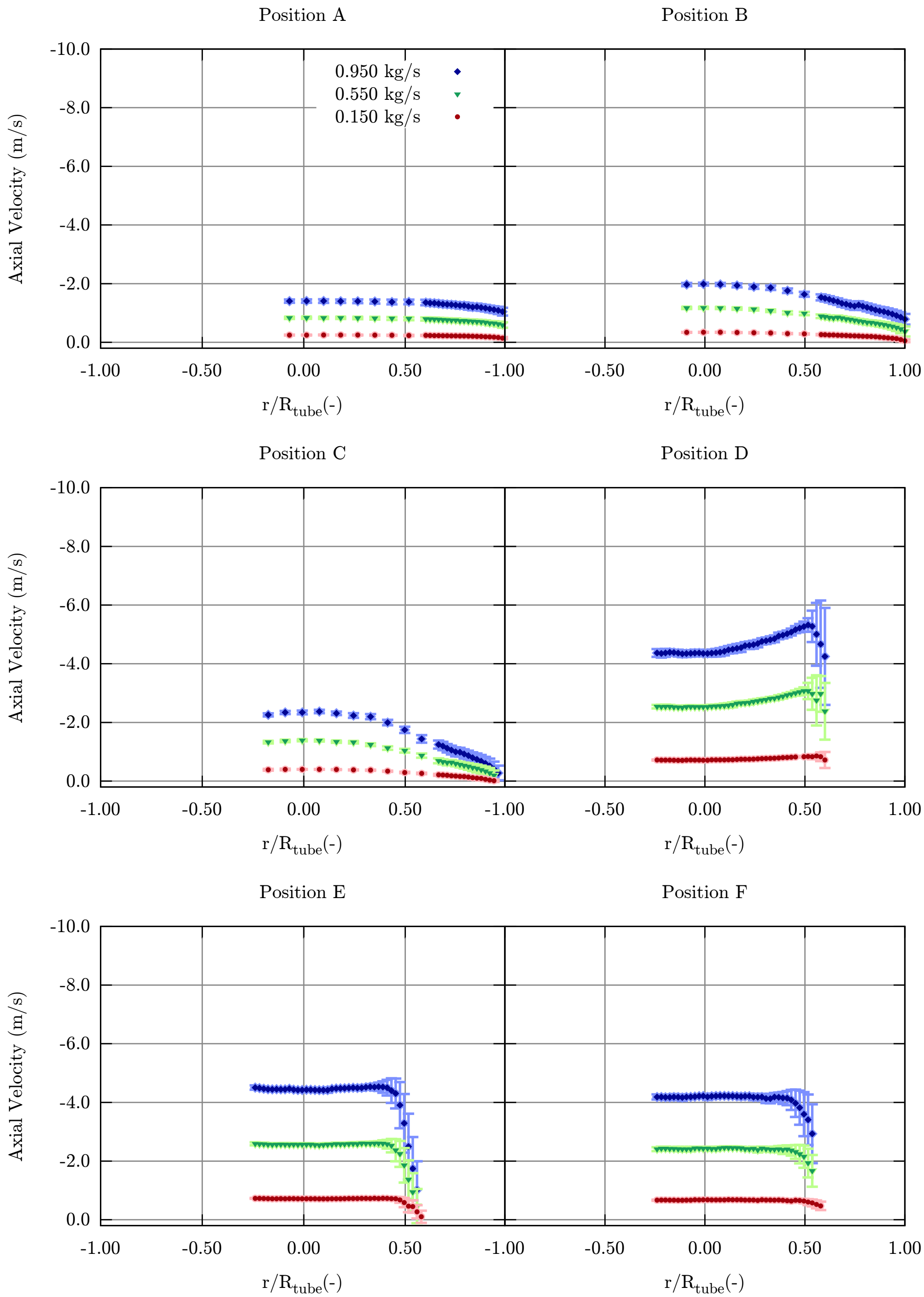

Figure 87: Velocity Data, 12.7 mm Test Section

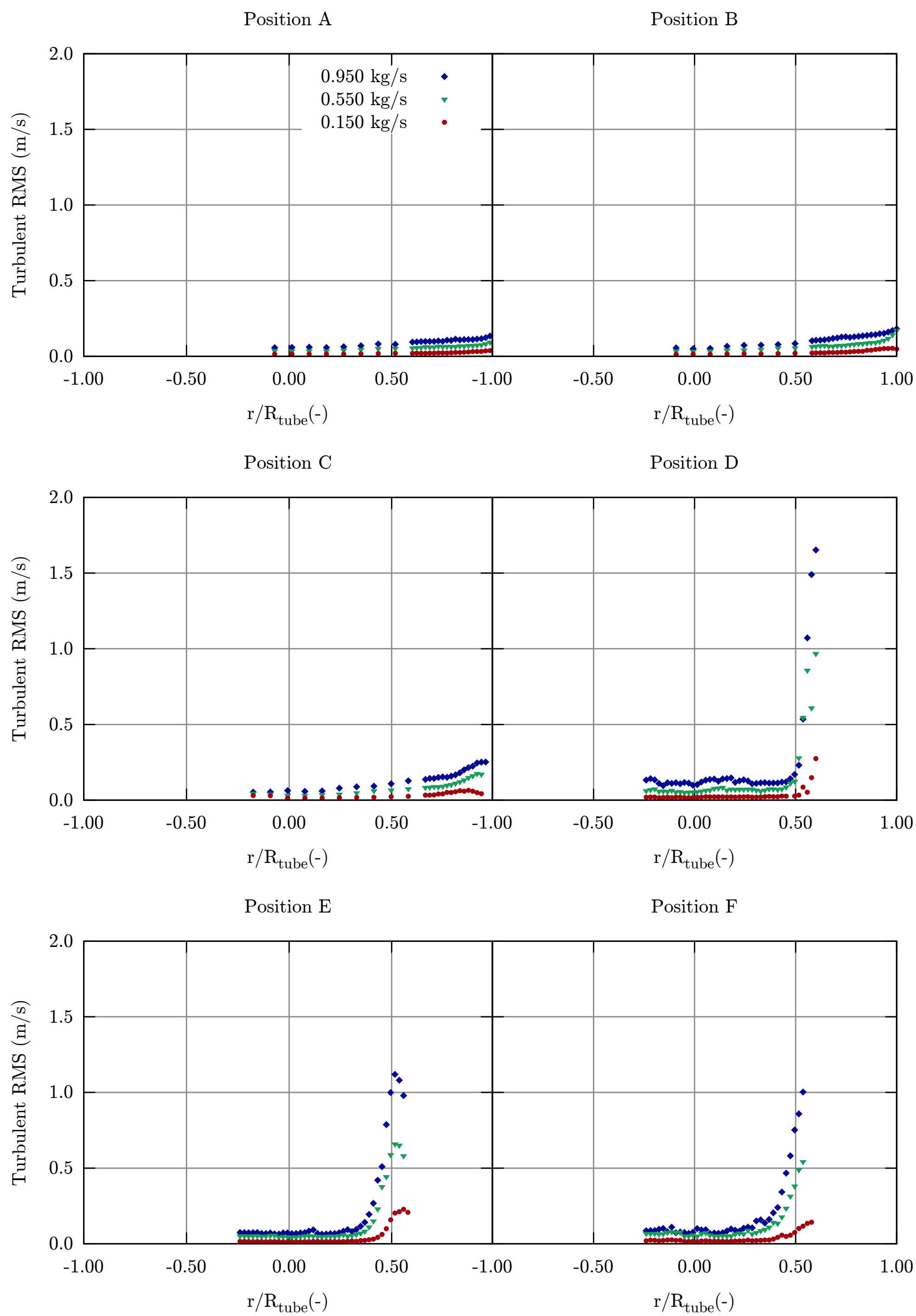

Figure 88: Turbulent RMS Data, 19.1 mm Test Section

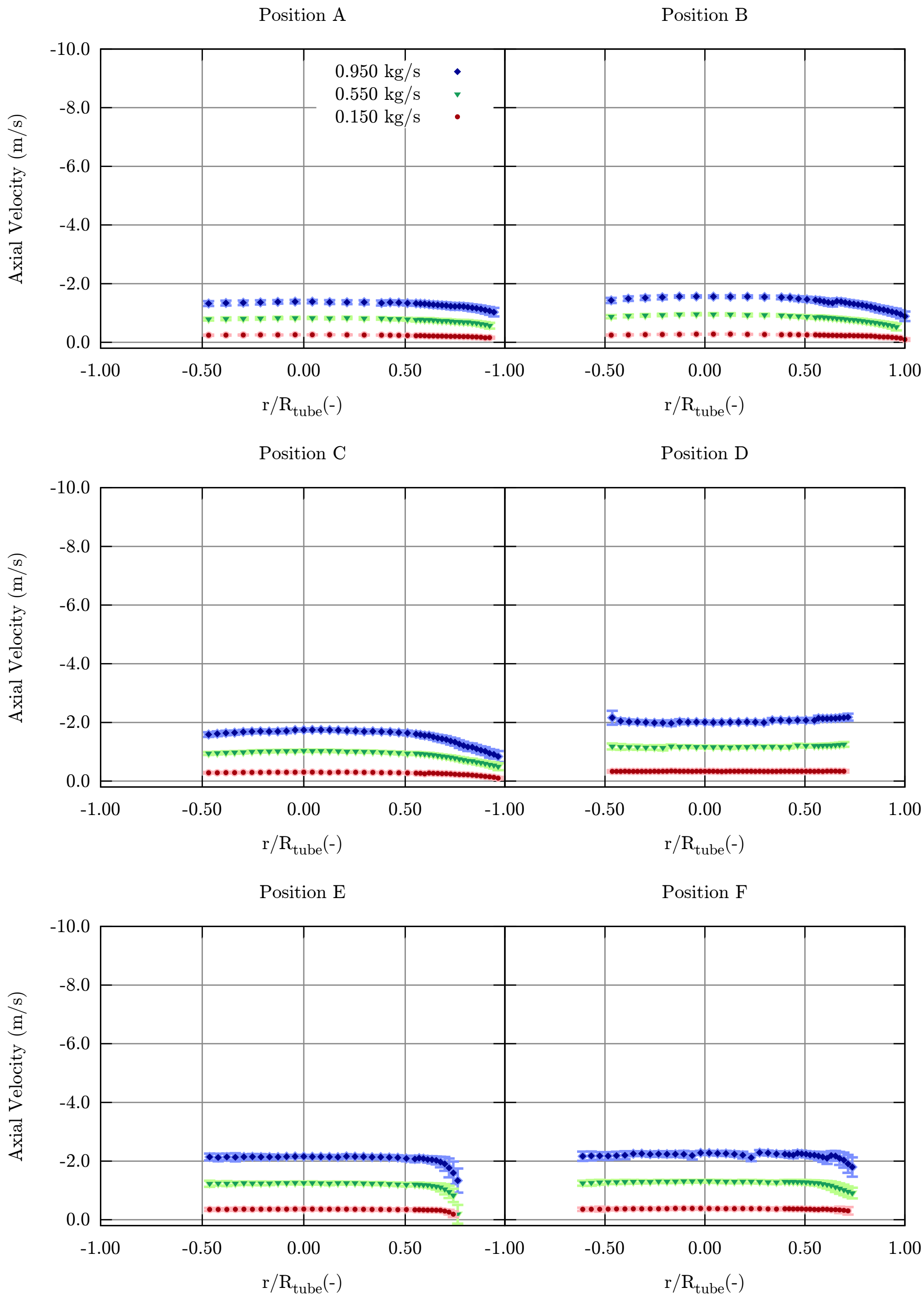

Figure 89: Velocity Data, 25.4 mm Test Section

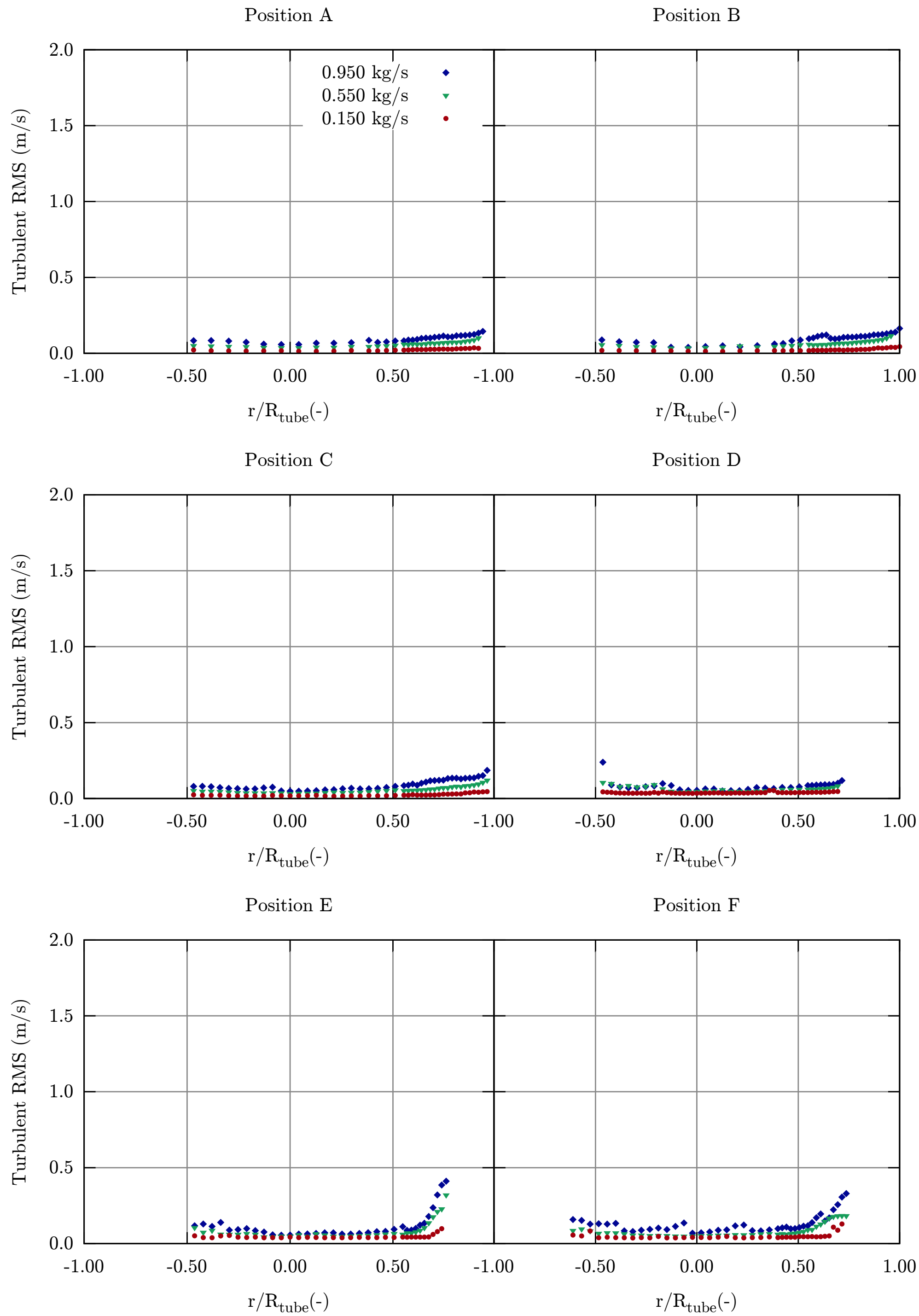

Figure 90: Turbulent RMS Data, 25.4 mm Test Section

Uncertainties and Derivations

C.1 Instrumentation Uncertainties

C.1.1 Flow Stability Uncertainties

The data for the interfacial area measurements are acquired in 6 minute blocks and repeated between 1 to 3 times at each flow condition.

During the tests, fluctuations in liquid flow rate were present due to the unstable nature of bubbly flows. Due to the lack of a bypass line between the pump and the inventory tank, this is particularly evident at low flow rates. In order to mitigate the effects of the flow instability, in tests conducted at $j_f < 0.447$ the VFD would be set to supply an arbitrarily higher ΔP, while a throttling valve would be used to control the flow to the test section. At higher flow rates, the throttling valve would be set fully open, and the flow rate would be controlled by the VFD alone.

To demonstrate the stability of the flow, during some of the tests, the liquid flow rate was recorded using a data acquisition system hooked up to the analog output of the liquid flow meter. The data acquisition system consisted of an NI cDAQ-9178 8-bay chassis with an NI 9208 current module capable of converting a $4 - 20\ mA$ signal into a 24-bit integer. The manufacturer states the device has an accuracy of the greater of $\pm 0.76\%$ of the reading or $\pm 0.04\%$ of the range.

The liquid and gas flow rate were set to their desired levels, and the meter output was recorded at 1 second intervals over the span of each 6 minute test.

Two tests were conducted at each of $\dot{m} = 0.150, 0.550$ and 0.950 kg/s. The mass flow rates correspond to superficial liquid velocities of $j_f = 0.191$ m/s, $j_f = 0.702$ m/s, and $j_f = 1.212$ m/s respectively. The gas superficial flow rate was set constant at $j_g = 0.012$ m/s for all of the runs. The results for the tests are plotted in figures 91, 92, and 93.

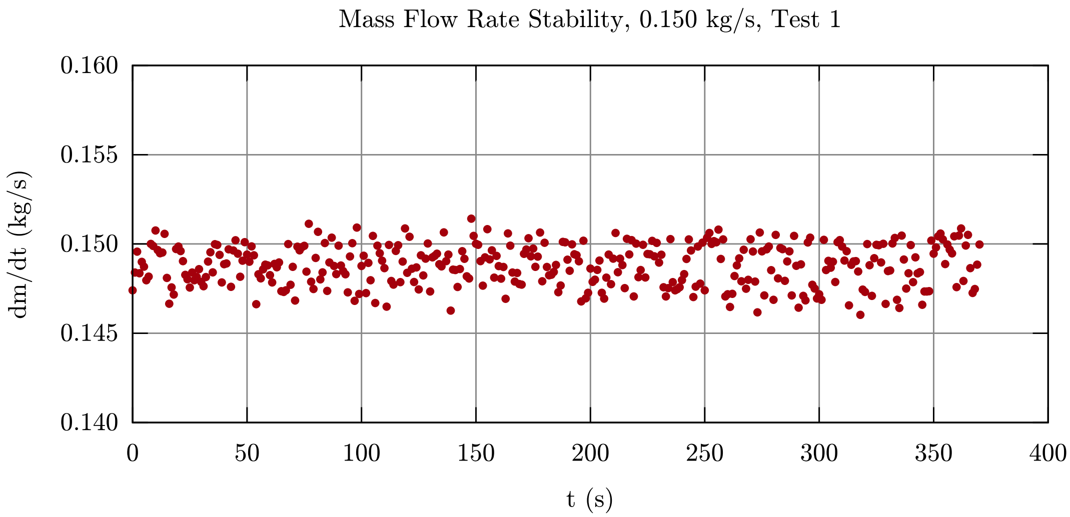

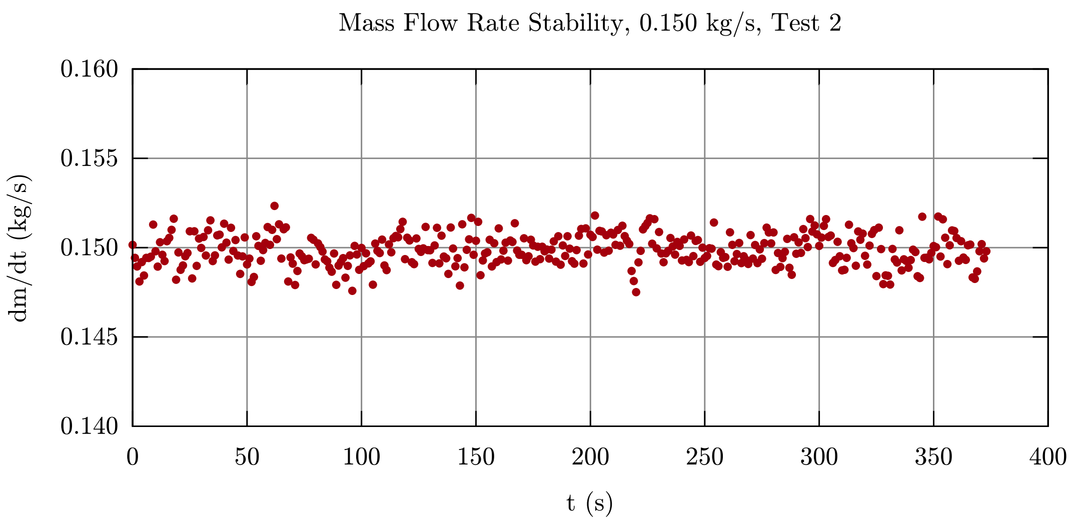

Figure 91: Flow stability at $\dot{m} = 0.150$ kg/s

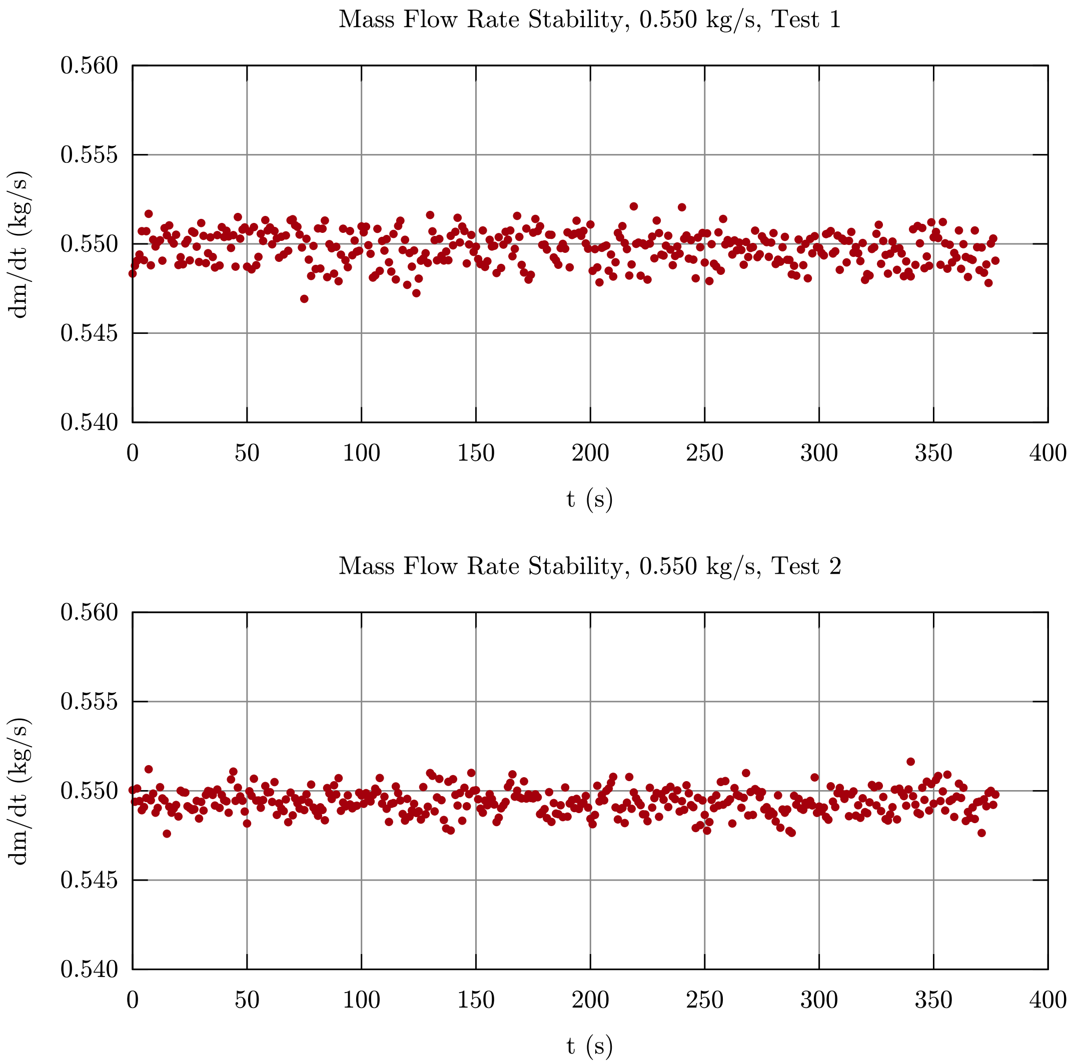

Figure 92: Flow stability at $\dot{m} = 0.550\ kg/s$

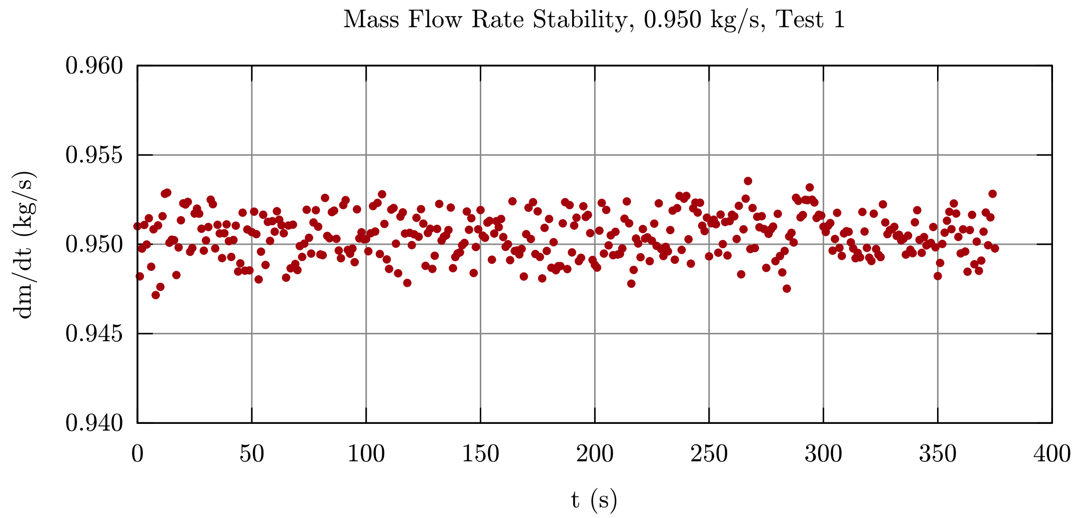

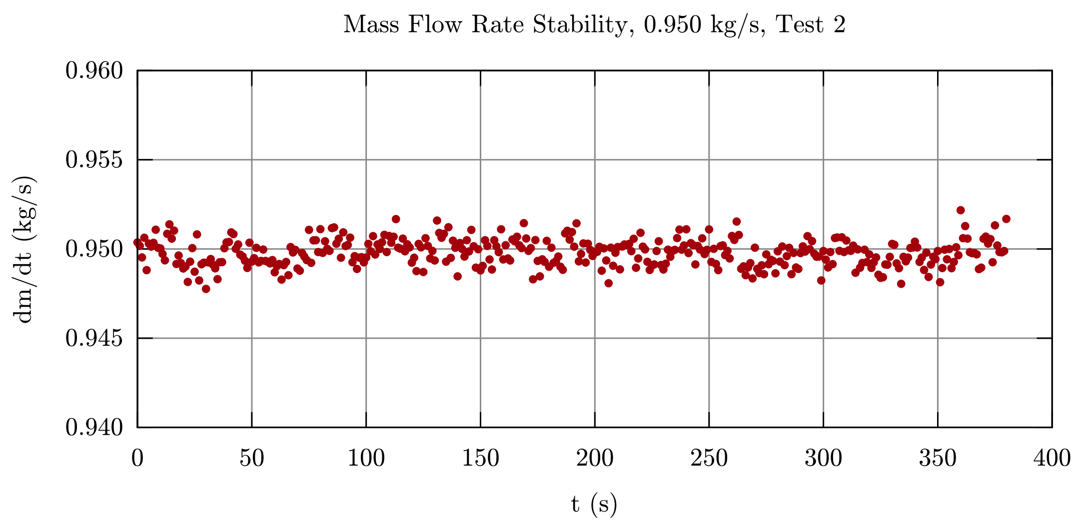

Figure 93: Flow stability at $\dot{m} = 0.950\ kg/s$

C.2 LDV Uncertainties

C.2.0.1 Beam Crossing Location

The intensity of each beam is assumed to follow a Gaussian distribution. When the two beams intersect, the intensity of the crossed region resembles a 3-dimensional ellipsoid. The dimensions of this ellipsoid are reported in terms of the distance between the points where the beam intensity is nominally a factor of e^{-2} of the peak. As illustrated in Figure 94, the distance between the e^{-2} points in the axial direction is 45 μm, which is relatively small in comparison to the width of the optical slit in the receiver (150 μm). However, the shallow slope of the beam means that the distance between the points in the lateral direction is estimated to be 767 μm, which is significant since the receiver slit will record measurements when focused in at any point within the crossing.

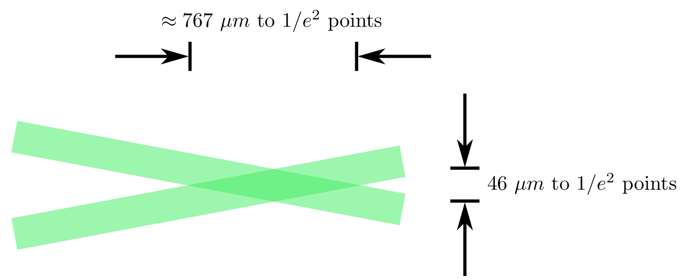

Figure 94: Dimensions of the beam crossing region

C.3 Repeatability

C.3.1 Verification Tests

Three types of tests were conducted in order to evaluate the quality of the results obtained by the LDA. The first set of tests was conducted to check the accuracy of the measurements by comparing against results found in literature for a similar geometry, and these are documented in section C.3.1.1.

The second set of tests was conducted to determine how repeatable two sets of measurements under the same conditions are. The repeatbility tests are conducted several hours or days apart, and are discussed in detail in section C.3.1.2.

The LDA samples and records a velocity measurement each time a particle in the fluid transits through the beam crossing region. Each data 'point' in the results section is comprised of 10,000 such samples. Both the mean velocity, $\overline{u}$, and the root mean square of the deviation, u', of the samples must be reported in order to obtain a description of the fluid behaviour. In practice, u' is used to represent to magnitude of the turbulence intensity. Since the number of samples acquired is arbitrarily selected, section C.3.1.3 examines its effect on the reported turbulence intensity.

C.3.1.1 Accuracy vs. Literature

A set of axial velocity and turbulent intensity measurements were obtained and compared to work in literature in order to verify that the values obtained were within reason. For the comparison, work conducted by Liu and Bankoff on vertical air-water flows in a 38 mm diameter tube (our tube $I.D. = 31.75\ mm$) was used due to the similarity in geometry and measurement detail [96]. In this particular work, the authors used hot wire anemometry to measure the axial velocity and turbulence intensity in a glass test section. Due to the similarity in flow area, the superficial velocity (rather than the Reynolds number) was matched so that the accuracy of the magnitude of the measurements could be evaluated. Measurements for two single phase cases were compared where $j_f = 0.376\ m/s$ and $j_f = 1.087\ m/s$. In our work, the velocities are measured at $z/d_{hyd} = 28$, which is about 2 hydraulic diameters upstream of where the orifice would be placed.

Equation 85 is the correction factor which was applied to the position of the beam crossing. The distance the beam travels in the water before it crosses (Δx_{water}) was determined by focusing the receiver on the beam crossing point, and then moving the traverse slowly until the crossing reaches the acrylic-water interface at the far side of the tube ($\Delta x_{water} = d_{tube}$). This interface is located by setting the band pass filters on the signal processor to only allow frequencies near the 40 MHz range to be accepted (this corresponds to $u = 0\ m/s$ when no downmixing is applied) and watching for a burst of data while the traverse is moved. From experience, once the acrylic-water interface is 'hit' by the crossing, the data rate increases from $\approx 10^2 - 10^3$ counts per second to $\approx 10^5$ counts per second. This point is used as the reference point for the measurements.

$$\Delta x_{water} = \frac{\frac{\Delta y_0}{2} - \Delta x_{air} tan\left(\theta_{air}\right) - \Delta x_{acr} tan\left(\theta_{acr}\right)}{tan\left[sin^{-1}\left(\frac{n_{acr}}{n_{water}} sin\left\{sin^{-1}\left(\frac{n_{air}}{n_{acr}} sin\theta_{air}\right)\right\}\right)\right]} \tag{85}$$

The position corrected axial velocities are illustrated in figure 95 which compares them beside the results of Liu & Bankoff [1]. The figure demonstrates that the axial velocities measured are in excellent agreement in both quantitative and qualitative terms for both cases examined. The velocity RMS and turbulence intensity profiles for the $j_f = 0.376\ m/s$ case are illustrated in figure 96, whereas the $j_f = 1.087\ m/s$ case is displayed in figure 97 [2]. These figures indicate that the turbulence results we have obtained are also in agreement with the work from literature, and that the positional adjustment factor we have derived is indeed correct.

[1] Reprinted from Int. J. Heat Mass Transfer, vol 36, T.J. Liu and S.G. Bankoff, Structure of air-water bubbly flow in a vertical pipe - I. liquid mean velocity and turbulence measurements, 1049–1060, 1993, with permission from Elsevier.

[2] Reprinted from Int. J. Heat Mass Transfer, vol 36, T.J. Liu and S.G. Bankoff, Structure of air-water bubbly flow in a vertical pipe - I. liquid mean velocity and turbulence measurements, 1049–1060, 1993, with permission from Elsevier.

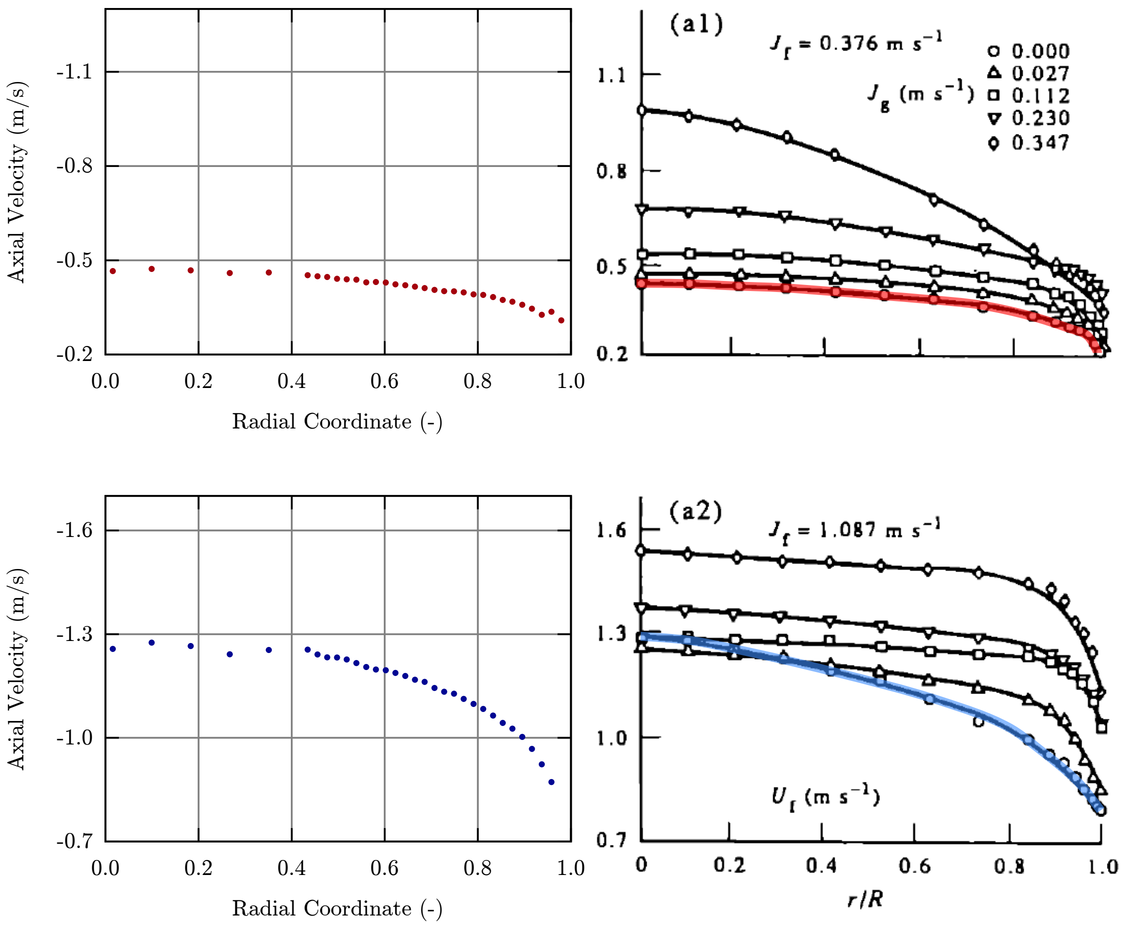

Figure 95: Position adjusted axial velocities (left) compared to results obtained by Liu & Bankoff [96] (right) for superficial fluid velocities of $j_f = 0.376\ m/s$ (top) and $j_f = 1.087\ m/s$ (bottom).

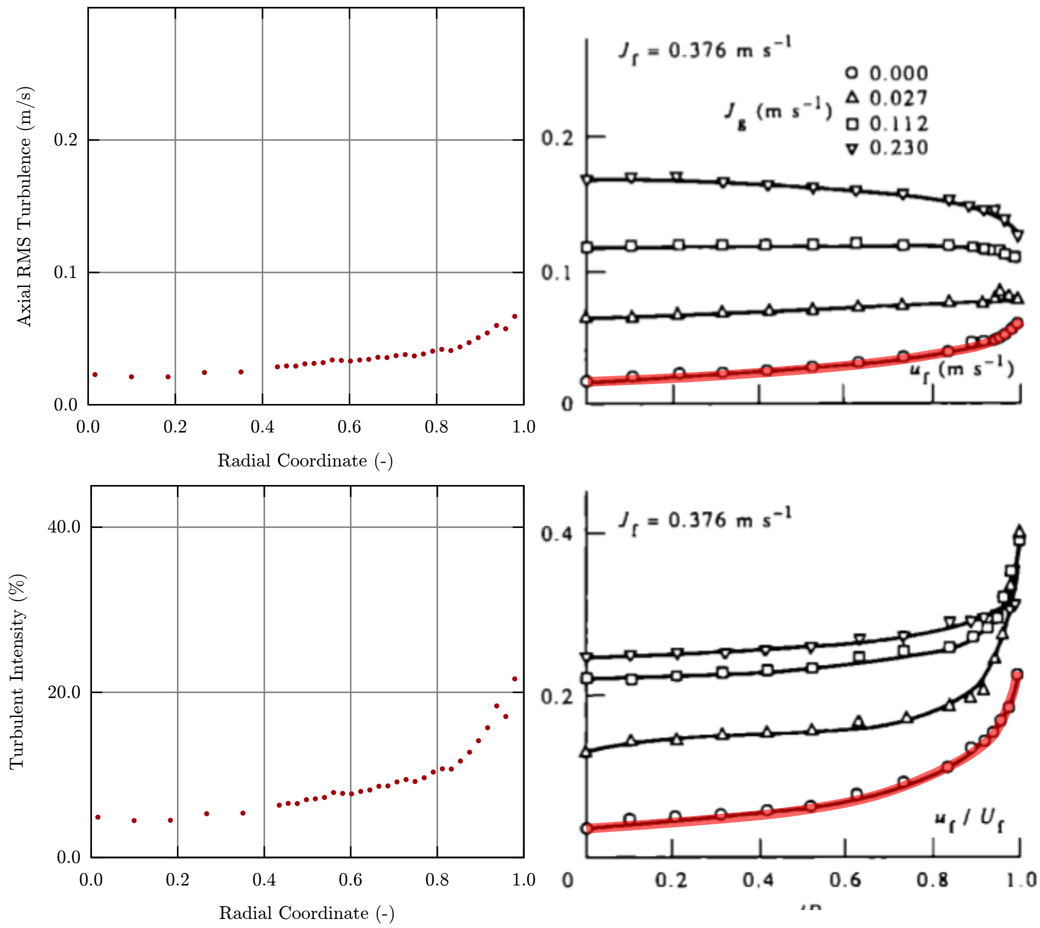

Figure 96: Position adjusted RMS turbulent fluctuations (top left) and turbulence intensity (bottom left) compared to results obtained by Liu & Bankoff [96] (top and bottom right) for superficial fluid velocity of $j_f = 0.376\ m/s$.

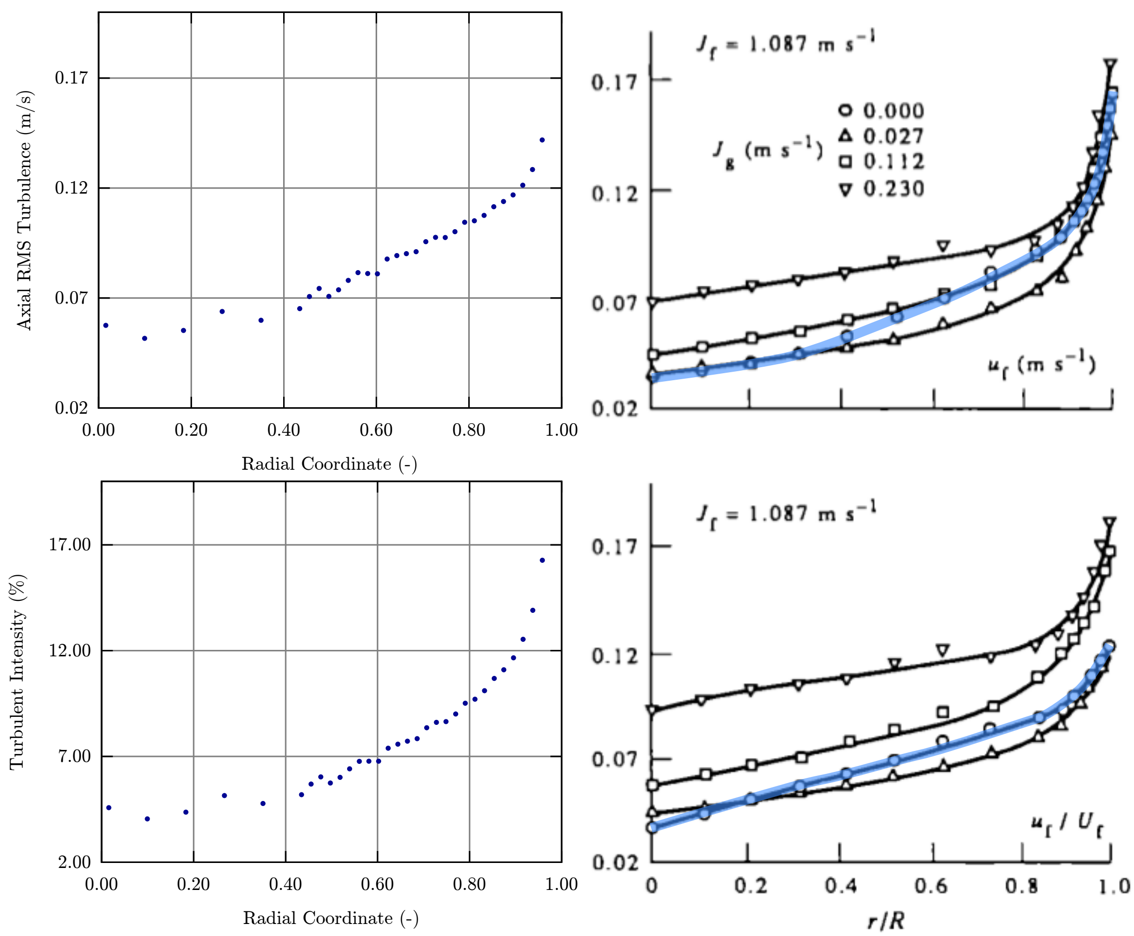

Figure 97: Position adjusted RMS velocity (top left) and turbulence intensity (bottom left) compared to results obtained by Liu & Bankoff [96] (top and bottom right) for superficial fluid velocity of $j_f = 1.087\ m/s$.

C.3.1.2 Repeatability

The repeatability tests were conducted over several days of data acquisition using the test section containing the $d = 19.05\ mm$ orifice.

The first test was conducted with a fluid mass flow rate of $\dot{m} = 0.450\ kg/s$ at position C (2 mm upstream of the leading edge of the orifice). A baseline set of data was acquired as part of the normal acqusition process, and this is illustrated in figure 98 as the set of points with a line running through. The data used for comparsion

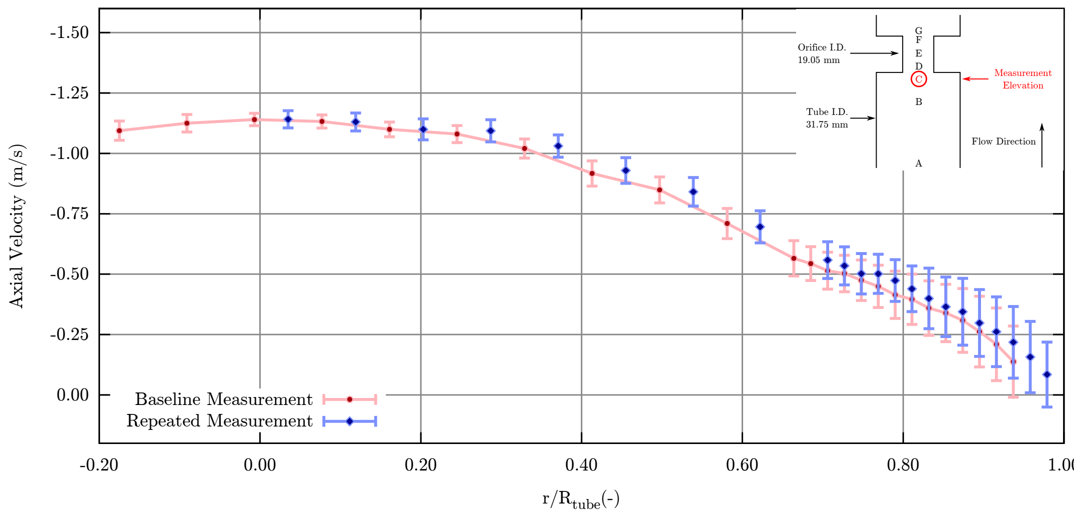

Figure 98: Repeatability Test 1 conducted at postion C using $\dot{m} = 0.450\ kg/s$. Baseline values (red connected circles) are plotted against results obtained 4 days later (blue diamonds).

was acquired 4 days later (with experiments at other positions and flow rates taking place during each of those days), and is plotted as the unconnected points.

A second test was conducted at higher spatial resolution using a mass flow rate of $\dot{m} = 0.550\ kg/s$ at position E (the midplane of the orifice) and is illustrated in figure 99. In this case, the baseline values were acquired at the beginning of the day, whereas the values for comparison were obtained at the end of the same day, between which experiments at other conditions and positions were taking place.

In both cases, there are only minor variations in both the reported mean and root mean square deviation of the velocity were observed for measurements taking place away from the wall. The samples in the second test are all taken at the same radial location, and so a direct numerical comparision is possible. Out of the 38 sets of measurements, the relative difference in the mean velocity between the baseline and the repeated tests is less than 1% at all locations except for those nearest the wall. The variances in this region are higher due to the difficulty focusing the receiver at precisely the same point in the beam crossing area. Normally this does not account for a significant variation in the measured velocities, however in the near wall region, much larger values of $\frac{d\bar{u}}{dx}$ exist which significantly magnifies any positional error.

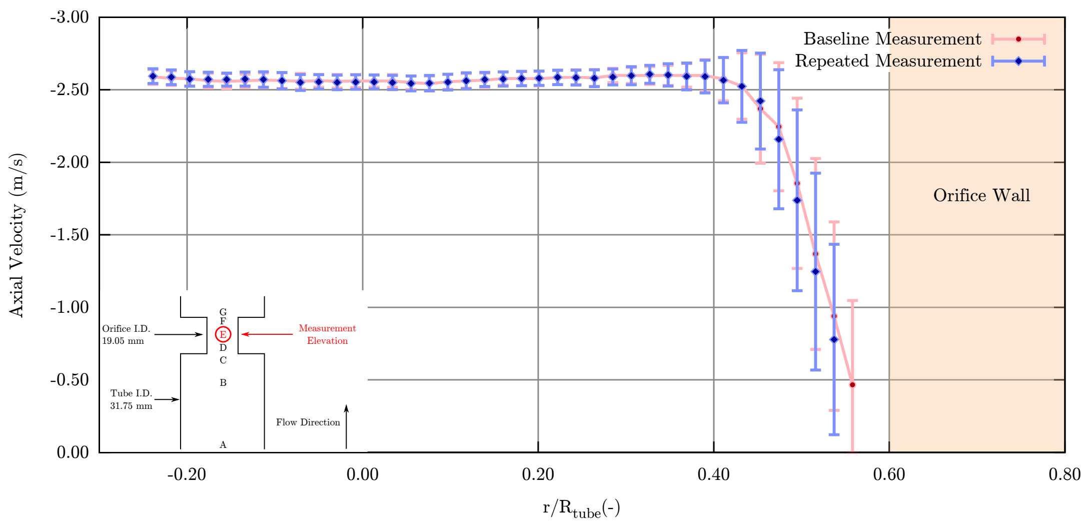

Figure 99: Repeatability Test 2 conducted at postion E using $\dot{m} = 0.550\ kg/s$. Baseline values (red connected circles) are plotted against results obtained 4 days later (blue diamonds).

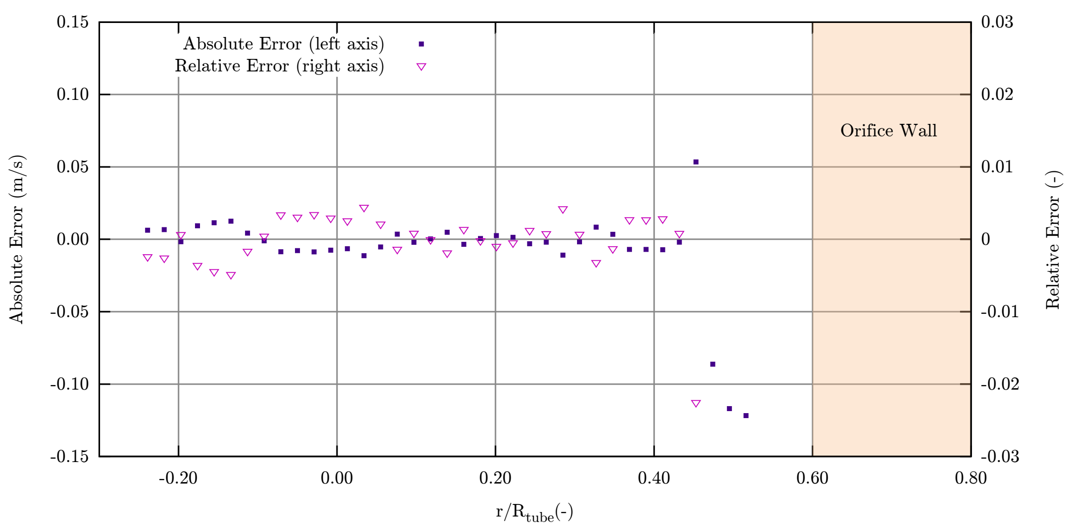

Figure 100: Absolute and relative errors of Repeatability Test 2.

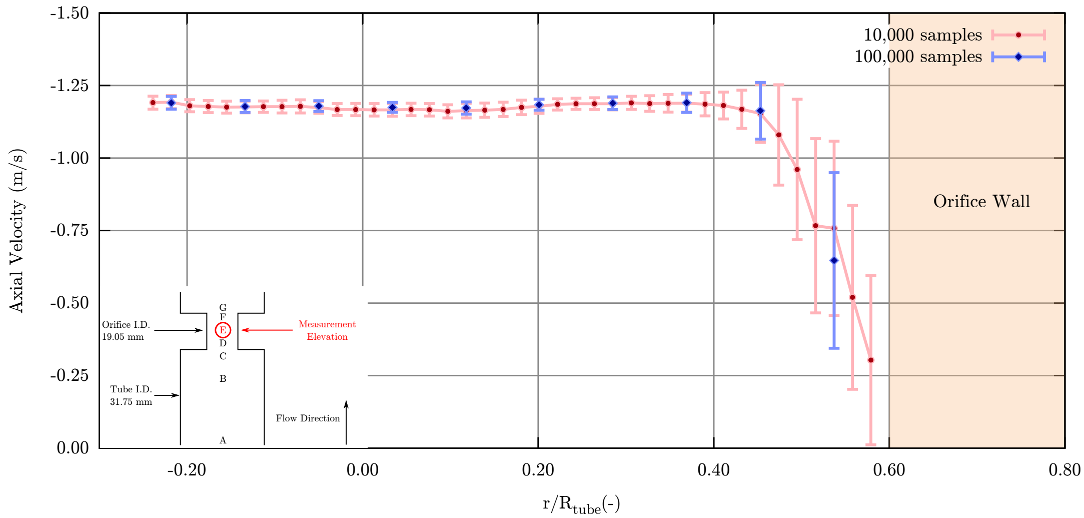

Figure 101: Velocity values from the sample length test conducted at postion E using $\dot{m} = 0.250\ kg/s$. Baseline values (red connected circles) are acquired using 10,000 samples per point and these are plotted against results obtained using 100,000 samples per point (blue diamonds).

C.3.1.3 Sample Length

At each measurement location 10,000 velocity samples are taken in order to evaluate both $\overline{u}$ and u'. Since a finite number of samples are taken to approximate a continuous distribution, a statistical uncertainty of $\epsilon \propto 1/\sqrt{n}$ is expected. With 10,000 samples, the true mean velocity is expected to fall within $\pm 1\%$ of the measured value.

A verification test was conducted using 100,000 samples per point (with the expectation that the true mean would fall within $\pm 0.3\%$ of the measured value), and the results were overlaid on top of the baseline values as shown in figure 101.

Of the 10 locations tested, only the point closest to the wall (at $r/R_{tube} = 0.537$) exhibited any significant variance between sample lengths. This mean velocity measured for this point differs by 0.111 m/s between the 10,000 sample measurement and the 100,000 sample test. Among the remainder of the sample locations, the average difference of the velocity means was 0.0044 m/s, with a maximum of 0.0098 m/s

The baseline measurement (red circle) at $r/R_{tube} = 0.537$ in figure 101 is clearly well above the established trend of the surrounding points (i.e. the slope du/dr

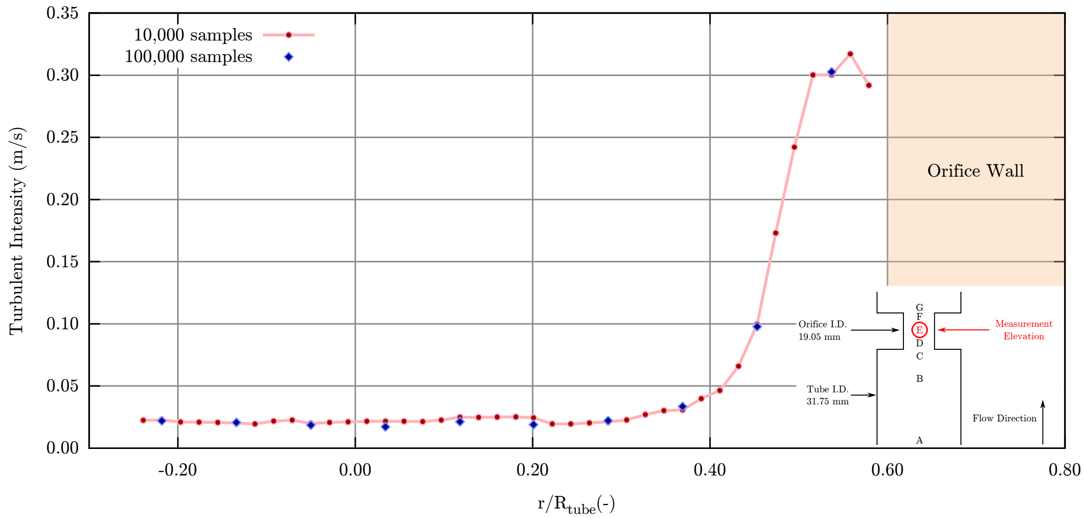

Figure 102: Turbulent intensity values from the sample length test at postion E using $\dot{m} = 0.250\ kg/s$. Baseline values (red connected circles) are acquired using 10,000 samples per point and these are plotted against results obtained using 100,000 samples per point (blue diamonds).

decreases abruptly for only that point). It is reasonable for this discrepency to be not a result of statistical uncertainty - but rather it stems from uncertainty in the position of the beam crossing. Specfically it appears that the baseline measurement at this point was taken immediately after the receiver was realigned.

The values reported for u' from both tests are illustrated in figure 102. Once again, the difference between tests is negligible, with an average variation between the baseline and extended sample lengths of $\Delta u' = 0.0015\ m/s$ if the point closest to the wall is considered an outlier.

The overall conclusion from this test is that little benefit is derived from increasing the number of samples taken per point. A ten-fold increase in the number of samples taken only results in an expected accuracy improvement of 0.7%. Under the conditions of the current test (neglecting the point closest to the wall), the average difference in the sample means 4.4 mm/s - a wholly insignificant result considering the error incurred due to the uncertainty in the position of the beam crossing.

C.4 Camera Sizing Uncertainties

The sources of uncertainty in the camera size measurements stem from the following:

1. Each of the pixels in the camera's CCD are specified by the manufacturer to be 20 $\mu m \times 20$ μm. No tolerances on these dimensions are provided.
2. The lens mounted on the camera has a magnification ratio of 1:1. Again, no tolerances are supplied.
3. The light passing through the water and acrylic will be refracted. The distortion this causes is discussed in section **??**.

In order to estimate the uncertainty in the camera sizing method, the following procedure was used:

1. A spool piece identical to ones used in the construction of the test sections was sealed and filled with water.
2. A pin was placed into the spool piece along the centerline, and pictures were taken with the camera using the same lens settings as in the experiment.
3. A bounding box around the shadow of the pin and the head were drawn, and the size (in pixels) was reported (figure 103).
4. The diameter of the head of a sewing pin is measured using digital calipers to be 3.66 ± 0.01 mm, about the size of a larger bubble.
5. The diameter of the head as measured by the camera was, a distance corresponding to 3.62 mm. The camera measurement was about 1% less than the size measured by the calipers.
6. The diameter of the pin was measured by the calipers to be 0.36 ± 0.01 mm, about the size of a small bubble.
7. The diameter of the pin was measured by the camera to be 19 pixels, a distance corresponding to 0.38 mm.

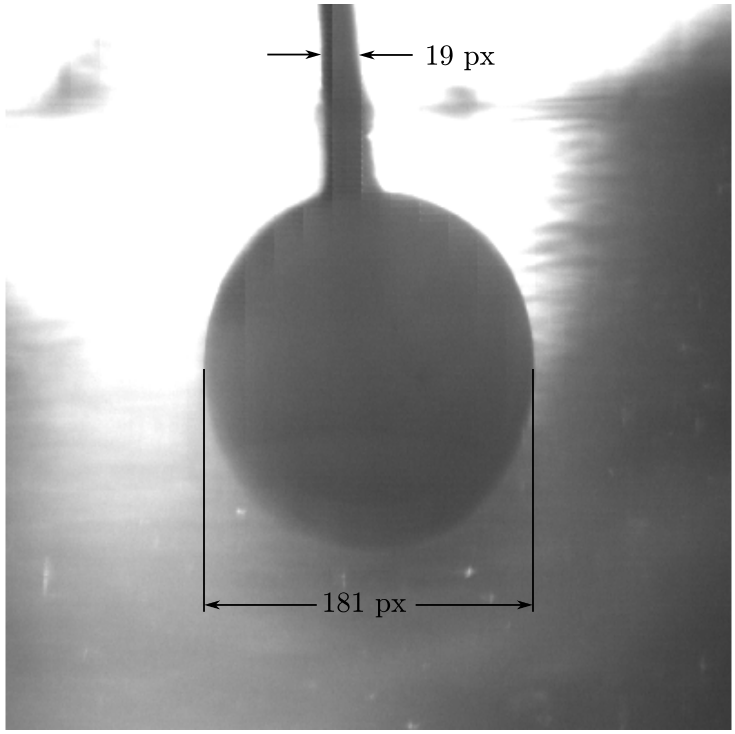

Figure 103: Imaged dimensions of a pin

Figure 104: Measured dimensions of a pin (left) and pin head (right)

C.4.1 Pixel Blurring

Motion blurring will occur in an image if a particle or bubble crosses more than one pixel during the time which the camera shutter is open.

The camera used in this experiment has an electronic shutter, and is capable taking exposures of times as little as 363 ns. Such short shutter times however reduce the amount of light detected by the sensor, and ultimately affect the dynamic range of each image. In other words the images are a lot darker, and it is more difficult to determine where the bubbles are.

In order to minimize the motion blurring yet have a uniform lighting intensity over all of the images, the shutter speed is set so that at the maximum liquid superficial velocity the bubble will not be expected to move more than one pixel.

- The height of each pixel is 0.02 mm.
- The bubbles are assumed to flow at the superficial velocity of the tube.
- At the maximum flow rate in the experiment, the liquid superficial velocity is $j_f = 1.212\ m/s$.
- Under these conditions, in order for the interface of the bubble to move from one pixel to another it will require roughly:

$$\Delta t = \frac{\Delta y}{u} = \frac{(0.02)(10^{-3})}{1.2} = (1.66)(10^{-5})\ s \tag{86}$$

- The shutter speed used in interfacial area experiments is $\Delta t = (1)(10^{-6})\ s$, which is sufficient to minimize the motion blurring.

C.4.2 AC Lighting Ripple

The test section is backlit using halogen lighting hooked up to the building mains. This causes a lighting intensity variation at $\approx 120\ Hz$ (2 peaks per cycle).

This was pulsing effect was reduced by:

1. Taking a several hundred background images over a 30 second span.
2. Averaging the background images.
3. Calculating the standard deviation of the intensity variation at each pixel.

C.5 Bubble Sizing Derivation and Examples

C.5.1 Derivation of the Joint Probability, Circles

The derivation of $P(y \mid D)$ here follows both the works of Simmons *et al.* [88] and Li *et al.* [90]. It yields the probability of measuring a chord of length y given a circle with a diameter of D.

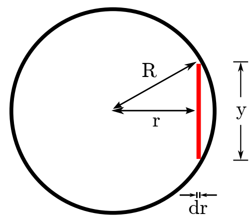

Figure 105: Definition of chord symbols

1. Assume that a bubble with a diameter D exists.

2. Assume that a chord is 'sampled' at some distance r from the center of the circle, where $0 < r < R$. The probability of selecting a chord between a distance of r and $r + dr$ from the center is given by:

$$P(r, r + dr|R) = \frac{dr}{R} \tag{87}$$

3. The relationship between r, R and the chord length y is given by:

$$\begin{aligned} R^2 &= r^2 + \left(\frac{y}{2}\right)^2 \\ r &= \sqrt{R^2 - \left(\frac{y}{2}\right)^2} \end{aligned} \tag{88}$$

4. Taking the derivative of both sides yields:

$$\begin{aligned} dr &= \frac{1}{2}\left(R^2 - \left(\frac{y}{2}\right)^2\right)^{-1/2}\left(-\frac{y}{2}dy\right) \\ dr &= \frac{-y}{4}\frac{1}{\sqrt{R^2 - \left(\frac{y}{2}\right)^2}}dy \end{aligned} \tag{89}$$

5. Substituting equation (89) into (87) yields the probability of selecting a chord between y and $y + dy$ in a bubble of radius R. According to Simmons [88], the negative sign in front of the y can be dropped "since a negative probability is meaningless".

$$P\left(y, y + dy|R\right) = \frac{y}{4R}\frac{1}{\sqrt{R^2 - \left(\frac{y}{2}\right)^2}}dy \tag{90}$$

6. The probability of a chord being between the sizes of y_1 and y_2, for a circular bubble of diameter D is [3]:

$$\begin{aligned} P\left(y_1, y_2|D\right) &= \int_{y_1}^{y_2} \frac{y}{4R}\frac{1}{\sqrt{R^2 - \left(\frac{y}{2}\right)^2}}dy \\ &= \frac{-1}{4R}\sqrt{R^2 - \left(\frac{y}{2}\right)^2}\Bigg|_{y=y_1}^{y=y_2} \\ &= \frac{-2}{4D}\sqrt{\left(\frac{D}{2}\right)^2 - \left(\frac{y}{2}\right)^2}\Bigg|_{y=y_1}^{y=y_2} \\ &= \frac{\sqrt{D^2 - y_1^2} - \sqrt{D^2 - y_2^2}}{D} \end{aligned} \tag{91}$$

[3]Note: $\int \frac{x}{\sqrt{C^2 - x^2}}dx = -\sqrt{C^2 - x^2}$

C.5.2 Example

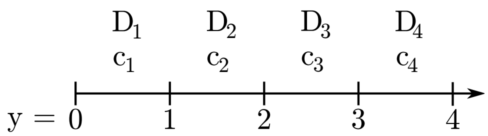

Figure 106: A number line.

In this example, suppose a number of chord measurements are taken and grouped into 4 bins: $\mathbf{c} = (c_1, ..., c_4)$

These chord measurements come from a population of spherical bubbles (projected as circles) distributed with diameters: $\mathbf{D} = (D_1, ..., D_4)$. The section shows how the two distributions are related via:

$$\mathbf{c} = \mathbf{PD}$$

Suppose a chord is measured and falls into size bin c_1. It is possible to make this chord measurement from any size of bubble larger than it. We denote $P_{i,j}$ as the probability that a chord measurement with a size corresponding to bin i is made given a bubble belonging to size bin j. Also, $P(D_j)$ is probability that a bubble belonging to diameter bin D_j is measured. The number of chords falling into bin c_1 may be calculated as:

$$c_1 = P_{1,1}P(D_1) + P_{1,2}P(D_2) + P_{1,3}P(D_3) + P_{1,4}P(D_4)$$

Each of the $P_{i,j}$ terms is calculated based on equation (91), with y_1 and y_2 representing the lower and upper sizes of bin i, and D being represented by the midpoint of bin j (we are assuming that all bubbles in diameter bin j have take on one size).

If a chord is measured which falls into size bin c_2, we know that it is geometrically impossible to measure a chord length in a circle which is longer than the diameter. Therefore, $P_{2,1} = 0$, and the equation for c_2 becomes:

$$c_2 = 0 + P_{2,2}P(D_2) + P_{2,3}P(D_3) + P_{2,4}P(D_4)$$

It is evident that the governing system of equations is in the form of:

$$\begin{pmatrix} c_1 \\ c_2 \\ c_3 \\ c_4 \end{pmatrix} = \begin{pmatrix} P_{1,1} & P_{1,2} & P_{1,3} & P_{1,4} \\ 0 & P_{2,2} & P_{1,3} & P_{1,4} \\ 0 & 0 & P_{3,3} & P_{1,4} \\ 0 & 0 & 0 & P_{4,4} \end{pmatrix} \begin{pmatrix} D_1 \\ D_2 \\ D_3 \\ D_4 \end{pmatrix} \tag{92}$$

Inverting the above equation yields the distribution of diameters.

C.6 Derivation of a_i

A single bubble contributes a surface area and volume of:

$$A_i = 4\pi r^2 = \pi d^2 \tag{93}$$

$$V_{bubble} = \frac{4}{3}\pi r^3 = \frac{\pi d^3}{6} \tag{94}$$

The interfacial area concentration is by definition a volume averaged quantity (eg. m^2 per m^3). Averaging the bubble area over its own volume provides nothing more than area to volume ratio. Instead, the averaging volume is typically defined as some larger volume. The volume occupied by the bubble within this larger averaging volume (V_{total}), is by definition the void fraction - a quantity which can be measured using photography.

$$\alpha \equiv \frac{V_{bubble}}{V_{total}} \tag{95}$$

Therefore the interfacial area concentration for a single sphere residing within the averaging volume is defined as:

$$a_i = \frac{A_i}{\frac{V_{bubble}}{\alpha}} = \frac{\pi d^2}{\frac{\pi d^3}{6\alpha}} \tag{96}$$

If n bubbles are measured, then the equation may be expressed in terms of the arithmetic mean of the surface area and volume.

$$a_i = \frac{\frac{1}{n}\pi \sum_{j=1}^{n} d_j^2}{\frac{1}{n}\frac{\pi}{6\alpha}\sum_{j=1}^{n} d_j^3} = 6\alpha \frac{\sum_{j=1}^{n} d_j^2}{\sum_{j=1}^{n} d_j^3} \tag{97}$$

In particle sizing, the Sauter Mean Diameter is conventionally defined as:

$$d_{32} \equiv \frac{\sum_{j=1}^{n} d_j^3}{\sum_{j=1}^{n} d_j^2} \tag{98}$$

Therefore the interfacial area concentration of n spheres is:

$$a_i = \frac{6\alpha}{d_{32}} \tag{99}$$